Investigation of Engineering Conditions to Enhance the Culture Efficiency of Human Mesenchymal Stromal Cells

Bo Zhang

Kellogg College



Institute of Biomedical Engineering,

Department of Engineering Science,

University of Oxford

Thesis submitted for

Doctor of Philosophy in Engineering Science

January 11, 2019

Abstract

As greater therapeutic potential is realized with human Mesenchymal stromal cells (hMSCs), the demand for hMSCs continues to grow. In order to improve the *in vitro* production rate and consistency, the effect of two key culture parameters, oxygen and culture surface, needs to be better understood. This study utilized biological experiments, mathematical modelling and RNA-sequencing to advance the knowledge on how *in vitro* hypoxia, and surface topography and hydrophobicity affect hMSCs growth rate.

Simulation and experimental results showed that severe hypoxia reduced, while mild hypoxia enhanced hMSCs growth rate. A novel linkage on how different oxygen levels regulate the cell cycle mechanism is proposed - through the rivalry effect of HIF1α and HIF2α. The highest growth rate was experimentally observed under 1% oxygen in two sources (one immortalized and one primary) of bone marrow-derived hMSCs.

Under normoxia, a shift in metabolism (represented by lactate production) was observed between slow-growing and fast-growing hMSCs. A flux-balance, genome-scale mathematical model was utilized with the incorporation of the proteomic resource allocation theory to capture the observed shift. Simulation results suggested the phenomenon was caused by the tricarboxylic acid cycle becoming interrupted at higher growth rates. Under hypoxia (1%), this phenomenon was not observed. Lactate production was found to positively correlate with growth rate with the interrupted Tricarboxylic acid cycle under all simulated growth rates.

Surfaces with different topographies and chemistry treatments were synthesized to culture hMSCs and were processed through RNA sequencing. hMSCs cultured on fibrous surfaces showed significantly lower growth rates and differentially regulated transcriptomes. The effect of different chemistry treatments was small, but its synergistic effect with topographical changes could be observed. Among the biomarkers commonly used for classifying hMSCs, many were significantly down-regulated on fibrous surfaces. Network and cluster analysis yielded a list of biomarkers that are not sensitive to changes in surface conditions. In addition, surface topography was found to significantly affect the expression of *HIF2A* and many *HIF2A*-correlated downstream targets. This finding suggests the possibility of designing future biomaterials to selectively activate or suppress certain hypoxic responses.

The findings from this work advance the understanding of how hypoxia and culture surfaces regulate the growth rate of hMSCs and encourages future studies to engineer an optimized set of culture conditions for hMSCs expansion *in vitro*.

Acknowledgements

The completion of this thesis would not have been possible without the support and encouragement from my supervisors, family, collaborators and friends. I would like to thank them for making my Oxford journey such an exciting and rewarding one.

I'm thankful to Professor Aidong Yang, Professor Cathy Ye and Professor Richard Darton for offering me the opportunity to study in one of the world's top universities. I'm indebted to my supervisors, Professor Aidong and Professor Cathy Ye, for supporting my research interests in different areas with unceasing guidance and encouragement.

Special thanks to Dr. Hui Wang, Dr. Naresh Kasoju, Dr. Jinmin Ma, Dr. Linh Nguyen, Dr. Bas Brinkhof, Dr. Erfan Soliman, Ms. Qiongfang Li, Mr. Robin Nyland, Ms. Hannah Zhang and Ms. Hong Zeng for generously sharing their expertise and working with me. Much appreciated also was the feedback from Prof. Zhanfeng Cui, Prof. Rene Banares-Alcantara, Prof. Jill Urban, Prof. Ester Hammond, Dr. Julian Dye, Dr. Michelle Kümin, Dr. Henry Jia, Dr. Julian George, Dr. Kasia Leszczynska, Ms. Katie St. Louis, the Tissue Engineering Group and the Systems Engineering Group.

I'm grateful to the funding support from China Regenerative Medicine International Limited, Department of Engineering Science – University of Oxford, Thomas H. Hogg Overseas Fellowship, Salters' Institute, Canadian Centennial Scholarship Fund and Kellogg College – University of Oxford.

To my friends, thank you for always being there for me and putting up with everything. To the Oxford basketball team, thank you for having me for the past three years, I will always cherish our time on the court together. To my God, thank you for blessing me with a healthy body and the strength to compete.

Finally, I would like to dedicate this thesis to my family and loved ones, especially, my parents and my fiancé, for bringing out the best in me and supporting me every step of the way.

List of Acronyms

AKGDH	α-ketoglutarate dehydrogenase
Am	Aminated surface
CDKI	CDK inhibitors
CoV	Coefficient of Variance
CT	Cell cycle commitment time
DEG	ROS-mediated degradation mechanism at greater than 10% oxygen
DGSM	Derivative-based global sensitivity measures
DNA	Deoxyribonucleic acid
FBA	Flux balance analysis
Fl	Flat surface
Fs	Fibrous surface
FPKM	fragments per kilobase of transcript per million mapped reads
Glc	Glucose
Gln	Glutamine
GO	Gene ontology
GRDP	Growth regime dependent production
hESCs	Human Embryonic stem cells
HIF	Hypoxia inducible factor
hMSCs	Human Mesenchymal Stromal/Stem Cells
HRG	Hypoxia-regulated genes
LAC	Lactate
ISCT	International Society for Cells and Gene Therapy
MSCs	Mesenchymal stromal cells

ODE	Ordinary differential equation
OXPHOS	Oxidative phosphorylation
p/p	p21/p27, CDKI
PCR	Polymerase chain reaction
PD	Population doubling
PLLA	Poly(L-lactide)
P-MSCs	MSCs acquired from PromoCell
PPP	Pentose phosphate pathway
Pr	Pristine surface
PRAT	Proteomic resource allocation theory
QMC	Quasi-Monte Carlo simulations
qRT-PCR	quantitative real-time PCR
RNA	Ribonucleic acid
ROS	Reactive oxygen species
RP	Restriction point
Stdev	Standard deviation
TCA	Tricarboxylic acid
TCP	Tissue culture treated polystyrene substrate

Table of Contents

Abstract i
Acknowledgements iii
List of Acronyms v
Table of Contents vii
Chapter 1: Introduction 11
1.1 Motivation 11
1.2 Aim 11
1.3 Thesis Structure 12
Chapter 2: Literature review 15
2.1 Human Mesenchymal stromal cells 15
2.2 Production challenge 16
2.3 Biomarkers 17
2.4 Oxygen 19
2.4.1 Oxygen level - Hypoxia 19
2.4.2 Hypoxic responses 20
2.4.3 Hypoxia sensing proteins - HIFα 21
2.5 Culture surface 22
2.6 Culture media 24
2.7 Mathematical models 25
2.8 Key knowledge gaps to be addressed 27
Chapter 3: Impact of hypoxia on growth rate 29
3.0 Summary 29
Journal Paper 1 − Mathematical modelling of interacting mechanisms for hypoxia mediated cell cycle commitment for Mesenchymal stromal cells 30
3.1 Abstract 30
3.2 Background 31
3.3 Methods 35
3.3.1 HIF modelling 38
3.3.2 Cell cycle modelling 40
3.3.3 Modelling of protein deactivation 44
3.3.4 Analysis with different parametrisation 46
3.4 Results 47
3.4.1 Dynamic behaviours 48
3.4.2 The effect of oxygen level on CT 50
3.4.3 Sensitivity of model parameters 53
3.4.4 Variability in minimum CT and optimal oxygen level 54

3.4.5 Consistency of the shape of the characterisation curve 56
3.4.6 Impact of ROS-mediated general protein deactivation 57
3.4.7 Roles of parallel mechanisms on cell cycle commitment 59
3.5 Discussion 62
3.6 Conclusions 67
Chapter 4: Metabolic shift under different growth regimes 70
4.0 Summary 70
Journal Paper 2 - Analysis of changes in the metabolic profiles of human Mesenchymal stromal cells in different growth regimes 71
4.1 Abstract 71
4.2 Introduction 72
4.3 Method 76
4.3.1 Cell culture 76
4.3.2 Cell cycle 76
4.3.3 Lactate Assay 77
4.3.4 Calibration of experimental measurements for proliferating cells 77
4.3.5 Flux balance analysis (FBA) 79
4.3.6 Proteomic Resource Allocation 80
4.3.7 Simulation Parameters 81
4.4 Results 82
4.4.1 Cell culture and lactate measurement under normoxia 82
4.4.2 Model adjustment 86
4.4.3 The incorporation of PRAT 87
4.4.4 Simulation results corresponding to normoxia 90
4.4.5 Hypoxic experiments and simulation results 95
4.4.6 Simulated glucose distribution in normoxia and hypoxia 98
4.5 Discussion 100
4.5.1 Contrasting experimental observations in normoxia and hypoxia 100
4.5.2 Learnings by mathematical modelling 102
4.6 Conclusions 107
Chapter 5: The effect of culture surfaces 110
5.0 Summary 110
Chapter 5A – Journal Paper 3 - Differential and Interactive Effects of Substrate Topography and Chemistry on Human Mesenchymal Stem Cell Gene Expression 112
5A.1 Abstract 112
5A.2 Introduction 113
5A.3 Materials and Methods 116
5A.3.1 Materials 116

5A.3.2 Study Groups 117
5A.3.3 Preparation and Characterization of PLLA Substrates 117
5A.3.4 Cell Culture 118
5A.3.5 RNA Extraction 119
5A.3.6 RNA-Seq and Data Analysis 120
5A.3.7 Statistical Analysis 121
5A.4 Results and Discussion 121
5A.4.1 Characteristics of Material 121
5A.4.2 Cell Growth and Morphology 124
5A.4.3 RNA-Seq Data Analysis 125
5A.5 Conclusions 133
5A.6 Acknowledgements 134
5A.7 Availability of data 134
Chapter 5B – Journal Paper 4 - Culture Surfaces Induce Hypoxia-Regulated Genes in Human Mesenchymal Stromal Cells 136
5B.1 Abstract 136
5B.2 Introduction 137
5B.3 Methods 140
5B.3.1 Sample preparations 140
5B.3.2 Sequencing data analysis 141
5B.3.3 Analysis of hypoxia-regulated genes 141
5B.3.4 Quantitative real-time PCR 142
5B.4 Results 143
5B.4.1 Cell culture data 143
5B.4.2 Sample variations of HRG expression levels 144
5B.4.3 Compiled expression of oxygen-sensitive surface proteins 145
5B.4.4 HIF2A is regulated by surface proteins 147
5B.4.5 Mapping HIF2A correlated genes and functions 150
5B.4.6 Quantitative PCR validation of HIF2A expression 153
5B.5 Discussion 154
5B.6 Conclusions 159
5B.7 Acknowledgements 159
5B.8 Availability of data 159
Chapter 5C – Journal Paper: Effect of Substrate Topography and Chemistry on Human Mesenchymal Stem Cell Markers: A Transcriptome Study 161
5C.1 Abstract 161
5C.2 Introduction 162
5C.3 Material and Methods 164

5C.3.1 Surface material, cell culture and RNA extraction 164
5C.3.2 RNA sequencing 165
5C.3.3 Data analysis 166
5C.4 Results and Discussion 167
5C.4.1 General characteristics of materials and cell response 167
5C.4.2 Analysis from the perspective of ISCT recommended markers 167
5C.4.3 Analysis from the perspective of a comprehensive list of markers reported in the literature 171
5C.4.4 Findings on biomaterial- stable and sensitive markers 173
5C.5 Conclusions 179
5C.6 Acknowledgements 180
5C.7 Availability of data 180
Chapter 6: Discussion and Conclusions 182
6.1 Summary of key findings 182
6.2 Limitations and future work 185
Appendices 189
Chapter 3 − Supplementary Information 189
Chapter 4 − Supplementary Information 200
Chapter 5A − Supplementary Information 206
Chapter 5B − Supplementary Information 209
Chapter 5C − Supplementary Information 219
Scholarships and Awards 221
List of Publications 222
Conference Posters 224
References 226

Chapter 1: Introduction

1.1 Motivation

Human Mesenchymal stromal cells (hMSCs) also known as Mesenchymal stem cells, can be extracted from various adult tissues, e.g. bone marrow, adipose, umbilical cord, and are widely studied for their therapeutic potential [1]. As of December 2018, there are 261 active clinical trials worldwide [2]. Various beneficial characteristics of hMSCs include immunosuppression, self-renewal, and the capacity to differentiate into adipocytes, osteoblasts, and chondrocytes [3].

Latest developments have demonstrated the positive potential of using hMSCs for treating various medical conditions, such as for myocardial infarction, osteoporosis, type I diabetes, multiple sclerosis, etc. [4-6]. Despite the encouraging evidence from *in vivo* studies and clinical trials, a few key factors need to be better understood to improve the feasibility of hMSCs-based therapy. In particular, during *in vitro* expansion, which is an important step for producing a sufficient amount of hMSCs for therapeutic uses, culture conditions can significantly affect the growth rate, plasticity, and senescence of hMSCs [7-9]. The mechanism of how a few key culture parameters, namely, oxygen level and surface characteristics (e.g. topography, chemistry) affect hMSCs status is still not well understood. In order to improve hMSCs production rate and consistency, the independent and synergistic effect of these culture parameters needs to be better understood.

1.2 Aim

The objective of this study is to better understand the impact of oxygen level and culture surfaces on the growth rate of hMSCs *in vitro*. Various techniques including

mathematical modelling and RNA sequencing were employed together with cell culture experiments to gain insights on intracellular responses by a change in oxygen or surface conditions. The findings from this study would facilitate the development of a set of optimal engineering conditions for hMSCs expansion by achieving the following objectives:

- Obtaining a better understanding of the linkages between oxygen-sensing and growth mechanisms
- Establishing a quantitative correlation between oxygen levels and hMSCs growth rate to identify an optimal oxygen level for maximizing growth
- Evaluating the changes in hMSCs metabolic uptake profile under different oxygen levels and growth regimes
- Investigating the induced changes in hMSCs transcriptome cultured on different surface topography and hydrophobicity
- Discovering any potential in using biomaterials for the regulation of key cellular functions (i.e., hypoxic regulations, cell cycle, etc.)

1.3 Thesis Structure

This thesis adopts the integrated format with reference to (and including) a total of 5 research journal papers, including 4 published and 1 to be submitted. The structure of the thesis is shown in Figure 1.1.

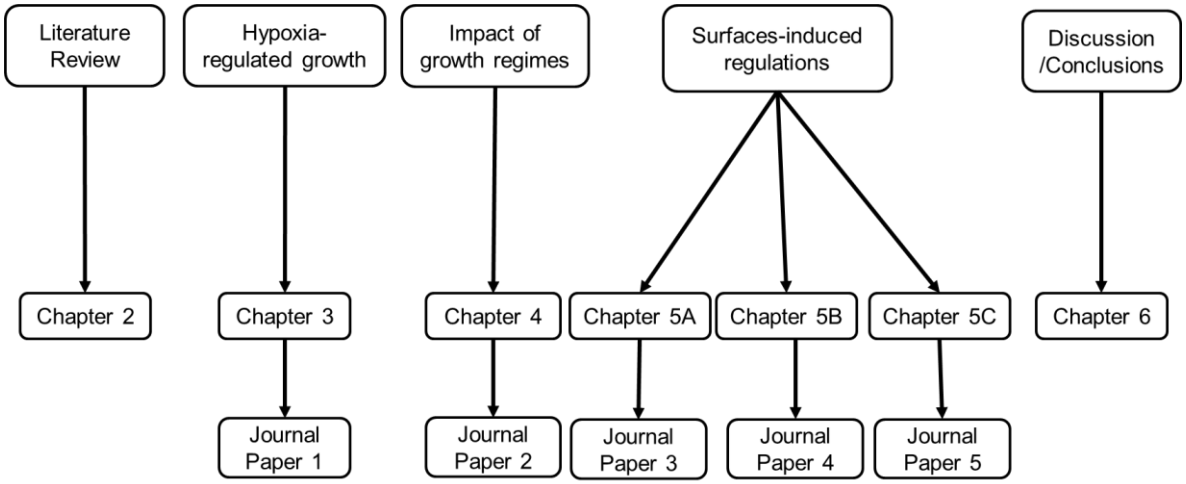

Figure 1.1: Structure of the thesis chapters and journal papers

- Literature review (Chapter 2): a brief literature review describing the general background and approaches for the intended field of study.
- The impact of hypoxia on hMSCs (Chapters 3): this chapter addresses the impact of hypoxic culture condition on the intra-cellular regulatory and proliferation of hMSCs.
- The impact of growth regimes (Chapter 4): this chapter analyzes the observed shifts in hMSCs metabolic profiles under different growth regimes and/or oxygen conditions.
- The impact of surface conditions on hMSCs (Chapter 5): this chapter investigates the effect of surface topography and chemistry on hMSCs growth rate and gene expression. Results from RNA sequencing revealed the effect of surface characteristics on altering the overall transcriptome and specific gene groups. Detailed findings are summarized into three different journal papers described in Chapters 5A, Chapter5B, and Chapter 5C.
- Discussion and Conclusions (Chapter 6): an integrated discussion and conclusions section.

List of journal papers:

Journal Paper 1 – Published in BMC Systems Biology (2018)

Mathematical modelling of interacting mechanisms for hypoxia mediated cell cycle commitment for mesenchymal stromal cells

Journal Paper 2 – To be submitted to PLOS One

Analysis of changes in the metabolic profile of human Mesenchymal stromal cells in different growth regimes

Journal Paper 3 – Published in International Journal of Molecular Science (2018)

Differential and Interactive Effects of Substrate Topography and Chemistry on Human Mesenchymal Stem Cell Gene Expression

Journal Paper 4 – Published in Biomedical Materials (2019)

Culture Surfaces Induce Hypoxia-Regulated Genes in Human Mesenchymal Stromal Cells

Journal Paper 5 – Published in International Journal of Stem Cells (2019)

Effect of Substrate Topography and Chemistry on Human Mesenchymal Stem Cell Markers: A Transcriptome Study

Chapter 2: Literature review

2.1 Human Mesenchymal stromal cells

In the past decades, the high proliferation and differentiation capacity of hMSCs has spurred great interests in studying their clinical applications [1, 10]. hMSCs can be extracted from various tissues of the human body (e.g. bone marrow, umbilical cord, and adipose) and are able to self-renew and differentiate into adipocytes, osteoblasts, and chondrocytes [11]. Ongoing research aims to better quantitatively and qualitatively characterize hMSCs identity and characteristics *in vitro*, and their benefits *in vivo*. Biological and computational techniques are used to improve the characterization and efficiency in hMSCs extraction, the capacity and robustness in hMSCs expansion, and the reliability and efficacy in post-transplantation tracking and evaluation.

Medical potential for hMSCs has been shown in tissue regeneration, cell therapy to combat sclerosis, liver diseases, diabetes, etc. [12-15]. Clinical trials have shown effective hMSCs treatments on cartilage defects [16], osteogenesis imperfecta [17, 18], systematic lupus erythematosus [19, 20], liver cirrhosis [21], and myocardial infarction [13, 22]. In addition, the study of hMSCs has been speculated to contribute to cancer therapy [23]. Clinical demands for hMSCs continue to grow as more plausible treatments are confirmed. The development towards an off-the-shelf model for hMSCs supply further increases the demand for production and preservation [4].

The database of *Web of Science* shows that the amount of publications and patents involving hMSCs grew at a steady pace from 2005 - 2018. Field estimated the market value for stem cell therapy market would grow from $5 million in 2012 to $8.7 billion in

2025, with over 90% coming from adult stem cells [24]. As of May 2019, using the search string of “Mesenchymal stromal cells” and “Mesenchymal stem cells”, a total of 986 trials is registered on *clinicaltrials.gov*, 396 of which are currently active [2]. Meanwhile, 267 trials involving hMSCs have been completed, among which 16 were in Phase-3 or Phase-4, further demonstrating the potential of utilizing hMSCs in facilitating the treatment of myocardial infarction, rheumatoid arthritis, graft-versus-host diseases, etc. [2]. Kim and Cho published a thorough review on the ongoing hMSCs clinical trials [23]. As more positive feedback from clinical trials is received, the market potential for hMSCs-based treatment is expected to continue to grow.

2.2 Production challenge

A large quantity (up to 6 billion cells [25]) of high quality hMSCs is needed for each cell therapy or *in vivo* implementation [26]. Traditionally, expansion is carried out by allowing hMSCs to grow on a static, flat surface, under 20% oxygen, 5% CO_2 and controlled humidity. This technique can only supply low doses of hMSCs (up to 50 million [27]), which is inadequate in meeting the increasing demand [4]. Novel approaches such as bioreactors have been developed in recent years to facilitate hMSCs production [28-35]. However, a lack of understanding on how different culture parameters regulate the intracellular mechanisms still poses a major challenge in enhancing the production capacity of hMSCs.

There are a number of research projects which aim to design culture parameters to mimic the hMSCs niche environment in human bodies by varying oxygen, surface, and properties of the culture media. Studies have investigated independent as well as

synergistic effects of these culture conditions on reducing hMSCs population doubling time, preserving stemness, extending longevity and reducing senescence [28, 36-40]. The impact of the individual parameters is described in detail in sections 2.4, 2.5 and 2.6.

In vitro culture conditions have yielded hMSCs with subpar proliferative capability, multipotency (or plasticity), and preservation longevity [41-43]. Reports have shown that primary hMSCs are able to expand and retain their potency up till passage 22 [44]. Growth rate is reduced with each passage, as reflected by an increase in population doubling time [42, 43]; the number of cells exhibiting stem cell characteristics is also reduced with each passage due to the loss of potency markers [41, 45-48]. This may be due to the combined effect of external culture conditions and intrinsic cell aging. It is important to understand how culture conditions affect the proliferative capacity of hMSCs in order to maximize production with limited longevity.

2.3 Biomarkers

The International Society for Cells and Gene Therapy (ISCT) proposed a list of criteria, including surface markers, for classifying hMSCs [49]. 3 positive (CD73, CD90, and CD105) and 6 negative (CD45, CD34, CD14 or CD11b, CD79α or CD19 and HLA-DR) markers have been defined for identifying hMSCs [49]. These biomarkers are used to select the subpopulation of cells with superior multipotency and colony-forming capacities and differentiate from hematopoietic cells. However, many studies have reported that the 3 positive biomarkers are not sufficient to accurately identify hMSCs and other surface markers may be required [50-52].

To date, it is not yet clear if any individual or set of surface markers are primarily responsible for regulating hMSCs multipotency and colony-forming potential; experimental results have shown that a wide range of surface markers are associated with these two cellular functions [50, 53].

Over 180 additional surface markers have been proposed to enhance hMSCs identification/classification [53-55]. Table 2.1 lists a few hMSCs biomarkers which have been proposed in multiple studies [53]; a detailed review on these biomarkers can be found in [53].

It remains to be elucidated if a list of surface markers can best represent and characterize hMSCs. With the commonly regarded heterogeneity of hMSCs and the lack of a consistent classification standard, it remains challenging to monitor and maintain hMSCs production quality and compare the findings from different studies.

Table 2.1: The list of additional hMSCs biomarkers that have been proposed in various studies.

Markers	References
Stro-1	[56-58]
CD271	[55, 59, 60]
CD146	[58, 61-63]
SSEA4	[61, 64]
CD49f	[65, 66]
GD2	[67]
3G5	[68, 69]
Sox11	[70]
TM4SF1	[71]

2.4 Oxygen

Oxygen plays an important signalling role in regulating hMSCs key cellular functions (e.g. growth, metabolism, migration, potency). Different levels of culture oxygen have been found to significantly affect hMSCs status.

2.4.1 Oxygen level - Hypoxia

Oxygen level in hMSCs niche ranges from 1-8% [5, 72]. The culturing of hMSCs under atmospheric oxygen level, or commonly known as *in vitro* normoxia, exposes hMSCs to a hyperoxic environment that can induce senescence and DNA damage [73, 74]. In order to mimic the environment of hMSCs niche, experimental studies have been designed to study culturing hMSCs under lower oxygen levels, i.e. under *in vitro* hypoxia (less than 20% oxygen).

2.4.2 Hypoxic responses

The culturing of hMSCs under *in vitro* hypoxia has been found with enhanced preservation of multipotency and reduced senescence [38, 75-84]. The study of the impact of hypoxia on regulating hMSCs growth rate yielded opposing results. The enhanced hypoxia-mediated growth rate was reported under 1% [75, 83], 2% [47, 79, 82], 3% [42, 85], and 5% [77, 86, 87] oxygen levels. However, other reports highlighted reduced growth rates under 1% [48, 88, 89], 2.5% [90], 3% [89], and 5% [90] oxygen.

Various factors may have contributed to the observed discrepancy. Inherently, hMSCs from different tissue origins, passage numbers, extraction/isolation techniques, donor conditions, were used in various studies carried out in different laboratories. In addition, the heterogeneity of hMSCs cell pool is widely regarded [91, 92]. In the culture environment, the presence and variability of serum provides an uncertain level of growth stimuli to cells. Certain apparatus used for hypoxic culture was not fully contained, and hMSCs experienced intermittent “oxygen shock” when cells were taken out of the hypoxic environment for operations (e.g., media change, sampling or imaging). The variation in these factors makes it challenging to compare the experimental data in the literature to study how hypoxia affects the growth rate of hMSCs.

As oxygen level significantly regulates the growth rate of hMSCs, it is crucial to understand what caused these contrasting experimental observations in order to engineer an oxygen condition to maximize cell yield. Further literature reviews are included in Chapters 3 of this thesis.

2.4.3 Hypoxia sensing proteins - HIFα

Cellular response to hypoxia is sensed and initiated by the hypoxia inducible factors (HIFα) [93, 94]. HIFα is constantly translated and degraded in the presence of molecular oxygen, e.g. under normoxia. Molecular oxygen modifies HIFα protein in the presence of 2-oxoglutarate and prolyl hydroxylase; the modified protein is recognized and degraded in a ubiquitin-dependent manner [93, 95]. Under hypoxia, the degradation mechanism ceases which allows HIFα to accumulate. In addition, hypoxia increases the transcriptional activity of HIFα [95-97].

Following the build-up of HIFα, HIFα forms a heterodimer with Hifβ (which is independent to oxygen level) and translocates into the nucleus, which then binds onto hundreds of targets to initiate hypoxic responses [94, 98]. The HIFα-mediated functions include cell cycle progression, multipotency, vascularization, glycolysis, migration, survival, etc. [99-101]. These functions facilitate cellular adaptation to an environment with lower oxygen availability. The metabolic network adjusts in a HIFα-dependent fashion to reduce oxygen consumption, and growth is hindered as a pro-survival response to reduce DNA damage [93, 102]. Other upregulated functions (i.e. angiogenesis, vascularization) facilitate blood vessel formation to enhance oxygen transport into oxygen-deprived tissue areas. Various key functions are regulated by HIFα-mediated pathways to facilitate the adaptation to short-term and long-term hypoxia.

Three isoforms of HIFα have been identified each with distinct functions and different oxygen-dependent profiles [96]. HIF1α is ubiquitously expressed in mammalian cells

[96, 103]. HIF2α are found with more restricted expressions [104, 105] and distinct roles in regulating stem cells and cancer cells [106-108]. Hif3α is the least understood isoform and has been considered to function in corroboration with HIF1α and HIF2α and form splice variants [109-111]. Despite sharing a similar oxygen-dependent domain, HIF1α and HIF2α have very different regulation targets [112-116], and pose rivalry effects on certain functions, e.g. regulating cell cycle progression [117, 118]. HIF1α and HIF2α are considered as the key hypoxic hallmark proteins and regulators on hypoxic responses [119, 120].

Further literature review on the regulation of HIF1α and HIF2α is included in Chapter 3 of this thesis.

2.5 Culture surface

As adherent cells, hMSCs need to attach to a surface to survive. It is therefore important to understand how the cell-material interactions affect hMSCs fate decisions [49]. Upon hMSCs firmly anchoring to the surfaces, focal adhesion complexes are formed of different size, length and density responding to surface properties and regulating cellular functions [121]. Culture surface can be modified through topography, material type, chemistry, and stiffness.

Studies have found that surface topography affects the availability and favourability of the binding sites [121, 122], material type and chemistry alter the adhesion strength and composition of the complex [123-125], and stiffness regulates the ability for cells

to generate tension through these complexes [126, 127]. Different combinations of these surface parameters can differentially regulate cellular responses via the activation of surface proteins, formation of focal adhesion complexes, and the subsequent signalling and regulatory pathways.

Traditionally, hMSCs are cultured on flat (two-dimensional), polystyrene surfaces. In order to better mimic the niche environment, three-dimensional environment have been designed for hMSCs culture in forms of overlaying electrospun fibres [36, 128, 129], 3D-printed nano-structured surfaces [130-133], and encapsulated in hydrogels [134-136]. These three-dimensional surfaces have enhanced paracrine functions [128, 129] and significantly regulated proliferative and differentiation capacity of the hMSCs cultured on these matrices [36, 137-142].

Surface chemistry properties including materials, chemical functionality, and stiffness all significantly affect hMSCs status [143]. Various polymeric [144], and inorganic materials [145] have been used to study hMSCs culture, having a significant impact on hMSCs differentiation and stemness. The typically applied polymer-based material includes polylactic acid, polydimethylsiloxane, polyglycolic acid, and polyethylene glycol [123]. In addition, functionalised culture surfaces can significantly regulate stemness, independently [146] and synergistically with a change in topography [147]. Furthermore, surface stiffness has shown significant impact on leading hMSCs differentiating towards a particular phenotype [126, 127]. Matrix stiffness can be altered by varying the degree of crosslinking in hydrogels, which subsequently regulates hMSCs differentiation capacity [143] and may also impact proliferation [148].

Stiffer surfaces (measured by Young's modulus) showed stronger tendency for hMSCs osteogenic differentiation while softer surfaces favoured adipogenesis and neurogenesis [148, 149].

Cell-biomaterial interactions have been reported to play a crucial role in regulating cell adhesion, migration, differentiation, and proliferation [123, 141, 150-152]. It is one of the key engineering factors that needs to be further studied. Detailed review on the effects of materials properties on stem cells can be found in [123, 153-155]. Further literature reviews on how different material properties impact different cellular functions are included in Chapter 5 of this thesis.

2.6 Culture media

Media composition plays an important role in the culture of hMSCs. The concentrations of different metabolites and growth factors can affect their proliferation and differentiation capacity [156-158]. To support hMSCs growth, sources of carbon and nitrogen need to be supplied in abundance. Different basal media (e.g. Modified Eagle's medium, Dulbecco's Modified Eagle's Medium, Roosevelt Park Memorial Institute) are available on the market, supplementing glucose, glutamine and other amino acids to sustain cellular demand. Growth factors and cytokines are needed in the medium to promote hMSCs growth [159-161], including fibroblast growth factor, platelet-derived growth factor, vascular endothelial growth factor, etc. [162]. Further literature reviews are included in Chapter 4 of this thesis. Years of research and development have led to various optimized MSCs-specific media being developed for hMSCs expansion, e.g. MesenCult (Stem Cell Technologies), CellGenix MSC

(CellGenix), Nutristem (Biological Industries), etc. The utilization of these chemically defined media reduces the batch-to-batch variability and improves experiment consistency.

2.7 Mathematical models

Mathematical models have been used to provide insights into biological systems. Due to the transient and complex nature of biological systems, mathematical simulations can economically and efficiently explore the impact of parameter variations and investigate areas that are challenging to explore using experimental techniques. Various mathematical techniques and databases have been developed to facilitate the applications ranging from optimizing bioreactors operations to discovering novel molecular mechanisms [163-166].

Various studies have used mathematical models to better understand interactions among biological species or to optimize culture conditions for the target objective. Models have been constructed at different scales which can be classified as microscopic/intracellular, mesoscopic/cellular, and macroscopic/population-based [164]. Intracellular models are constructed based on detailed or simplified reaction equations to study molecular interactions, pathways, and networks in a biological system. For instance, models based on differential equations have been constructed for studying protein-protein interactions and suggesting novel molecular functions [167-170] or for confirming certain hypothesized regulatory pathways [171, 172]. On the other hand, models based on a mass/mole-balance framework have been used to elucidate the distribution of fluxes in cellular metabolic networks [173]. At the

mesoscopic scale, the models aim to capture the interactions between single cells and how they subsequently regulate or evolve the system. Simplified intra-cellular models may be incorporated to represent the response and processing of cellular signals. This type of model can be used to study cell-cell interactions and regulations in co-culture systems [174-176]. Population-based models aim to evaluate the impact of culture parameters (e.g. diffusion factors, oxygen, fluid-induced shear stress) on regulating cell pool status. They can be applied to optimize bioreactors operating conditions [29, 34, 40, 177] or in understanding hMSCs behaviours in three-dimensional tissue constructs [30, 178-182].

Various toolboxes, packages, solvers, and databases have been compiled to improve the approach and accuracy of simulations. Different platforms have been detailed in [164], describing the available computational models and relevant experimental data. The development of various -omics (i.e. genome, transcriptome, proteome, metabolome, interactome, and phenome) techniques generates large datasets which can be used to advise the construction and calibration of mathematical models; a detailed review can be found in [163].

Despite the advancement in experimental and computational techniques, the complex and transient nature of biological systems challenges the quantitative findings from simulations. Experimentally measured parameter values are, in most cases, not available for the phenotype of interest. In addition, not all of the interactions for the biological species of interest (e.g. proteins, intracellular complexes, cells) have been confidently identified and quantified. The impact of certain species may have been

over- or under-estimated due to experimental bias. All these factors can have a significant impact on the accuracy of the simulation. Different techniques (e.g. global sensitivity analysis, bifurcation analysis) need to be employed to evaluate the robustness of simulation findings. In order to evaluate the confidence of simulation results, it is crucial to understand how a change in parameter values, initial conditions, and key interactions affect the simulation outcome.

The utilization of mathematical models complementary to experimental studies can generate novel discoveries. However, due to the complex nature of biological networks, the constructed models suffer drawbacks of lacking reliable parameter values. The objective and available resources (e.g., toolbox, experimental data) need to be carefully considered in choosing the appropriate model structure. The confidence in the simulation findings also needs to be evaluated. Further literature reviews on intracellular and flux-based models are included in Chapter 3 and Chapter 4 of this thesis, respectively.

2.8 Key knowledge gaps to be addressed

The growth rate of hMSCs under *in vitro* hypoxia showed contrasting results in the literature. Most literature studies used different experimental setup and have data from less than 2 hypoxic oxygen levels; it is therefore challenging to determine the oxygen level for maximizing hMSCs production. Currently, a set of experiments evaluating the growth rate of hMSCs under different *in vitro* hypoxic oxygen levels is missing. In addition, despite the advanced understanding on hypoxia-sensing proteins (HIFα), the mechanism of how molecular oxygen affects growth rate is still not well understood.

Traditionally, the study of biomaterials involves testing specific markers to represent its compatibility and functions. Various studies in the literature have examined how different topography and surface chemistry affect the status of hMSCs. However, these studies only reported the selected gene expressions and biological functions, a change in the global representation of the hMSCs transcriptome has not been evaluated.

Chapter 3: Impact of hypoxia on growth rate

3.0 Summary

This work is motivated by the contrasting findings reported in the literature on whether hypoxia facilitates the growth rate of hMSCs. The findings are presented in Journal Paper 1 and additional Supplementary Information attached in the Appendices.

A mathematical model was constructed to study the intracellular regulation of hypoxia on the growth rate of hMSCs. It was a single-cell model using parameter values obtained from the literature. The model was able to simulate the varying rate of cell cycle progression in response to different oxygen levels. Simulation findings are presented in Journal Paper 1, along with the relevant literature review and methodology.

Experiments were designed to reduce the variability in culture parameters and evaluated to confirm that the findings from the mathematical model. hMSCs from two origins were tested to confirm the effect of hypoxia on growth rate is preserved. The findings are presented in the Appendices. Due to space constraint, only key findings are included.

The findings from this chapter improved on the understanding of how hypoxia regulates the growth rate of hMSCs. Findings from the simulation results proposed a hypothesis on the mechanistic relationship between hypoxia-sensing proteins and cell cycle mechanism. Experimental and simulation data both suggest the existence of an oxygen level which allows maximizing the growth rate of hMSCs *in vitro*.

Journal Paper 1 − Mathematical modelling of interacting mechanisms for hypoxia mediated cell cycle commitment for Mesenchymal stromal cells

- Published in BMC Systems Biology (2018)

Bo Zhang[1, 2], Hua Ye[2], Aidong Yang[1, *]

[1]Department of Engineering Science, University of Oxford, Oxford, United Kingdom

[2]Institute of Biomedical Engineering, Department of Engineering Science, University of Oxford, Oxford, United Kingdom

* Corresponding author

3.1 Abstract

Existing experimental data have shown hypoxia to be an important factor affecting the proliferation of mesenchymal stromal cells (MSCs), but the contrasting observations made at various hypoxic levels raise the questions of whether hypoxia accelerates proliferation, and how. On the other hand, in order to meet the increasing demand of MSCs, an optimised bioreactor control strategy is needed to enhance *in vitro* production. A comprehensive, single-cell mathematical model has been constructed in this work, which combines cellular oxygen sensing with hypoxia-mediated cell cycle progression to predict cell cycle commitment as a proxy to proliferation rate. With oxygen levels defined for *in vitro* cell culture, the model predicts enhanced proliferation under intermediate (2-8%) and mild (8-15%) hypoxia and cell quiescence under severe (<2%) hypoxia. Global sensitivity analysis and quasi-Monte Carlo simulation revealed that within a certain range (+/-100%), model parameters affect (with varying significance) the minimum commitment time, but the existence of a range of optimal oxygen level could be preserved with the hypothesized effects of Hif2α and reactive oxygen species (ROS). It appears that Hif2α counteracts Hif1α and ROS-mediated protein deactivation under intermediate hypoxia and normoxia (20%), respectively, to regulate the response of cell cycle commitment to oxygen level. Overall, this modelling study offered an integrative framework to capture several interacting mechanisms and allowed *in silico* analysis of their individual and collective roles in shaping the hypoxia-mediated commitment to cell cycle. The model offers a starting point to the establishment of a suitable mechanism that can satisfactorily explain the different existing experimental observations from different studies and warrants future extension and dedicated experimental validation to eventually support bioreactor optimisation.

3.2 Background

Hypoxia has been shown to enhance the proliferation of cancer cells, stromal cells and stem cells [183-185], though the exact mechanisms remain to be elucidated. It has been hypothesised that a lower oxygen concentration facilitates cell cycle progression and reduces the generation of reactive oxygen species (ROS) [108, 117, 118], which would otherwise incur elevated apoptosis and mutation [186]. On the other hand, experiments have found that hypoxia can drive cells into quiescence to escape from oxidative stress [48, 77, 89, 186]. These inconsistent experimental findings in the literature could potentially be attributed to cell pool heterogeneity or different culture conditions. With the increasing market demand for large-scale *in vitro* stem cell production, it is crucial to establish the definitive impact of hypoxia on stem cell proliferation. In particular, a mathematical model that incorporates the key mechanisms regulating the influence of oxygen concentration on cell cycle can be instrumental, which is currently lacking.

One factor that contributes to the controversy over the effects of hypoxia on cell proliferation is the lack of agreed definition for “hypoxia” and “normoxia” [100]. Physiologically, oxygen concentration in blood is around 5-13%, and is further reduced in tissues [184]. Some reports used oxygen levels of less than 5% as the normoxic oxygen standard [184, 187] to reflect the physiological “in situ normoxia” [188]. Contrastingly, a majority of others used atmospheric oxygen level of 20% to represent a controlled normoxia environment for cell culture *in vitro* [48, 77, 183]. Additionally, a wide range of oxygen levels have been referred to as hypoxia in cell cultures, from 0.2% - 5% [185, 189-191]. The collective ambiguity in these definitions imposes further challenges in identifying how lower oxygen conditions affect cell proliferation. To avoid

confusion, the following ranges defining *in vitro* cell culture oxygen levels are used consistently throughout the current paper: severe hypoxia (<2%), intermediate hypoxia (2% - 8%), mild hypoxia (8% - 15%), normoxia (15% - 20%).

In general, each cell line possesses a unique set of characteristics to govern how it responds to oxidative stress. This work was designated as part of an effort to improve *in vitro* culture of human mesenchymal stromal cells (MSCs). However, due to the lack of a complete set of protein expression data for MSCs from a single source, results from experimental studies of different cell lines have been used. The mechanisms/systems that are evolutionarily conserved and shared across cell lines are distinguished from those that are distinct in each tissues/species. The basic cell cycle model has been found in yeast, *drosophila*, mammalian cells, etc. [192]. It is believed that the mechanisms are comparable, despite the genetic differences. Hypoxic responses can be split into the downstream actors of hypoxia inducible factor (HIF) isomers, Hif1α and Hif2α. Hif1α expression has been found in most cells and it affects cell metabolism, angiogenesis, cell cycle progression, survival, etc. [193]. Hif1α has also been reported to maintain MSCs pool in a primitive state by allowing selective self-renewal [194]. Hif2α is cell line specific and regulates cell proliferation, vascularization and maintains stem cell characteristics [195]. Intracellular oxygen molecule allows prolyl hydroxylase and 2-oxoglutarate to corroborate in tagging HIF for ubiquitin-dependent degradation [193]. Despite similar mechanisms, the characteristics of this oxygen-dependent degradation are different between the isomers. As a result, the relative protein accumulation under normoxia is different between the two isomers, albeit always much lower than their hypoxic levels.

In the existing literature, most hypoxia-induced quiescence was reported under severe hypoxia [48, 77, 89, 90], where the Hif1α level and activities are prominent. Enhanced proliferation was observed under intermediate and severe hypoxia conditions [75, 82, 83, 183-185, 196], where the relative strength of Hif2α overshadows that of Hif1α. The differential responses of Hif1α and Hif2α to oxygen level are believed to be key in explaining seemingly contradictory observations with respect to cell cycles under the broadly defined hypoxia conditions [100, 117]. Other hypoxia-mediated factors (i.e., Notch [197]) are not captured in this work because of a missing consensus on their impact on cell cycle progression.

Various sophisticated models [169, 198, 199] have been proposed to predict the level of Hif1α protein in response to cellular oxygen level, which are continuously evolving as more mechanisms are discovered. On the other hand, an exponential decay model has been used as a proxy for a simplified estimation of total Hif1α protein as a function of oxygen level [198, 200], which is also adopted in this work.

A proliferating cell commits to cell cycle when it passes the restriction point in late G1 phase, which is a process that has been represented by a few existing models. Bedessem and Stephanou [200] established a model describing how hypoxia prolongs cell cycle commitment, expanding on Novak and Tyson's work [192]. The effect of oxygen on cell cycle was linked through Hif1α protein. Hif1α was assumed to have a direct inhibitory effect on cyclin D, based on the findings from Wen *et al.* [191]. Threshold levels for cyclin E and SCF, a cyclin E antagonist, were set to collectively mark G1-S phase transition. The model showed that the time required by the commitment to cell cycle increases as oxygen level decreases. At below 0.06%

oxygen, cell quiescence was reached. The Hif1α estimation is only applicable in the case of up to 6% oxygen. The authors acknowledged the activation effect of Hif2α on cyclin D but only focused on the effect of Hif1α in their model.

Dong *et al.* [201] modelled the effect of E2F level on cell cycle entry with experimental validation. More than 100 single-cell analyses were performed to correlate cell proliferation status against their E2F level. The level of E2F was found to govern G1-S phase commitment, whereas the levels of cyclins D and E and Myc affect the time required to reach the transition point. Different Myc-inhibitors were tested to indicate the significance of Myc protein in regulating cell cycle. The model presented in Dong *et al.* [201] incorporates the cumulative findings from the previous simulation and experimental discoveries by their group [202, 203]. The effect of CDKI (cyclin dependent kinase inhibitor) and possible linkage to hypoxic responses were not addressed in the study.

Another approach in modelling proliferation has been associated with cellular metabolism and the consideration of nutrient supplies [204]. HIF alters cellular metabolic pathways and nutrient uptakes under hypoxia [102]. The current study does not include the metabolic impacts on proliferation and assumes the nutrient supply to be always in excess. Other HIF-mediated hypoxic regulation of proliferation has been reported [205] but the incorporation of these pathways is beyond the scope of this study.

With the purpose of enhancing stem cell proliferation, this work aims to distinguish the effects of hypoxia on cell proliferation qualitatively and quantitatively, through

modelling the protein-level variations. To this end, models described in the literature mentioned above, although very relevant, need to be further enhanced particularly in two respects, namely (i) incorporating both Hif1α and Hif2α into the cell cycle model to encompass their distinctive roles, and (ii) connecting the hypoxia sensing model with the cell cycle model, through Myc protein, to enable the direct prediction of the effect of hypoxia level on cell cycle commitment. The intention of this work is to build such an improved model and use it to (i) make predictions of the impact of hypoxia on cell proliferation over the whole range of relevant oxygen concentration levels, against various experimental observations as introduced earlier, (ii) elucidate the likely roles of parallel mechanisms regulating cell cycle progression that underpin the predicted and observed behaviours, and (iii) identify significant model parameters and hypotheses that deserve special attention of further investigation. The learning from this work thus may hold the potential to form a foundation of future research for enhancing the *in vitro* culturing efficiency of MSCs and other cell lines by the optimal control of oxygen concentration in bioreactors.

3.3 Methods

A model to quantitatively reflect how hypoxia affects cell proliferation has been constructed (Figure 3.1). The key features of the model include linking hypoxia sensing and cell cycle progression. Furthermore, Myc protein is used as the primary intermediate actor to correlate HIF protein levels to various cell cycle regulators. Hif1α and Hif2α physically bind to Myc to inhibit or enhance its activity, respectively. As the availability of two HIF isoforms varies with oxygen concentration, the effective Myc level is affected and results in the change in the cell proliferation status. A direct transcriptional inhibition of Hif1α on cyclin D is included [191, 200].

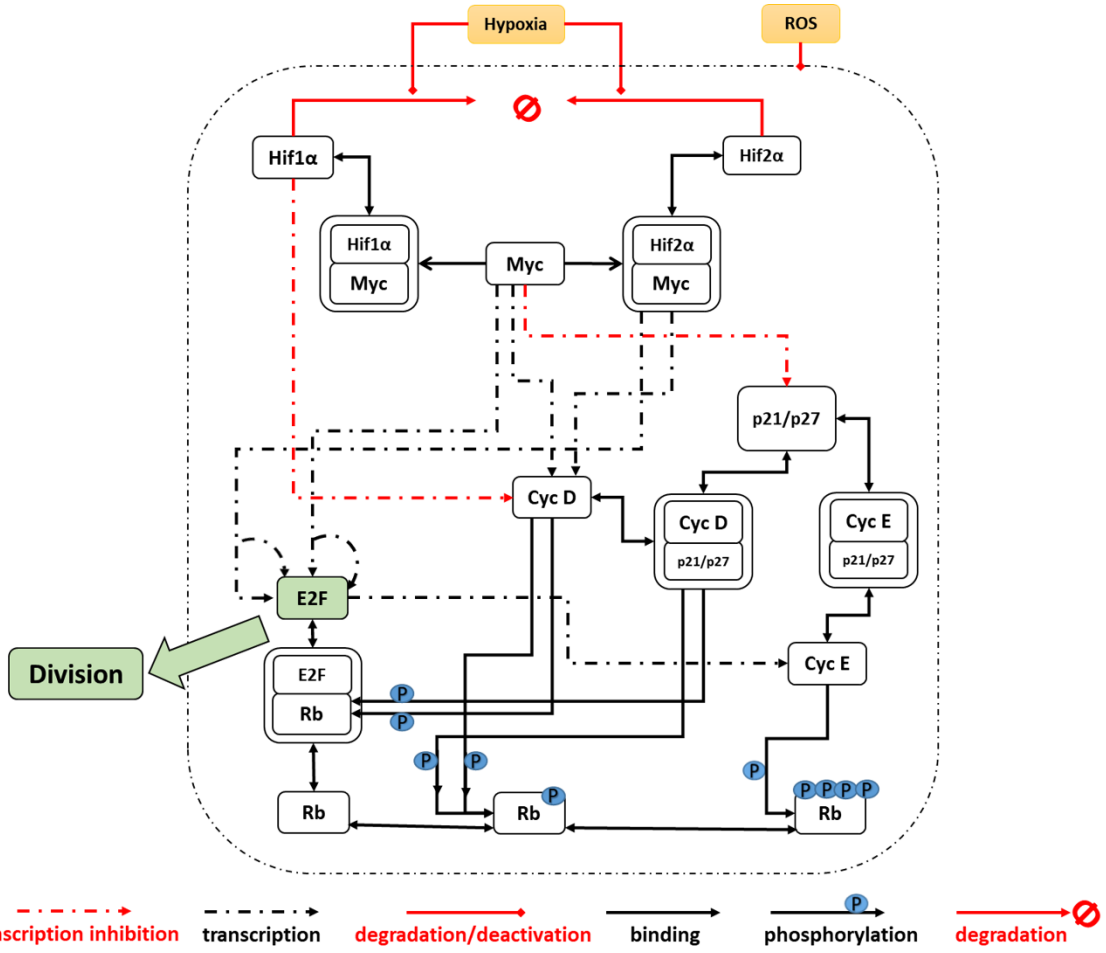

Figure 3.1. Assumed simplified mechanisms for the effects of hypoxia on cell cycle commitment. Hypoxia varies the active amount of Hif1α and Hif2α proteins, through which cell cycle regulating proteins are regulated. The variation in cell cycle regulators positively (cyclin D, cyclin E, Myc) or negatively (p21/p27 and Rb) controls the downstream protein level of E2F. The progression of cell cycle G1-phase into S-phase commitment is controlled by the accumulation of E2F protein exceeding a set threshold level. Different biological interactions are shown in the figure.

The current model aims to capture the effects of oxygen content in regulating the time required for a proliferating cell to commit to progressing past the restriction point, after which the process of cell division becomes irreversible. The model considers a hypoxic culture condition with a specific oxygen level which determines the concentrations of HIF. To focus on key mechanisms and maintain simplicity, assumptions were made in several parts of the model, in comparison with the more detailed treatments available in the literature [169]. Non-stem-cell data was used to calibrate Hif1α and cell cycle

models, as they appear to be common among different cell types. No literature evidence was found to question the validity of using these data for stem cell modelling. Stem cells data on Hif2α expression were obtained from the literature.

The model equations are presented in the following sections. In general, the mechanisms for protein-protein binding, transcription and phosphorylation are represented by the Hill function to capture the sigmoidal or hyperbolic behaviour. The behaviours that are regulated by more than one factor (e.g., the Myc-dependent auto-catalytic transcription of E2F) are captured by multiplying the relevant terms. Protein-protein interactions are described with mass-action kinetics, consistent with literature models [201, 203]. In these equations, variables in brackets represent concentrations of various species (including proteins and oxygen). “k”, “m” and “n” are used to denote different types of constants, which are further distinguished by subscripts. “kf” and “kr” are the respective forward and reverse rate constants. “g” indicates the basal generation rate and “d” represents the basal degradation rate of respective proteins. Protein-to-protein binding is represented by “-” that connects two proteins. “DEG” is a parameter that represents a basal protein deactivation and degradation mechanism. Exponential and absolute value functions are expressed by “exp” and “abs”, respectively.

Overall, the hypoxia sensing – cell cycle progression model consists of 13 ODEs and 3 algebraic correlation equations (Equations 3.1, 3.2, 3.8). The parameters and initial conditions were obtained or adjusted from literature data, as shown in the Supplementary Information. Unless stated otherwise, these values have been taken as nominal values in the simulation studies reported in this work.

3.3.1 HIF modelling

An exponential expression is used in place of the more complex depiction to estimate the available HIF protein. Bedessem and Stephanou [200] and Dayan *et al.* [198] applied such an approach to estimate the total amount of Hif1α protein at different oxygen concentrations. Experimental data from six different cell lines from Bracken *et al.* [206] confirms the validity of the exponential relationship. It is further assumed that all available Hif1α proteins are functionally active and nucleus-bound. Equations 3.1 and 2 estimate the level of Hif1α and Hif2α proteins, respectively. "t_i" is the normalization oxygen level and "p_i" is the oxygen level where HIF protein peaks, i=1 or 2.

$$[\boldsymbol{Hif1\alpha}] = m1 * exp\,(b1 * (1 - abs\,(p1 - [O_2]) / t1)) \qquad \textbf{\textit{Equation 3.1}}$$

$$[\boldsymbol{Hif2\alpha}] = m2 * exp\,(b2 * (1 - abs\,(p2 - [O_2]) / t2)) \qquad \textbf{\textit{Equation 3.2}}$$

Jiang *et al.* [190] reported the measured Hif1α level for 0.5 -10% oxygen, which was used for model calibration. A decline in Hif1α level at below 0.5% was also observed [190]. Various reports found that Hif1α protein was undetectable at greater than 5% oxygen in stem cells [185, 189]; Bracken *et al.* reported that Hif1α protein became negligible at higher than 10% oxygen in various cell lines [206]. In our model, the operating range for Hif1α is set at 0.5%-10% oxygen with an exponential decline behaviour. The simulation result is shown in Figure 3.2. The maximum Hif1α concentration is assumed to be 5 μM, using data reported from abcam [207]. Note that Hif1α protein has been detected under atmospheric oxygen condition; this

phenomenon may be cell line or medium specific [206], and will be accounted for when a complete, comprehensive data set becomes available in the future.

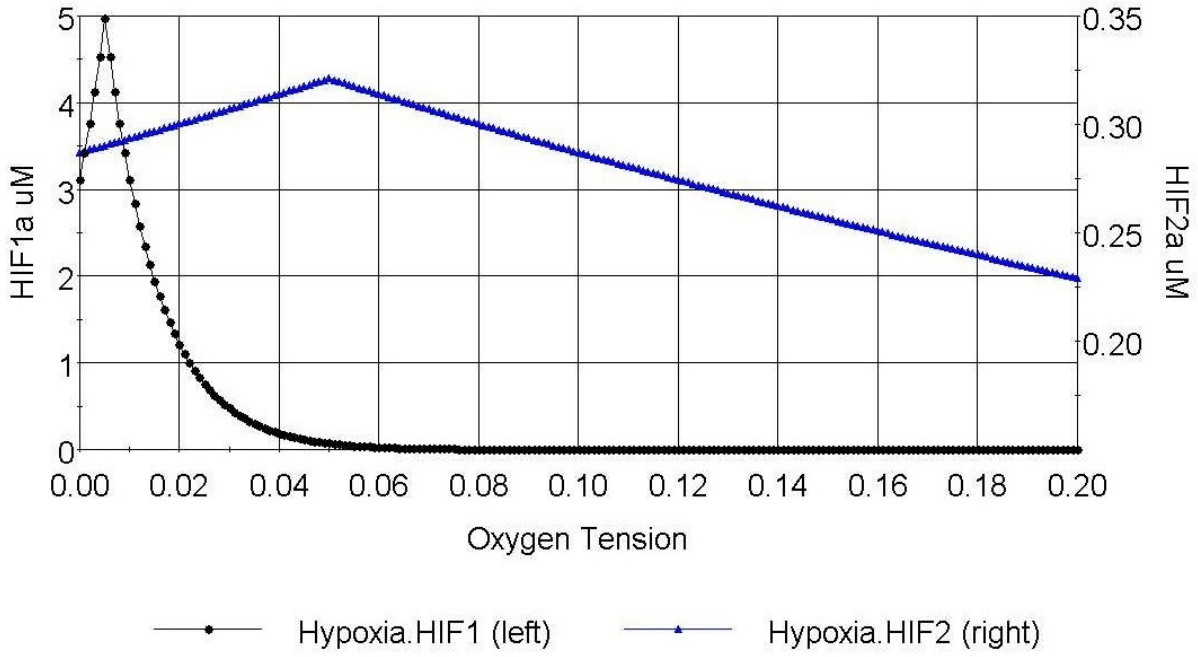

Figure 3.2: Simulated expression of Hif1α and Hif2α at different oxygen levels from this study. Hif1α (black) level corresponds to the primary axis. Hif2α (blue) level corresponds to the secondary axis.

No existing model for the response of Hif2α to oxygen level was found in the literature. Hif2α is thus assumed to behave in the same exponential fashion as Hif1α. In stem cells, Hif2α protein was found to peak at oxygen levels between 2-5%, higher than that of Hif1α [117]. The model sets a peak value for Hif2α protein at 5% oxygen. At below 5% oxygen, Hif2α protein level is assumed to mirror its behaviour at greater than 5%. Hif2α proteins are detectable in cells cultured under 20% oxygen [185, 189]; therefore, the exponential decline is assumed to be valid for the entire range of the simulated oxygen level. The expression level of Hif2α appears to vary significantly across cell lines, therefore it is necessary to use stem cell data for calibrating its model. The western blot data of human Embryonic stem cells (hESCs) from Forristal *et al.* [185] distinguished the relative expression of Hif2α protein between 5% and 20% oxygen,

while Hif1α level was not detectable at 5%. Narva *et al.* [189] measured the relative level of Hif1α and Hif2α proteins at 4% oxygen. The relative ratios acquired from the two papers were used to derive the exponential decay model of Hif2α with respect to oxygen. The simulated trend of Hif2α protein level is shown in Figure 3.2.

3.3.2 Cell cycle modelling

A cell cycle model was built on the basis of several published models in the literature [170, 192, 200, 201]. The model describes the interactions between Myc, CDK, cell cycle regulatory protein-Rb, cyclins and cell cycle commitment determinant protein-E2F, as shown in Figure 3.1. Cell cycle is modelled up to the restriction point (RP) in late-G1 phase, beyond which cell proliferation is imminent. Different basal generation and degradation rates are applied to different proteins.

The binding of Hif1α and Hif2α to Myc respectively alters its activity negatively or positively. The activity of Myc and Hif1α alters downstream accumulation of cell cycle regulators. Previous models used different identifiers to indicate progression past RP (or commitment to S-phase). The exceeding of a target E2F concentration is used in our model to indicate commitment to cell cycle, as confirmed with simulation and experimental results in Dong *et al.* [201]. Yao *et al.* [203] reported the limit of 1 μM E2F concentration in turning the cell “on” to proliferate. The duration required for cells to reach the E2F threshold, termed “commitment time” thereafter, is dependent on the oxygen level via the levels of HIFs, governed by the following equations (Equations 3.3 – 3.7).

$$\frac{d[Hif1a-Myc]}{dt} = - kr_{3A} \cdot [Hif1a - Myc] + kf_{3A} \cdot [Hif1a] \cdot [Myc] - d_{Hif1a\text{-}Myc} \cdot [Hif1a - Myc] \cdot DEG$$ ***Equation 3.3***

$$\frac{d[Hif2a-Myc]}{dt} = - kr_{3B} \cdot [Hif2a - Myc] + kf_{3B} \cdot [Hif2a] \cdot [Myc] - d_{Hif2a\text{-}Myc} \cdot [Hif2a - Myc] \cdot DEG$$ ***Equation 3.4***

$$\frac{d[Myc]}{dt} = g_{Myc} + kr_{3A} \cdot [Hif1a - Myc] - kf_{3A} \cdot [Hif1a] \cdot [Myc] + kr_{3B} \cdot [Hif2a - Myc] - kf_{3B} \cdot [Hif2a] \cdot [Myc] - d_{Myc} \cdot [Myc] \cdot DEG$$ ***Equation 3.5***

$$\frac{d[cycE]}{dt} = kr_{12} \cdot [cycE - p/p] - kf_{12} \cdot [cycE] \cdot [p/p] + m_9 \cdot \frac{[E2F]}{[E2F]+k_9} - d_{cycE} \cdot [cycE] \cdot DEG$$ ***Equation 3.6***

$$\frac{d[E2F]}{dt} = m_{13} \cdot \frac{[Myc]}{[Myc]+k_{13}} \cdot \frac{[E2F]}{[E2F]+k'_{13}} + m_{E2F} \cdot \frac{[Myc]}{[Myc]+k_{E2F}} + m_{13} \cdot \varepsilon \cdot \frac{[Hif2a-Myc]}{[Hif2a-Myc]+k_{13}} \cdot \frac{[E2F]}{[E2F]+k'_{13}} + m_{E2F} \cdot \frac{[Hif2a-Myc]}{[Hif2a-Myc]+k_{E2F}} + m_{E2F-RbP} \cdot \frac{[E2F-RB] \cdot ([cycD] + [cycD-p/p])}{[E2F-RB]+k_{E2F\text{-}RbP}} - k_8 \cdot [RB] \cdot [E2F] - d_{E2F} \cdot [E2F] \cdot DEG$$ ***Equation 3.7***

Among the CDKIs, p21 and p27 are used in the model to represent the CIP/KIP family of its inhibitory action on cyclin D-CDK4/6 and cyclin E-CDK2. In the literature, different side functions for p21 and p27 were reported [208]. Our model only focuses on the shared cyclin-CDK inactivation of the two proteins. Owing to the much shared commonality between cancer cells and stem cells, a cell mass-independent p27 production rate, previously applied to cancer cells [170], is assumed. INK4 family is another type of CDKI with specific inhibitory effect on cyclin D-dependent kinase [209], which however can be captured through the function of p21/p27 and thus is not included as a separate mechanism in this model.

The concentrations of CDK2, CDK4 and CDK6 do not vary throughout cell cycle and are not expected to be rate limiting [201]. The cyclins are introduced in the model to represent the respective cyclin-CDK dimers. The three different isoforms of cyclin D (cyclin D1, D2 and D3) are not distinguished in the model for simplicity. Cyclin D and cyclin E carry out their functions through Rb phosphorylation [192, 201] and p21/p27 inactivation. Cyclin D physically binds to p21/p27 and deters it from inactivating cyclin E [37]. Equation 3.8 captures the effect of Hif1α, Myc and Hif2α-Myc on cyclin D transcription, alongside the binding effect of p21/p27. Different factors regulating p21/p27 (denoted by "p/p") and the associated complexes are shown by Equations 3.9, 10 and 11. The complex of cyclin D-p21/p27 is assumed to share the same activity as cyclin D for Rb phosphorylation [210].

$$\frac{\boldsymbol{d[cycD]}}{\boldsymbol{dt}} = g_{cycD} \cdot \left(1 - \frac{[Hif1a]}{[Hif1a]+k_{3a}}\right) - kf_{6B} \cdot [p/p] \cdot [cycD] + kr_{6B} \cdot [cycD - p/p] + m_{5cycD} \cdot \varepsilon \cdot \frac{[Hif2a-Myc]}{[Hif2a-Myc]+k_{5cycD}} + m_{5cycD} \cdot \frac{[Myc]}{[Myc]+k_{5cycD}} - d_{cycD} \cdot [cycD] \cdot DEG \qquad \textbf{Equation 3.8}$$

$$\frac{\boldsymbol{d[p/p]}}{\boldsymbol{dt}} = g_{p/p} \cdot (1 - k_4 \cdot [Myc]) - kf_{6B} \cdot [p/p] \cdot [cycD] + kr_{6B} \cdot [cycD - p/p] - kf_{12} \cdot [p/p] \cdot [cycE] + kr_{12} \cdot [cycE - p/p] - d_{p/p} \cdot [p/p] \cdot DEG \qquad \textbf{Equation 3.9}$$

$$\frac{\boldsymbol{d[cycD-p/p]}}{\boldsymbol{dt}} = kf_{6B} \cdot [p/p] \cdot [cycD] - kr_{6B} \cdot [cycD - p/p] - d_{cycD-p/p} \cdot [cycD - p/p] \cdot DEG \qquad \textbf{Equation 3.10}$$

$$\frac{\boldsymbol{d[cycE-p/p]}}{\boldsymbol{dt}} = kf_{12} \cdot [p/p] \cdot [cycE] - kr_{12} \cdot [cycE - p/p] - d_{cycE-p/p} \cdot [cycE - p/p] \cdot DEG \qquad \textbf{Equation 3.11}$$

The mechanisms associated with Rb activities are based on Dong *et al.* [201]. Free Rb protein binds to E2F and inhibits its downstream transcription. Rb is inactivated through cyclin D or cyclin E-dependent phosphorylation. Cyclin D can also dissociate

E2F-Rb complex through Rb phosphorylation [201, 203]. Equations 3.12 and 3.13 quantify the responses of Rb and E2F-Rb complex and incorporate the mechanisms of cyclin D-dependent phosphorylation and Rb-to-E2F binding.

$$\frac{d[Rb]}{dt} = g_{Rb} - m_{cycD-Rb} \cdot \frac{([cycD]+[cycD-p/p]) \cdot [Rb]}{[RB]+k_{cycD-Rb}} + m_{RbP} \cdot \frac{[RbP]}{[RbP]+k_{RbP}} - k_8 \cdot [Rb] \cdot [E2F] - d_{Rb} \cdot [Rb] \cdot DEG$$ ***Equation 3.12***

$$\frac{d[E2F-Rb]}{dt} = k_8 \cdot [Rb] \cdot [E2F] - m_{E2F-RbP} \cdot \frac{[E2F-Rb] \cdot ([cycD]+[cycD-p/p])}{[E2F-Rb]+k_{E2F-RbP}} - d_{E2F-RbP} \cdot [E2F-RbP] \cdot DEG$$ ***Equation 3.13***

Hypo-phosphorylation of Rb is assumed to be carried out only by cyclin D; subsequent cyclin E-dependent hyper-phosphorylation can then take place. Different levels of hyper-phosphorylation have been claimed in the literature; our model assumes a maximum binding of 4 phosphate groups onto Rb. Equations 3.14 and 3.15 quantify the change in the concentration of hypo-phosphorylated and hyper-phosphorylate Rb, respectively.

$$\frac{d[RbP]}{dt} = m_{cycD-Rb} \cdot \frac{([cycD]+[cycD-p.p]) \cdot [Rb]}{[Rb]+k_{cycD-Rb}} - m_{cycE-RbP} \cdot \frac{[cycE] \cdot ([RbP])\text{^}(n-1)}{([RbP])\text{^}(n-1)+k_{cycE-RbP}} - m_{RbP} \cdot \frac{[RbP]}{[RbP]+k_{RbP}} + m_{E2F-RbP} \cdot \frac{[E2F-RB] \cdot ([cycD]+[cycD-p/p])}{[E2F-RB]+k_{E2F-RbP}} + m_{Rb-nP} \cdot \frac{[Rb-nP]\text{^}(n-1)}{[Rb-nP]^{n-1}+k_{Rb-nP}} - d_{RbP} \cdot [RbP] \cdot DEG$$ ***(n=4)*** ***Equation 3.14***

$$\frac{d[Rb-nP]}{dt} = m_{cycE-RbP} \cdot \frac{[cycE] \cdot ([RbP])\text{^}(n-1)}{([RbP])\text{^}(n-1)+k_{cycE-RbP}} - m_{Rb-nP} \cdot \frac{[Rb-nP]\text{^}(n-1)}{[Rb-nP]\text{^}(n-1)+k_{Rb-nP}}$$ ***(n=4)*** ***Equation 3.15***

Different isoforms of E2F are not considered in the model, for simplicity. Our model allows the total concentration of different E2F-involving species to be dynamically

varied (Equation 3.14) [201, 203], unlike the conservation of individual E2F-involving species assumed by Novak and Tyson and Bedessem and Stephanou [192, 200].

Previous models used different identifiers to indicate progression past RP (or commitment to S-phase). The exceeding of a target E2F concentration is used in our model to indicate commitment to cell cycle, as confirmed by simulation and experimental results in Dong *et al.* [201]. Yao *et al.* [203] reported the limit of 1 μM E2F concentration in turning the cell "on" to proliferate. The results from Dong *et al.* [201] and Yao *et al.* [203] showed that a 0.66 μM E2F would lead 75% of cells committing to proliferation. The duration required for cells to reach E2F threshold is simulated at different oxygen conditions.

Other models have correlated the basal generation rates of certain cell cycle species to cell mass [170, 200]. The mass-dependent synthesis is not yet incorporated in our model, as it currently focuses on commitment time only and does not offer a full account of cell growth.

3.3.3 Modelling of protein deactivation

A first-order basal degradation rate is inferred from the literature for each expressed protein. This work assumes an additional ROS-mediated protein deactivation as a function of oxygen level beyond a threshold oxygen level, which includes proteolytic protein degradation, alteration of protein orientation, oxidation of functional groups and other interactions that remove proteins from actively engaging in reactions. ROS is a collection of reactive species (i.e. superoxide, hydroxyl radicals, etc.) generated as by-products of respiration in mitochondria, as a function of local oxygen level [211, 212].

Enzymes, such as superoxide dismutase (SOD), combat superoxides to reduce cell senescence and ageing [213]. Superoxides are reduced by these enzymes to H_2O_2 or, in the presence of reduced transitional metal, to hydroxyl radicals [214]. Compared to niche-grown stem cells, normoxically cultured cells experience elevated pericellular oxygen level which results in greater ROS generation and reduced ROS metabolism [215]. An elevated intracellular ROS level facilitates protein degradation through an ATP-independent and calcium-independent proteolytic pathway [216].

At an oxygen level below a certain threshold, ROS level is thought to be negligible due to the limited intracellular oxygen availability. However, various literature reports have demonstrated higher ROS levels between 1-3% oxygen [217, 218]. This may be credited to additional ROS production mechanisms under severe hypoxia [212, 219]. Under intermediate and severe hypoxia, superoxides are recognized to facilitate Hif1α stabilization and the induction of hypoxic responses [218, 220]. Due to insufficient understanding and high ROS detection variability, this ROS-mediated Hif1α stabilization has not been included in the model. Instead, Hif1α activity is thought to be solely dependent on oxygen level.

An accurate quantitative correlation between oxygen level and the overall intracellular ROS level has not been established in literature. This work assumes that a threshold oxygen level ($[O_2]_{TH}$ = 10%) may exist, beyond which superoxide production surpasses the neutralising capacity of combating enzymes and results in efflux out of mitochondria and influx to other cellular compartments [211]. If oxygen level exceeds this level, the amount of intracellular ROS surpasses the cell's inherent anti-oxidant capacity and initiates ROS-mediated deactivation mechanism across all proteins.

Different activation levels have been tested in this study. An exponential decay function is assumed for this general deactivation mechanism (Equation 3.16), where *n_deg* is an adjustable parameter.

$$DEG = exp(\, n_deg * ([O_2] - [O_2]_{TH}) / [O_2]_{TH}\,) \qquad \textit{(if } [O_2] > 10\%\textit{)}$$

Equation 3.16

3.3.4 Analysis with different parametrisation

Sensitivity analysis was performed to capture the significance of model parameters within the range of +/-100%. In particular, the derivative-based global sensitivity measures (DGSM) approach [221] was adopted to identify the most prominent parameters in regulating model output independently and interactively. The principle of DGSM can be described by Equations 3.17 - 3.19 [222]:

$$E_i = \frac{\partial f}{\partial x_i} = \frac{f(x_i*(1+d\%)) - f(x_i)}{d\%} \qquad \textbf{Equation 3.17}$$

$$g_i = \int_{H^n} E_i^2 \, dx \qquad \textbf{Equation 3.18}$$

$$G_i = g_i \,/\, (\sum_{i=1}^{n} g_i\,) \qquad \textbf{Equation 3.19}$$

In the above equations, E_i calculates the local derivatives of the model output *f* (which is the commitment time, CT, in this case) with respect to the ith parameter (x_i) in a n-dimensional parameter space (denoted as H^n), where n is the number of studied parameters. g_i represents an averaged value of E_i^2 over the space H^n. Finally, the value of G_i (referred to as G-score) indicates the relative significance of parameter i on impacting the simulation outcome. The integration in Equation 3.18 can be approximated by using a quasi-Monte Carlo (QMC) sampling method [48]; this work has adopted particularly the Sobol sequence [222] with an incremental sampling size

of 500 in the course of obtaining a converged value for a G-score. In order to reduce the computational cost, a preliminary screening based on local sensitivities was used to pick out a subset of parameters, which demonstrated greater impact on the simulation output and were therefore subjected to further analysis by DGSM.

In addition to support DGSM, the set of (parameter value) samples generated by the QMC method has also been adopted for carrying out simulations to assess to what extent the predicted minimum CT and optimal oxygen level vary with the parameter values adopted. This set of simulations is referred to as QMC simulation (named after how the parameter values are sampled). The simulation results have also been used to study the variation in the shape of the curve of CT vs. oxygen level, referred to as the "characterisation curve" in this work, which is quantified through a factor k according to Equation 3.20:

$$k = \frac{CT_{norm} - CT_{min}}{20\% - O_{2_{eq}}} \qquad \textbf{\textit{Equation 3.20}}$$

where CT_{norm} and CT_{min} are the CT corresponding to normoxia (i.e 20% O2) and the minimum CT, respectively; O_{2eq} is the hypoxic oxygen level at which the CT is identical to CT_{norm}.

3.4 Results

Dynamic numerical simulations revealed the temporal change in concentrations of key cell cycle regulators for a specified oxygen level. The CT was found to vary with a change in oxygen level. A "U-shape" characterisation curve has been discovered from simulation results, which offers a hypothesis that could potentially explain the varied

experimental observations reported in literature. The sensitivity analysis highlighted the relative significance of the model parameters under different oxygen levels. For each set of parameter values, the oxygen level that results in the lowest CT is termed the optimal oxygen level ($O_{2\text{-optimal}}$). The persistency of the existence of an optimal oxygen level ($O_{2\text{-optimal}}$) is demonstrated by the QMC simulation results. The shape of the characterisation curve was generally preserved but appeared sensitive to the degree of ROS-mediated protein deactivation. Hif2α was found to play a crucial role in facilitating commitment to cell cycle under different gradients of hypoxia.

3.4.1 Dynamic behaviours

Figure 3.3 shows an example of the simulation output for key cell cycle regulators, at 2% oxygen. It should be noted that, although the model presented above could mathematically predict steady states, they do not carry any biological significance. The useful output of the simulation is only the transient behaviour leading to the accumulation of E2F towards its threshold level, which is reached at 13.5 hours in the case shown in Figure 3.3. The effective Myc rises steadily, contributed by the basal generation of Myc and the formation of Hif2α-Myc. p21/p27 level rises initially until the Myc-dependent inhibitory effect becomes dominant. Cyclin D is kept at a sustained low level due to the direct inhibition from Hif1α. Rb increases initially due to the disintegration of the pre-existing E2F-Rb dimers. As more E2F is generated, the synthesis rate of Rb-E2F complex increases until all the available Rb is consumed. E2F experiences the initial lag phase due to Rb binding. The sharp sigmoidal behaviour of E2F can be attributed to its Myc-dependent, auto-catalytic mechanism. The level of Cyclin E rises trailing that of E2F, as a result of the E2F-dependent transcription. The trajectories of E2F and cyclin E share the same sigmoidal behaviour.

Cyclin E was used as the marker for proliferation identification in Bedessem and Stephanou [200], which would yield a comparable CT according to Figure 3.3, also consistent with the range shown in Dong *et al.* [201].

The behaviour shown in Figure 3.3 was predicted using the (default) initial conditions (presented in the Supplementary Information). To reveal the potential impact of the initial conditions on the qualitative behaviour of the system, dynamic simulations with different initial conditions sampled from a hypercube space formed by +/-100% of the default initial condition values were carried out, for each of the parameter value sets similarly sampled from a parameters space (details are given in the Supplementary Information), and across the entire range of oxygen levels. In this analysis, the steady states predicted by the simulations were recorded which, although not carrying any biological significance in themselves as stated earlier, were used to indicate alternative trajectories of the transient behaviour leading to the threshold level of E2F that could arise from different initial conditions. It was found that multiple steady states are indeed present for the combination of a sub range of oxygen levels and a subset of parameter values, but these cases (where a steady state different from that from the default initial conditions was reached) represent only a small potion (less than 2%) of all the simulations carried out. Therefore, model predictions with the default initial conditions are considered to be able to reveal the representative behaviour of the system, and hence have been used for the analysis reported in this work.

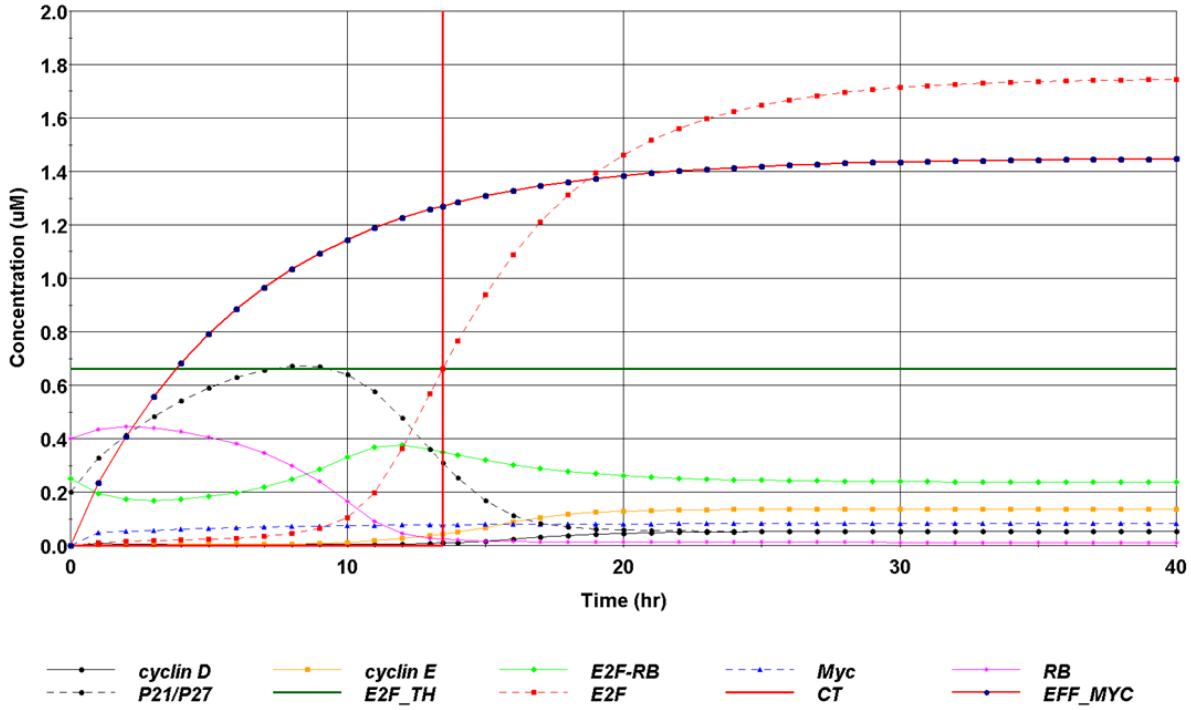

Figure 3.3: Simulation results showing the dynamic change of selected cell cycle regulators under 2% oxygen. This simulation was completed with the nominal model parameter setting. E2F threshold level (*E2F_TH*) is shown as the horizontal forest green line. The vertical red line indicates commitment time marking the time when E2F level exceeds the threshold level.

3.4.2 The effect of oxygen level on CT

Simulated CT results under different oxygen concentrations are shown in Figure 3.4a. A lower hypoxic CT indicates an enhanced proliferative behaviour, whereas, a greater CT corresponds to a prolonged period till cell cycle commitment. With a culture oxygen level under 2.9%, E2F accumulates much slower, as the inhibitory effect of Hif1α on Myc and cyclin D begins to dominate cell cycle regulation. More severe hypoxia further exacerbates E2F accumulation and leads to cell quiescence at less than 1.2% oxygen.

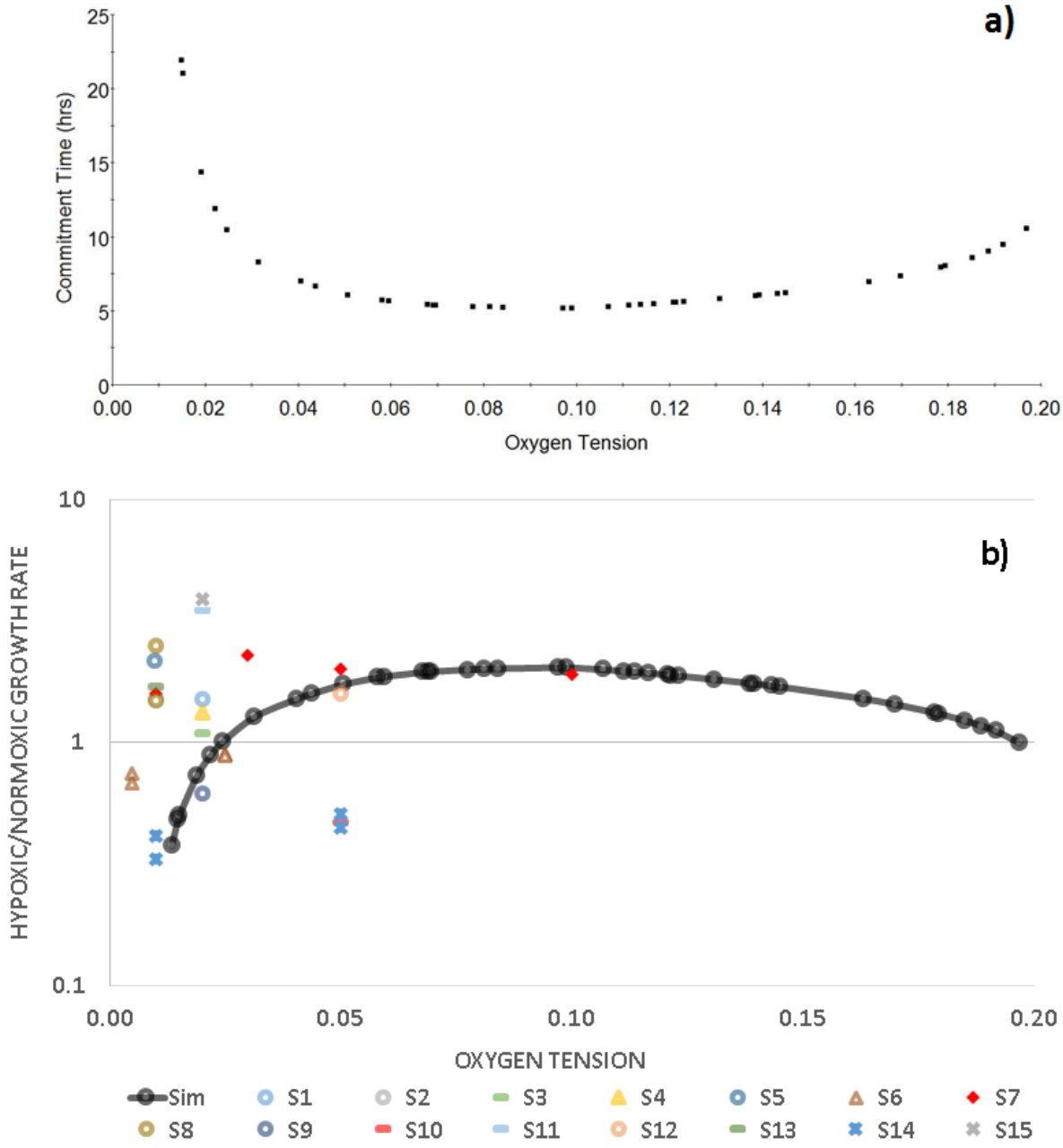

Figure 3.4. (a) Simulated cell cycle commitment time under different oxygen levels at the nominal model parameter setting. (b) Compiled literature experimental data of the hypoxic proliferation rate. The ratio between hypoxic and normoxic proliferation rate for each set of the literature data (S1-S15) is plotted. A list of the corresponding references is included in the Supplementary Information. The simulation results from this study (Sim) are shown for the swept oxygen levels.

When the oxygen level is greater than 2.9%, the inhibitory activity of Hif1α is hampered. Myc proteins are less inhibited by Hif1α binding and more E2F and cyclin D are produced. The Hif2α-Myc complex and Myc contribute to E2F availability directly through transcription, and indirectly, through enhancing the production of cyclin D

protein for Rb inactivation. Shortened protein accumulation and cell division time under mild hypoxia are revealed from the simulation. The difference in CT is small in the mid-range of oxygen concentration. As oxygen level rises into the normoxia regime, the effect of ROS-mediated protein deactivation becomes more pronounced reducing the accumulation rate of proliferation determining proteins, which is reflected as ascending CT values. Overall, a minimum CT lies between 8-10% oxygen, which is the optimum oxygen concentration for commitment to cell cycle, with the nominal model parameters setting adopted for producing Figure 3.4a.

Past experiments on a specific cell type (e.g. MSC) at various individual levels of oxygen below 20%, though all referring to as hypoxic conditions, have shown both higher and lower proliferation rates compared to that with normoxia (20%), hence leading to some ambiguity as to the role of hypoxia in cell proliferation. A compiled list of hypoxic literature experimental data for MSCs, converted in this work to the ratio of hypoxic proliferation rate to the rate at normoxia (20% oxygen), is shown in Figure 3.4b [75, 79, 81-83, 85, 88, 90, 196, 223-227], as well as the hypoxia-to-normoxia ratio of the inverse of cell cycle commitment time (as an indicator of proliferation rate) obtained in simulation as presented in Figure 3.4a. The rate ratios are shown on a logarithmic scale. The majority of the available data was collected under the range of *in vitro* intermediate or severe hypoxia, which limited the applicable range of comparison. Figure 3.4b demonstrates that the simulation yielded results at the same level of magnitude as most of the literature findings. It also shows the lack of consensus between the experimental studies with respect to hypoxia-mediated effects on proliferation, possibly caused by the difference in cell line, culture condition and duration between these existing experimental studies. Future experimental work to

produce a consistent data set that covers a sufficient range of oxygen level is thus needed to allow further validation and calibration of the model.

3.4.3 Sensitivity of model parameters

Global sensitivity analysis was conducted to test the robustness of the constructed model. The selected eight sensitive parameters are shown in Table 3.1. The two parameters for modelling ROS-mediated protein deactivation were investigated separately due to their special status. The converged G-scores across selected oxygen levels are shown in Figure 3.5. The effect of each parameter to cell cycle commitment time is sensitive to the applied oxygen level. Parameters P1, P3, P8 are identified as the top three parameters of significance. P1 dominates the proliferation response at oxygen level less than 0.05, consistent with its role in positively regulating Hif1α level. Under mild hypoxia, Hif1α protein becomes negligible alongside with the diminishing importance of P1. P3 and P8 regulate Myc-facilitated E2F protein transcription and enhance Hif2α-Myc activity, respectively. Under mild hypoxia and normoxia, Hif1α-mediated Myc inactivation is liberated, allowing more Myc and Hif2α-Myc to take part in E2F transcription. This effect is reflected by the rising G-scores for P3 and P8 with an increase in oxygen level. The results of DGSM highlight a few parameters that have a greater impact on simulation output, depending on the hypoxic oxygen level. The parameters with high sensitivities shall be prioritized in future model calibration and experimental validation.

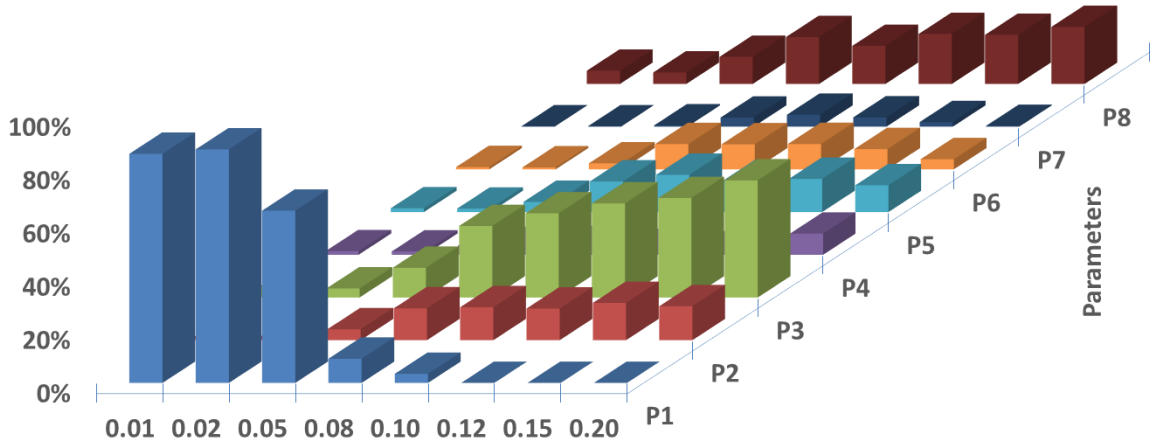

Figure 3.5: Derivative-based global sensitivity measure (DGSM) results for the selected model parameters. Relative parameter global sensitivity is shown as the calculated G-score on the z-axis. Eight different parameters have been evaluated under seven oxygen levels (0.01, 0.02, 0.05, 0.08, 0.1, 0.15 and 0.2).

Table 3.1: Parameters evaluated in DGSM study.

P1	P2	P3	P4	P5	P6	P7	P8
b1	k'13	m13	k8	g_rb	m_e2f_rbp	d_cyce_pp	ε

3.4.4 Variability in minimum CT and optimal oxygen level

Figure 3.6a) and 6b) plot results of $O_{2\text{-}optimal}$ and the corresponding minimum CT from the QMC simulation.

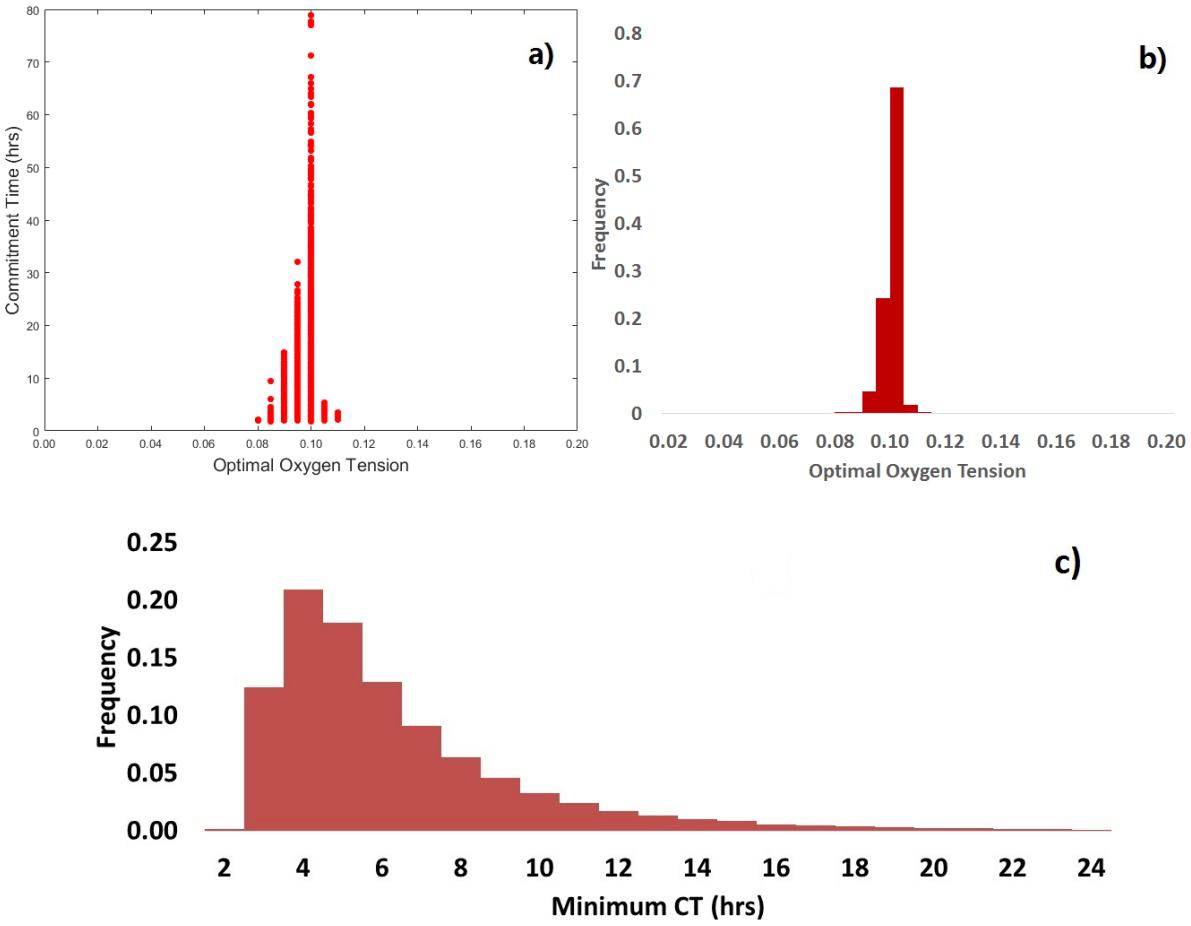

Figure 3.6: Results of QMC simulation with 39,000 sets of parameter values. (a). Commitment time at optimal oxygen levels. Each point shows the minimum CT in each simulation. (b). Frequency plot of optimal oxygen level. (c). Frequency plot of minimum commitment time (CT) across hypoxic oxygen levels.

Figure 3.6a) shows the large spread of CT at different optimal oxygen levels and Figure 3.6b) confirms the existence of a concentrated range of the optimal oxygen level, which leads to the shortest commitment time. Despite the variation in parameter values, 98% of the simulated sample sets reported an optimal oxygen level within 9 - 10.5%, suggesting that the optimal oxygen level is relatively independent of the 8 highlighted parameters (P1-P8). This range is expected to change with different types of cells (cf. the later section on ROS-mediated protein deactivation), subject to their inherent and niche properties, but the convexity of the “U-shape” characterisation

curve (as shown in Figure 3.4) may be consistently preserved under the assumed mechanisms of HIFs and ROS, as shown by the QMC simulation results.

Figure 3.6c) plots the frequency of minimum CT from each QMC run. The minimum CT appears to be sensitive to parameter settings, contrary to the narrow range observed for $O_{2\text{-}optimal}$. A change in parameter values represents a quantitative shift in cellular behaviour, which directly affects the accumulation rates of cell cycle regulating proteins, hence the minimum CT. Nevertheless, approximately 90% of the minimal CT has been identified within the range of 3 – 11 hours.

3.4.5 Consistency of the shape of the characterisation curve

The QMC simulation results show that the convexity of characterisation ("CT – O_2 level") curve is preserved across the parameter sets. The shape of the characterisation curve was assessed with several exemplary cases, shown in Figure 3.7a), via their respective k factors. A smaller k signifies a flatter parabola and a greater k indicates a higher oxygen dependency. For reference, the k value for the curve shown in Figure 3.4a is 27.9. The frequency of k values for 39,000 QMC simulations (with *n_deg* = 1) is shown in Figure 3.7b) (among results corresponding to other *n_deg* values, which are discussed in the later section). When *n_deg* (i.e. the parameter that controls protein deactivation) assumes this nominal value, the k values for over 99% of the simulated runs are within 1 – 40, representing the expected parabolic characterisation curves. The local derivatives of CT at $O_{2\text{-}optimal}$ are relatively small, showing the robustness of cell cycle progression to a small perturbation in oxygen level in the vicinity of $O_{2\text{-}optimal}$. This suggests that a rather tolerating range of oxygen control for cell growth may be accepted in designing the bioreactor control strategy.

If the value of k drops below 1, CT decreases significantly under severe and intermediate hypoxia with alleviated hypoxic stress, and then plateaus with negligible further reduction. The “U-shape” convexity is no longer present. This behaviour is only applicable in special scenarios, which are discussed in later sections.

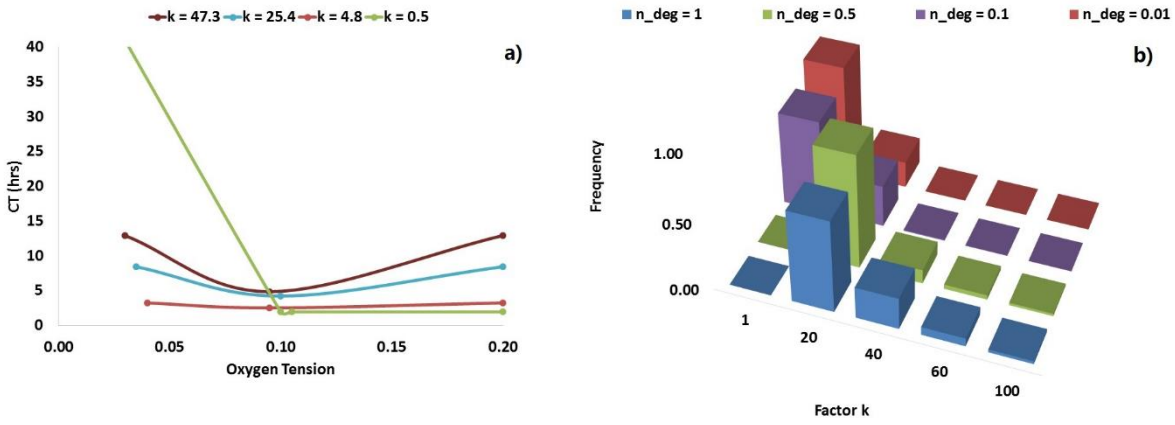

Figure 3.7: The shape of characterisation curves. (a) Sample curves for characterisation curves convexity factor k. The curves are selectively extracted from QMC simulation results for representation. (b) The frequency plot of the effect of parameter *n_deg* on factor k from compiled 39,000 sets of QMC simulation results.

3.4.6 Impact of ROS-mediated general protein deactivation

Both *n_deg* and $[O_2]_{TH}$ are parameters associated with ROS-mediated general protein deactivation (shown in Equation 3.16). Due to limited information and the distinct nature of these two parameters (they were fixed and not included in the global sensitivity analysis), separate sensitivity analysis was performed, to explore the impact of the extent of protein deactivation and the activation level.

Values of *n_deg* between 0.01 and 1 have been studied. When *n_deg* = 0.01, ROS-mediated protein deactivation is negligible. Figure 3.8a) and 3.8b) show that a smaller

n_deg shifts the peaked optimal oxygen level towards normoxia with negligible impact on minimal CT. The reduction of *n_deg* also significantly alters the shape of the characterisation curve, as shown by an increase in the frequency of k values below one (Figure 3.7b)). With *n_deg* below 0.1, the prolonged commitment to cell cycle under normoxia is mitigated, making higher oxygen level more favourable for proliferation (Figure 3.8a)).

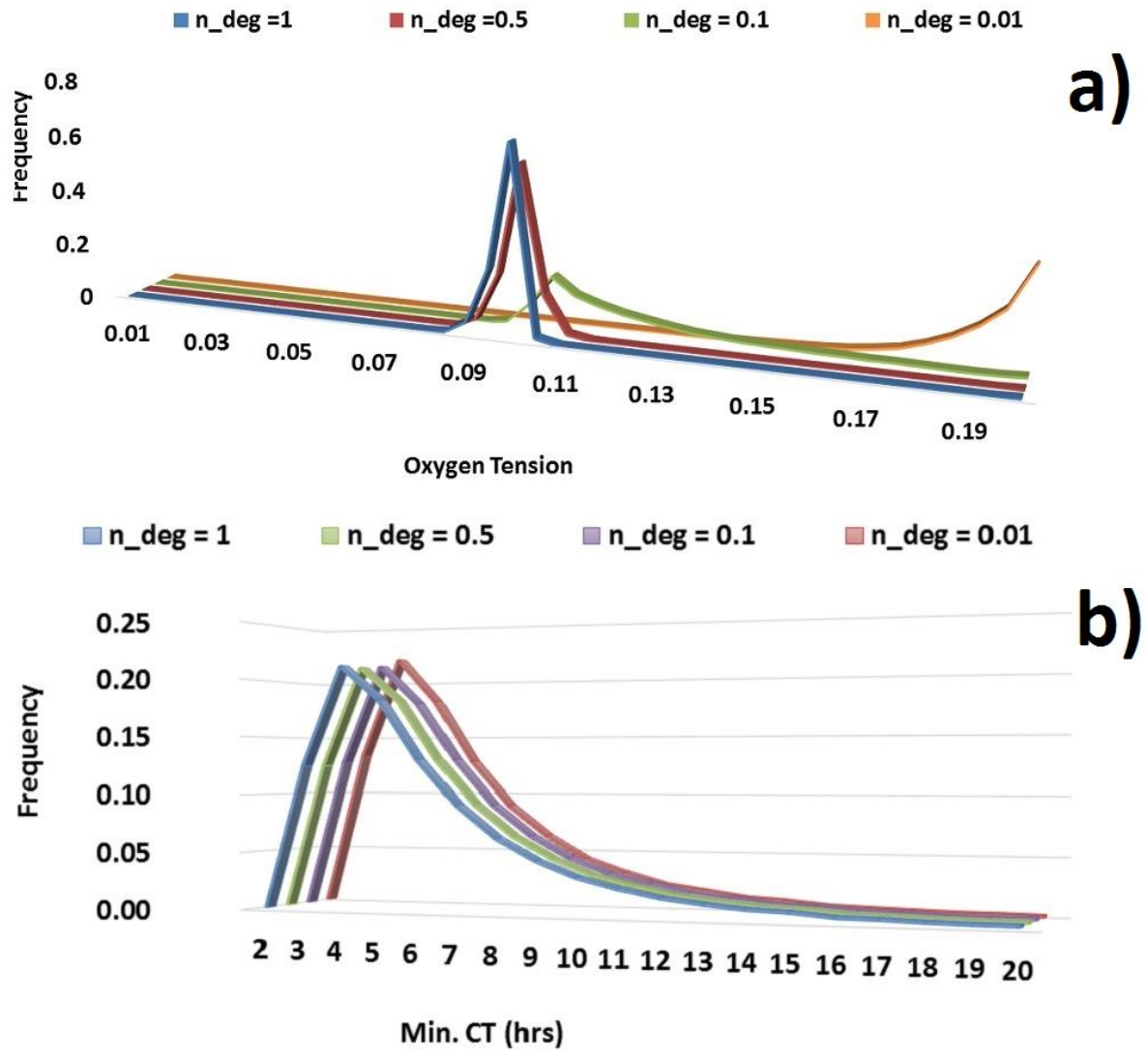

Figure 3.8: Impact of *n_deg* inferred from 39,000 sets of QMC simulation results. (a) The effect of *n_deg* on the frequency of optimal oxygen levels. (b) The effect of *n_deg* on the frequency of minimum CT.

The ROS activation level ($[O_2]_{TH}$) was varied from 5% to 15% reflecting oxygen levels potentially leading to different degrees of superoxide production that surpassed the

inherent cellular degradation rate. Figure 3.9 plots the distribution of optimal oxygen level from QMC runs. $O_{2\ TH}$ is shown to have a significant impact on the oxygen level for quickest commitment to cell cycle; the level of dependency varies with the position of $[O_2]_{TH}$ within the range of hypoxic stress. Under intermediate hypoxia ($[O_2]_{TH}$ = 5%), other factors such as Hif1α and Hif2α-mediated responses share the control together with protein deactivation over cell cycle commitment time. Moving towards normoxia ($[O_2]_{TH}$ = 15%), proliferation responses from the two hypoxic factors are negligible. This further implies the significance of ROS-mediated protein deactivation on regulating commitment to cell cycle under the higher oxygen end of the hypoxic condition.

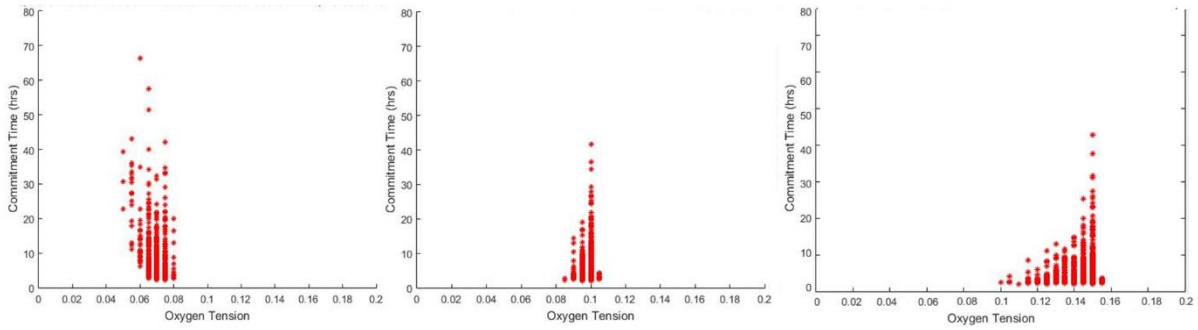

Figure 3.9: Simulations of various ROS-mediated protein deactivation activation oxygen level. The simulations were completed with activation oxygen level of 5% (left), 10% (central) and 15% (right). Each simulation was completed with the same 1,000 QMC parameter value sets. The red dots represent the optimal oxygen level for each parameter set, showing the minimum commitment time in each simulation.

3.4.7 Roles of parallel mechanisms on cell cycle commitment

A primary hypothesis during model building was the counteracting effects of Hif1α and Hif2α on commitment to cell cycle. From the simulation results, Hif1α competes with Hif2α for Myc binding and inactivates Myc for E2F production. Hif2α contributes consistently to E2F production individually and through paired Hif2α-Myc dimer under different gradients of simulated hypoxia. Under severe hypoxia, the pro-proliferation

effect of Hif2α is to be overshadowed by that of Hif1α, which dominates the proliferation response and delays the progression towards meeting the cell cycle commitment requirement. As severe hypoxic stress is alleviated, the effect of Hif2α becomes more prominent and shortens CT.

Under oxygen levels greater than 10%, ROS-mediated general protein deactivation, when $[O_2]_{TH}$ is set to 10%, acts on all cell cycle regulators (Myc, Hif2α-Myc, E2F, etc.) and postpones the net accumulation of E2F. Hif2α-mediated E2F generation partially offsets the deactivation loss, when the effect of ROS is accounted for (with *n_deg* = 1). At *n_deg* = 0.01, ROS-mediated protein deactivation is negligible, Hif2α continues to facilitate commitment to cell cycle in the absence of any counteracting force under mild hypoxia and normoxia. A decrease in Hif2α concentration is expected with rising oxygen level beyond 5%, but the associated effect appeared to be mitigated by other dynamics embedded in the system. The peak oxygen level of Hif2α was found to have negligible effects (results not shown). Consequently, the flat-bottomed “L-shape” is observed when ROS-mediated protein deactivation is absent, making normoxia the favoured proliferation condition (Figure 3.10).

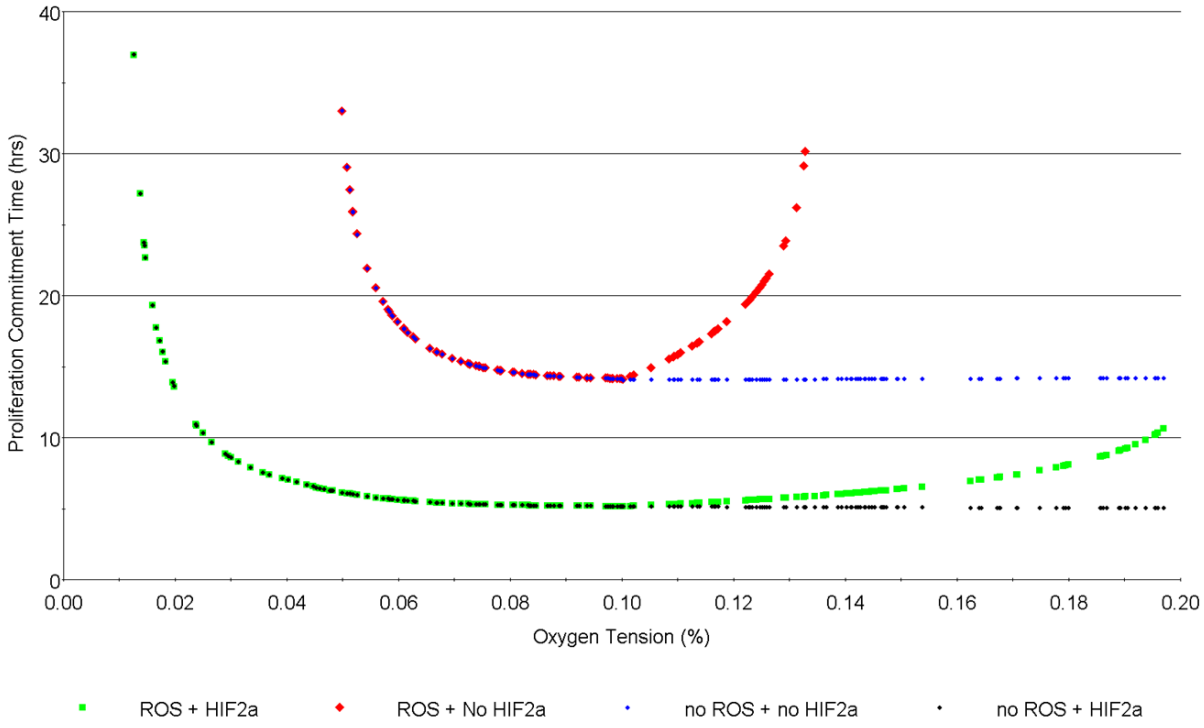

Figure 3.10: Comparative simulation results on the effect of ROS-mediated protein deactivation and Hif2α. The green dots indicate the nominal model parameter setting condition with ROS-mediated protein deactivation and the effects of Hif2α. The black dots account for Hif2α but not ROS-mediated protein deactivation. The blue and red simulations do not account for Hif2α. Simulations in red account for ROS-mediated deactivation, whereas simulation in blue does not. Note that in all cases Hif1α was assumed to function normally. The results were simulated with nominal parameter settings unless stated otherwise.

Additionally, Hif2α is found to have dual effects on regulating E2F production and commitment to cell cycle. On the one hand, Hif2α-Myc dimer enhances E2F transcription activity. On the other hand, the displaced Myc is prevented from direct E2F transcription and cyclin D generation to free RB-bound E2F. Even though the two effects work in competition, both are needed to facilitate cell cycle commitment. This combined effect from the dual actions seems to be responsible for the decoupling of the optimal oxygen level (9 - 10.5%) with the peak Hif2α oxygen level (5%).

If ROS-mediated protein deactivation is absent, the optimal oxygen level extends to normoxia rather than falls within mild hypoxia. This is because the negative impact of

Hif2α in Myc displacement plays a more prominent role when ROS-mediated protein deactivation is not in place, which leads to the “L-shape” characterisation curve. A characterisation curve with protein deactivation but without the presence of Hif2α can also be found in Figure 3.10. In this case, the applicable range that leads to cell cycle commitment is much narrower, the minimal CT is greater, and the optimal oxygen level deviates from normoxia, as expected.

In summary, the simulation results indicate that Hif2α counteracts proliferation delay caused by ROS-mediated protein deactivation and Hif1α under normoxia and severe hypoxia, respectively, through facilitating E2F build-up. ROS-mediated protein deactivation may be a primary driver in causing proliferation delay under normoxia, which results in the observed hypoxia-mediated enhanced proliferation with certain cell lines.

3.5 Discussion

Culturing MSCs under hypoxia *in vitro* has several observed advantages, such as stemness preservation and reduced senescence. This work has focused on the impact of hypoxic oxygen level on the rate of cellular proliferation. Due to the resource-intensive process in experimentally testing all hypoxic oxygen levels, most of the experimental work compare data from 1-3 hypoxic levels against the result acquired under normoxia (Figure 3.4b); consistent experimental data on culturing MSCs over a full range of oxygen concentration have not yet been reported. This study incorporated a number of known mechanisms and hypotheses into a mathematical model to predict quantitatively the hypoxic response of cell cycle under conditions ranging from severe hypoxia to normoxia. In the following, we discuss about our model and the simulation

results against data, knowledge and hypotheses given in the literature, highlight key implications, and also identify important limitations of this work to be addressed in the future.

Different reports have shown the counteracting effects between the Hifα isoforms on proliferation [108, 116-119] and their functions in regulating many hypoxic functions [193, 228, 229]. To our knowledge, this study is the first attempt to integrate hypoxia sensing and cell cycle progression to capture the oxygen-dependent differential proliferation responses. The Myc protein was used to quantitatively couple and directly regulate key cell cycle regulating proteins. The simplified mechanism (Figure 3.1) neglects the potential interactions from other Hifα-dependent [80, 205, 230] or Hifα-independent [197, 224, 231] hypoxic proliferation pathways. These pathways have been considered during model construction, but not included in the model. Some of their downstream regulators have been captured by the considered mechanisms, while others are either less significant or lack consensus in the literature. As confirmed knowledge about these and new pathways emerges, the first working model established in this study needs to be extended.

The simulation results, from applying a unified model over a wide range of oxygen levels, show that the effect of hypoxia on proliferation is dependent on its severity, due to the combined regulation originated by the two HIF factors and ROS-mediated protein deactivation. As such, the model has the potential to offer a reconciliation of the previously reported experimental results [38, 48, 76, 80, 89, 183, 205, 230]. Generally, a “U-shape” characterisation curve appears to be followed by the response of the commitment time to a change in *in vitro* hypoxic oxygen level (Figure 3.4a)). The

characterisation curve is subject to shift and contract, depending on the model parameter values, which in principle are dictated by properties of different cell lines and other culture conditions (medium, surface characteristics, etc.). However, under the assumptions of ROS-mediated protein deactivation, a specific, relatively narrow range of optimal oxygen levels (9% - 10.5%) that would allow the quickest cell cycle commitment was consistently observed, despite the variation in parameter values (Fig 3.6). This shows that, although the model has not been calibrated with a complete data set of any specific cell line hence is not suitable to make accurate predictions, a number of cell lines and culture systems may find their optimal oxygen concentration level within this range.

Global sensitivity analysis revealed the relative significance of selected parameters on impacting simulation output (Figure 3.5). The parameter-specific dependency on oxygen level was observed, which in some cases, were due to the nature of certain model equations (e.g., P1); other high impact parameters (e.g. P3 under *in vitro* normoxia) were a result of the interactions between multiple mechanisms modelled. The obtained ranking of parameters significance under different oxygen levels shall be used to prioritize future work in experimental validation and parameter calibrations. Meanwhile, when comparing literature experimental findings, the sensitive parameters under the relevant oxygen level shall be accounted for to ensure a reflective comparison.

The net oxidative stress activation level (ROS-mediated protein deactivation threshold) has shown a significant impact over determining the range of the optimal oxygen levels (Figure 3.9).In the complete absence of the ROS-mediated generic protein

deactivation, the resultant “L-shape” characterisation curve is not an accurate reflection of the observed effect of hypoxia-enhanced proliferation [38, 48, 89, 100, 108, 230]. This behaviour, however, may be applicable for other types of cells with higher niche oxygen level, a projection to be confirmed by future experimental observations. Inherent anti-oxidant enzymes are expressed in stem cells to combat oxidative stress, however, with limited capacity, overwhelming ROS would lead to higher senescence and apoptosis [232, 233]. Bertolo et al. showed higher intracellular ROS led to longer division time in MSCs, which more than doubled in late passaged cells [234]. When exposed to the atmospheric oxygen level, which is much higher than MSCs niche condition, the levels of intracellular ROS and other reactive species could rise [215, 235-237]. The anti-oxidant capacity is believed to be cell type specific, which would result in a variation in the threshold and magnitude of ROS-mediated protein deactivation and consequently (as shown in our simulation) a shift in the range of optimal oxygen level. This theoretical prediction however still needs to be validated through carefully designed experiments. Beyond what has been implemented in the current model, an increase in mitochondrial intracellular ROS production under severe hypoxia have also been reported [74, 212, 238]. The ROS also facilitates the stabilization of Hifα isoforms [218, 219, 239]. The impacts of those effects shall be considered in future studies.

To our knowledge, this work is the first one that mathematically models the role of Hif2α in cell cycle regulation. As a key hypoxia-regulating factor, it links to multiple functions in stem cell maintenance, pluripotency, and proliferation [103, 106, 108, 195, 205, 240-242]. In particular, various studies have reported the opposing effects of Hif2α with Hif1α [116-119]. The simulation in this study showed that under

intermediate hypoxia, Hif2α combats the negative effect of Hif1α on cell cycle progression; under normoxia, Hif2α can partially mitigate the delayed proliferation response caused by ROS-mediated protein deactivation. In this work, the Hif2α expression rate as a function of oxygen concentration was estimated by synthesizing various literature data; an improved measurement of intracellular Hif2α protein in MSCs through dedicated experimentation would yield a more accurate function. The dynamic variation of individual cell cycle regulating proteins during different stages of G1-phase progression provides insights into establishing a dynamic control strategy (i.e. for bioreactor operations) that may reduce the proliferation period via other controls, e.g. specific growth factors.

Several assumptions and simplifications were made to allow the construction of the current model, which require caution in interpreting the simulation results and, in many cases, point to important future work:

- The model focuses on the overall oxygen-dependent behaviour of cell cycle commitment and is not expected to be taken for making predictions at rather extreme conditions. In particular, under severe hypoxia pro-survival response in stem cells is expected to dominate and could result in quiescence to reduce DNA damage [77, 90, 243] despite a few reports showed the successful proliferation of MSCs under anoxic conditions [244, 245], which may be due to different factors as addressed in the original papers.
- The current model only estimates the time required for commitment to cell cycle in late-G1 phase. Future work will expand to include the entire cell cycle process to capture the rate of proliferation. The process of cell growth and metabolic uptake may also be considered in future work.

- More detailed Hif1α mechanistic models are available in the literature [167, 169] and may be incorporated to improve model accuracy and help identify cytokines to improve Hifα stabilization during *in vitro* culture.
- A key limitation of this study has been on data availability. The on-going growth in proteome and transcriptome studies poses the possibility of offering data with enhanced quantity and quality [246, 247]. With these newly available data, estimation of cell proliferation rate and identification of the optimal oxygen concentration and cell cycle commitment time could then be become more accurate.
- Finally, this single-cell model is intended to be integrated with a dynamic population model to capture the status of the overall cell pool in a bioreactor, addressing the growth kinetics and the heterogeneity of the MSCs pool.

3.6 Conclusions

A single-cell mathematical model has been established to predict the time required for cell cycle commitment in a hypoxic environment as a proxy to proliferation rate. Incorporating known roles of HIF factors and introducing a hypothesis on ROS-mediated protein deactivation within a cohesive quantitative framework, the constructed model represents the first attempt to mechanistically capture these key factors in hypoxia sensing and cell cycle regulation. In particular, it implements a novel approach in using Myc to link oxygen sensing and G1 phase progression, allowing the differential responses of Hif1α and Hif2α to Myc activities and their respective oxygen-dependent availabilities to be quantified so as to predict cell proliferation status under different oxygen levels.

Through extensive simulation that explored the parameters space using the quasi-Monte Carlo approach, the model revealed the preservation of optimal oxygen level and the convexity of characterisation curve under the assumption of ROS-mediated protein deactivation, which suggests that the behaviours of severe hypoxia-mediated cell cycle arrest and mild hypoxia-mediated facilitated proliferation may be a rather common cellular response. Furthermore, the interactive effects of Hif2α on cell cycle progression with Hif1α and ROS-mediated protein deactivation appeared to act as opposing forces in regulating hypoxia-mediated proliferation.

The model developed in this work has been based on a synthesis of known biology and limited literature data. It offers a first vehicle for prediction cell cycle commitment overall a wide range of oxygen levels, which has not been covered by any existing experimental data set. While the order of magnitude of its predictions appears to be consistent with published data, it remains an important task to validate and calibrate the model with experimentation on specific cell lines, so that the model can eventually be used to suggest optimal operational strategies of bioreactors. The outstanding importance of certain model parameters revealed by the global sensitivity analysis, together with the high sensitivity of some mechanisms identified through the simulation studies, could offer useful guidance to the planning of future experimental work.

The simulation and experimental results from this chapter demonstrated the significance of hypoxia in regulating hMSCs growth. Although the relative effect of hypoxia was consistently observed, the absolute growth rates varied across experimental runs. The next chapter aims to understand how the metabolic network adapts to a change in growth rate as well as in the *in vitro* oxygen level.

Statement of Authorship for joint/multi-authored papers for PGR thesis

To appear at the end of each thesis chapter submitted as an article/paper

The statement shall describe the candidate's and co-authors' independent research contributions in the thesis publications. For each publication there should exist a complete statement that is to be filled out and signed by the candidate and supervisor **(only required where there isn't already a statement of contribution within the paper itself).**

Title of Paper	Mathematical modelling of interacting mechanisms for hypoxia mediated cell cycle commitment for mesenchymal stromal cells
Publication Status	☐Published
Publication Details	Author list: Zhang, B., Ye, H., & Yang, A. (2018). Mathematical modelling of interacting mechanisms for hypoxia mediated cell cycle commitment for mesenchymal stromal cells. BMC systems biology, 12(1), 35.

Student Confirmation

Student Name:	Bo Zhang		
Contribution to the Paper	• Constructed mathematical models • Performed data analysis • Wrote manuscript		
Signature		Date	May 5, 2019

Supervisor Confirmation

By signing the Statement of Authorship, you are certifying that the candidate made a substantial contribution to the publication, and that the description described above is accurate.

Supervisor name and title: Prof. Aidong Yang			
Confirmed.			
Signature	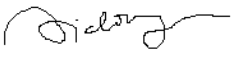	Date	May 13, 2019

This completed form should be included in the thesis, at the end of the relevant chapter.

Chapter 4: Metabolic shift under different growth regimes

4.0 Summary

This chapter describes the study on how different hMSCs growth rates are associated with a change in their metabolic profile. This work was motivated by the observed changes in lactate production in hMSCs undergoing different growth rates. Despite the same culture conditions, slow-growing and fast-growing hMSCs exhibited different trends on how their lactate production correlated with growth rate. In addition, hMSCs cultured under *in vitro* hypoxia and normoxia demonstrated different lactate production trends.

Flux balance analysis (FBA) incorporated with a proteomic resource allocation constraint was used as a mathematical technique for modelling metabolic networks to provide insights on the intracellular flux distribution and to hypothesize a cause for the observed behavior. In particular, the observed characteristic trends in lactate production appear to be closely associated with the re-distribution of key fluxes in the tricarboxylic acid cycle (TCA). Furthermore, the observed difference between normoxic and hypoxic cultures corresponds to the difference in the model-estimated relative proteomic efficiencies of key metabolic pathways under these two conditions. The findings from this study show the significance of hypoxia and cellular growth regime on regulating the metabolic uptake/excretion profile of hMSCs. Relevant literature review, methods and findings are reported in Journal Paper 2.

Journal Paper 2 - Analysis of changes in the metabolic profiles of human Mesenchymal stromal cells in different growth regimes

- To be submitted to PLOS ONE

Bo Zhang[1,2], Hong Zeng[1], Zhanfeng Cui[1,2], Hua Ye[1,2], Aidong Yang[2,*]

[1]Department of Engineering Science, University of Oxford, Oxford, United Kingdom

[2]Institute of Biomedical Engineering, Department of Engineering Science, University of Oxford, Oxford, United Kingdom

* Corresponding author

4.1 Abstract

Culture conditions have shown a significant impact on the metabolic uptake of Human Mesenchymal stromal cells (hMSCs). Various studies have reported hMSCs growth rate and their metabolic uptake data, but few have investigated whether a consistent metabolic profile is retained over different growth rates. This study investigated the correlation between the specific lactate production and specific growth rate of hMSCs cultured under normoxia and hypoxia. Under normoxia, the specific lactate production rate of proliferating hMSCs showed two opposing (i.e. increasing and then decreasing) trends as the specific growth rate increases, whereas only an increasing trend was observed under hypoxia. A genome-scale, flux balance analysis (FBA) mathematical model was implemented with the proteomic resource allocation theory (PRAT) to simulate the intracellular metabolic fluxes in the two culture conditions. The opposing lactate production trend was found to be caused by a change in the TCA status, switching from regular progression to interrupted. The findings from this study showed the importance of considering the cellular proliferative status when comparing the metabolic data from different studies. Simulation results revealed that glycolysis was a preferred pathway under normoxia and hypoxia, and the reliance on oxidative phosphorylation was reduced as cells grew faster. A significantly different metabolic profile was found under hypoxically cultured hMSCs. The modelling approach of an FBA integrated with PRAT was able to predict the key experimentally observed trends and provided insights to complement the experimental findings. To the best of our knowledge, this is the first study to utilize such a modelling approach for the investigation of mammalian cells.

4.2 Introduction

Human Mesenchymal stromal/stem cells (hMSCs) have been widely studied for their therapeutic and medical potential. The traditional static culture environment is limited by the continuous depletion of nutrients and buildup of waste products. The composition of culture media plays a crucial role in supplying nutrients for cell growth as well as acting as a sink for the secreted byproducts (e.g. lactate). Exposure to inadequate culture media conditions can lead to increased cell detachment, senescence, apoptosis, and loss of stemness [248, 249]. Numerous supplements are present in culture media. For example, the commonly used Dulbecco's Modified Eagle's Medium includes 32 different components [250]. With the addition of serum, it becomes very challenging and resource demanding to evaluate the impact of the present components.

The metabolic network produces the required energy and biomass precursors to sustain cell maintenance and growth. Various studies have looked into how the concentration of key metabolites affect the status of hMSCs in vitro. Glucose, as the primary carbon source in culture media, is consumed by cells through both respiratory (i.e., oxidative phosphorylation) and glycolytic pathways. Respiration (or oxidative phosphorylation) is highly efficient in ATP generation (36 ATP/glucose consumed [251]) under aerobic conditions. However, most proliferating cells adopt a much less efficient mechanism of aerobic glycolysis (4 ATP/glucose consumed [251]), known as the "Warburg effect". Studies have found that stem cells and cancer cells preferentially undergo aerobic glycolysis as a more efficient pathway for synthesizing the required biomass precursors [251-253]. For fast-growing cells, the protein and amino acid synthesis consumes 35 times more glucose than that of ATP production, requiring the

more efficient NADPH-generating, glycolytic pathways for meeting this demand [251]. As a result of the elevated glycolytic fluxes, a high level of lactate production/secretion is expected for proliferating stem cells [254]. Under hypoxia, the downstream targets of HIF1α include key factors of the glycolytic pathway, which often resulted in increased glucose uptake and lactate secretion [102, 255]. The hMSCs cultured under hypoxia are expected to demonstrate a different metabolic uptake profile as a result of HIFα induction and the altered hypoxia-mediated growth.

Oxygen serves a complex role in cell metabolism. It acts as the terminal electron acceptor in the electron transport chain. Insufficient oxygen supply directs more glucose to be metabolized through anaerobic glycolysis. In addition, dissolved oxygen level regulates the transcription and activity of hundreds of metabolic factors via cellular hypoxic responses, including glucose transporters, lactate dehydrogenase, regulators for pyruvate entry in the TCA cycle, etc. [120, 255, 256]. During oxygen deficiency, the metabolic network is reprogrammed to enhance the capacity of glycolytic uptake and reduce oxygen consumption [93].

Lactate is produced as a byproduct during cell metabolism, resulting from glycolysis. The ratio between the lactate production and the glucose uptake has often been used to estimate cell glycolytic activity. Several reports have reported the ratio of close to 2 for hMSCs cultured under normoxia, and a strong reliance of growth on glycolytic pathways [79, 196, 257, 258]. The buildup of lactate in culture media inhibits cell growth due to the decrease of culture pH [259] and the reduction of the colony forming potential [260]. The amount of lactate produced needs to be closely monitored and mitigated, via media change or perfusion, for the cells cultured *in vitro*.

Experimental techniques (e.g., fluorescence-based assays) allow the evaluation of the concentrations and specific uptake or production rates of key metabolites. However, the measured results are the ensemble average across the studied cell pool. The heterogeneous nature of hMSCs [261, 262] suggests the existence of sub-groups with different growth and metabolic capacities. With the aim of enhancing the *in vitro* growth of hMSCs, it is important to better understand the profiles of sub-groups with different proliferative status (e.g. resting, actively proliferating). The experimental data, especially growth rate and lactate production, needs to be calibrated to reflect only that of the actively proliferating cells to allow more precise interpretation.

Complementary to experimental studies, mathematic modelling has been utilized to simulate intracellular interactions and predict the cellular response to external stimuli [170-172, 263]. To gain insights on the thousands of reactions in a metabolic network which are difficult to directly observe through experiments, metabolic models based on flux balance have been applied [173, 264-266]. In particular, a human cell genome-scale metabolic model (Recon 1) was established in 2006 to show the fluxes through the network, including 3,311 reactions and 2,766 metabolites [267]. Many studies have utilized this basic model for the discovery of novel metabolic functions or specializing it for the study of a specific cell type [268, 269]. In 2015, Fouladiha *et al.* compiled glucose, amino acids, and oxygen uptake data from the literature to calibrate the model for hMSCs (iMSC1255) [264, 270]. Despite the advancement by Fouladiha *et al.* on predicting the metabolic uptake in hMSCs, various inconsistencies and biological inaccuracies appear to remain. Preliminary tests in the present study showed that the model was not able to reasonably predict a change in growth rate

when varying the availability of key metabolites (e.g., glucose, oxygen). In addition, inherited from Recon 1, there lacks an overarching biological constraint to regulate the cell's decision for choosing the preferred allocation of metabolic activities between alternative pathways such as glycolysis and oxidative phosphorylation.

With respect to the introduction of overarching constraints, a proteomic resource allocation theory (PRAT) was proposed to show the cellular preference of the seemingly inefficient aerobic glycolysis is driven by its lower proteomic cost compared to that of respiration (known as the "overflowing metabolism" in bacteria, or "Warburg effect" in mammalian cells) [251, 252, 271]. Basan *et al.* recently demonstrated the applicability of such a theory with experiments and simulations in E.*coli* and hypothesized its applicability in mammalian cells [271]. Various other studies have used different approaches to simulate the "Warburg effect" in mammalian cells [266, 272-274] with their own advantages and compromises [253, 275].

This study aims to utilize flux balance analysis by means of a genome-scale metabolic model in conjunction with the autonomous regulation based on the PRAT to interpret the observed experimental data for actively proliferating hMSCs. The development model, which is an improvement to that by Fouladiha *et al.* [264], is used to simulate the changes in the intracellular fluxes that can particularly offer a reasonable explanation of the observed trends in lactate production under both normoxic and hypoxic conditions and over a range of growth rates.

4.3 Method

4.3.1 Cell culture

The immortalized hMSCs were cultured in a xeno-free, serum-free media (MSCs NutriStem, Biological Industries) for 3 days in 6-well plates (Costar, Thermo Fisher) with 3 or 6 repeats. Cell number was tracked every 24 hours *in silico* with SpectraMax i3x Microplate Reader (Molecular Devices). A seeding density of 5,000 cells/cm^2 was adopted. Cells from passages 6 - 10 were used. The culture incubator was maintained at 100% relative humidity, 5% CO_2 and 20% oxygen for the cells cultured under normoxia. Cells cultured in hypoxia were maintained in a Hypoxystation-H35 (Don Whitley Scientific) at 1% oxygen, 5% CO_2 and 85% humidity. 1% oxygen level was selected as it demonstrated the highest hypoxic growth rate (shown in Supplementary Figure S3.1 and S3.2).

Thymidine (T9250, Sigma) was added into the culture media at a concentration of 2μM to pause cell cycle progression to acquire data of non-proliferating cells.

4.3.2 Cell cycle

Cells were collected at the end of culture (Day-3) and fixed in 70% ethanol. Dilutions were made with propidium iodide (P4864, Sigma) to a final concentration of 50 μg/mL and ribonuclease (R4875, Sigma) to a final concentration of 100 μg/mL. Flow cytometer (ADP LX High-Performance Research Flow Cytometer, CyAn, Beckman Coulter) was used to measure the fluorescence. Single cells were gated with forward scatter and pulse width.

4.3.3 Lactate Assay

Culture media were collected after 3 days of culture. The volume of the remaining culture media was recorded to account for evaporation. Lactate assay kit (MAK064, Sigma) was used to measure the concentration of the samples. Dilutions were made to ensure all measured samples were in the applicable range of detection. The assay was carried out per supplier's instruction.

4.3.4 Calibration of experimental measurements for proliferating cells

The measured ensemble-average cell pool data was calibrated to obtain that of the actively proliferating cells. Cell cycle data was used to estimate the amount of actively proliferating cells (*P%*, Equation 4.1), which comprise (1) the cells in the S-phase (*S%*), (2) the cells in the G2/M-phase (*G2-M%*), and (3) the cells that progressed through the G1-phase, assumed to be a proportion of the total number of cells in the G1-phase (*G1%*) at the time of detection, with the proportion assumed to be equal to the sum of the percentages of the cells in the first two categories (i.e. *S% + G2-M%*). The remaining cells were regarded as not actively proliferating (*Q%*, Equation 4.2). The *P%* and *Q%* were calculated from the experimental data at the end of culture period (i.e. after 72 hours).

$$P\% = S\% + G2\text{-}M\% + G1\% * (S\% + G2\text{-}M\%) \qquad \textbf{Equation 4.1}$$

$$Q\% = 1 - P\% \qquad \textbf{Equation 4.2}$$

The counted cell number at Day-1 is represented by *m*, the number of seeded cells is represented by m_0. Day-1 cell number (as opposed to the number of seeded cells) was used to assess the growth rate as a lag phase was expected in the first 24 hours

after seeding. The percentage of cells that were proliferating after each population doubling was assumed to remain constant. The amount of proliferating and non-proliferating cells at population doubling *i* are represented by Equations 4.3 and 4.4.

$P_i = \quad P\% * m * (1 + P\%)^i$ ***Equation 4.3***

$Q_i = \quad Q\% * m * (1 + P\%)^i$ ***Equation 4.4***

At the end of culture period, assuming that cells have undergone *k-th* population doubling,

$k = \frac{log(\frac{F}{m})}{log(1+P\%)}$ ***Equation 4.5***

where *F* denotes the counted cell number after 72 hours of culture, the population doubling time T_{PD} can be calculated with Equation 4.6. The calibrated specific growth rate was acquired from Equation 4.7. Further explanation on the derivation of Equations 4.3 - 4.5 is included in the Supplementary Information.

T_{PD} *(in hours)* $= \frac{48}{k}$ ***Equation 4.6***

Specific growth rate (newly produced cells/proliferating cells/hr) $= \frac{F-m}{m*P\%*48}$

Equation 4.7

The sum of the product of (i) the time the proliferating (P_{time}) and non-proliferating cells (Q_{time}) spent in the culture media between Day-1 and Day-3 and (ii) the corresponding amount of cells, denoted by P_{time} and Q_{time}, can be calculated with Equations 4.8 and 4.9, respectively.

P_{time} *(in hours)* = $\sum_1^k [P_i] * T_{PD} + \frac{(m+m_0)}{2} * P\% * 24$ ***Equation 4.8***

Q_{time} *(in hours)* = $\sum_1^k [Q_i] * T_{PD} + \frac{(m+m_0)}{2} * Q\% * 24$ ***Equation 4.9***

In both equations, the first term of the right-hand-side corresponds to the period of cell culture from 24 h to 72 h, and the second term offers an estimation during the lag phase in the first 24 hours. The specific lactate production rate for the proliferating cells (*R-LAC$_P$*) was calculated using Equation 4.10, after deducting the lactate produced by the non-proliferating cells (*R-LAC$_Q$*) from the total secreted lactate (*LAC$_{TOT}$*). *R-LAC$_Q$* was measured from the cells with thymidine-mediated, interrupted cell cycle.

R-LAC$_P$ (µmol/cell/hr)= $\frac{(LAC_{TOT} - R{-}LAC_Q * Q_{time})}{P_{time}}$ ***Equation 4.10***

4.3.5 Flux balance analysis (FBA)

A recently published hMSCs genome-scale metabolic model (*iMSC1255* [264]) was used as a base model in this study. The model utilized FBA [173] to simulate the metabolic network. Various adjustments and improvements were made in this work to allow the model to predict the metabolic uptake profile for different biomass growth rates. The metabolism for glutamine uptake was enabled. In addition, improvements on reactions and boundary limitations were also made to enhance its biological relevance. All implemented adjustments are included in the Supplementary Information. The improved model is able to simulate the metabolic uptake requirement and the intracellular flux distribution for a range of growth rates. The simulations were

run with Cobra toolbox to determine optimal flux distribution and Gurobi 6.0 as a linear programming solver [276, 277].

4.3.6 Proteomic Resource Allocation

The single-cell model simulates the intracellular metabolic fluxes while allowing exchanges of key metabolites (e.g. glucose, amino acids, bicarbonate ion, water, etc.) across cell boundaries. The proteomic resource allocation constraint was implemented in light of the recent development [271, 274]. PRAT was added into the model to constrain the glucose metabolic preference through the glycolytic or the respiratory pathway. Simulation was performed with PRAT constraints and boundary conditions to determine the optimal solutions for the target objectives, i.e. maximum biomass synthesis or minimum glucose intake.

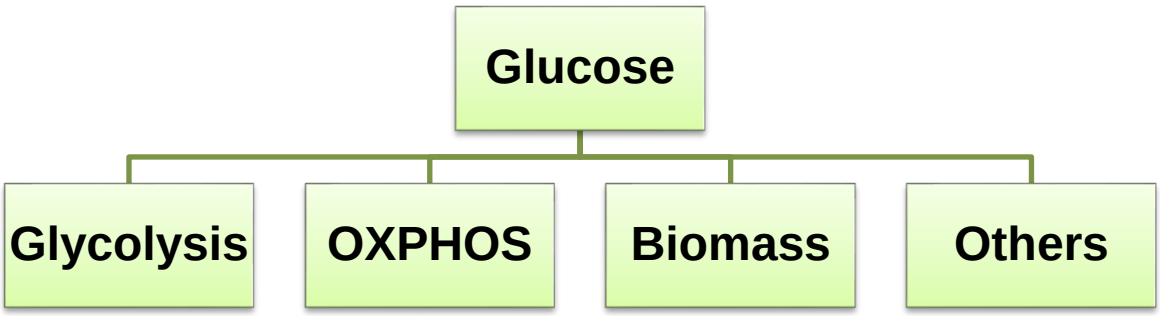

Figure 4.1: The simplified roadmap for the destination of intake glucose used in the simulation.

As a simplified illustration (Figure 4.1), glucose can be processed through glycolysis, oxidative phosphorylation (OXPHOS), biomass synthesis, and other functions. The total proteomic resource and enzymatic utilization by these 4 sections is constrained to add up to 100%. This study focuses on the proteome consumption of the first three sections, using Φ_{max} to denote the normalized maximum fraction attainable from these three sections (Equation 4.11). In Equation 4.11, v represents the flux going through

glycolysis (“g”) or oxidative phosphorylation (“o”), and *w* indicates the relative proteome burden associated with processing each unit flux. For biomass synthesis, the flux and the proteome cost are represented by *μ* and *b*, respectively.

$$w_g * v_g + w_O * v_O + b * \mu \leqslant \Phi_{max} \qquad \textbf{Equation 4.11}$$

PRAT parameters (w_g, w_O, and b) and the PPP% were determined with the specific growth rate and specific lactate production data acquired in this study. The ENO and CS fluxes were selected to respectively represent the glycolysis and OXPHOS flux for model fitting. The objective function was set to minimize glucose uptake at each given growth rate (μ) to determine the respective fluxes going through glycolysis, OXPHOS and biomass synthesis. A linear relationship [271] between the fluxes going through glycolysis and OXPHOS and the growth rate was assumed (Equations 4.12 and 4.13),

$$v_g = k_1 * \mu + c_1 \qquad \textbf{Equation 4.12}$$

$$v_O = k_2 * \mu + c_2 \qquad \textbf{Equation 4.13}$$

where k and c are constants. The constants k_1, k_2, c_1, and c_2 were dictated by the μ-v_g and μ-v_O correlations obtained from the FBA simulation. Equation 4.11 was then added into the FBA model as the PRAT constraint.

4.3.7 Simulation Parameters

With the integration of the PRAT constraint, the model simulated cell growth with different metabolic uptake profiles. The glucose uptake flux was taken as an input to the model with incremental increases to simulate the maximum attainable growth rate

corresponding to each level of glucose uptake. The uptake upper bound for the essential amino acids was set to exceed those from the required growth to ensure they were not limiting the growth. The oxygen uptake rate was set with an upper bound of 0.5 and 0.05 mmol/g-drymass/hr for normoxic and hypoxic simulations, respectively. The amount of glutamine uptake was allowed with the maximum bound set at 1 mmol/g-drymass/hr. Several different percentages of glucose channeling through the pentose phosphate pathway (denoted as PPP%) were simulated to determine the one leading to the best fit to the trend observed in experimental data.

Figure 4.2 summarizes the key steps for constructing the model as carried out in this study.

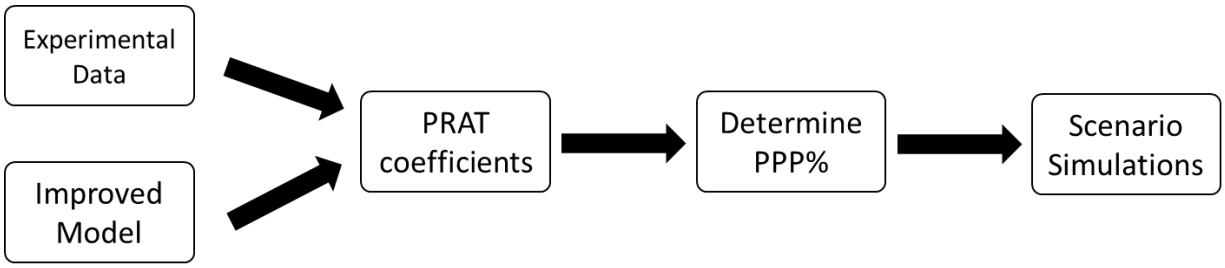

Figure 4.2: The major steps for model construction.

4.4 Results

4.4.1 Cell culture and lactate measurement under normoxia

The immortalized hMSCs were cultured under 20% oxygen in a serum-free media. The spent media was extracted to measure the secreted lactate content. Cell number was tracked *in silico* every 24 hours and used to estimate the growth rate. Lactate production was assessed with cells during the growth phase before 70% confluency

was reached. The experiment was repeated nine times, and a total of 30 sets of data were collected.

Figure 4.3A) shows that a majority of the hMSCs displayed spindle-like morphology, with the nucleus highlighted with DNA-stain in Figure 4.3B). In all data presented, the end-point cell viability was higher than 85%. After 3 days of culture, cells were harvested and analyzed for their distribution throughout the cell cycle. Figure 4.3C) shows an example of the parameters used for single-cell gating and outlier removal, and Figure 4.3D) shows an example for identifying the peak locations and areas. The cell numbers from the 30 experimental sets are shown in Figure 4.3E), displaying variable specific growth rates. The growth rate and lactate production rate mentioned in the rest of the manuscript all refer to the specific rates that have been calibrated for proliferating cells.

This study aims to assess the amount of lactate produced only from the proliferating cells, therefore the number of the non-growing cells and their associated lactate production were quantified for calibration. Cell cycle data revealed the percentages of cells in different cell cycle phases. In the example shown in Figure 4.3D), 64.3% of the cells was found in the G1/G0-phase, 19.4% in the S-phase and 16.3% in the G2/M-phase. Equation 4.1 was used to determine the number of proliferating cells. As a result, 58.7% of the cells shown in Figure 4.3D) was estimated to be proliferating. The proportion of the proliferating cells was assumed to be conserved over each population doubling. Equations 4.1 and 4.7 were used to evaluate cellular growth rate, which was found to range from 0.022 to 0.010 (new-cell/parental-cell/hr). Population doubling time was found between 13.4 – 25.0 hours (Equation 4.6). Table 4.1 shows the

tabulated results from Run 1 and Run 2, each with three repeated sets; the full list of data is given in the Supplementary Information.

Over the 3-day culture period, the lactate production by the proliferating cells was calibrated using Equations 4.1 - 4.10 after discounting the amount of lactate produced from the non-growing cells. The lactate production rate by the non-growing cells was found to be 0.9 ± 0.03 μmol/ million-cells/hr, and that of the proliferating cells was calculated between 0.52 – 2.26 μmol/ million-cells/hr. Figure 4.3F) shows lactate production rate versus growth rate for the proliferating cells from each experimental run.

The data shown in Figure 4.3F) was acquired from hMSCs cultured under the same culture media and oxygen level, showing a significant difference in growth rate between different runs. In addition, the amount of lactate secreted from the proliferating cells was found to be strongly dependent on their growth rate, showing a negative parabolic trend. For the purpose of this study, this trend is referred to as the "growth regime dependent production" (GRDP). The existence of a turning point that separates an increasing tendency and a decreasing tendency suggests that a significant alteration in the carbon metabolism may have occurred in the fast-growing hMSCs under 20% oxygen.

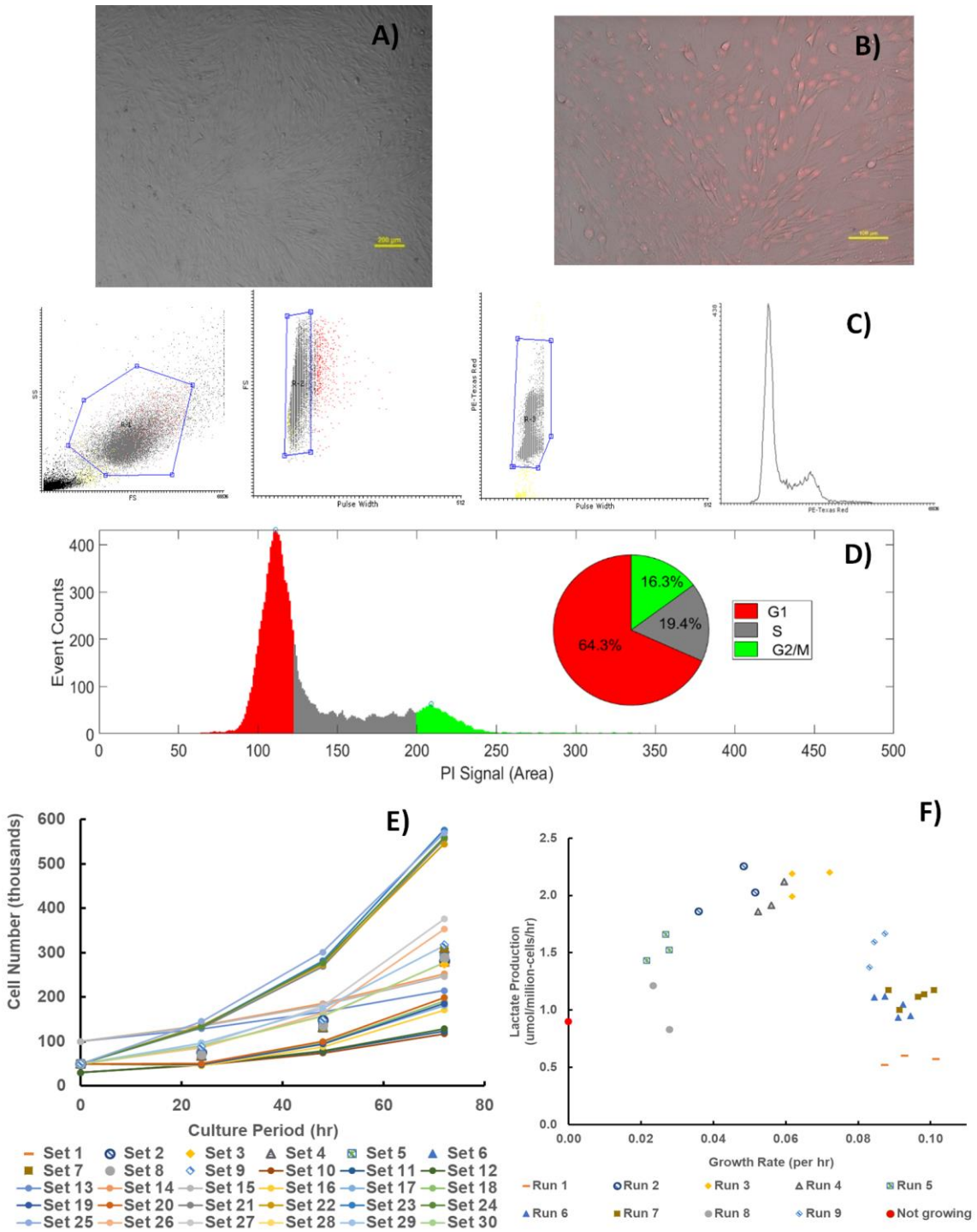

Figure 4.3: The compiled experimental data for hMSCs cultured under 20% oxygen. A) The microscopic image of hMSCs. B) The microscopic image of hMSCs with nucleus stain. C) An example of the gating parameters used for single-cell gating and outlier removal from flow cytometry data. From left to right, the parameter pairs are forward scatter vs. side scatter, forward scatter vs. pulse width, pulse width vs. PI, PI vs. event counts. D) An example for identifying the peaks and areas under-the-peak to determine the proportion of cells in different cell cycle stages. The results were processed using a MATLAB script. E) The counted cell numbers with culture duration from different experiment sets. F) Specific lactate production rate vs. specific growth rate, calibrated for the actively proliferating hMSCs from different experiment runs.

Table 4.1: Partial tabulated results for the cell cycle, specific growth rate, population doubling time and specific lactate production data for the actively proliferating hMSC. Data from three repeated sets are shown from Run 1 and Run 2. The full tabulated result is included as Supplementary Table 4.1.

Experiment Run	Sample	Specific Lactate production (µmol/million cells/hr)	Specific growth rate (hr^{-1})	t_{PD} (hr)	G1 %	(S+G2/M) %	Proliferating%
Run 1	**Set1**	0.77	0.093	17.7	64%	36%	59%
	Set2	0.77	0.101	16.8	64%	36%	59%
	Set3	0.67	0.087	18.3	64%	36%	59%
Run 2	**Set4**	2.03	0.052	18.2	58%	42%	66%
	Set5	2.26	0.048	19.0	58%	42%	66%
	Set6	1.86	0.036	23.9	58%	42%	66%

4.4.2 Model adjustment

This study aims to establish a mathematical model to address the observed GRDP described in the previous section. The *iMSC1255* model reported by Fouladiha *et al.* [264] was used as the base model, which was derived from Recon 1 and calibrated with hMSCs transcriptomic, proteomic and metabolic data. The *iMSC1255* improved hMSCs specificity of the generic human metabolic network model, however, various critical issues needed to be resolved for the intended use for this study, including the following: (1) the model was not able to predict cell growth rate with a change in key metabolites (glucose, oxygen, lactate) uptake/production; (2) glutamine uptake was disabled; (3) the availability of amino acids was the factor limiting the growth rate, which was not applicable to this study; and (4) certain key reactions appeared to have been removed or altered without clear justification. This study resolved the prediction challenges associated with the model and improved its biological relevance. All

amended changes are listed in the Supplementary Information. The updated model was able to predict the metabolic uptake requirement to achieve the target biomass growth rate.

Figure 4.4 shows the simulation results for a few key metabolic exchange fluxes corresponding to the maximization of cell growth rate with different glucose uptake levels. The glucose uptake and the CO_2 production both increased with the growth rate, indicating a strong correlation between growth and OXPHOS. No lactate production was predicted, contradicting with experimental observations, which highlights an inherent flaw of the model even after the aforementioned improvements: the lack of a biological constraint on guiding the metabolic uptake regime, i.e. through OXPHOS or glycolysis.

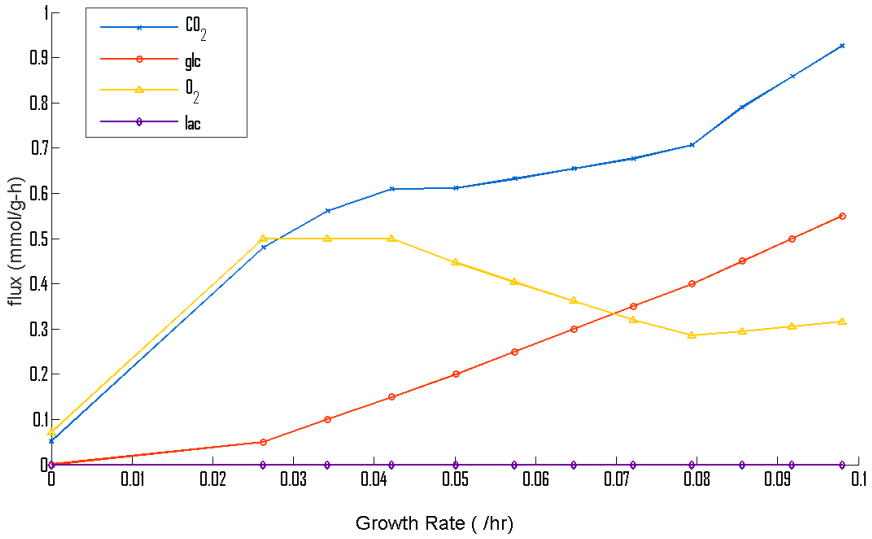

Figure 4.4: The simulation result in the absence of the PRAT. The exchange fluxes for CO_2, O_2, glucose and lactate are shown at different growth rates.

4.4.3 The incorporation of PRAT

The improved model still required a biological constraint to account for the difference in the performance of alternative pathways in terms of the cost associated with energy

biogenesis and biomass production, which appeared to be required to more accurately simulate the metabolic uptake profile for a proliferating cell. To address this issue, The PRAT was incorporated, particularly to account for the proportional proteome utilization associated with the different cellular functions as shown in Figure 4.1.

The PRAT coefficients (Equation 4.11) associated with OXPHOS (W_O), glycolysis (W_g), biomass production (b) and the pentose phosphate pathway (PPP) were determined to yield a comparable trend to the experimentally measured lactate production and growth rate data from Figure 4.3F). It should be noted that for reasons yet to be further identified, the calibration of the model was only able to yield a match with the experimental data in terms of the qualitative trend (i.e. GRPD), but quantitatively such a model can only predict the lactate production rate over a feasible range of growth rate narrower than the experimentally observed range. In all the relevant results presented here (including Figures 4.5-4.10), the experimental data has thus been re-scaled (downward for both lactate production and growth rate) in order to ease the (qualitative) comparison with the modelling results. The comparisons presented as such do not imply the quantitative accuracy of the model.

The calculated PRAT coefficients are shown in Table 4.2. The fitted normalized biomass production coefficient was found at 0.25. W_O and W_g differ by two orders of magnitude, showing a significantly more efficient proteome utilization through the glycolytic pathway.

Table 4.2: The normalized PRAT coefficients with 3% PPP allocation for the proliferating hMSCs cultured under 20% oxygen.

	W_g	W_o	b
Normoxia	0.117	10.25	0.25

The PPP plays a major role in cell proliferation, synthesizing a plethora of the required NAD, NADPH, nucleotides, and other biomass precursors. The proportion of the intake glucose directed towards the PPP affects the rest of the metabolic network (e.g., in the balance of NADPH, nucleotides, etc.). Different percentage allocations of glucose into the PPP (glucose-to-PPP) were tested to determine the best fit with the trend observed in experimental data, as shown in Figure 4.3F). The simulation results are shown in Figure 4.5. The tested percentage allocation was implemented in the FBA model as the maximum allowable bound. The 3% of glucose-to-PPP allocation resulted in the best fit and was thus adopted for further simulation and analysis.

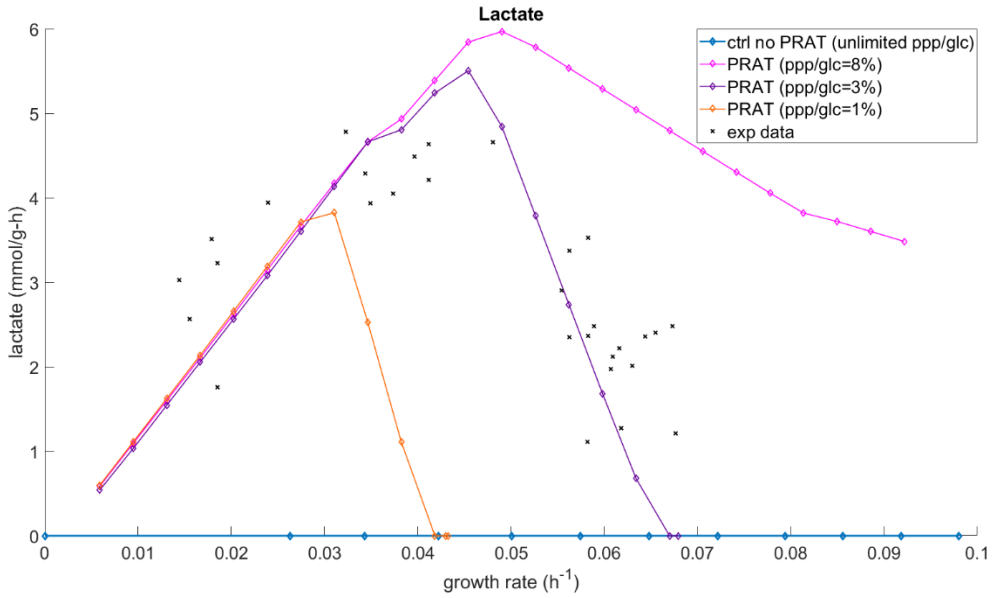

Figure 4.5: The effect of the glucose-to-PPP on the simulation results. Experimental data is shown along with different glucose-to-PPP percentages (1%, 3% and 8%). The simulation results in the absence of the PRAT constraint is also shown.

4.4.4 Simulation results corresponding to normoxia

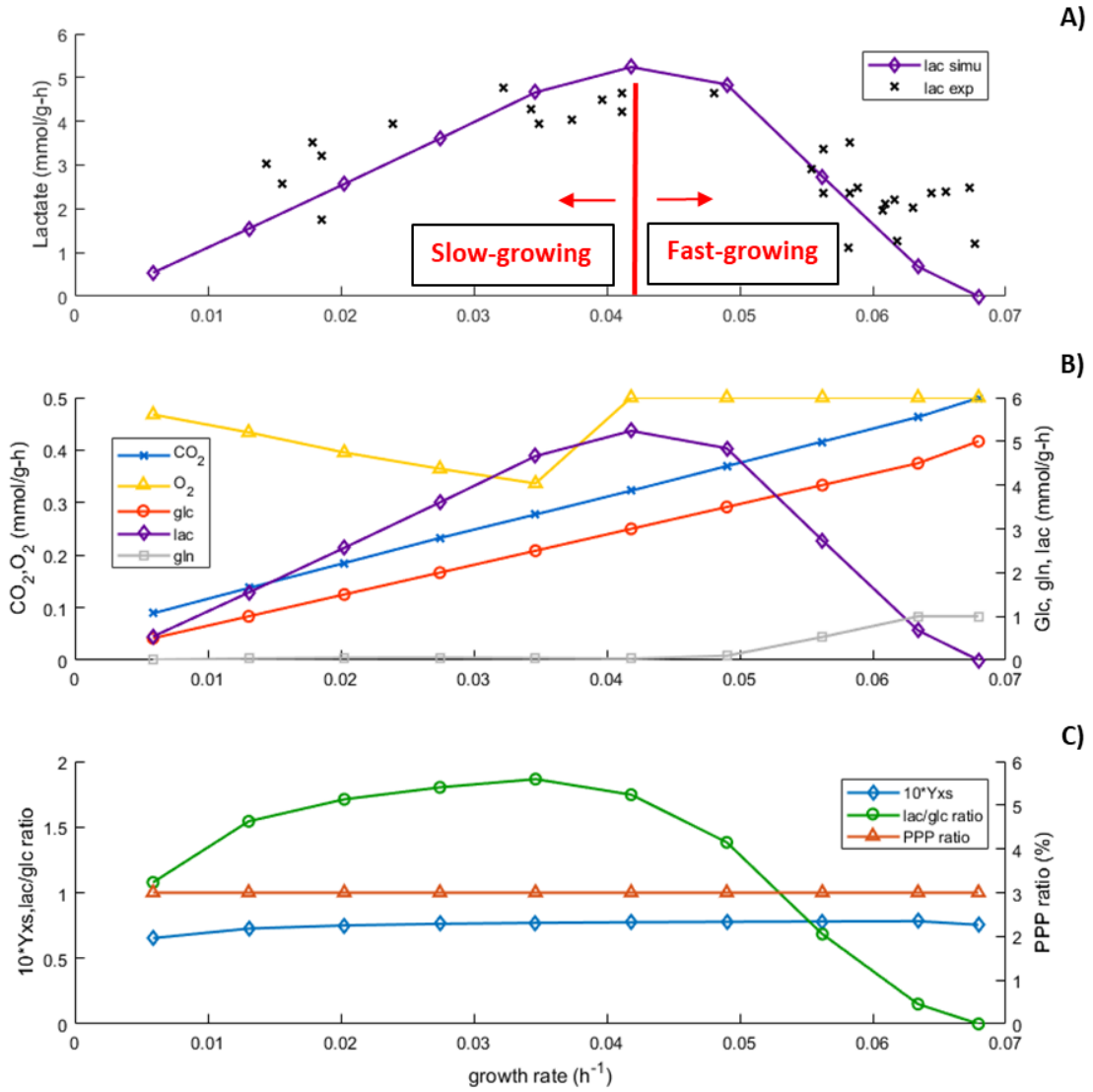

Figure 4.6: Simulation results with the PRAT constraint for hMSCs cultured under 20% oxygen. Simulated growth rates are shown on the x-axis. A) The simulated and experimentally measured lactate production (lac). Slow-growing cells and fast-growing cells were defined. B) The fluxes of the key metabolites, CO_2, O_2, glucose (glc), glutamine (gln), and lactate. C) The biomass utilization efficiency, biomass produced per glucose intake, is shown with a factor of 10 (10*Yxs), along with the percentage utilization of PPP (PPP ratio, referred to earlier as PPP%) and specific lactate/glucose ratio (lac/glc).

With the incorporation of the PRAT constraint, the improved model was able to capture the GRDP. Figure 4.6A) shows the simulation and experimental results for how specific lactate production varies with growth rate, with the highest lactate-producing

growth rate at μ=0.042. For the purpose of this study, the cells grew slower than μ=0.042 under 20% oxygen are referred to as slow-growing cells whose lactate production increased with growth rate. The fast-growing cells, with μ>0.042, showed a decline in lactate production as the growth rate increased. Meanwhile, the corresponding exchange fluxes for a few key metabolites, i.e. O_2, CO_2, glucose, and glutamine, are shown in Figure 4.6B). The specific production of CO_2 closely correlated with glucose uptake, although smaller than the latter by an order of magnitude. This low production of CO_2 suggests a small role played by the OXPHOS. Glutamine was only required in the fast-growing cells. At the highest simulated growth rate (μ=0.068 hr^{-1}), glutamine was consumed at a ratio of 1:5 to the amount of glucose required. Oxygen consumption varied to satisfy the growth requirement. A trend similar to the GRDP was not shown in the exchange flux of other key metabolites. After reaching peak lactate production, the succeeding reduction is mediated by the adjustment in the metabolic network to satisfy the demand in energy and precursors for delivering the target growth rate. The simulated lactate production for the fast-growing cells in Figure 4.6A) appears to be consistently higher than the experimentally measured results. It may be due to the additional uptake of other metabolites in fast-growing cells which allowed some of the carbon to be secreted out of cells in the form of lactate.

With an increase in the growth rate, the efficiency in glucose conversion into biomass (Yxs) showed a slight increase, from the per gram conversion of 6.5% at μ=0.006 hr^{-1}, to 7.6% at μ=0.068 hr^{-1} (Figure 4.6C)), indicating more glucose was used to generate biomass at higher growth rates. The ratio of glucose-consumed to lactate-produced ($Y_{L/G}$) showed a similar trend to that of lactate production. $Y_{L/G}$ increased from 1.1 to

1.9 and then declined to close to 0 at the highest growth rate. The amount of glucose consumed through the PPP was utilized to the maximum allowable bound at 3% for all growth rates.

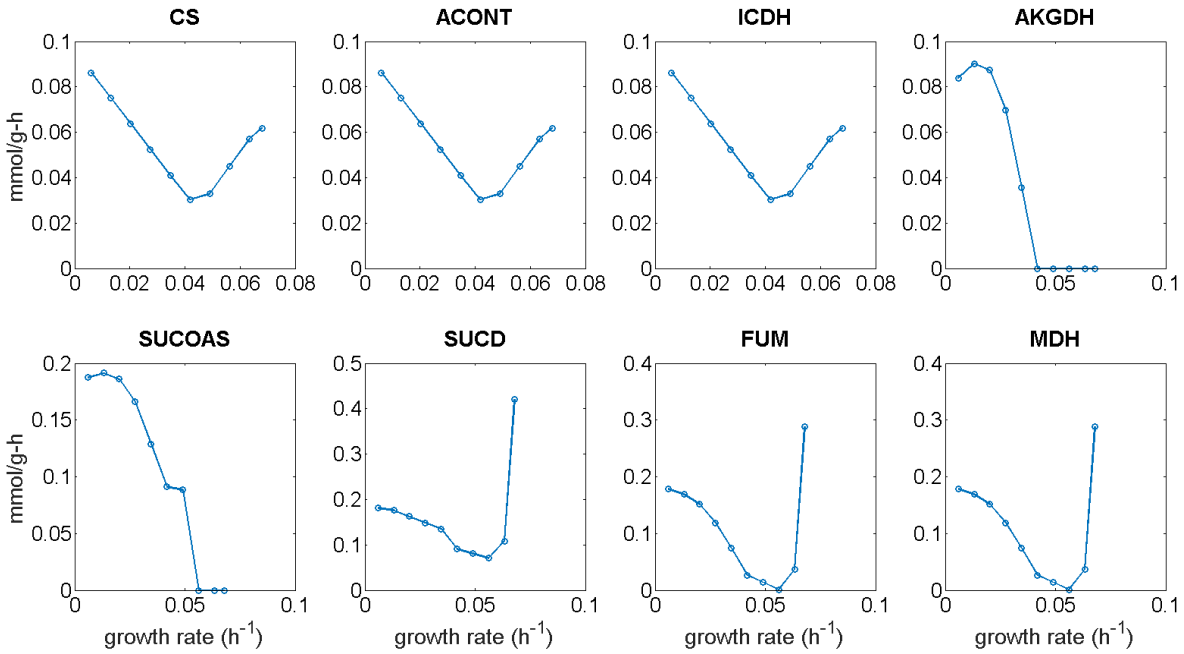

Figure 4.7: The simulated key fluxes in the TCA cycle at different growth rates under normoxia.

Several key fluxes in the TCA cycle are plotted in Figure 4.7 to identify the cause for the opposing trends observed in the GRDP. The scale of the fluxes shown in Figure 4.7 is much lower than that of the total glucose uptake (Figure 4.7B)), confirming a small role of the OXPHOS in proliferating cells. Meanwhile, the majority of the glucose was processed through the glycolytic pathway. In the slow-growing cells, the increase in biomass requirement was met with ramping up the glycolytic and downregulating the OXPHOS pathway, due to the more efficient proteome utilization of glycolysis (Table 4.2). This is shown for the 8 key TCA fluxes in Figure 4.7 in the slow-growing cells. For example, the flux through 2-oxoglutarate dehydrogenase (AKGDH), the enzyme responsible for catalyzing a-ketoglutarate and coenzyme A, was reduced from 0.08 (μ=0.006) to 0 (μ=0.042). When growth rate exceeds 0.042 h^{-1}, in the fast-growing

cells, the reduction in all of the TCA fluxes were no longer feasible, as AKGDH, an intermediate flux, has reached 0. Therefore, the metabolic network was rebalanced to satisfy the growing demand in energy and biomass precursors. Following the abolished AKGDH, the succeeding flux (SUCOAS) plunged to zero at μ=0.056. The adjusted TCA fluxes showed increasing trends in the fast-growing cells as the growth rate increases. The decline and eventual cease of AKGDH was hypothesized to be a key response associated with the increase in growth rate; the preceding (CS, ACONT, and ICDH) and succeeding (SUCOAS, SUCD, FUM, and MDH) fluxes were fully or partially dependent on that of AKGDH.

Different simulation boundary parameters were tested to evaluate the robustness of the simulated GRDP. With the PRAT coefficients presented in Table 4.2, different combinations of glucose and oxygen uptake were simulated to capture the maximum growth rate, lactate production and PRAT utilization (Figure 4.8). Figure 4.8A) shows that such a phenomenon was conserved with different oxygen uptake levels. A higher oxygen uptake reduced the amount of lactate produced for a given growth rate. Figures 4.8B) and 4.8C) show that, with the obtained PRAT parameters from Table 4.2, the normalized proteome utilization did not reach 100% when oxygen uptake was low; moving away from the severe hypoxic condition, the simulated cases showed a 100% utilization of proteomic resource, and the growth rate was only dependent on the uptake of glucose, not oxygen.

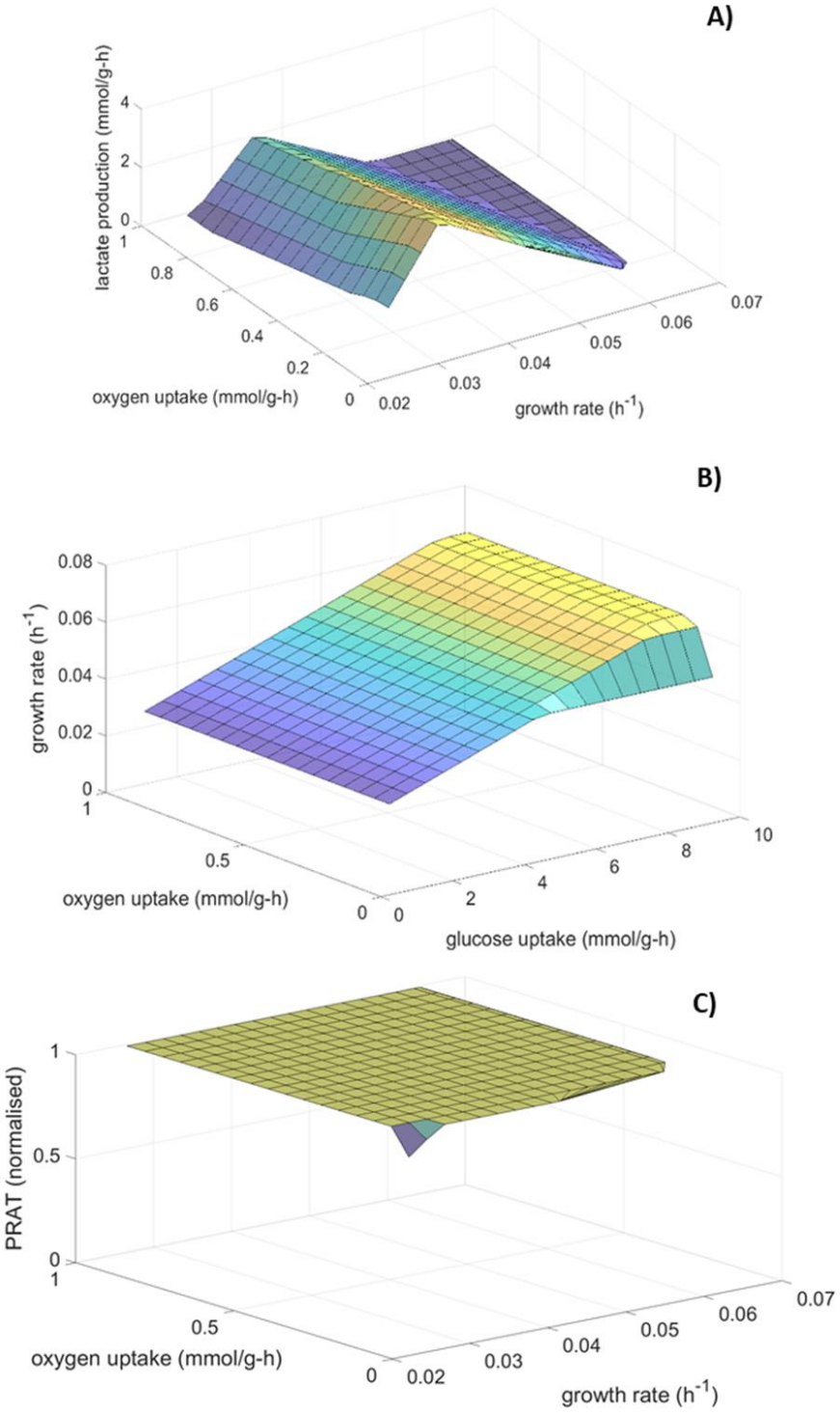

Figure 4.8: Simulation results showing how different oxygen and glucose uptake affect growth rate. Different combinations of different glucose and oxygen uptake were simulated to show the achieved maximum growth rate, lactate produced and PRAT utilization for each case. A) Different oxygen uptake, lactate production, and the associated growth rate are shown. The GRDP was found to be preserved across different oxygen uptake levels. B) Different combination of oxygen, glucose uptake, and the associated growth rates. Oxygen uptake was not a key factor in regulating growth rate except for under severe hypoxia. C) The normalized proteome utilization rate (PRAT) with different oxygen and glucose uptake.

4.4.5 Hypoxic experiments and simulation results

The growth and lactate production data for hMSCs cultured under hypoxia (1% oxygen) is shown in Figure 4.9, with the experimental result in Figure 4.9A), the fitted PRAT coefficients in Figure 4.9B), and the simulation results in Figure 4.9C) – E). The fitted PPP% (i.e. the glucose-to-PPP percentage) was found to be 12%. The tabulated results shown in Figure 4.9 are included in the Supplementary Table 4.2.

Compared to hMSCs cultured under 20% oxygen, an enhanced cell growth rate was observed under hypoxia, as the experimentally measured growth rate ranges from 0.048 – 0.143 (in contrast with the range of 0.022 – 0.10 observed under normoxia). In addition, the GRDP was not observed in the hypoxic culture experiments. Instead, a simple linear regression better described the relationship between the growth rate and the lactate production rate (Figure 4.9).

As in the normoxic case, the fitted PRAT coefficients showed a higher proteome utilization efficiency in the glycolytic pathway than in the respiration pathway. However, the W_g/W_o ratio was reduced to 25.4, two-folds smaller than the ratio calculated from the normoxic coefficients (which was 87.6). Although under both oxygen levels glycolysis was preferred over that of OXPHOS, hMSCs cultured under 1% showed an increased preference for the OXPHOS relative to the normoxic case.

The simulated lactate production is plotted on Figure 4.9C). Key metabolites (CO_2, glutamine, and glucose) all showed linear increases with growth rate (Figure 4.9D)). Oxygen consumption reached the maximum allowable uptake of 0.05 in all simulated

cases. The glutamine to glucose uptake ratio was found at 1:20, a lower glutamine demand than under normoxia.

The increase in growth rate was mediated by a consistent increase in $Y_{L/G}$, from 0.75 at μ=0.037 to 1.67 at μ=0.094 (Figure 4.9E)). The amount of glucose converted into biomass, *Yxs*, decreased with growth rate by 4.4-folds between the lowest (μ=0.036) and highest (μ=0.094) growth rates. This indicates a higher proportion of glucose was turned into lactate, signifying an increase in the significance of glycolysis at higher growth rates.

Under hypoxia, the key fluxes in the TCA cycle were examined (Figure 4.10). The three early TCA fluxes (CS, ACONT, and ICDH) showed an (insignificant) increase with $\mu \leqslant 0.068$, this was due to the PRAT constraint (the left-hand-side of Equation 4.11) not reaching 100% utilization, allowing additional glucose being processed through the less efficient OXPHOS. At $\mu > 0.068$, the PRAT constraint became active at 100% utilization, any further increase in growth rate resulted in the undertaking by the more efficient proteome utilization pathway, i.e. glycolysis. As a result, the TCA fluxes were reduced by 70% when the maximum growth rate (μ=0.094) was reached. The three intermediate TCA fluxes, AKGDH, SUCOAS, SUCD were not activated, indicating the TCA cycle was not fully functional under hypoxia. The remaining two TCA fluxes FUM and MDH, both predicted with a magnitude much lower than under 20% oxygen, showed continuous increasing trends with growth rates. It should be noted that the reactants associated with these fluxes were produced in metabolic reactions outside of the TCA cycle and transported into the mitochondria, which may explain their predicted trends.

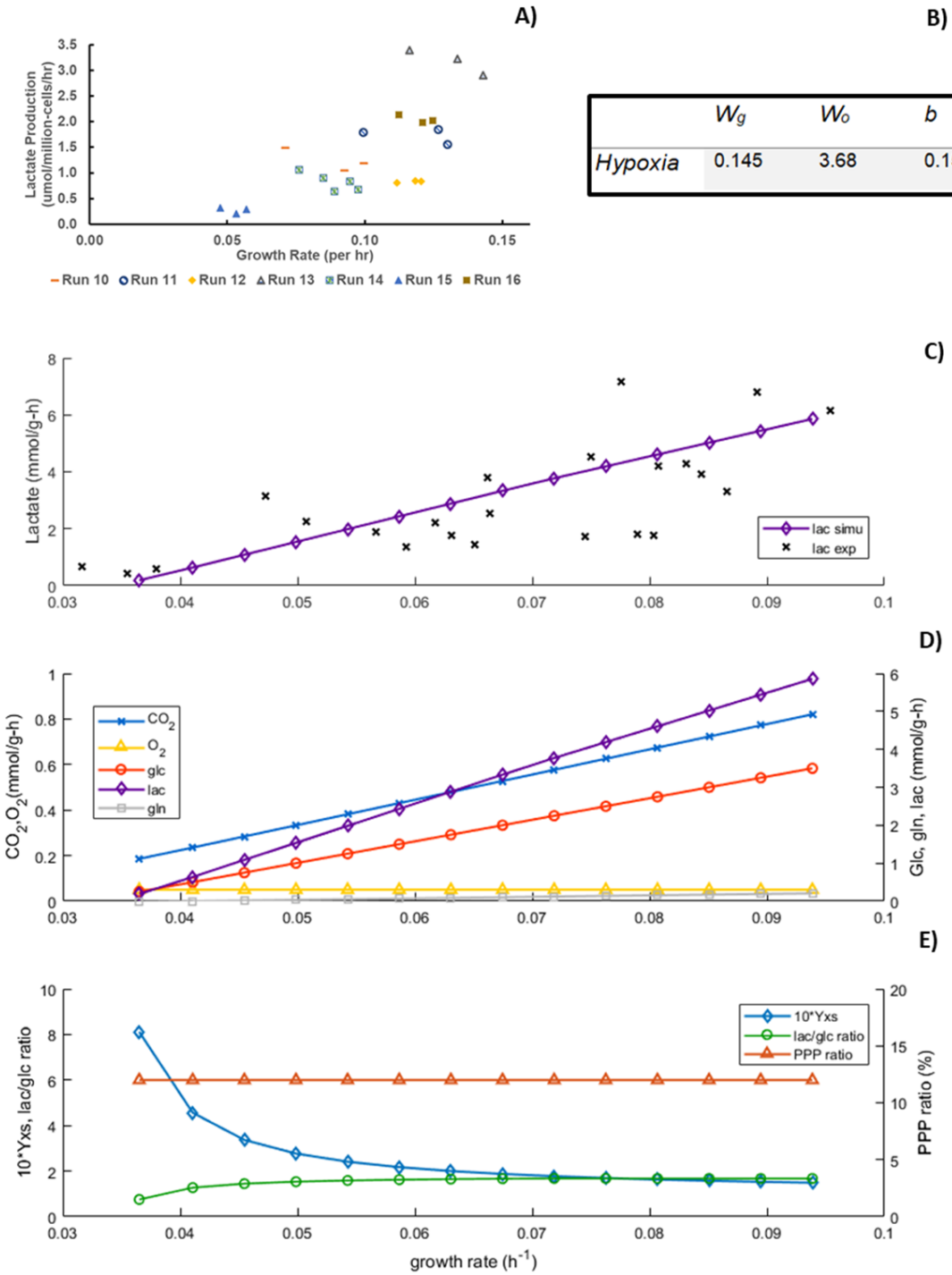

	W_g	W_o	b
Hypoxia	0.145	3.68	0.154

Figure 4.9 Experimental and simulation results with the PRAT constraint for hMSCs cultured under 1% oxygen. Growth rates are shown on the x-axis. A) Calibrated experimental results for growth rate and specific lactate production for the actively proliferating hMSCs. B) The fitted PRAT coefficients for hMSCs cultured under 1% oxygen. C) The simulated and experimentally measured specific lactate (lac) production. D) The uptake fluxes of the key metabolites, CO_2, O_2, glucose (glc), glutamine (gln), and lactate. E) The biomass utilization efficiency, biomass produced per glucose intake, is shown with a factor of 10 (10*Yxs), along with the percentage utilization of PPP (PPP ratio) and lactate/glucose ratio (lac/glc).

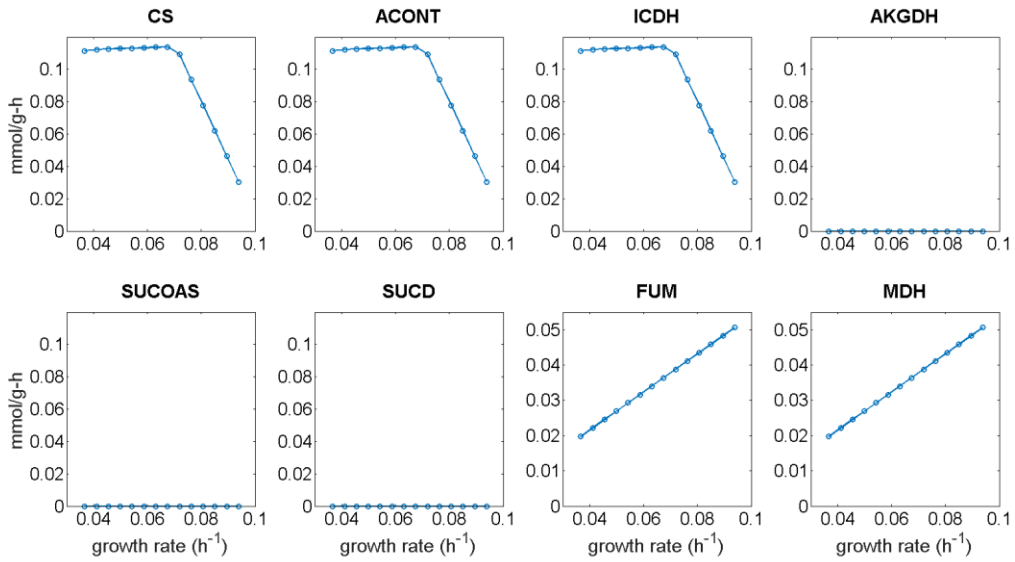

Figure 4.10: The simulated key fluxes in the TCA cycle under hypoxia.

4.4.6 Simulated glucose distribution in normoxia and hypoxia

The proportion of glucose utilized for each cellular function was further investigated under both oxygen conditions (Figure 4.11). The utilization of glucose was traced by its destinations, i.e. pyruvate-to-lactate (*Glycolysis%),* pyruvate-into-TCA (*OXPHOS%*), glucose-to-PPP (*PPP%*) and all other destinations (*Other%*). The ratio between the amount of glucose converted into lactate to that transferred into the TCA is shown as *Glycolysis/OXPHOS*.

Under 20% oxygen (Figure 4.11A)), the GRDP was reflected by the trend of *Glycolysis%*. The *OXPHOS%* showed a continuous decline with growth rate, indicating that although TCA fluxes increased in the slow-growing cells (Figure 4.7), the scale of increase was smaller than that of the uptake glucose. In the fast-growing cells, a significant amount of glucose was utilized through other pathways (*Other%*), primarily for amino acid synthesis. These produced amino acids may subsequently be converted into substrates to contribute to biomass synthesis or being secreted. The

ratio of *Glycolysis/OXPHOS* were found to be greater than 2, indicating for every part of glucose entering the TCA cycle there was always more than 2 parts of glucose being converted into lactate, showing a consistent employment of aerobic glycolysis. Under hypoxia, a continuous increase for the *Glycolysis%* and *Glycolysis/OXPHOS* were observed. Similar to normoxia, the *OXPHOS%* was reduced with growth rate. The amount of glucose utilized for amino acid production varied. At lower growth rates, the PRAT constraint was not limited, which resulted in glucose being used for synthesizing different amino acids to satisfy the experimentally observed trend for lactate production. This requirement was reduced as proteome utilization reached 100%, an additional small amount of glucose was needed to synthesize amino acids to achieve high growth rates.

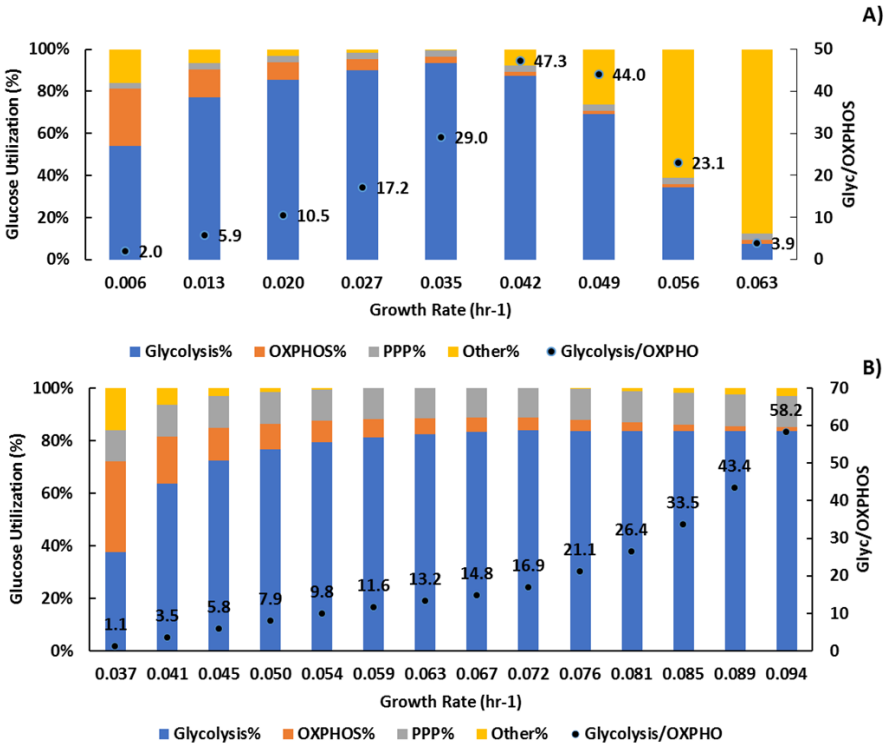

Figure 4.11: Compiled simulation results for glucose utilization at different growth rates. The percentage of glucose entering the TCA cycle, OXPHOS%; converted to lactate, Glycolysis%; processed through the PPP, PPP%; through other pathways, Other%. The ratio between Glycolysis% and OXPHOS% is shown on the figure and corresponds to the secondary axis. A) Results for actively proliferating cells under normoxia. B) Results for actively proliferating cells under hypoxia.

4.5 Discussion

4.5.1 Contrasting experimental observations in normoxia and hypoxia

This study measured the growth rate and lactate production in the culture of hMSCs. A distinction between the actively proliferating and the non-growing cells was made in the calculation. The measured cell cycle data was used to categorize hMSCs with the two proliferative statuses. Literature experimental findings have shown different metabolic adaptations in actively growing and quiescent cells [278, 279]. The growth rate and lactate production were calibrated to show those of the actively proliferating hMSCs, taking a first step to address the heterogeneity in hMSCs. The highest growth rate was calculated to be 0.14 hr^{-1}, higher than some of the literature experimental findings [79, 82, 180, 204, 257, 259]. This discrepancy is most likely due to the fast-growing nature of the immortalized hMSCs cell line and the aforementioned assumption, more precise treatment of attributing the population doubling only to the proliferating cells.

The experimentally measured lactate production rate of hMSCs showed a strong dependency on their growth rate under both oxygen levels. Under normoxia, in the slow-growing cells, lactate production showed a positive correlation with growth rate. In contrast with the fast-growing cells, lactate production was reduced with an increase in growth rate. In the literature, a majority of the studies showed a preference for glycolysis in growing cells [252, 280, 281]; however, a decline of lactate production with growth rate has also been reported [204, 259, 282]. The reason for such an unexpected decline was not explicitly addressed in these studies. These two opposing trends of lactate production (i.e. GRDP) were observed, and to the best of our knowledge, reported for the first time in cells cultured under the same condition. In this

study, hMSCs were cultured under the atmospheric oxygen level in serum-free media, cell number was tracked *in silico* every 24 hours and no prolonged lag phase was observed. In addition, the end of culture viability was over 85% and confluency was not reached. The difference in growth rates from different runs of the experiment, and the distinction between slow-growing and fast-growing cells, is hypothesized to originate from the parental cell pool status, seeding density, experimental handling, etc. In addition, the integrity of mitochondria was shown to be linked to lactate production [283]. Depending on the severity of mitochondrial damage or dysfunction, cells may undergo senescence and/or elevated lactate production as well as ROS-mediated cell damage [284, 285]. Future work shall measure and compare the mitochondrial integrity for the slow-growing and fast-growing cells. When comparing the experimental metabolic data, it is therefore important to consider the growth regime, whether lactate production is increasing or decreasing with growth rate, to avoid any false interpretations.

Under hypoxia, the GRDP was not observed. Throughout a range of growth rates that encompassed that of the normoxic case, the lactate production consistently increased with the growth rate, which suggests a major shift in the metabolic network compared to the hMSCs cultured under atmospheric oxygen. The greater reliance of glycolysis is demonstrated in cells cultured under hypoxia. This is very likely the result of cellular hypoxic responses, including the upregulation of key glycolytic factors and glucose transporters [114, 120, 256]. Besides, higher achievable growth rates were observed for hypoxically cultured cells. Various past studies have shown that low oxygen conditions could enhance the proliferative capacity of hMSCs [75, 79, 81]. The lower achievable growth in normoxically culture hMSCs may have been restrained by its low

glucose transporter activity [286], which may have also forced the metabolic shift in the fast-growing cells. This limitation is likely to be alleviated under hypoxic conditions as hypoxia allowed greater glucose transport to sustain the metabolic uptake profile. Overall, hypoxia showed significant impacts on the proliferative status and the metabolism of hMSCs.

4.5.2 Learnings by mathematical modelling

In order to further study the GRDP, mathematical modelling was used to capture the changes in the intracellular metabolic fluxes. A human genome-scale model was used to simulate the metabolic uptake of hMSCs. Major improvements were made on a published model [264] to enhance its biological relevance and enable its capacity as a descriptive model. In the improved model, glucose was considered as the key metabolite while uptake of amino acids, including glutamine, were allowed. The model was able to predict different metabolic uptake profiles dependent on cell growth rates. A biological constraint based on the proteomic resource capacity [271] was added to guide the preference for glucose utilization, i.e. through OXPHOS, glycolysis or biomass production. With the incorporation of PRAT, the calibrated model was able to simulate the experimentally observed trends in lactate production under normoxia (i.e. GRDP) and hypoxia.

The fitted PPP%, the maximum allowed glucose into the PPP, was found at 3% and 12% under normoxia and hypoxia, respectively. In the literature, the glucose-to-PPP allocation in human cells range from 5-13%, and in most cases below 10% [287-290]. In addition, the higher flux through the PPP has previously been found to correspond to higher growth [291-293], which is in line with the fitted data from this work. Overall,

the calibrated PPP% from this study is in range and consistent with experimental findings in the literature.

The PRAT coefficients (W_O and W_g) were determined with trends observed in experimental data. The relative proteomic cost associated with processing glucose through glycolysis over OXPHOS (W_g/W_O) were 87 and 24 folds under normoxia and hypoxia, respectively. This finding is yet to be confirmed by experimental proteomic measurements, and a detailed mechanistic explanation of the possibility for such a difference to arise from the two culture conditions is beyond the scope of this work. Nevertheless, as an initial consideration, the higher relative glycolytic cost under hypoxia may be caused by the changes in the cell's proteome and transcriptome, with differentially regulated functions including cell growth, survival, oxidative defense, metabolism, etc. [100, 185, 196, 263, 294]. Under hypoxia, with an oxygen level that's closer to its niche condition, hMSCs would not be exposed to the hyper-oxidative stress caused by atmospheric oxygen level, and thus would be expected to have a different cost/preference associated with the two means of energy biogenesis.

The significantly lower cost of glycolysis (W_g/W_O) confirmed the strong preference of glycolysis under both oxygen conditions. In addition, in all simulated cases, a higher amount of glucose was converted into lactate than being processed through the TCA (Figure 4.11). Therefore, the simulation results provide supporting evidence on the preference of glycolysis in growing cells under normoxia ("Warburg effect") [251, 253, 254, 281] and hypoxia [79, 196]. Nevertheless, a certain amount of glucose being processed through the TCA cycle was predicted by all the simulated cases, which

implies an irreplaceable role played by the OXPHOS in facilitating cell growth, which is consistent with the report by Fogal *et al. [295].*

More importantly, the simulation results have provided insights on the possible cause for the observed GRDP under normoxia. Unlike in hypoxia where the simulation has predicted a constant zero level of the AKGDH fluxes at all the simulated grow rates, the progression through the TCA cycle seems to be unhindered in slow-growing cells in the normoxic cases (Figure 4.12A)). Some reports have shown that HIF1α, a key hypoxia hallmark protein, reduced the activity of AKGDH [296]. The results from a collaborating work showed that the RNA expression of AKGDH was significantly reduced under hypoxia (results not published). As cells grow faster, the increasing reliance on glycolysis would reduce the fluxes in the TCA cycle, including AKGDH, the enzyme responsible for catalyzing a-ketoglutarate to succinyl-CoA. As the AKGDH flux reaches zero, the forward progression of TCA halts, more a-ketoglutarate is exported for the subsequent lipid biosynthesis (Figure 4.12B)). The simulation results have shown that AKGDH would remain inactive with the further increase in the growth rate, while the reduction in the upstream and downstream fluxes is alleviated (Figure 4.7), as a response to the growing energy and biomass demand. The proportion of glucose entering the TCA cycle would continue to decline as the total glucose uptake increases. Meanwhile, a growing proportion of glucose would be converted into amino acids and other biological factors (Figure 4.11A)). Overall, the simulation results suggest that the GRDP is a consequence of the TCA cycle transitioning from regular progression to being interrupted, in order to accommodate the cellular demands at high growth rates.

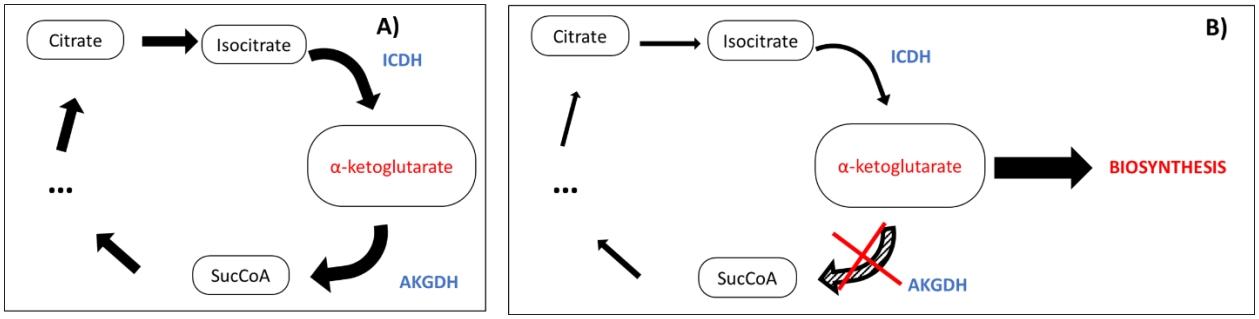

Figure 4.12: The simplified status of the TCA cycle under normoxia. A) In the slow-growing cells, the TCA cycle was able to progress regularly. B) In the fast-growing cells, the TCA cycle became interrupted with AKGDH declining and eventually remaining inactive. The α-ketoglutarate was exported for the subsequent biosynthesis. The thickness of the arrow indicates the relative flux level.

Several previous studies have found that a reduced AKGDH activity was crucial for fast-growing cells. Vatrinet *et al.* reviewed the significance of AKGDH in cancer cell metabolism which exemplifies fast proliferating cells [297]. The hindered activity of AKDGH was crucial for facilitating fast tumour growth, forcing the TCA cycle into a reverse mode with an elevated ratio of α-ketoglutarate/citrate, facilitating biosynthesis [296, 298-300]. DeBerardinis *et al.* showed the reduction in AKGDH and the subsequent SUCD, were associated with the reverse TCA cycle in fast-growing cancer cells, [301]. The simulation result showed a net reduced forward flux through the ICDH to form α-ketoglutarate (Figure 4.12B)) but was unable to indicate whether it was caused by a reduced forward flux or an increased reverse flux. The reduced AKGDH activity in fast-growing cells in the literature is consistent from the finding in this study, however the simulation could not confirm the reverse progression of the TCA cycle.

Several other studies have employed computational models to simulate the metabolic network of mammalian cells. Schuster *et al.* reviewed a set of published mathematical models addressing the “Warburg effect” [253]. Both kinetics model and constraint-based models have been established to evaluate the relative cost of glycolysis versus

respiration [272-274], all of which showed a preference for glycolytic uptake, similar to the finding in this study. In addition, the debate for using genome-scaled models or simplified core models is ongoing [275].

Damiani *et al.* used a core metabolic model and FBA to simulate the utilization of glucose and glutamine in lactate production [265]. Their simulation showed that glutamine contributed to the production of lactate at high utilization. In this study, the amount of simulated glutamine uptake was low comparing to that of glucose, experimental results (shown in the Supplementary Information) showed supporting evidence for the observed simulation. The contribution of glutamine to lactate production was expected to be negligible in this study.

Shlomi *et al.* used FBA in conjunction with the constraint-based model on the total enzyme solvent capacity to model cancer cell metabolism [266]. In their model, the enzymatic reaction rates were set for over 3,700 reactions, however, due to the biological complexity and data availability, more than 85% of the reaction rates had to be assumed. The lack of a reliable enzyme turnover dataset for the intended cell type affects the accuracy of their model. In the study by Shlomi *et al.*, a higher OXPHOS pathway was observed in the slow-growing transformed fibroblasts and glycolysis dominated in the fast-growing cells [266]. Similar trend was observed in the normoxically cultured cells in this study, as shown in Figure 4.11A). The glycolytic activity increased with grow rates, however, experimental data was only available for growth rates between 0.042-0.066 [302, 303], which share the behavior of the slow-growing hMSCs from this study.

In this study, the authors intended to address the observed GRDP in normoxically cultured hMSCs. The enzyme constraint approach used in Shlomi *et al.* [266] offers too many degrees of freedoms for calibration, the fitted model may be the result of updating only a few enzyme capacity factors, which is difficult in proving biological relevance and does not offer greater confidence in the simulation. This study opted to integrate the proteomic resource allocation-based constraint as a biological limitation. To the best of our knowledge, this is the first study to combine the PRAT and FBA approaches for the study of mammalian cells.

4.6 Conclusions

The hMSCs cultured under atmospheric oxygen showed opposing trends of specific lactate production with specific growth rates despite the consistent preference for aerobic glycolysis. Lactate production increased with proliferation in slow-growing cells and decreased in fast-growing cells. This study is the first to report on this behavior, i.e. the trend of growth rate dependent production of lactate. Assisted by a flux balance analysis model incorporating a proteomic resource allocation constraint, the observed trend is hypothesized to be the result of an interrupted TCA cycle. A different metabolic regime was found for hMSCs cultured under hypoxia, whose enhanced growth rate heavily depended on glycolysis. This study shows the flexibility of cellular metabolism in accommodating different growth demand and highlights the significance in considering cell growth characteristics when comparing the metabolic data from different experiments.

The impact of hypoxia and growth regimes significantly affect hMSCs metabolic network and growth rate. As an adherent cell type, hMSCs are also regulated by the

surfaces that they bind onto. The next chapter investigates the impact of surface biomaterials in regulating hMSCs status.

Statement of Authorship for joint/multi-authored papers for PGR thesis

To appear at the end of each thesis chapter submitted as an article/paper

The statement shall describe the candidate's and co-authors' independent research contributions in the thesis publications. For each publication there should exist a complete statement that is to be filled out and signed by the candidate and supervisor **(only required where there isn't already a statement of contribution within the paper itself).**

Title of Paper	Analysis of changes in metabolic profiles of human Mesenchymal stromal cells in different growth regimes
Publication Status	☐Unpublished and unsubmitted work written in a manuscript style
Publication Details	Author list: Bo Zhang, Hong Zeng, Zhanfeng Cui, Hua Ye, Aidong Yang*

Student Confirmation

Student Name:	Bo Zhang		
Contribution to the Paper	• Conceived the idea of this work and facilitated project progression • Conducted experiments and data analysis • Participated in model construction/simulation and in the interpretation of the results • Wrote up the manuscript (with contributions from Hong Zeng to the Methodology section)		
Signature	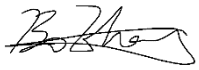	Date	Jan 4, 2019

Supervisor Confirmation

By signing the Statement of Authorship, you are certifying that the candidate made a substantial contribution to the publication, and that the description described above is accurate.

Supervisor name and title: Prof Aidong Yang		
Supervisor comments Overall, this work was led by Bo Zhang, who was also the sole worker completing the experimental studies. Hong Zeng, the co-worker, contributed mainly by leading the model construction, to which Bo Zhang also contributed.		
Signature 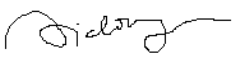	Date	Jan 7, 2019

This completed form should be included in the thesis, at the end of the relevant chapter.

Chapter 5: The effect of culture surfaces

5.0 Summary

This chapter investigates the effect of different culture surfaces on regulating hMSCs status. Different surfaces were synthesized for the culture of hMSCs which resulted in varying growth rates and transcriptomic statuses. The change in gene expressions was captured by RNA-sequencing and bioinformatics. Findings, literature review, and methods from this study are summarized in Chapter 5A, 5B, and 5C.

The independent and synergistic effect of surface topography and chemistry independently on regulating hMSCs growth rate and gene expression are presented in Journal Paper 3. Ontology and pathway enrichment analysis revealed key shift in cellular functions, including differentiation, metabolism, cell cycle progression, etc. The study revealed the impact of culture surface on the overall transcriptome and specific gene groups. Further analysis led to two additional discoveries which are presented in Journal Paper 4 and 5. The expressions of key hypoxia-regulated genes were analyzed with those of the surface proteins. In addition, experimental studies from the literature were used to evaluate the linkage between these two groups. A novel hypothesis is proposed in Journal Paper 4, the changes in culture surface led to the differential activation of different surface proteins, which then subsequently regulated key hypoxia-regulated genes and pathways. In addition, the expressions of the commonly regarded hMSCs biomarkers were evaluated and reported in Journal Paper 5. Network and cluster analysis were employed to investigate the sensitivity of these markers on different surface characteristics. A list of biomarkers with stable and non-correlated expression on the tested surfaces is proposed.

The findings from this study improve the understanding of culture surface on regulating hMSCs, which can be used in designing future biomaterials to regulate growth rate while maintaining hMSCs identity. The crosstalk between surface signaling and hypoxia sensing pathways may be translated into designing novel biomaterials for inducing hypoxic responses without maintaining an expensive low oxygen environment. The improved design of biomaterials has the potential to serve as one of the key pillars in optimizing the operational efficiency of bioreactors.

Chapter 5A – Journal Paper 3 - Differential and Interactive Effects of Substrate Topography and Chemistry on Human Mesenchymal Stem Cell Gene Expression

- Published in International Journal of Molecular Science (2018)

Qiongfang Li[1,†], Bo Zhang[2,3,†], Naresh Kasoju[2,†], Jinmin Ma[1,†], Aidong Yang[3], Zhanfeng Cui[2], Hui Wang[1,2,4,*] and Hua Ye[2,*]

[1] China National GeneBank-Shenzhen, BGI-Shenzhen, 518083 Shenzhen, China; liqiongfang@genomics.cn (Q.L.); majinmin@genomics.cn (J.M.)
[2] Institute of Biomedical Engineering, Department of Engineering Science, University of Oxford, OX3 7DQ Oxford, UK; bo.zhang@eng.ox.ac.uk (B.Z.); zhanfeng.cui@eng.ox.ac.uk (Z.C.)
[3] Department of Engineering Science, University of Oxford, OX1 3PJ Oxford, UK; aidong.yang@eng.ox.ac.uk
[4] Oxford Suzhou Centre for Advanced Research, Suzhou Industrial Park, 215123 Jiangsu, China
***** Correspondence: hui.wang789@gmail.com (H.W.); hua.ye@eng.ox.ac.uk (H.Y.)

† These authors contributed equally to the paper.
* Corresponding author

5A.1 Abstract

Variations in substrate chemistry and the micro-structure were shown to have a significant effect on the biology of human mesenchymal stromal cells (hMSCs). This occurs when differences in the surface properties indirectly modulate pathways within numerous signaling networks that control cell fate. To understand how the surface features affect hMSCs gene expression, we performed RNA-sequencing analysis of bone marrow-derived hMSCs cultured on tissue culture-treated polystyrene (TCP) and poly(L-lactide) (PLLA) based substrates of differing topography (Fl: flat and Fs: fibrous) and chemistry (Pr: pristine and Am: aminated). Whilst 80% of gene expression remained similar for cells cultured on test substrates, the analysis of differentially expressed genes (DEGs) revealed that surface topography significantly altered gene expression more than surface chemistry. The Fl and Fs topologies introduced opposite directional alternations in gene expression when compared to TCP control. In addition, the effect of chemical treatment interacted with that of topography in a synergistic manner with the Pr samples promoting more DEGs than Am samples in all gene ontology function groups. These findings not only highlight the significance of the culture surface on regulating the overall gene expression profile but also provide novel insights into cell-material interactions that could help further design the next-generation biomaterials to facilitate hMSCs applications. At the same time, further studies are required to investigate whether or not the observations noted correlate with subsequent protein expression and functionality of cells.

5A.2 Introduction

Human mesenchymal stromal cells (hMSCs) are multi-potent, plastic-adherent, and fibroblast-like cells found in the human body. They were first discovered in bone marrow, but, subsequently, various non-marrow tissues were found to harbor similar cells [1–4]. In terms of potency, hMSCs of a particular tissue type were found to differentiate into cell types of tissue-specific lineage. However, with the advent of more developed *in vitro* culture protocols, it is now possible to achieve a cross-lineage differentiation [5,6]. Besides this intrinsic multi-potent property, several other beneficial characteristics of MSCs have recently been discovered. For instance, they have been found to facilitate neovascularisation both in the context of pathology and regeneration [7,8], the modulation of the immune response both innate and adaptive [9,10], and protection of certain cells by compromising auto-immunity, cytotoxicity, or the inflammatory response [11,12]. hMSCs are becoming an attractive source of cells for application in regenerative medicine. However, translation from bench to bedside requires better understanding of how environmental factors affect cells during cell isolation, *in vitro* expansion, and/or differentiation and delivery. Conventional approaches such as optimizing glucose, oxygen, and other culture conditions to maintain the expansion rate and the use of novel biochemical cocktails to control the differentiation are promising for enabling large-scale production of therapeutic stem cells.

More recently, biomaterials are being explored in various aspects of the research involving MSCs [13–16]. It is crucial for understanding cell-biomaterial interactions in order to maximize the potential in the designed material since many cellular processes including adhesion, migration, and stem cell differentiation are governed by the non-

soluble components of the matrix. To this end, enhanced cell biological activities and narrowed integrin usage of cells cultured on three-dimensional matrices compared to their two-dimensional counterparts was shown to highlight the importance of substrate topography in regulating cell behavior and paracrine functions [128, 129]. Additionally, various studies have shown enhanced osteogenic capacities with three-dimensional fibrous culture surfaces [131, 137-140] and have shown regulations of the differentiation potential of other lineages [151, 304-306]. Additionally, the induction of osteogenic and adipogenic differentiation on amine functionalized surfaces in contrast to pristine samples showed the effect of surface chemistry on the cell response {Phillips, 2010 #679}.Despite the various studies on understanding the role of the culture substrate topography and chemistry in modulating cell behavior, the detailed mechanism and impact remain to be elucidated. This is due to the limitations associated with conventional cellular scale assays such as microscopy and molecular scale assays such as quantitative real-time (qRT-PCR). Given the complex interplay of several signaling networks that control the MSCs fate {Walters, 2015 #683}[29–35], landscape-scale understanding of the MSCs molecular response is needed to capture a detailed, global representation in a change in cellular status.

In this regard, high-throughput assays such as microarray and next generation sequencing-based transcriptomics have advanced the field of stem cell biology and technology [36]. Particularly, whole transcriptome shotgun sequencing known as RNA-sequencing or RNA-seq for short, is currently being explored in order to understand the gene expression profile of MSCs in various contexts [36]. One of the areas of significant interest is in the expansion of MSCs. Currently, flat or nanofibrous substrates-based surfaces are being actively investigated in cell cultures [24,37].

However, knowledge is limited regarding the molecular differences induced by surface topography or by changes in surface material from the tissue culture treated polystyrene substrate (TCP). The effect of culture surfaces on regulating MSCs differentiation, proliferation, paracrine function, and stemness preservation have been reported by various studies [23,38,39]. To design the culture surfaces with the topography and chemistry that are best suited for different downstream applications such as *in vitro* expansion and transplantation to facilitate tissue repair, it is important to gain an overall understanding of the induced gene expression changes. The fundamental questions that need to be addressed are (i) whether surface topography and chemistry mediate gradual changes or directional alternations and (ii) what kind of interactive effects they would impose on each other (Figure 5A.1). To answer these questions, in the current study, we performed RNA-seq analysis on hMSCs cultured on flat (Fl) and fibrous (Fs) poly(L-lactide) (PLLA) substrates. Variables of surface chemistry were also introduced by modifying the PLLA substrates by using aminolysis (Am: aminated) in comparison to untreated substrates (Pr: pristine). The relative variations and the relationships between hMSCs cultured on Fl-Pr-PLLA, Fl-Am-PLLA, Fs-Pr-PLLA, Fs-Am-PLLA (test samples), and TCP (control sample) and the analytical strategy for investigating the interactions between topography and chemistry are shown in Figure 5A.1.

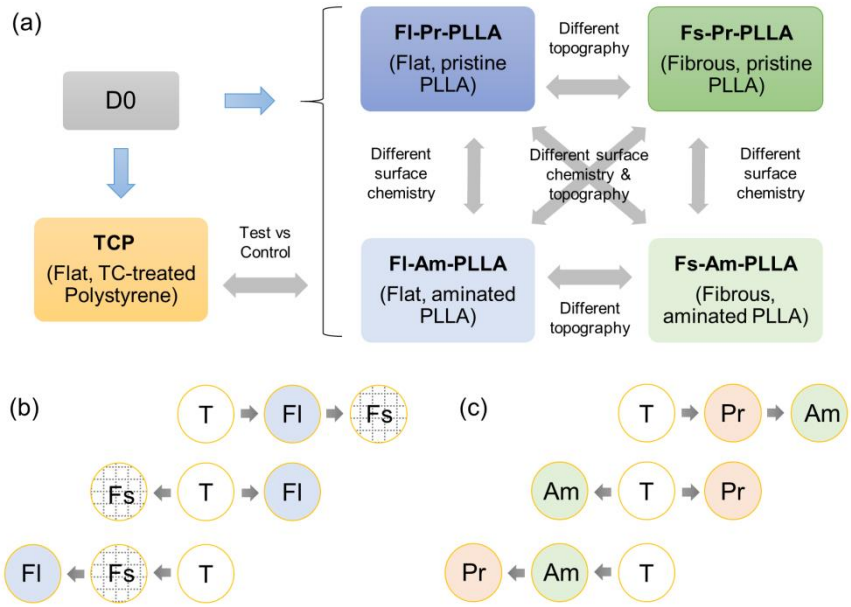

Figure 5A.1: Schematics of potential relationships and underlying parameters: Experimental design and underlying variability within the test samples in terms of substrate topography and chemistry. (A) Hypothesized relationships between MSCs cultured on test substrates that differ in surface topography (B) and surface chemistry (C). In the latter case (B and B), the arrow direction indicates the gene expression characteristics between samples in relation to T (cells cultured on standard tissue culture dish).Hypothesis 1 (top) shows a gradual effect where Fs dominates Fl and Am dominates Pr, hypothesis 2 (middle) shows a directional polarity effect, and hypothesis 3 (bottom) shows another gradual change where Fl dominates Fs and Pr dominates Am. Starting cell suspension (before cell seeding) was assayed at day 0 (D0) while the cells grown on the test and the control samples were assayed at days 3, 5, and 7.

5A.3 Materials and Methods

5A.3.1 Materials

Purasorb PL 24 (PLLA with an inherent viscosity of 2.38 dL/g) was purchased from Corbion, Amsterdam, Netherlands. Other reagents used in the material preparation were, unless otherwise stated, purchased from Sigma-Aldrich, St. Louis, MO, USA. Other cell culture related reagents were, unless otherwise stated, purchased from Thermo Fisher Scientific Inc, Waltham, MA, USA. The RNeasy Mini kit was purchased from Qiagen, Hilden, Germany.

5A.3.2 Study Groups

D0: cell suspension before seeding onto the test and control substrates. TCPS are cells cultured on tissue culture treated polystyrene dishes. Fl-Pr-PLLA are cells cultured on flat pristine PLLA electrospun mats. Fl-Am-PLLA are cells cultured on flat aminated PLLA electrospun mats. Fs-Pr-PLLA are cells cultured on fibrous pristine PLLA electrospun mats and Fs-Am-PLLA are cells cultured on fibrous aminated PLLA electrospun mats.

5A.3.3 Preparation and Characterization of PLLA Substrates

Flat films of PLLA (Fl-PLLA) were prepared by the melt-pressing technique. The PLLA granules were placed between aluminum foil-covered metal plates and were pressed using a portable hot press at 210 °C for 15 min. The hot metal plates were carefully snap-cooled under running water. The PLLA film was then recovered from the plates. The nonwoven fibrous matrices of PLLA (Fs-PLLA) were prepared by the electrospinning method. The PLLA granules were dissolved in hexafluoroisopropanol to make a 7.5% (*w*/*v*) solution and the electrospinning was done in a custom-made setup at following optimized parameters: the voltage of 15 kV, which is 15 cm distance, and the flow rate of 0.1 mL/h.

To introduce the amine groups and to turn the surface from hydrophobic to hydrophilic, the PLLA substrates, which are both flat and fibrous, were subjected to aminolysis or amination reaction. First, they were saturated in 5 ml of isopropanol for 30 min at ambient temperature. This step was carried under a slight vacuum to remove the trapped air especially from the electrospun scaffolds. The isopropanol was then exchanged with 5 ml of freshly prepared hexamethylenediamine (HMDA) solution (5%

w/*v* in isopropanol) for 30 min at 30 °C under mild agitation. The samples were washed with an ample amount of ultrapure water for 4 h with at least 10× water exchanges to get rid of the excess HMDA.

To determine the surface morphology, the samples were initially coated with platinum for 90 s in a sputter coating unit (SC7620, Quorum Technologies, Lewes, UK) and were then analyzed by using a scanning electron microscope (SEM, Evo LS15, Carl Zeiss, Oberkochen, Germany). Next, to confirm the successful amination, the samples were stained with fluorescein isothiocyanate (FITC, 0.05% *w*/*v* in absolute ethanol) for 4 h followed by imaging with a confocal laser scanning microscopy (CLSM, $C2^{+}$, Nikon; excitation wavelength = 490 nm and emission wavelength = 525 nm). Any changes to substrate morphology and chemistry after aminolysis were tracked by SEM and attenuated total reflectance Fourier transform infrared spectroscopy (ATR-FTIR, Tensor 37, Bruker, Billerica, MA, USA).

5A.3.4 Cell Culture

Poietics™ normal human bone marrow-derived mesenchymal stem cells (hbm-MSCs, cat. no. PT-2501) along with the proprietary growth medium kit (cat. no. PT-3001) were obtained from Lonza, UK. Cells were expanded in the proprietary hMSCs growth medium supplemented with penicillin (10 U/mL) and streptomycin (10 µg/mL). Cells were cultured in 5% CO_2 in air at 37 °C with a relative humidity of 95%. The PLLA substrates known as Fl-Pr-PLLA (flat, pristine PLLA), Fl-Am-PLLA (flat, aminated PLLA), Fs-Pr-PLLA (fibrous, pristine PLLA), and Fs-Am-PLLA (fibrous, aminated PLLA) were cut into 20 mm circular discs to fit into the wells of a 12-well plate. They were sterilized by treating with 70% ethanol for 1 h. A vacuum was applied to remove

any trapped air especially in fibrous matrices. The samples were thoroughly washed with sterile phosphate buffered saline (PBS) and were then pre-saturated with culture medium overnight in a CO_2 incubator. hMSCs (passage 3) were seeded onto the substrate at a rate of 50,000 cells/well and cultured in the incubator for 24 h. Cells were cultured for one week with fresh media changes every alternative day. Cell viability at day 3, 5, and 7 was tested with an Alamar blue-based non-destructive assay. The 10% of Alamar blue reagent was added directly to each well. After 3 h of incubation, the supernatant was collected and the fluorescence was read in a multi-plate reader (SpectraMax M2, Molecular Devices, San Jose, CA, USA). Cell morphology was observed by staining the samples (paraformaldehyde fixed) with Alexa Fluor® 488 phalloidin and the observation was conducted under a confocal microscope.

5A.3.5 RNA Extraction

Total RNA from each sample was extracted with the RNeasy Mini Kit following supplier's instructions. A total of 500 µL of lysis buffer was added to each sample and pipetted vigorously to rupture the cell membrane. An equal volume of 70% ethanol was added to allow the precipitation of nucleic acids. The mixture was then transferred to the RNeasy spin column to let the matrix capture the nucleic acids. The column with captured nucleic acids was washed with 500 µL of washing buffer and treated with 80 µL of DNase (10 µL DNase stock + 70 µL of buffer) to digest DNA. The digested DNA was then washed three times with 500 µL of washing buffer. Lastly, the RNA was eluted with 25 µL of RNase-free water and stored at –80 °C until further use. An aliquot of the extracted total RNA was analyzed for its quality and quantity by using a NanoDrop UV/VIS spectrophotometer (1000, Thermo Scientific, Waltham, MA, USA)

and RNA agarose gel electrophoresis. It is to be noted that, for all the test samples including TCP, the lysis buffer was added directly to the cell culture well while, for the starting material (Figure 5A.1A), Day 0 cell suspension), the lysis buffer was added to the cell suspension after trypsinization.

5A.3.6 RNA-Seq and Data Analysis

Next generation sequencing was conducted on a BGISeq-500 sequencing platform (BGI, Shenzhen, China) for six samples (Day 0 cell suspension, Day 3 TCP control, and treatments of Fl-Pr-PLLA, Fl-Am-PLLA, Fs-Pr-PLLA, and Fs-Am-PLLA) with a read length of 100-bp. Raw sequencing data was filtered to remove low quality reads using SOAPnuke (http://soap.genomics.org.cn/) with the following criteria: reads with adapters, reads with greater than 10% unknown bases, or reads with more than 50% low-quality bases. The Bowtie2 [62] and HISAT [63] toolbox was used for gene and genome mapping against the human genome reference hg19, respectively. A unique gene and genome mapping percentage were calculated. Sequencing saturation and reads distribution checks were performed as quality controls to the alignment process. Gene expression levels for each sample were quantified using the FPKM method (fragments per kilobase of transcript per million mapped reads) and processed for analysis. Differentially expressed genes (DEGs) were determined in pairwise comparisons when the expression ratio was greater than 2 and the false discovery rate was less than 0.001. No upper or lower limit cut-off on the gene expression level was imposed to filter DEGs. The FPKM value was set to two decimal points to avoid error during downstream data processing. Hierarchical cluster analysis assessed the gene expression FPKM values between samples. Samples with fewer differences were grouped together with the result shown in a dendrogram. Gene ontology analysis

classified and counted the number of genes responsible in the identified biological functions [64].

5A.3.7 Statistical Analysis

For the cell culture measurements, all the studies were run in replicates of six. The qualitative data were illustrative of the individual group. The numerical data were presented as the Mean ± Standard Deviation (SD). Student *t*-tests were used to determine statistically significant differences of cell proliferation responses to topography and chemistry treatments. For RNA-seq, all replicates (n = 6) were pooled prior to sequencing. Differences on the number of up-regulated DEGs and down-regulated DEGs were determined by using the Chi-square test (p<0.05).

5A.4 Results and Discussion

5A.4.1 Characteristics of Material

In this study, we have chosen a commonly used biocompatible polymer, PLLA, processed it into either a flat or fibrous material, and compared the results of the cell culture with cultures on standard TCP. Furthermore, the PLLA substrates were subjected to aminolysis to incorporate amine groups and, thereby, to alter the surface chemistry from hydrophobic to hydrophilic [40]. The morphological features, which were analyzed by SEM, are presented in Figure 5A.2A) and B). The flat substrate was made by melt compression molding and the fibrous substrate was made by electrospinning with a mean fiber diameter of 603nm (±197nm SD). The surface functionalization was confirmed by using a FITC staining technique where upon

specific binding to amine groups, light emission at 515nm is increased when excited at 492nm (Figure 5A.2C)). In ATR-FTIR spectroscopy, the aminated substrate showed characteristic peaks with a significant peak at 3300 cm^{-1} and two insignificant peaks at 1650 and 1550 cm^{-1} [41,42]. This confirmed the success of the amination reaction while the core structure of the polymer appears to remain unaffected (Figure 5A.2D)). Furthermore, as evident from SEM imaging, the surface morphology was not altered after the functionalization reaction (Figure 5A.2E) and F)).

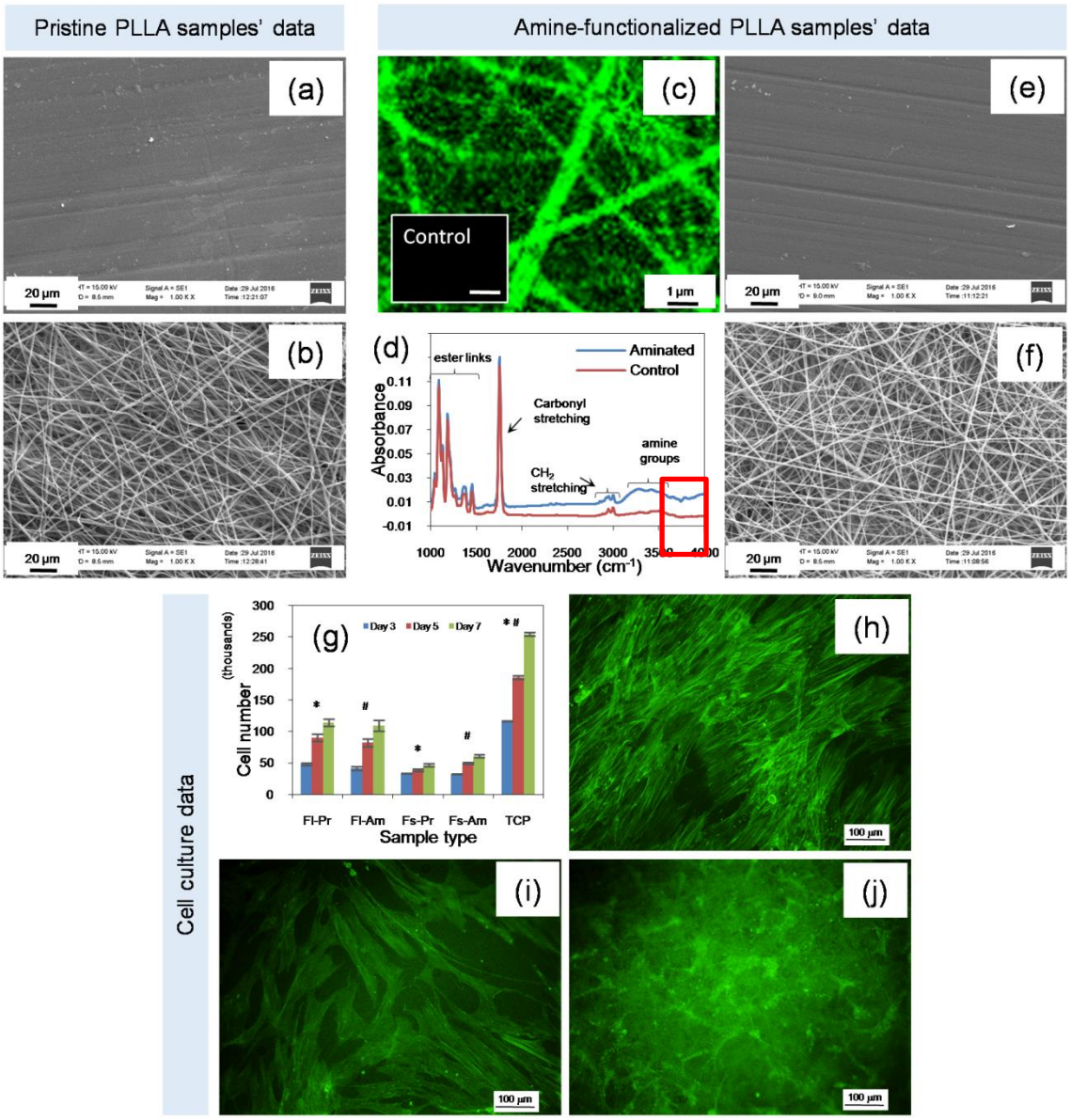

Figure 5A.2: Substrate characteristics and cell response: SEM analysis showed the flat surface of Fl-Pr-PLLA (A) and the fibrous surface of Fs-Pr-PLLA. (B) FITC staining of Fs-Am-PLLA compared to Fs-Pr-PLLA (control) demonstrated the introduction of amine groups. (C) ATR-FTIR analysis of Fs-Am-PLLA further confirmed the successful amination against the untreated control without detrimental changes in the bulk structure. (D) SEM analysis of functionalized samples revealed the intactness of the morphological properties. (E,F) The Alamar blue assay suggested a higher cell proliferation on TCP followed by Fl-PLLA and then Fs-PLLA. (G) Statistically significant differences between groups compared are denoted by * or #, *t*-test $p < 0.001$, respectively). Lastly, confocal microscopy of cells stained for cytoskeleton with Alexa Fluor® 488 phalloidin revealed relative differences in cell morphology and numbers (H) TCP, (I) Fl-PLLA, and (J) Fs-PLLA.

5A.4.2 Cell Growth and Morphology

The conventional cellular assays such as the Alamar blue-based cell viability test and the microscopy-based cell morphology analysis are simple yet invaluable tools to obtain first-hand information on the cell response. Analysis using a cell metabolic assay (Alamar Blue) revealed that MSCs seeded on standard TCP proliferated more rapidly than those cultured on the test materials ($p< 0.001$, *t*-test, Figure 5A.2G)). Cytoskeleton imaging also confirmed that the cell number and cellular spreading were relatively higher on TCP than on the test materials and cells on flat PLLA film showed more similar morphology to those on TCP (Figure 5A.2H) – J)). These observations suggest that the hMSCs favored a flat surface. The overall trend in the cellular rate of proliferation was the highest on TCP followed by on Fl-PLLA and then on Fs-PLLA. Among the test conditions, topography made a significant difference ($F = 39.27$, $df = 1$, $p< 0.001$, GLM) on cell proliferation while chemistry was not a significant factor ($F = 0.03$, $df = 1$, $p = 0.868$, GLM). There was no significant interaction ($F = 1.56$, $df = 1$, $p = 0.217$, GLM) between topography and chemistry based on the cell proliferation data. This behavior may be caused by a lack of RGD (Arg-Gly-Asp) or other cell adhesion molecules on the PLLA substrates, the overwhelming effect of serum presence in the culture medium over the modification on surface chemistry, or the low sensitivity of the applied amine group in affecting the cellular proliferation assay [43–46]. Recent studies showed that the substrate properties including topography and composition as well as culture conditions significantly influence the hMSCs response including cell proliferation, colony forming efficiency, tri-lineage differentiation potential, and immunomodulatory ability [47,48].

5A.4.3 RNA-Seq Data Analysis

For the day 3 hMSCs in this study, over 134 million clean reads were reported with a minimum quality score (Q20) of 89.7%. Over 69% of reads were identified as uniquely mapped human genes. Sequencing saturation data confirmed that a sufficient number of genes have been identified for all six samples (Supplementary Figure S5A.1). The distribution of reads across a full gene length showed an acceptable level of sequencing randomness (Supplementary Figure S5A.2).

The expression levels of all detected genes were calculated as fragments per kilobase of transcript per million mapped reads (FPKM) (Supplementary Table S5A.1). The results of unsupervised clustering on the six samples using all detected genes are shown in Figure 5A.3. The largest Euclidean distance was displayed between the topography treatments Fl-PLLA and Fs-PLLA while close similarities were detected between chemistry treatments, i.e., Fl-Pr-PLLA to Fl-Am-PLLA and Fs-Pr-PLLA to Fs-Am-PLLA. Such a difference in distance clearly indicated that the surface topography was a dominating factor over the surface chemistry for inducing gene expression changes in hMSCs. It was surprising that the two control samples (D0 and TCP) did not exhibit the largest differences from either of the two topography treatments (Figure 5A.3), which supports the polarity model of topography postulated in Figure 5A.1B) (middle row). When TCP and PLLA samples were compared, TCP showed a closer resemblance to Fl-PLLA samples than to Fs-PLLA samples, which indicated that the Fs substrate was more efficient to alter hMSCs gene expression than Fl substrate. To our knowledge, both the topography polarity model and the difference of Fs and Fl efficiency on altering hMSCs gene expression have not been previously reported in the literature.

Hierarchical cluster analysis was also used to represent pairwise FPKM comparisons for detecting DEGs (Figure 5A.4). As shown by two columns with the least color gradient, amination treatment (Fl-Pr vs. Fl-Am and Fs-Pr vs. Fs-Am) induced relatively small numbers of DEGs. The clustering results on DEGs confirmed earlier findings (Figure 5A.3), i.e., the effect of surface chemistry is less significant than that of surface topography and the gene expression of TCP shows greater similarity to Fl-PLLA than to Fs-PLLA samples. The change in gene expression levels between Fl-PLLA, Fs-PLLA, and TCP is greater. However, the ensemble expression results again supported the polarity model (directional alternation) in Figure 5A.1B).

A total of 14,547 non-differentially expressed genes were detected among all six samples (Figure 5A.5A)). This group contains certain housekeeping genes that are responsible for basic cellular functions, metabolism, cytokines, stem cell characteristic genes, and hMSCs markers. In total, 277 gene expressions were either detected uniquely for a particular sample or shown to be differentially up-regulated or down-regulated by different culture conditions. Such a differential response of MSCs, in terms of proliferative and differentiation potential, towards surface topography or surface chemistry have been reported in the literature [25,49–51]. Taking the advantages of transcriptome sequencing, DEGs were sorted to eight sets to further understand the topography (Figure 5A.5B)) and chemistry impact (Figure 5A.5C)) on altering hMSCs gene expression patterns.

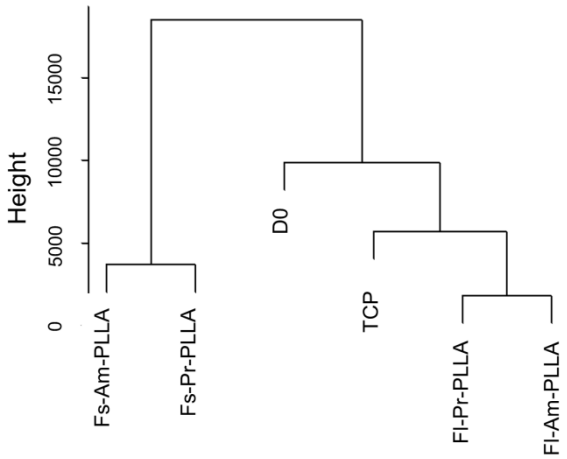

Figure 5A.3: Unsupervised hierarchical clustering dendrogram: Relative sample similarities are represented by the distance along the *y*-axis. Samples or sample groups with greater similarities are arranged under the same hierarchy clades.

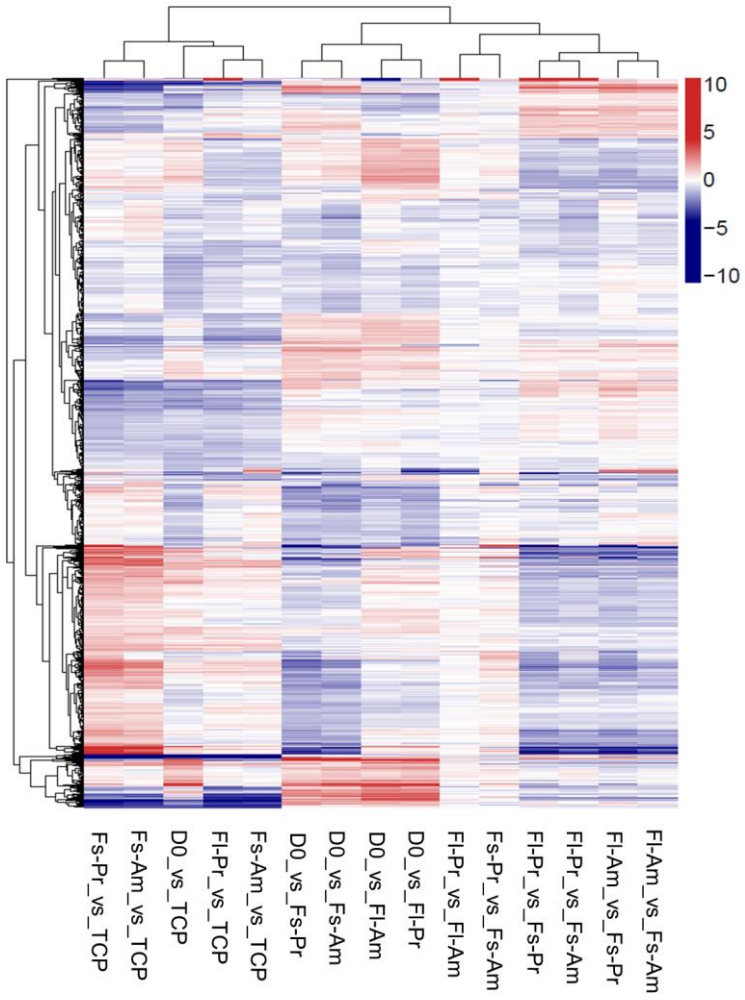

Figure 5A.4: Comparison between DEGs from each sample pairs, which includes hierarchical cluster analysis of the DEGs between each sample pair. The sample pairs are listed on the primary *x*-axis while all reported DEGs are listed on the *y*-axis with their expression ratio (log_2) expressed by the color gradient shown. The secondary *x*-axis groups the results based on the similarity in the sample pairs. Gene clustering is presented on the secondary *y*-axis.

Earlier findings have shown that surface topography was more effective than chemistry at inducing hMSCs gene expression changes (Figures 5A.3 and 5A.4) and that the topography treatments fit with the polarity model (Figure 5A.1B)).The two topography sample sets (including both chemistry treatments Pr-PLLA and Am-PLLA) were compared respectively to the TCP control. A higher number of DEGs between Fs-PLLA and TCP than that of Fl-PLLA and TCP (Figure 5A.5B)) confirmed the findings in Figure 5A.3, which showed a greater differential distance between the two groups. A total of 271 DEGs were found between Fl-PLLA and TCP among which 241 genes (89%) were up-regulated in Fl-PLLA. Contrastingly, among the 509 DEGs between Fs-PLLA and TCP, 304 genes (60%) were down-regulated in Fs-PLLA. There existed 78 and 23 common genes that were up-regulated and down-regulated, respectively, in both Fl-PLLA and Fs-PLLA when compared to TCP (Figure 5A.5B)). Detection of these shared DEGs suggested that Fl and Fs induced gene expression changes that were not completely opposite even though the majority of the DEGs were unique to either Fl or Fs. Fl uniquely induced 163 up-regulations and only one down-regulation to TCP while Fs uniquely induced 127 up-regulations and 281 down-regulations (Figure 5A.5B)). The significant difference ($\chi^2 = 218.038$, df = 1, $p < 0.001$) of up-regulated DEGs and down-regulated DEGs between Fl and Fs further supported the polarity model (Figure 5A.1B)).

Key differentiation markers were significantly altered by culturing with fibrous surfaces when comparing the Fs and Fl samples (Figure 5A.6). Among osteogenic markers, ALPL, MCAM, and BMP4 were down-regulated and BMP2 and FN1 were up-regulated in Fs while RUNX2 remained unaltered (Supplementary Table S5A.2). ACAN, which is one of the chondrogenic markers, was down-regulated in Fs while SOX9, CD44,

and SOX6 displayed notable increases. The expression levels for the adipogenic marker, FABP4, were down-regulated and a negative regular, DLK1, was up-regulated in Fs. Comparing to the markers for osteogenesis and chondrogenesis, the adipogenic markers have shown consistently low expression in all samples. Expression levels of all differentiation markers are included in Supplementary Table S5A.2. However, the recorded findings were indicative of the early fate decisions in hMSCs caused by the substrate properties. Furthermore, the cells from the Fs samples are not believed to be constrained by the nutrient diffusion of the microenvironment. The local shortage of dissolved oxygen would upregulate expression levels of certain hypoxic proteins, e.g., MMP9, VEGF, MIF, PGK1, HIF1A, LDHA, TWIST, HGF, FGF, etc. [52–57]. Yet, none of these proteins were found to be upregulated in the Fs samples. The thickness of the synthesized fibrous surface was in the same magnitude of the peripheral zone (100–300 μm) reported in the literature [58–60].

To examine the chemistry-topography interaction, i.e., the impact of the chemistry factor on topography induced gene expression changes, DEGs of Fl-Pr-PLLA vs Fs-Pr-PLLA were compared with DEGs of Fl-Am-PLLA vs Fs-Am-PLLA (Figure 5A.5C)). Separate from Figure 5A.5B), there were 291 shared DEGs between the two chemistry treatments while 282 DEGs were unique for Pr-PLLA and 131 DEGs were unique for Am-PLLA. Among the 291 shared DEGs, 240 and 47 common genes were found respectively to be up-regulated and down-regulated in the comparison between Fl-PLLA and Fs-PLLA samples, which were insensitive to the difference in chemistry, while only four DEGs showed opposite trends between samples with the two chemistry conditions. These DEGs with the similar pattern in both sets of comparisons (Figure 5A.5C)) represented the dominant responses in the chemistry-topography interaction

and may further suggest a synergistic rule between chemistry and topography. Such a synergistic effect between surface topography and chemistry was reported earlier by Li et al. in regulating mesenchymal markers in cancer cells. However, a different set of modifications on topography and surface chemistry was used in their study. Therefore, the level of synergistic effects may depend on different combinations of abiotic culture conditions [61].

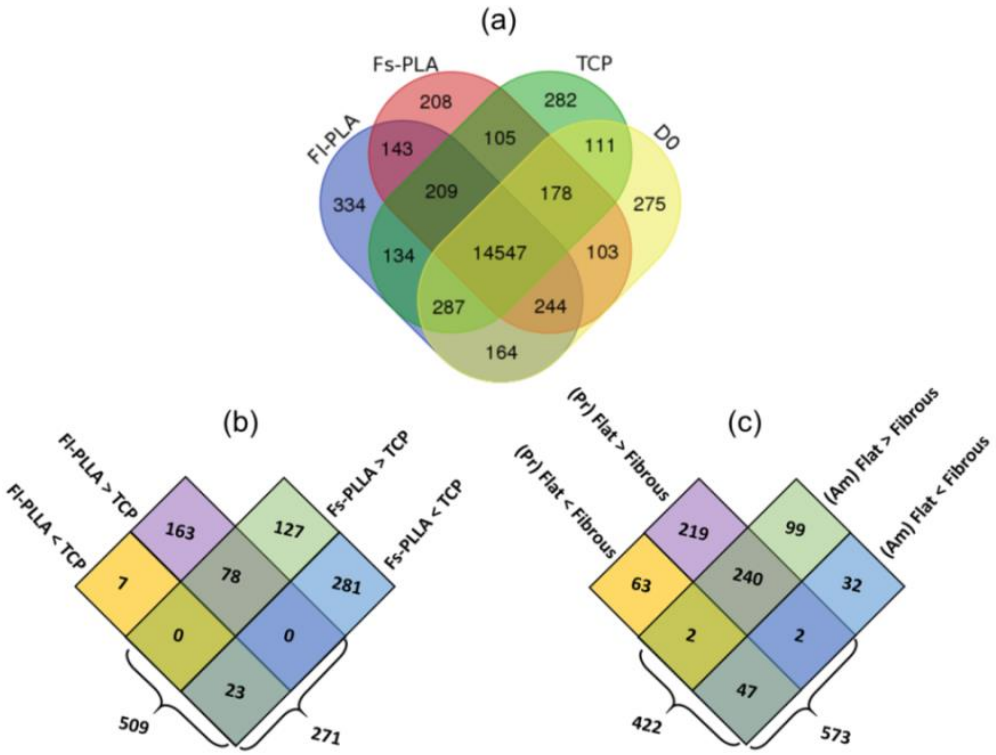

Figure 5A.5: The sequencing summary and comparative analysis of samples cultured on different surfaces. (a) Venn diagram indicating the number of common genes detected for different samples. Common genes between Fl-PLLA and Fs-PLLA samples with Am and Pr functionalization treatments are extracted and compared with TCP and D0 samples. (b) The number of DEGs in Fl-PLLA and Fs-PLLA when compared to the TCP sample. (c) The number of DEGs between Pr-PLLA and Am-PLLA samples. In all cases, unique or shared up-regulated genes in each sample are shown.

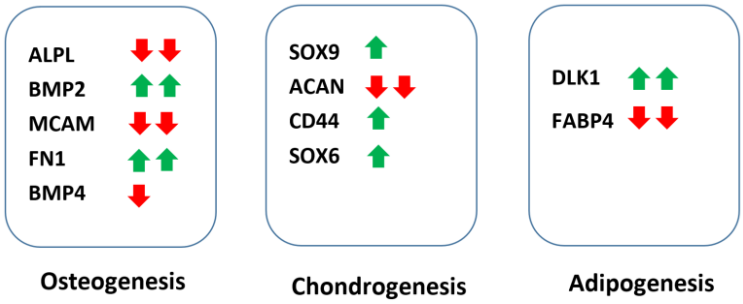

Figure 5A.6: Differences in expression of key differentiation markers: in comparison to cells cultured on flat surfaces, cells cultured on fibrous matrices exhibited significant up-regulation (up arrow) and down-regulation (down arrow) in osteogenic, chondrogenic, and adipogenic markers. One arrow labels fold changes < 1.75 and two arrows label fold changes > 1.75.

In spite of the supporting evidence on the polarity model of the topography factor (Figure 5A.1B), middle row)between Pr-PLLA and Am-PLLA, the numbers of unique up-regulations and down-regulations (Figure 5A.5C)) were not statistically different (χ^2 = 0.220, df = 1, p = 0.639) against the polarity model but did support the gradual change models of the chemistry factor. In this regard, the chemistry model T-Am-Pr (Figure 5A.1C), bottom row) was supported, which indicates that Pr-PLLA was synergistically more powerful than Am-PLLA to induce hMSCs gene expression alternations in response to topography treatments. To further clarify the interactions between chemistry and topography treatments, changes in the key differentiation markers and gene ontology (GO) analysis was performed by comparing the Fl-PLLA and Fs-PLLA samples. The numbers of DEGs associated with GO functions were shown in Figure 5A.7. The proportion of genes corresponding to each function remained similar for Pr-PLLA and Am-PLLA. The majority of the DEGs were associated with cellular biogenesis, metabolism, binding, and organelle functions. In all of the detected GO functions, Pr-PLLA induced more DEGs than Am-PLLA, which highlights that Pr-PLLA made hMSCs more sensitive with regard to responding to the

topography treatments than Am-PLLA did, which provides further evidence to support the gradual model of T-Am-Pr for surface chemistry (Figure 5A.1C), bottom row).

The scope of this study focuses on the impact of culture surfaces on the transcriptome profile of hMSCs. The GO results shed light on the commonly associated functionality of the genes. However, the variation observed at the gene level may not be representative for the corresponding proteomic profile and the subsequent functionality of the cells. Future work will focus on verifying whether the changes observed in gene expressions resemble the alteration on cell functions and their corresponding protein expressions.

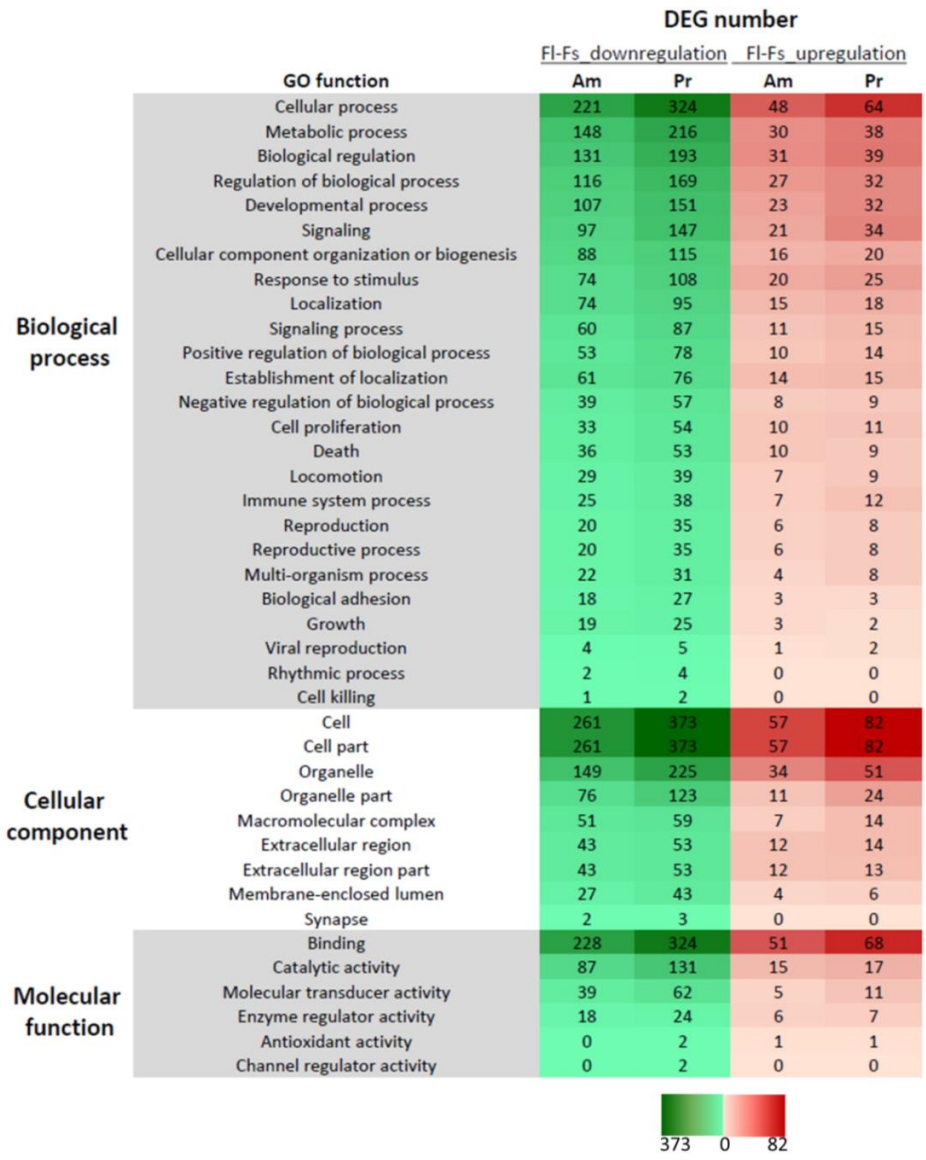

Figure 5A.7: Gene ontology analysis for DEGs: DEGs associated with biological processes, cellular components, and molecular function were grouped and counted.

5A.5 Conclusions

While the effects of substrate topography and chemistry on hMSCs behavior are reported in the literature, we present a global perspective of the cell-material interactions. We explored RNA-seq to understand the differential gene expression in hMSCs cultured on TCP, Fl-Pr-PLLA, Fl-Am-PLLA, Fs-Pr-PLLA, and Fs-Am-PLLA. Various statistical analyses were performed to understand the gene expression patterns. The influence of surface topography (Fs-PLLA and Fl-PLLA samples) was

much more influential on regulating gene expressions than the chemistry treatments (Am-PLLA and Pr-PLLA samples). On topography, the induced differences between TCP and Fs-PLLA samples were more polar than those between TCP and Fl-PLLA. Despite the relatively small impact of the chemistry treatments, Pr-PLLA samples showed a higher sensitivity in strengthening the differentiating role of topography than the Am-PLLA samples. The tested independent factors of surface chemistry and topography imposed their effects on the overall gene expression profiles interactively. These findings offer an enriched understanding of the impact of culture surface properties on hMSCs gene expression and facilitate advanced planning when engineering in vitro culture materials for hMSCs. Meanwhile, further studies are needed to verify if the observations noted at a gene expression level correlates with subsequent protein expressions and functionality of cells.

5A.6 Acknowledgements

We are grateful to China Regenerative Medicine International Limited, Hong Kong for funding this work. We extend our thanks to our colleague Dr. Michelle Kümin for critical reading.

5A.7 Availability of data

All the processed data are presented in the manuscript or in the supplementary information. Information on raw data and materials are available from the NCBI BioProject number PRJNA395968 and from the corresponding authors upon request.

Statement of Authorship for joint/multi-authored papers for PGR thesis

To appear at the end of each thesis chapter submitted as an article/paper

The statement shall describe the candidate's and co-authors' independent research contributions in the thesis publications. For each publication there should exist a complete statement that is to be filled out and signed by the candidate and supervisor **(only required where there isn't already a statement of contribution within the paper itself).**

Title of Paper	Differential and Interactive Effects of Substrate Topography and Chemistry on Human Mesenchymal Stem Cell Gene Expression
Publication Status	☐Published
Publication Details	Author list: Li, Q.*, Zhang, B.*, Kasoju, N.*, Ma, J.*, Yang, A., Cui, Z., ... & Ye, H. (2018). Differential and interactive effects of substrate topography and chemistry on human mesenchymal stem cell gene expression. International journal of molecular sciences, 19(8), 2344. *These authors contributed equally to the paper.

Student Confirmation

Student Name:	Bo Zhang		
Contribution to the Paper	• Contributed to cell culture and RNA extraction • Performed bioinformatics and data analysis • Wrote the majority of the manuscript with Dr. Naresh Kasoju The following statement describing authors' contribution has been included in the publication. The student's contribution is described under "B.Z." " Conceptualization, N.K., H.Y., and H.W.; Methodology, N.K., B.Z., and J.M. Data Curation, N.K., B.Z., J.M., and Q.L. Writing-Original Draft Preparation, N.K., B.Z., and H.W. Writing-Review & Editing, Z.C., H.W., H.Y., A.Y., and J.M. "		
Signature	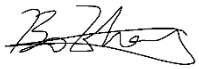	Date	May 5, 2019

Supervisor Confirmation

By signing the Statement of Authorship, you are certifying that the candidate made a substantial contribution to the publication, and that the description described above is accurate.

Supervisor name and title: Prof. Cathy (Hua) Ye		
Supervisor comments: The supervisor agrees with the student's statement.		
Signature 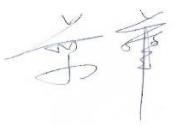	Date	May 10, 2019

This completed form should be included in the thesis, at the end of the relevant chapter.

Chapter 5B – Journal Paper 4 - Culture Surfaces Induce Hypoxia-Regulated Genes in Human Mesenchymal Stromal Cells

- Published in Biomedical Materials (2019)

Bo Zhang[1,2,†], Naresh Kasoju[1,†], Qiongfang Li[3†], Erfan Soliman[1], Aidong Yang[2], Zhanfeng Cui[1,4], Jinmin Ma[3,*], Hui Wang[1,3,4,*], Hua Ye[1,4,*]

[1]Institute of Biomedical Engineering, Department of Engineering Science, University of Oxford, Oxford, United Kingdom.
[2]Department of Engineering Science, University of Oxford, Oxford, United Kingdom.
[3]BGI-Shenzhen, Shenzhen 518083, China.
[4]Oxford-Suzhou Centre for Advanced Research (OSCAR), Suzhou, China.
[*]Correspondence and requests for materials should be addressed to J.M. (email: majinmin@genomics.cn), H.W. (email: huiwang789@gmail.com) and H.Y. (email: hua.ye@eng.ox.ac.uk)

† These authors contributed equally.
* Corresponding author

5B.1 Abstract

Culturing human Mesenchymal stromal cells (hMSCs) *in vitro* in hypoxic conditions resulted in reduced senescence, enhanced pluripotency and altered proliferation rate. It has been known that *in vitro* hypoxia affects expression of cell surface proteins. However, the impact of culture surfaces on the hypoxia-regulated genes (HRG) have not yet been reported. This study utilized Next-Generation sequencing to analyse the changes in the gene expression levels of HRG for hMSCs cultured on different culture surfaces. The samples, which were cultured on four different synthesized surfaces (treatments) and tissue culture plate (control), resulted in a difference in growth rate. The sequencing results revealed that the transcription of a number of key genes involved in regulating hypoxic functions were significantly altered, including *HIF2A*, a marker for potency, differentiation, and various cellular functions. Significant alternations in the expression levels of previously reported oxygen-sensitive surface proteins were detected in this study, some of which closely correlate with the expression levels of *HIF2A*. Our analysis of the hMSCs transcriptome and HRG mapped out a list of genes encoding surface proteins which may directly regulate or be regulated by *HIF2A*. The findings from this study showed that culture surfaces have an impact on regulating the expression profile of HRG. Therefore, novel culture surfaces may be designed to selectively activate *HIF2A* and other HRG and pathways under *in vitro* normoxia. The understanding of the crosstalk between the regulating genes of hypoxia and culture surfaces may be utilized to strengthen desired hypoxic functions.

5B.2 Introduction

The culturing of human Mesenchymal stromal cells (hMSCs) in hypoxia has shown benefits in reducing senescence, preserving pluripotency, and improving anti-oxidative defence [48, 75, 230, 307, 308]. However, contradictory evidence has been reported on the rate of proliferation [42, 48, 75, 80, 89, 195, 236] and the differentiation potential [75, 77, 183, 231, 309-311] of hMSCs cultured in hypoxia. Similarly, the production of reactive oxygen species (ROS) has been the subject of some debate in hypoxic conditions [217, 218, 312]. These contrasting results may well have arisen from a wide range of factors, including for example, different levels of hypoxia, cell source, cell pool heterogeneity, donor-to-donor variation, culture conditions and extraction techniques [4, 313-315].

Recent developments in the field of materials science and engineering have facilitated the use and study of different biomaterials to regulate stem cells proliferation and differentiation [316-318]. For instance, Lee *et al.* demonstrated that bone-marrow-derived hMSCs cultured on biomimetic polyacrylamide based hydrogel substrates were able to differentiate without the use of expensive and unreliable media supplements [141]. Furthermore, a significant number of reports have demonstrated that by fine tuning the biomaterial substrate properties, such as topography, chemistry, stiffness, etc., it is possible to modulate MSCs responses [36, 154, 319-322]. Cukierman *et al.* reported enhanced cell biological activities and narrowed integrin usage of cells merely by switching to a three-dimensional substrate topography [323]. Furthermore, Guvendiren and Burdick revealed that the spatial and temporal alignment and organization of hMSCs can be reversibly controlled by the topography and substrates of the culture surfaces [142]. Similarly, Phillips *et al.* demonstrated the

induction of osteogenic and adipogenic differentiation in hMSCs by functionalizing the culture surface with amine groups [146]. The modification of surface properties may be inter-dependent in modulating the fate of hMSCs by unconventional mechanisms. Zhang *et al.* reported a synergistic effect of substrate topography and chemistry on the adhesion and differentiation of canine bone-marrow-derived MSCs [147]. Several other notable investigations have also described the effects of other materials properties on stem cells [36, 153-155].

To date, only a few culture parameters have been studied to regulate hMSCs behaviour, i.e. oxygen level, metabolic feed, and cell-surface interaction. hMSCs are plastic adherent by nature, and the cell-surface interaction is primarily dictated by the characteristics of the applied surface in a static culture environment. The cellular effects induced by these three parameters are expected to be interlinked, as shown in Figure 5B.1. Hypoxia has been shown to alter the rate of metabolic uptake and favour the glycolytic pathway for energy production; in addition, survival under hypoxia is strictly dependent on glucose availability [78, 87, 324]. Glucose has also been found to induce the production of ROS and to regulate the expression of *HIF1A*, a pivotal transcription factor in the biological response to hypoxia [325, 326]. Similarly, the impact of culture surfaces on glucose uptake, and *vice versa*, have been reported [156, 327]. Hypoxic conditions and the presence of elevated ROS were found to alter surface proteins and the arrangement of the extra-cellular matrix [47, 83, 328, 329]. However, the impact of culture surface on regulating hypoxic pathways has not been investigated. Azevedo *et al.* prepared a type of “bioactive glass” that can induce hypoxic responses based on the dissolution of Cobalt ions [330]. The stabilization effect observed in their study was chemically induced, by a hypoxia mimicking agent,

not caused by the alteration of surface interactions. The possibility of culture surfaces regulating the expression of hypoxia-regulated genes (HRG) remains to be elucidated. This may be due to the challenges in capturing a global representation of the induced changes by culture surfaces from traditional cell culture surfaces. With the development of RNA sequencing (a.k.a. Next-Generation sequencing) the expression levels of the entire transcriptome can be easily measured, effectively capturing genome-wide changes in gene expression [331, 332]. A number of studies and reviews have addressed the relative advantages of this technique [246, 333, 334].

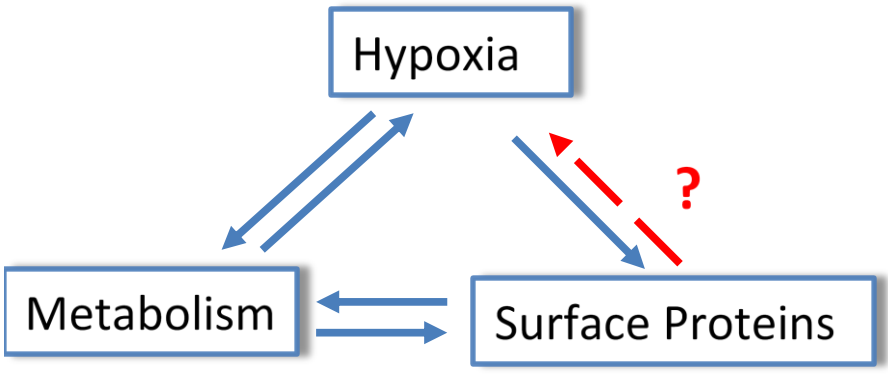

Figure 5B.1: Current knowledge on the interactions between the three key culture parameters [47, 78, 83, 87, 156, 324-329].

This study aims to address the missing knowledge gap on whether culture surfaces can induce HRG, which in turn can be used to emphasize specific hypoxic functions in the future. The commercial hMSCs were cultured on four surfaces which were prepared in-house. The RNA sequencing technique was applied to obtain a global gene expression of each sample [36], from which the HRG were analysed. This study provides novel insights into the novel application of designing culture surfaces to selectively activate hypoxia-regulated functions.

5B.3 Methods

5B.3.1 Sample preparations

Details of cell culture, surface characterization and RNA extraction have been reported previously [36]. Four surfaces (S1-S4) were synthesized and the tissue culture plate (Control) was prepared to culture hMSCs [36]. Briefly, the synthesized surfaces were prepared from poly(L) Lactic acid (PLA) material. Two flat surfaces (S1 and S2) were made by pressing PLA granules at 210 °C for 15 min using a portable hot press. Nonwoven fibrous matrices (S3-S4) were made by electrospinning (an in-house setup) a 7.5% PLA solution. Subsequently, PLA substrates, both flat and fibrous (S2 and S4), were subjected to aminolysis reaction in 5% hexamethylenediamine solution (w/v, in isopropanol) for 30 min at 30 °C under mild agitation, in order to introduce amine groups that alters the surface from hydrophobic to hydrophilic [335]. The flat PLA surface mimics a conventional two-dimensional cell culture plate surface topography, while, the fibrous PLA topography imitates the latest three-dimensional cell culture matrix and/or native extracellular matrix architecture. The pristine PLA surface denotes a hydrophobic surface - typical of synthetic polymers, while, the aminated PLA surface signifies a hydrophilic surface - typical of natural polymers.

Human bone marrow-derived mesenchymal stem cells (Lonza, UK) were incubated under 37 °C, 20% oxygen, 5% CO_2, with saturated humidity. The hMSCs were seeded onto the four different synthesized substrates (i.e. flat, pristine (S1); flat, aminated (S2); fibrous, pristine (S3); fibrous, aminated (S4)) at 50,000 cells per sample across 2 cm discs and cultured for 7 days with media changed at day 1 and then every other day. Standard tissue culture polystyrene substrate was used as control. Cell viability was measured at day 3, 5 and 7 using the Alamar blue based non-destructive assay

(Thermo Scientific, UK). *A standard curve was prepared by taking known concentration of cells in serial dilutions. The absorbance of the test samples was compared with the standard curve in order to convert absorbance values into cell number.* Total RNA from each sample was extracted with the RNeasy Mini Kit (Qiagen, UK). NanoDrop UV/VIS spectrophotometer (1000, Thermo Scientific) and RNA agarose gel electrophoresis methods were used to assess the quality and quantity of the total extracted RNA [36].

5B.3.2 Sequencing data analysis

RNA sequencing was completed on the Day 3 samples. The sequencing experiment and the upstream bioinformatics pipeline has been reported previously [36], further analysis and additional tests were done in this study. Genes with over 100% change in their expression levels against control, and a false discovery rate less than 0.001 were considered to be differentially expressed (DEG). A threshold of expression level (FPKM >1) was set to filter out genes with low abundance.

5B.3.3 Analysis of hypoxia-regulated genes

The gene set describing the HRG was obtained from an online database (HypoxiaDB, www.hypoxiadb.com) [336]. The transcriptome datasets of the five samples (NCBI sample number: SRS2493619; SRS2493628; SRS2493629; SRS2493630; SRS2493885) were compared and analysed for the HRG. Hierarchical cluster analysis compared the gene expression profile for the ensemble HRG between samples.

A list of the hypoxia-altered surface proteins in hMSCs were compiled from the literature database and checked against the detected expressions in this study. Gene

expression correlation and cluster analysis were both conducted with the criteria of Pearson coefficient (R) > 0.9 or < -0.9 and p < 0.01.

The genes encoding hMSCs surface proteins were obtained from the compiled literature surface proteome [53, 54, 337]. Pathway enrichment analysis and the identification of functional gene sets (e.g., genes involved in each cell cycle stages) were conducted utilizing the KEGG database [338]. Gene ontology was done using the DAVID database [339].

5B.3.4 Quantitative real-time PCR

RNA extracted from the Day-5 samples were used for quantitative real-time PCR (qRT-PCR) testing of expression levels of *HIF2A* (also known as *EPAS*). The RNA samples were reversely transcribed, with a genomic DNA wipeout step, using the QuantiTect Reverse Transcription Kit (Qiagen, Stanford, USA) according to the manufacturer's instructions. qRT-PCR was performed using Rotor-Gene 6000 (Qiagen, Stanford, USA), with the following cycle parameters: enzyme activation at 95°C for 2 min, 40 cycles of denaturation for 5 seconds of 95°C followed by 60°C for 25 seconds. The fluorescence acquisition was performed with the SyGreen Blue Mix Lo-ROX (Pcrbiosystems, UK) following the manufacturer's instructions. 3 repeats were run for each sample-gene pair. The fold change was calculated using the delta-delta-Ct method with *GAPDH* as the reference gene. The primers were designed using Primer-BLAST (ncbi.nlm.nih.gov/tools/primer-blast/) and ordered from Sigma, UK. The tested primer sequences are listed below as: *HIF2A-f: GCGCTAGACTCCGAGAACAT; HIF2A-r: TGGCCACTTACTACCTGACCCTT; GAPDH-f: GGATTTGGTCGTATTGGG; GAPDH-r: GGAAGATGGTGATGGGATT.*

5B.4 Results

As a part of the previous experimental design [36], hMSCs were cultured on 5 different surfaces for 3 days before total RNA was extracted and processed for sequencing. The overall sequencing quality was confirmed by mapping the saturation and distribution of the reads [36]. A total of 2,147 HRG were detected, with 1,873 genes exceeding a threshold expression level (Supplementary Table S5B.1). The HRG were analysed, to examine their dependency on culture surface conditions, unless otherwise specified.

5B.4.1 Cell culture data

The samples seeded on different culture surfaces resulted in significant differences in growth rate over the culture period, as shown in Figure 5B.2. The control surface supported the fastest proliferation rates and had a much shorter lag phase compared to the cells cultured on the synthesized surfaces (until day 3). Compared to the samples cultured on flat surfaces (S1 and S2), fibrous surfaces (S3 and S4) resulted in higher levels of growth suppression and resulted in the slowest growth rate. The modification of surface chemistry induced negligible changes on cell growth. Readers interested in cell culture and material characterization data can refer to the Supplementary Information or our earlier work [36].

Key cell cycle regulators and hallmark genes involved in different cell cycle stages were analysed (Supplementary Table S5B.2). Despite the treated samples experienced slower growth rate than the Control, several positive cell-cycle regulating genes were up-regulated, including *CCND1*, *CCNE2*, *CCNB2*, *E2F1*. Meanwhile, some other genes involved in cell cycle progression were found to be down-regulated,

e.g. *TGFB2*, *INHBA*, *THBS1*, etc. The genes involved in the G1 phase were relatively stable with only 2 genes (*CDC6* and *TBRG4)* changing by more than 50%; none of the G1 phase genes were highly expressed. No genes involved in the S phase transition was differentially expressed. Contrastingly, the expression levels of 7 genes involved in regulating the M phase (AURKA, MAD2L1, KPNA2, TGFB1, PPP5C, NOLC1, PAM) were significantly altered, suggesting a greater variation during phase progression between samples which may have contributed to the observed differences in cell growth rate, as shown in Figure 5B.2.

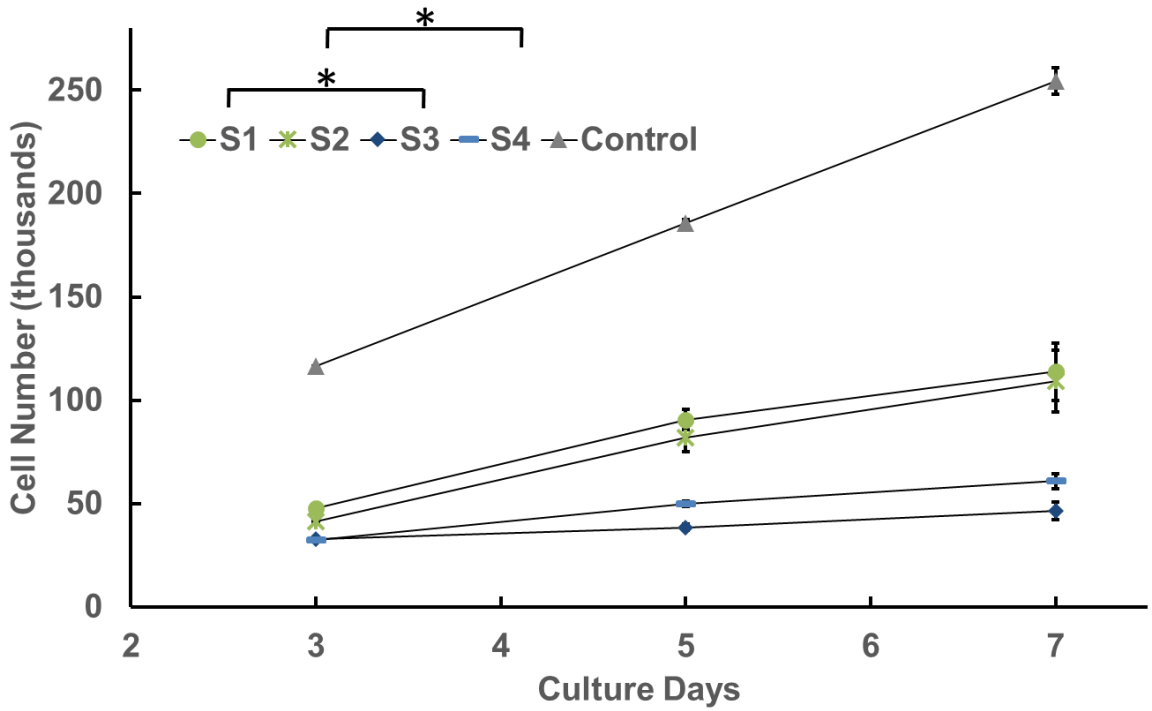

Figure 5B.2: Cell growth data for samples cultured on the five different surfaces. The cell number (mean) on each day is represented with standard error. The difference between the Control and the treated samples are statistically different ($p<0.001$). The difference between S1 and S3, and S2 and S4 are also statistically different (marked with asterisk) ($p<0.001$). Figure adapted from data presented in [36].

5B.4.2 Sample variations of HRG expression levels

The expression variations of HRG across the different samples are shown in Figure 5B.3. Samples with similar expression patterns and small Euclidean distances were paired. The HRG expression profile of the cells cultured on the synthesized surfaces

exhibited a significant difference compared to the control sample. Small expression variations were observed between S1 and S2, and between S3 and S4, the two pairs were cultured on flat and fibrous surfaces, respectively. As described previously for all genes [36], the alteration of the surface topography resulted in a greater impact on cell HRG expression profile than the changes made on surface chemistry. Similar markers (e.g., frequency of gene expression levels, the distribution of coefficient of variation, etc.) were found to be comparable between the HRG and the complete transcriptome profile.

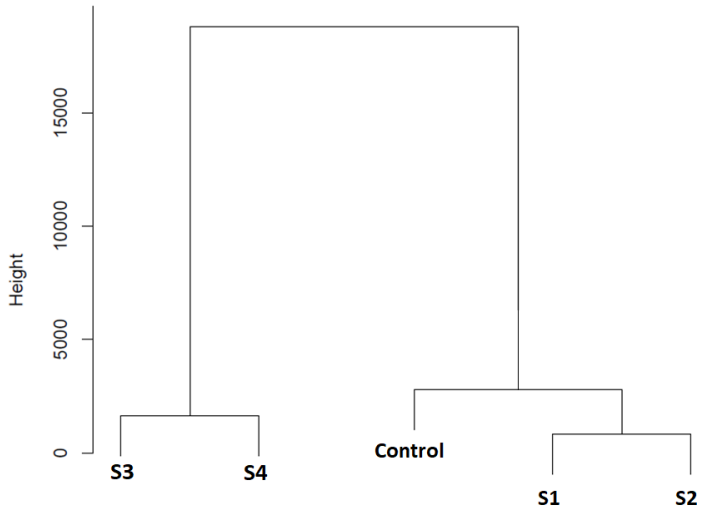

Figure 5B.3: Dendrogram representing hierarchical cluster distributions of the samples cultured on the four synthesized surfaces and Control for the 1,873-detected hypoxia-regulated genes. The Euclidean distance is shown on the vertical axis. Samples with smaller pairwise difference is grouped together.

5B.4.3 Compiled expression of oxygen-sensitive surface proteins

In the literature, various surface proteins were affected by *in vitro* hypoxic cell culture. It is important to determine whether the expressions of these proteins were altered in this study. A list of 15 reported hypoxia-altered surface proteins in hMSCs is shown in Table 5B.1, their respective expression levels from samples in this study are shown. The expression levels for six of these genes, i.e., *CD93, PLCAP, ESAM, SMOC2,*

CDH and *PLEKHA6*, were below the threshold for further analysis in all samples. The measured level of *ITGB1* and *ITGA5* were consistently detected.

Table 5B.1: The compiled expression of surface proteins which were altered under in vitro hypoxia. The expression of the two hypoxic hallmark genes, HIF1A and HIF2A (EPAS) are also shown. The measured gene expression levels from the control (C) and the four synthesized surfaces are reported. Up- and down-regulated genes are highlighted in green and red, respectively. The Pearson coefficient (R) and p values for the expressions of each gene are shown.

Entrez ID	Gene	*R*	*p*	S1	S2	S3	S4	C	Ref.
83483	PLVAP	-	-	-	-	-	-	-	[77]
90952	ESAM	-	-	0	0.1	0	0.1	0.1	[77]
22918	CD93	-	-	0	0	0	0	0	[77]
22874	PLEKHA6	-	-	0.1	0.1	0	0.1	0.3	[77]
64094	SMOC2	-	-	0	0.2	0	0	0	[77]
999	CDH	-	-	0.2	0	0	0	0.1	[340]
3688	ITGB1	-0.62	0.26	788	802	943	834	820	[340]
7412	CD106	0.89	0.04	10.1	13.2	7	10	24.2	[77]
1000	N-CAD	0.97	0.01	69.6	75.1	44.9	52.5	83.7	[340]
3693	ITGB5	-0.62	0.26	144	126.3	127	128	88	[340]
3678	ITGA5	-0.83	0.08	165	135.9	192	159	121	[340]
3673	ITGA2	-0.86	0.06	2.9	3.3	6.9	4	1.7	
2335	FN1	-0.83	0.08	7149	7037	15,579	14,297	8124	[63, 340]
3690	ITGB3	-0.93	0.02	5.6	5.4	17.8	13.9	3.3	[340]
6387	CXCL12	0.42	0.48	82.4	78.9	45.4	44.2	53.4	[63]
3091	HIF1A	-0.83	0.08	140	169	186	184	148	-
2034	HIF2A (EPAS)	1	0	137	135	48.3	56.8	214	-

The two hypoxic hallmark genes, *HIF1A* and *HIF2A (EPAS)* were detected in all samples in this study, with *HIF1A* being consistently expressed. *HIF2A* was down-regulated in cells cultured on the synthesized surfaces, including a 4-fold decrease in samples cultured on fibrous surfaces, similar to the trend for *N-CAD*. Interestingly, the remaining eight genes exhibited large expression variations across samples. The genes with up- or down-regulation of greater than 1.5-fold change are highlighted in green and red in Table 5B.1, respectively. The samples cultured on fibrous surfaces, were found with significantly higher expressions of *ITGA2*, *ITGB3* and *FN1*, than the control. Conversely, *N-CAD*, a differentiation marker [151, 341, 342] was found to be

reduced by 50%. *CXCL12*, a chemokine to increase hMSCs homing and the interaction with hematopoietic stem cells [343, 344], was detected with a 2-fold increase in samples cultured on flat surfaces over those on fibrous surfaces. The expression level of a typical MSCs marker, *CD106*, was found to be supressed in all samples cultured on the synthesized surfaces, whereas, *ITGB5* was found to be consistently upregulated.

In the reported literature data, a few of these genes were found to be altered by hypoxia. In Mathew *et al*., expression levels of *FN1, N-CAD, ITGB1, ITGB3, ITGB5, CDH1*, and *ITGA2* were reported with 1.5- to 2.5-fold increase in hypoxic culture; the increase with *CDH1* and *ITGA2* were not statistically significant [340]. The increase in the hypoxic expression of *FN1* and *CXCL12* was also reported [63]. The signal measured via flow cytometry for *CD106* was greater in 1.5% oxygen culture condition. The induced fold change, because of *in vitro* hypoxia, is in a similar magnitude as induced by culture surfaces in this study.

5B.4.4 HIF2A is regulated by surface proteins

Table 5B.1 compiled the reported hMSCs genes which encode surface protein and are sensitive to culture oxygen level. This study utilized the RNA sequencing to show a change in culture surfaces could also alter the expression levels of genes encoding these oxygen-sensitive surface proteins. The expression level of *HIF2A*, a hallmark hypoxic gene, was measured to be significantly down-regulated. From the results reported in the literature [345, 346] and from this study, HIF2α is hypothesized to be a key mediator in both regulating and being regulated by different surface proteins.

The Pearson coefficient (*R*) and the *p*-value across the samples are also presented in Table 5B.1. Expression levels of *CD106* and *N-CAD* were found to be statistically significant and positively correlated with the expression profile of *HIF2A* across the tested samples, which may suggest a direct up- or downstream regulation between the two and *HIF2A*. The positive correlation between *CD106* and *N-CAD* expression was reported by Aomatsu *et al.* [347]. In their study, the overexpression of *N-CAD* was able to rescue the suppressed expression of *CD106*, and the overexpression of a dominant negative *N-CAD* reduced the level of *CD106*. Yamashita *et al.* discovered the direct regulation of *HIF2A* on *CD106* via *HIF2A* knockdown and chromatin immunoprecipitation assays [345]. The downregulation of *CD106* expression is therefore hypothesized to occur downstream to that of *HIF2A* and *N-CAD*. Leonel showed that the secretion of VEGF, a downstream HIF2α target, significantly increased after the incubation of bone-marrow derived MSCs with additional N-cadherin in the solution [348]. Despite the results demonstrated by Leonel, no direct gene expression level correlation between *N-CAD* and *HIF2A* has been reported, it remains to be elucidated that whether *N-CAD* is altered upstream to *HIF2A*.

Additionally, *N-CAD* has been reported to regulate the differentiation potential of MSCs [134, 349-351]. Liu *et al.* found that the expression level of *CD106* was greatly reduced after differentiation while the expression levels of other MSCs markers remained stable [352]. *HIF2A* has been reported to contribute to the maintenance of cell pool stemness [185, 353]. *CD106* and *N-CAD* may contribute to the regulation of cell pool potency via pathways involving *EPAS* (*HIF2A*). Additionally, the high *CD106* expressing population of MSCs have demonstrated strong elevated angiogenic

capacity with numerous marker genes and produced cytokines being significantly upregulated [354].

On the other hand, *ITGB3* (*CD61*) negatively correlated with the expression of *HIF2A* (Table 5B.1). Various studies have found that *ITGB3* has a regulatory potential in controlling tumour growth and angiogenesis, whereas the inhibition of *ITGB3* has reduced cellular angiogenic potential [355-359]. Furthermore, we found that the expression of *VEGFA* was found to be positively correlated with *ITGB3*, showing a negative correlation with that of *HIF2A*. In the first 3 days of culture, other pathways may be the more dominant factors in affecting the expression of *VEGF* other than *HIF2A*. Kracun *et al.* reported the overexpression of the ITGB3 protein receptor, β3-endonexin, was found to negatively regulate the expression of HIF1a mRNA under hypoxia; HIF2α protein, however was not affected [360]. Therefore, incorporated with the findings from this study, the surface-induced negatively correlated *ITGB3* expression, may be a result of the downstream *HIF2A* regulation. The impact of *ITGB3* on MSCs have not been reported; its reported functions in regulating growth and angiogenesis in tumour cells [361, 362] are expected to be analogous to those in MSCs.

Martin *et al.* reported that HIF2α binds to the promoter of *CXCL12* under hypoxia and may be used to regulate angiogenesis [363]. HIF2α has been observed to induce FN1, which also regulates cytoskeleton arrangement, under hypoxia in lung cancer endothelial cells [364], and melanoma cells [365]. A partial impact of *HIF2A* on *ITGB1* and *ITGA5* was reported by Hughes *et al*. in cancer cell lines [366]. The four types of synthesized surfaces selectively altered the expression of *HIF2A* and the gene

expression profile, which may in turn, differentially regulate the respective downstream hypoxic signalling pathways and functions. From the experimental data reported in the literature and this study, the change in HIF2A expressions is hypothesized to be the result of different activated surface proteins.

5B.4.5 Mapping HIF2A correlated genes and functions

In order to infer how the synthesized surfaces altered the HRG, four gene sets were studied, including the genes encoding hypoxia-sensitive surface proteins (Table 5B.1), all detected HRG, hMSCs cell surface proteome markers [53, 54, 337] and the detected genes from this study that are correlated to the expression of *HIF2A*. 573 genes were found to be correlated with the expression of HIF2A (full details shown in Supplementary Table S5B.3). Figure 5B.4 shows the number of unique and shared genes from the four gene sets. The genes that are shared by three sets are listed in the diagram, e.g. hypoxia-regulated and *HIF2A*-correlated surface proteins: *CD47, HM13, COL6A1, TGFBR1, CD44*, and *PVR*. This finding provides insights for future studies to validate specific gene and pathway interactions between the interaction of surface and hypoxia signalling.

Across the samples cultured on the five types of surfaces, 1,873 of the 2,289 HRG were detected. These HRG significantly enriched key signalling, adhesion, and cancer related pathways, e.g., FoxO, PI3K-Akt, MAPK and HIF1A signalling, focal adhesion, cell cycle, colorectal, pancreatic cancer and leukaemia pathways (Table 5B.2). 102 HRG were found to be differentially expressed in more than two sets of surfaces, demonstrating the effective alteration in the expression of HRG (Supplementary Table S5B.4).

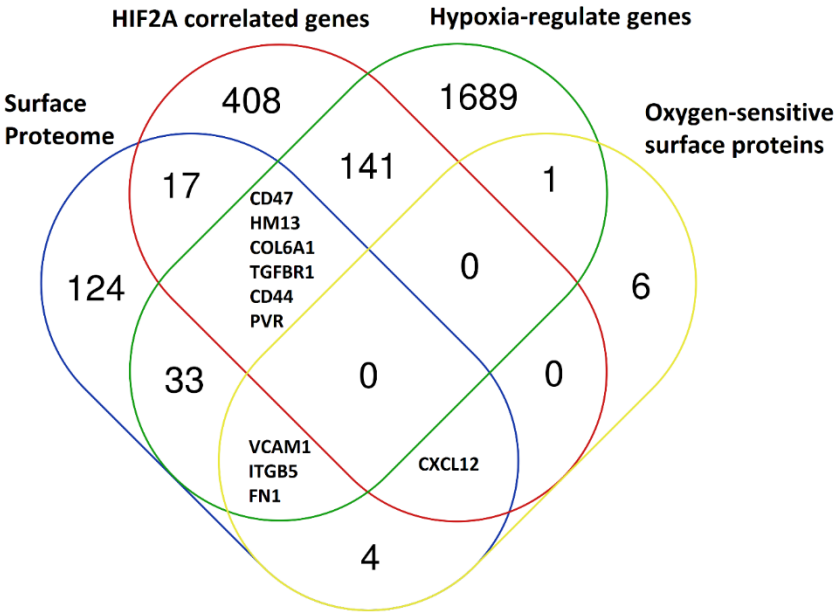

Figure 5B.4: Venn diagram indicating the number of shared genes between the four gene sets. The genes with the expression levels correlating with that of HIF2A in samples cultured on the five surfaces, the detected hypoxia-regulated genes, genes encoding hMSCs surface proteome and the literature reported oxygen-sensitive surface proteins.

Among the genes encoding the 15 oxygen-sensitive surface proteins in Table 5B.1, only *VCAM1*, *ITGB1*, *CXCL12* and *FN1* were both detected in our samples and reported in the hypoxia database. The other four detected genes encoding integrin subunits were not found in the database; among the six undetected genes, only *CD93* was referenced to be regulated by hypoxia.

Comparing with the expression levels of *HIF2A* across samples, 321 positively and 252 negatively correlated genes were found. *N-CAD*, a hypoxia-sensitive differentiation marker, positively correlated with the expression of *HIF2A* with a 1.5-fold expression reduction in the samples cultured on fibrous surfaces. 147 of the correlated genes were found to be also regulated by hypoxia (Supplementary Table S5B.5), and 24 genes were detected in the hMSCs surface transcriptome (Supplementary Table S5B.6); *CD44, CD47, HM3, COL6A1, TGFBR1* and *PVR* were found in both lists. Figure 5B.5A) shows the gene ontology results for the 37 correlated

HRG (with the legend shown in Figure 5B.5B) contributing to the functions of extracellular matrix organization, cell adhesion, regulation of hypoxia, growth, and angiogenesis; the six HRG classified to negatively regulate angiogenesis were all found to positively correlate to the expression of *HIF2A* (Figure 5B.5C). *CCL2* and *COL4A2* were reported to be in both the positive (GO:0001525) and negative (GO:0016525) regulation of angiogenesis.

Certain correlated genes were differentially expressed across the samples cultured on different surfaces. 33 and 17 DEGs were found in the positively and negatively correlated genes, respectively. The induced signalling responses from the culture surfaces are more pronounced on the expression of certain genes, significantly up- or down-regulate their expression. Two pathways were found to be significantly enriched by these DEGs, i.e. Hippo signalling pathway, and the pathways in cancer. The genes encoding two surface proteins, *LGALS3* and *TFGBR1*, were differentially expressed.

Table 5B.2: Gene ontology analysis for the HIF2A-correlated and hypoxia-regulated genes. The number of genes and the percentage of the genes found in the function is reported. The statistical p values and q values (Benjamin) are shown.

Functions	G.O. Number	Gene Count	%	*p*	*q*
Extracellular matrix organization	0030198	14	9.5	1.40E-08	1.80E-05
Cell adhesion	0007155	15	10.2	4.10E-05	2.70E-02
Regulation of cell growth	0001558	7	4.8	6.40E-05	2.80E-02
Response to hypoxia	0001666	9	6.1	1.20E-04	3.80E-02
Angiogenesis	0001525	10	6.8	1.30E-04	3.40E-02
Negative regulation of angiogenesis	0016525	6	4.1	1.90E-04	4.10E-02

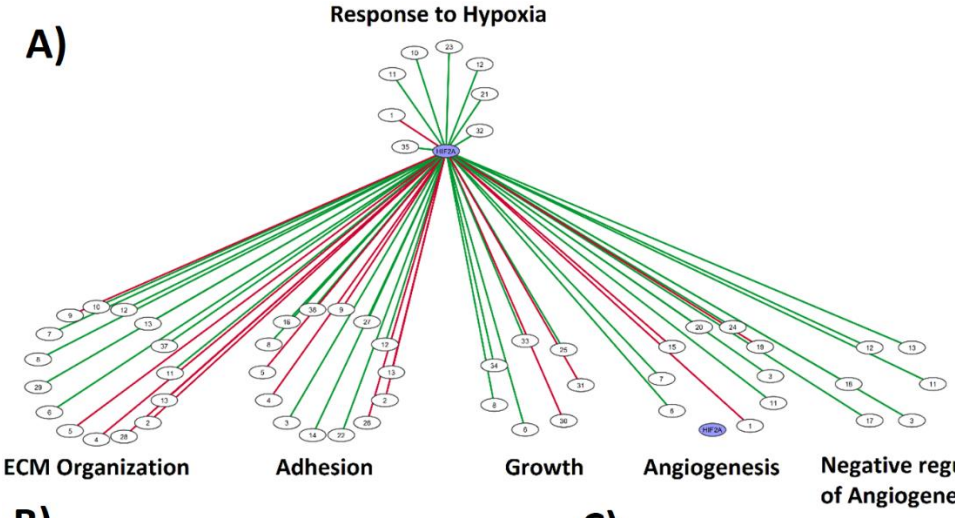

B)

1	CAV1	13	CD44	25	SGK1
2	CD47	14	THBS2	26	SOX9
3	COL4A2	15	COL4A1	27	PXDN
4	COL6A1	16	FGF1	28	PPFIBP1
5	COL7A1	17	FGF2	29	CNTNAP1
6	CTGF	18	FOXC1	30	BLZF1
7	CYP1B1	19	GTF2I	31	H2AFY
8	CYR61	20	RBPJ	32	CITED2
9	LAMB3	21	LEPR	33	PLCE1
10	LOXL2	22	SMAD3	34	CRIM1
11	CCL2	23	TNFRSF11B	35	DDIT4
12	THBS1	24	PLOD2	36	JAM2
				37	TINAGL1

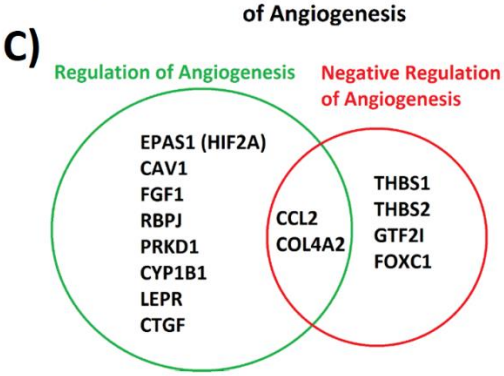

Figure 5B.5: HIF2A-correlated and hypoxia-regulated genes. A) The 37 positive and negative correlations are shown in green and red, respectively. Different functions from gene ontology analysis are labelled, and each unique gene is numbered with the gene names shown in B). The genes reported for the positive and negative regulation of angiogenesis are shown in part C).

5B.4.6 Quantitative PCR validation of HIF2A expression

Quantitative PCR was performed to confirm the trend observed in the sequencing results using Day-5 samples. The Ct values and the fold change for *EPAS* (*HIF2A*) against Control are shown in Figure 5B.6. The reduced expression of *HIF2A* on the synthesized surfaces was confirmed with qRT-PCR. A modest down-regulation in S1 and S2, and a significant down-regulation in S3 and S4 samples were confirmed for, as previously shown in Table 5B.1. The comparable results between RNA sequencing and qRT-PCR using Day-3 and Day-5 samples, respectively, demonstrated stable down-regulation of *EPAS* (*HIF2A*) expression on fibrous surface.

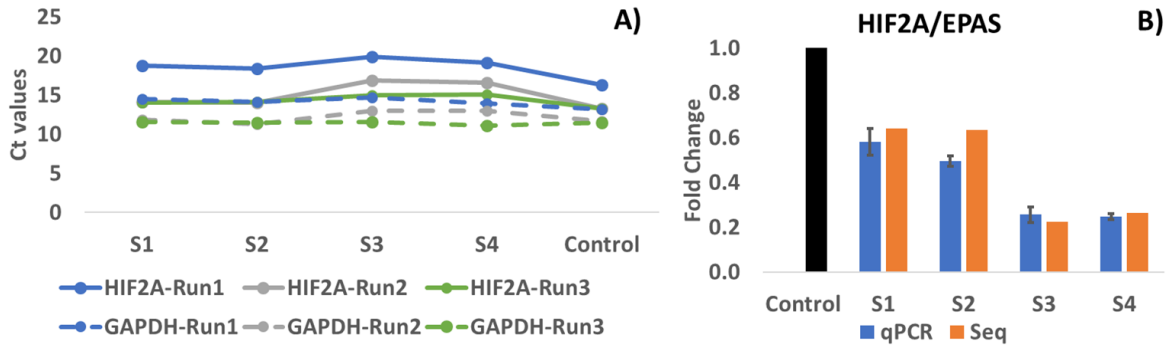

Figure 5B.6: Quantitative real-time PCR results showing the Ct values (A) and the relative fold change of the samples compared to the Control (B), n=3. The results from RNA sequencing is shown for each sample-gene pair.

5B.5 Discussion

Hypoxic cell culture has exhibited outstanding impacts on the rate of proliferation, stemness, differentiation and other capacities of hMSCs. However, by far, the deterministic impact of hypoxia is difficult to be drawn from experimental results, due to the different culture parameters used [188, 307]. Although various studies have reported the alterations in expression levels of surface proteins under *in vitro* hypoxia [77, 83, 329, 367], the understanding of whether different culture surfaces affect the expression of HRG remains to be elucidated (Figure 5B.1). With the available knowledge in the field, it is not feasible to design a controlled experiment to test the induction of surface proteins on hypoxic responses. This study utilized the advantage of RNA sequencing in capturing the entire transcriptomic expressions to address this challenge. The change in the HRG expression in the hMSCs cultured on the four different synthesized surfaces were examined. By addressing this missing link, it may shed insights into addressing some controversies on the effects of hypoxia on MSCs. In addition, certain HRG and hypoxia-regulated pathways may be selectively enhanced or suppressed by different culture surfaces. Certain benefits from *in vitro*

cell culture may be specifically induced without subjecting cells to a hypoxic environment.

In this study, the hMSCs cultured on four different surfaces were analysed for the induced HRG and enriched pathways. The expression levels of several key hypoxia functional genes were significantly altered, e.g. *HIF2A, VEGFB, THBS1*, etc. Various surface proteins and their encoded genes may have enacted upstream of *HIF2A*, which led to the regulation of *HIF2A*, as shown in Figure 5B.7; *CD106* is hypothesized to be downstream of *HIF2A* and *NCAD*. This finding suggests the effect of surface protein activations on oxygen-sensing/hypoxia-regulating pathways, providing supporting evidence and encouraging future studies to fill the missing knowledge gap in Figure 5B.1. *HIF2A* is hypothesized to play a key intermediate role in linking the surface sensing and hypoxic response pathways.

The expression level of *HIF1A* was comparable across different samples. The capacity of HIF1α in responding to different oxygen levels and regulating hypoxic functions are carried out at the protein level, its gene expression is expected to be relatively stable [93, 112, 119]. Different experiments in the literature have reported that HIF2α protein is less sensitive to the protein-level degradation as HIF1α [185, 196, 206], therefore, a change in its gene expression is expected to be reflected at the protein level. Different stem cell markers and the rate of proliferation have been traced back to *HIF2A* activity [105, 106, 108, 117, 368]. This study observed the reduction in *HIF2A* gene expression in hMSCs cultured on all the synthesized surfaces. Alterations in pluripotency and differentiation markers were also observed in a surface-dependent fashion. The variation in these markers was selective to specific surfaces, which may

have contributed to some controversial observations on their differentiation capacities [48, 77, 183, 231, 311, 369].

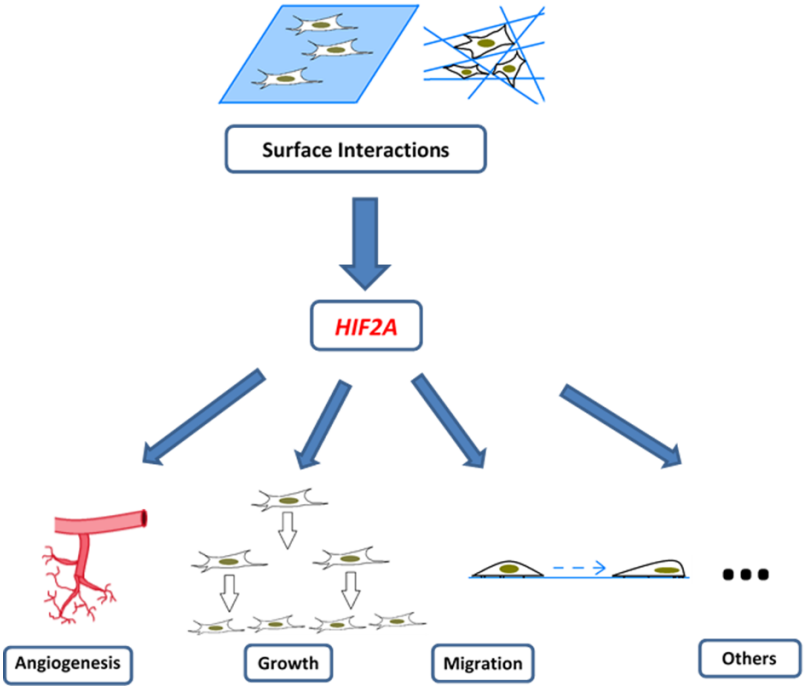

Figure 5B.7: A hypothesis of HIF2A-regualted functions in the hMSCs cultured on different culture surfaces.

A list of the 2,289 oxygen-sensitive genes was analysed in this study. Their dependency on oxygen level may originate from their roles in the various oxygen sensing pathways. This study detected 1,873 of these genes, some of which demonstrated strong dependency to the culture surfaces hMSCs adhered to. Outstanding differences were observed for *ITGA2, FN1, ITGB3*, and *CXCL12*, in samples cultured on both fibrous and flat surfaces. The expressions of the genes encoding various hypoxia-regulated surface proteins were found to be closely related to that of *HIF2A*. Considering of the reported oxygen-sensitive surface proteins, this study found that culture surfaces regulate the gene expression of various surface proteins, some of which subsequently alter the expression of *HIF2A* and its

downstream functions. Culture surfaces triggered part of the oxygen sensing and its downstream signalling pathways.

This study found *HIF2A* to be regulated by a change in activated surface proteins. The analysis of *HIF2A* expression across the samples cultured on different surfaces yielded 573 genes with significant expression correlations (Supplementary Table S5B.3), 147 of which have been reported with regulation dependency to hypoxia (Supplementary Table 5B.S5). Among the correlated genes, the DEGs showed outstanding differences between the compared samples, including genes encoding hMSCs surface proteins. The significant reduction in the *HIF2A* gene expression in the samples cultured on fibrous surfaces (Table 5B.1 and Figure 5B.6) was induced by their surface topography, which regulated the expression of certain genes encoding surface proteins and led to the downstream alteration on *HIF2A*. Subsequently, *HIF2A* was transcribed and translated to regulate various crucial functions in hMSCs, such as survival [195]. Gene ontology analysis revealed the functions associated with the correlated HRG, including regulation on cell growth, hypoxic functions, angiogenesis, and cell surface interactions. *HIF2A* activity has been reported to promote hMSCs growth [196, 205]; in this study, the change in the measured *HIF2A* expression levels (Table 5B.1 and Figure 5B.6) is in line with the observed trend of cellular growth rate (Figure 5B.2).

The rate of degradation of PLA was not expected to be significant in this experiment. All material was handled under the suggested conditions [370]. Therefore, the pH in culture medium was not expected to be affected by PLA degradation and the subsequent reduction of cell proliferation. No change in media colour was observed.

In addition, culture media was changed every alternative day to reduce the impact of material degradation and to ensure the availability of metabolites and growth factors. Furthermore, with the moderate cell density, oxygen level was not expected to be significantly different for the hMSCs cultured on different surfaces. The change in the expressions of HRG was considered to be independent of oxygen level.

In storage, transportation, and therapeutic applications, maintaining a consistent hypoxic environment may be challenging, research has shown short-term exposure to normoxia can result in lasting changes [63, 88]. The findings from this study showed the possibility of using specially designed culture surfaces in regulating HRG and pathways in hMSCs under *in vitro* normoxia. A few other studies have reported on the altered gene expressions induced by culture surfaces [147, 371-375]. Furthermore, *in vitro* hypoxia and culture surface may interactively affect the regulation of surface proteins and their downstream pathways. This effect may have contributed to some contrasting results when comparing hypoxic experimental data from different research groups. Lastly, fibrous surfaces induced a more complex array of pathways which could play a major role in further reducing cellular growth rate. *In vitro* rate of proliferation dictates the required time for a large-scaled hMSCs production, it is important to establish a set of culture conditions (hypoxia, culture surfaces, etc.) which can optimize the process. Novel surfaces can be designed to up- or downregulate *HIF2A* and its downstream functions such as angiogenesis, cell migration, growth, etc. The preservation of hMSCs also need to be monitored during culture, hypoxia has been reported to effectively manage the process; specialized surfaces can be designed to reverse the undesired tendency. Future research will investigate on the potential of utilizing hypoxia and culture surfaces to collectively regulate hMSCs status.

5B.6 Conclusions

The results from RNA sequencing demonstrated that culture surfaces play a role in altering the expressions of HRG and hypoxia-regulated pathways. The sensitivity of the incurred effects was found to be pathway and surface specific. Expression levels of key hypoxic functional genes were altered because of a change in culture surface. Fibrous surfaces induced more hypoxia regulated DEGs which encoded a complex array of cellular functions and resulted in slower rates of proliferation than hMSCs cultured on flat surfaces. The expression levels of several oxygen-sensitive surface proteins were found to be affected by a change in culture surfaces, some of which are hypothesized to act upstream of *HIF2A* and subsequently modulated its expression. Culture surfaces with different substrates hold great potential towards designing surfaces to selectively activate hypoxia-induced pathways under *in vitro* normoxia or to enhance specific functions under hypoxia.

5B.7 Acknowledgements

We are grateful to China Regenerative Medicine International Limited, Hong Kong for funding this work. We extend our thanks to our colleague Dr. Michelle Kümin for critical reading.

5B.8 Availability of data

All the processed data are presented in the manuscript or in the supplementary information. Information on raw data and materials are available from the NCBI BioProject number PRJNA395968 and from the corresponding authors upon request.

Statement of Authorship for joint/multi-authored papers for PGR thesis

To appear at the end of each thesis chapter submitted as an article/paper

The statement shall describe the candidate's and co-authors' independent research contributions in the thesis publications. For each publication there should exist a complete statement that is to be filled out and signed by the candidate and supervisor **(only required where there isn't already a statement of contribution within the paper itself).**

Title of Paper	Culture Surfaces Induce Hypoxia-Regulated Genes in Human Mesenchymal Stromal Cells
Publication Status	☐Published
Publication Details	Author list: Zhang, B.*, Kasoju, N.*, Li, Q.*, Soliman, E., Yang, A., Cui, Z., ... & Ye, H. (2019). Culture surfaces induce hypoxia-regulated genes in human mesenchymal stromal cells. Biomedical Materials, 14(3), 035012. * These authors contributed equally to the paper.

Student Confirmation

Student Name:	Bo Zhang		
Contribution to the Paper	• Performed bioinformatics and data analysis • Wrote the majority of the manuscript with Dr. Naresh Kasoju		
Signature	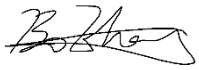	Date	May 5, 2019

Supervisor Confirmation

By signing the Statement of Authorship, you are certifying that the candidate made a substantial contribution to the publication, and that the description described above is accurate.

Supervisor name and title: Prof. Cathy (Hua) Ye		
Supervisor comments: The supervisor agrees with the student's statement.		
Signature 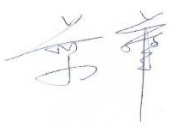	Date	May 10, 2019

This completed form should be included in the thesis, at the end of the relevant chapter.

Chapter 5C – Journal Paper: Effect of Substrate Topography and Chemistry on Human Mesenchymal Stem Cell Markers: A Transcriptome Study

Bo Zhang[1,2,†], Naresh Kasoju[1,†], Qiongfang Li[3,†], Jinmin Ma[3], Aidong Yang[2], Zhanfeng Cui[1], Hui Wang[1,3,4*], Hua Ye[1,*]

[1]Institute of Biomedical Engineering, Department of Engineering Science, University of Oxford, Oxford, United Kingdom
[2]Department of Engineering Science, University of Oxford, Oxford, United Kingdom
[3]BGI-Shenzhen, Shenzhen, China
[4]Oxford Suzhou Centre for Advanced Research, Suzhou Industrial Park, Jiangsu, China
[*]Correspondence to: hui.wang@eng.ox.ac.uk (HW) or hua.ye@eng.ox.ac.uk (HY)

[†]These authors contributed equally to the paper.
* Corresponding author

5C.1 Abstract

The International Society for Cellular Therapy (ISCT) proposed a set of minimal markers for identifying human mesenchymal stromal cells (hMSCs) in 2007. Since then, with the growing interest of better characterising hMSCs, various additional surface markers have been proposed. However, the impact of how culture conditions, in particular, the culture surface, vary the expression of hMSCs markers was overlooked. In this study, we utilized the RNA sequencing data on hMSCs cultured on different surfaces to investigate the variation of the proposed hMSCs biomarkers. One of the three ISCT proposed positive biomarker, CD90 was found to be significantly down regulated on hMSCs culture on fibrous surfaces when compared to flat surfaces. The detected gene expression values for 177 hMSCs biomarkers compiled from the literature are reported here. Correlation and cluster analysis revealed the existence of different biomarker communities that displayed a similar expression profile. We found a list of hMSCs biomarkers which are the least sensitive to a change in surface properties and another list of biomarkers which are found to have high sensitivity to a change in surface properties. This study demonstrated that substrate properties have paramount effect on altering the expressions of hMSCs biomarkers and the proposed list of substrate-stable and substrate-sensitive biomarkers would better assist in the population characterisation. However, proteomic level analysis would be essential to confirm the observations noted.

5C.2 Introduction

Mesenchymal stromal cells (MSCs), the clonogenic fibroblastic colony-forming units, hold immense potential as cells of choice in tissue engineering and regenerative medicine applications. Though bone marrow was the first and widely recognized source tissue, the latest investigations have led to the discovery of a wide variety of MSCs-harbouring placenta, umbilical cord and virtually any vascularized tissue [376]. MSCs can not only be differentiated into tissue-specific lineages but can also be trans-differentiated across lineages [377]. Apart from such multipotency, the immunomodulatory property of MSCs is attracting attention [378]. While these developments highlight the potential of MSCs, they also lead to some confusion in the field, majorly due to the identity paradox. To this effect, the International Society for Cellular Therapy (ISCT) proposed (a) plastic-adherence nature, (b) $CD105^{+}$, $CD73^{+}$, $CD90^{+}$, and $CD45^{-}$, $CD34^{-}$, $CD14^{-}$ or $CD11b^{-}$, $CD79\alpha^{-}$ or $CD19^{-}$ and $HLA\text{-}DR^{-}$ surface markers, and (c) tri-potency ability as the defining criteria to identify MSCs [379]. Recently, a few others such as Stro-1, CD146 and CD49f were also proposed as candidate markers. However, source dependent differences left MSCs identity still obscure. Besides, the discovery of culture conditions dependent effects on surface marker expression, such as induction of SSEA-4 by fetal calf serum [380], and suppression of CD49f by confluency [66], further enhanced the ambiguity over MSCs identity. Pham *et al.* showed that cryopreservation reduced the expression of *CD73 [381]*. Lv *et al*. articulated these issues in great detail in their recent review [382].

Along with conventional culture conditions optimization studies, investigations on the use of biomaterials to help translate MSCs therapy from bench to bedside are on the rise [383]. It is an indisputable fact that the use of biomaterials in facilitating isolation

[384], in enhancing *in vitro* expansion [27], in long-term storage [385], in modulating differentiation [141], and in aiding site specific delivery [386], has expanded the horizons of MSCs to the next level. In this regard, it is important to understand the underlying cell – biomaterial interactions since subtle alterations in substrate topography and chemistry influence the cell fate to a significant extent [321, 387, 388]. For instance, McMurray *et al.* discovered that a nanostructured surface retains stem-cell phenotype and maintains stem-cell growth over eight weeks [389], while, Dalby *et al.* demonstrated the use of nanoscale disorder to stimulate MSCs to produce bone mineral *in vitro* [390]. Similarly, Benoit *et al.* reported that substrates functionalized with small molecules can control MSCs differentiation encapsulated in hydrogels [391], while, induction of osteogenic and adipogenic differentiation on amine functionalized surfaces in contrast to pristine samples shows the effect of surface chemistry on cell response [146]. Whereas there is evidence on how biomaterials act in terms of controlling stem cell differentiation, there is little information on whether or not these biomaterials have any influence on surface marker expression in the context of MSCs expansion.

Such information is needed not just to ensure quality control of the expanded MSCs but to design next-generation biomaterials-based substrates for MSCs expansion. Inspired by observations of Zamparelli *et al.* [392] and Duffy *et al*. [393] on the effect of biomaterials on surface antigen expression in MSCs, here, we designed a study to unravel the effects of substrate topography and substrate chemistry on expression levels of surface markers in bone marrow-derived hMSCs. However, unlike conventional flow cytometry or qRT-PCR methods, here we tested the gene expression levels by following the whole transcriptome shotgun sequencing, also

known as RNA-sequencing [394, 395]. This next-generation sequencing approach helps to (a) evaluate the stability and sensitivity of ISCT and few other known hMSCs markers, (b) identify potential gene networks or molecular pathways associated with these markers, and (c) screen for new substrate-stable and substrate-sensitive candidate markers. For this, we have prepared poly(L-lactide) (PLLA) based substrates with two variables of topography viz. flat (Fl) and fibrous (Fs) and two variables of chemistry viz. pristine (Pr) and aminated (Am). The flat PLLA surface (Fl-PLLA) represents a conventional two-dimensional culture substrate, whereas, the fibrous PLLA (Fs-PLLA) surface represents an advanced three-dimensional culture substrate. The pristine PLLA (Pr-PLLA) surface represents a hydrophobic surface that a majority of synthetic polymers exhibit, whereas, the aminated PLLA (Am-PLLA) surface represents a hydrophilic surface that a majority of natural polymers exhibit. The cell response on the test materials (Fl-Pr-PLLA, Fl-Am-PLLA, Fs-Pr-PLLA and Fs-Am-PLLA) was compared with that on a control plate (TCP).

5C.3 Material and Methods

5C.3.1 Surface material, cell culture and RNA extraction

The detailed information on surface preparation, cell culture and RNA extraction has been reported previously [36]. A total of four synthesized surfaces and tissue culture plate were used for cell culture. The four surfaces were synthesized with poly(L) Lactic acid (PLLA), including two types of surface topography (flat – Fl or fibrous -Fs) and two types of surface chemistry (aminated – Am or non-aminated – Pr). The standard tissue culture polystyrene substrate was used as the control surface.

Human bone marrow-derived mesenchymal stem cells (hbm-MSCs, Poietics™, cat. no. PT-2501, Lonza UK), were cultured in a proprietary medium (cat. no. PT-3001, Lonza UK), supplemented with antibiotics (10 U/mL penicillin and 10 µg/mL streptomycin, Thermo Scientific, UK). Cells were routinely incubated in a CO_2 (5%) incubator maintained at 37 °C temperature, 95% relative humidity. hMSCs (passage 3) were seeded onto various test and control substrates at a rate of 50,000 cells/well and cultured for 7 days with viability measured at day 3, 5 and 7 using the Alamar blue assay (Thermo Scientific, UK).

RNA extraction was done using the RNeasy Mini Kit and followed the supplier's instructions (Qiagen, UK). RNA agarose gel electrophoresis and Nanodrop spectrophotometer (1000, Thermo Scientific) were used to check the quality and quantity of the extracted RNA [36]. RNA was isolated at each time point; however, RNA *Seq* was done for day 3 sample to capture the substrate-induced early commitment of MSCs.

5C.3.2 RNA sequencing

Total RNAs were extracted from all samples using a commercial extraction kit (RNeasy Mini kit, Cat No. 74106). Sequencing platform of BGI-500 (BGI, Shenzhen, China) was used to obtain gene expression profiles. SOAPnuke was used to remove low quality reads. Quality control checks were performed to confirm sequencing saturation and gene mapping distribution. Fragments per Kilobase of Transcript per Million mapped reads (FPKM) value were used to express relative gene abundance. Genes with expression levels less than 1 across all samples were neglected in order to increase data set confidence.

5C.3.3 Data analysis

Previously reported 177 hMSCs biomarkers were compiled from the literature [54, 337, 382], including proteoglycans, adhesion molecules, receptors, etc. The full list of genes is included in Supplementary Table S5C.1. The expression levels for these biomarkers were checked against the samples cultured on different surfaces in this study. Hierarchical cluster analysis was conducted on the compiled biomarkers and the total sequenced genes, samples were grouped based on their pairwise differences.

Gene-wide correlation analysis was performed with $p < 0.01$ and the Pearson coefficient $(r) > 0.9$ or <-0.9. Normalized standard deviation, also known as coefficient of variation, was used to quantify the stability or sensitivity of gene expression across samples. The stability and sensitivity of the biomarkers was examined by evaluating the consistency of expression in samples cultured on the different types of surfaces. Differentially expressed genes were determined with greater than one-fold change in pairwise comparison and a false discovery rate less than 0.001.

The biomarker expressions and correlations were used to develop a network structure and was graphically represented using Cytoscape [396]. Positive and negative correlations of each gene expression across samples was determined. The average expression levels for each gene and their ranked percentile determines the size of the node. Cluster analysis was conducted using Newman's method, edge between-ness and modularity were determined as the method described in [397].The Octave-networks-toolbox was utilized [398]. The modularity for the different number of communities were screened, the number of communities with the highest modularity was selected as the optimal clustering configuration. The optimal clustering

configuration was processed using the Newman-Girvan algorithm to generate the distribution and the specific genes for each cluster. The clusters with more than five nodes/genes were considered as true clusters and further analysed.

5C.4 Results and Discussion

5C.4.1 General characteristics of materials and cell response

Details of the material characteristics such as morphological features of Fl-PLLA and Fs-PLLA before and after amination by SEM, confirmation of amine functionalization by FITC staining and ATR-FTIR was previously reported by our group (26). The diameter of electrospun fibres of Fs-PLLA scaffold used in the study was 603 ± 197 nm (Mean ± SD). There was no significant change in the fibre diameter after amine functionalization, as confirmed by SEM. Besides, qualitative and quantitative analysis of cell adhesion and proliferation on various substrates was also previously reported by our group (26). Briefly, the cellular adhesion and proliferation was relatively high on control TCP substrate compared to test PLLA substrates. This was apparently due to lack of RGD moieties on PLLA. Amongst the test substrates, significant changes in the overall cell response was noted amongst substrates varying in surface topography (Fs-PLLA and Fl-PLLA) than the surface chemistry (Pr-PLLA and Am-PLLA).

5C.4.2 Analysis from the perspective of ISCT recommended markers

The set of surface markers proposed by ISCT has not only streamlined the scientific investigations on hMSCs, but has also assisted commercial organizations in characterising hMSCs-based products for clinical trials [392]. Although there is variability in the marker set reported in the literature, in many cases, the ISCT-proposed set of markers is considered the gold standard [382]. Following this trend, in

the current study, we started off by investigating the expression profiles of ISCT-proposed markers. With no surprises, irrespective of the culture substrate properties, hMSCs expressed *CD105, CD73* and *CD90*, and were negative for expression of*CD45, CD34, CD14, CD19* and *HLA-DR* (Figure 5C.1; the expression levels of the negative markers were undetected or found to be negligible, thus are ignored). However, a close look at the relative expression levels revealed two compelling observations: firstly, the expression level of a given marker varied depending on the culture substrate. Typically, hMSCs cultured on flat substrates (Fl-PLLA) showed up regulated surface marker expression as compared to those cultured on fibrous substrates (Fs-PLLA). There was no visible distinction in the surface marker expression in hMSCs cultured on pristine (Pr-PLLA) and aminated (Am-PLLA) substrates. Although the substrate properties were known to modulate the hMSCs fate, little was known of their effects on the surface marker expression levels. Previously, Skardal *et al.* described that immune-histochemical (IHC) staining for surface markers such as CD90 and CD105 was strong for cells cultured on synthetic substrates with 2 – 5 kPa stiffness as compared to the cells cultured on stiffer (15, 50 kPa) substrates. Our observations not only support the findings of Skardal *et al.* but also provide quantitative evidence towards substrate-dependant effects on surface marker expression [399].

The second curious finding from Figure 5C.1 was that the overall expression levels of *CD105* and *CD90* were positively correlated ($p = 0.0186$, $r = 0.916$, Figure 5C.1) whereas correlation between *CD73* and *CD90* was not significant ($p = 0.305$, $r = -0.276$, Figure 5C.1). Intrigued by this observation, we performed a correlation analysis. Out of 17,748 genes, identified by RNA-seq, across hMSCs samples cultured on five

different surfaces, a total of 871 genes were found to have a positive or negative correlation. Of these, 464 genes were correlated with *CD90*, 467 genes with *CD105* and 334 genes with *CD73* (Figure 5C.2). It was again apparent that expression levels of *CD105* and *CD90*were interactive whereas the*CD73* level was independent. Our results comply with those reported by Zamparelli *et al.* where rat bone marrow-derived MSCs cultured on PLLA substrates showed, using flow cytometry, an 82 ± 8% CD 90 positive population but only a 35 ± 19% CD73 positive population [400], and by Skardal *et al.* where human amniotic fluid-derived MSCs cultured on synthetic substrates showed comparable IHC staining for CD105 and CD90 markers [399]. Furthermore, in the current study, *CD90* and *CD105*shared over 84% (n = 394) of their individually correlated genes, whereas *CD73* showed no commonly correlated genes with either of the other two markers (Figure 5C.2). As evident from the NCBI Gene Database, although the genomic context is different, *CD90* (*THY1*) and *CD105* (*ENG*) encode proteins that are involved in cell communication, whereas *CD73* (*NT5E*) encodes a protein that catalyses the conversion of extracellular nucleotides to membrane-permeable nucleosides. Such functional relations may perhaps explain why *CD90* and *CD105* were expressed correlatively. Additionally, based on a report by Colgan *et al.* suggesting a major involvement of CD73 in nucleotide metabolism during hypoxia and ischemia, it was most likely that the lower *CD73* expression level in the current study may be attributed to the normoxic culture conditions [401].

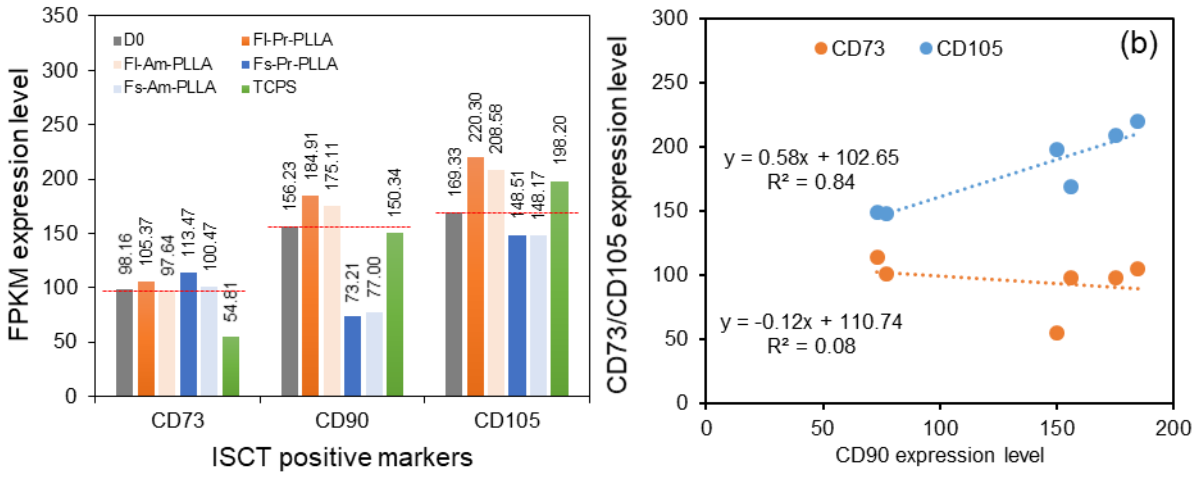

Figure 5C.1: Expression levels of ISCT recommended hMSCs surface markers: A) *CD90* and *CD105* showed substrate-sensitive response whereas *CD73* showed substrate-stable response. *CD90* and *CD105* showed variations on expression levels that were higher than that of *CD73*. B) The FPKM values for *CD90* were plotted against the FPKM values of *CD73* and *CD105*, line of best fit and R-square is shown in the figure.

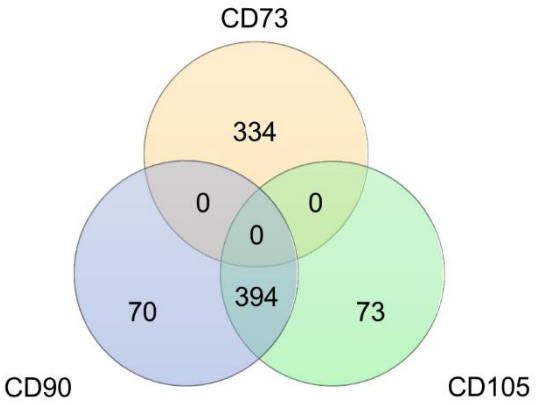

Figure 5C.2: Genes correlated with the three positive ISCT recommended hMSCs markers: The total number of correlated genes with *CD73* (334) was less than that with *CD90* (464) and *CD105* (467). *CD90* and *CD105* share over 84% of their individually correlated genes, whereas, *CD7 3* has no common genes with the other two markers.

5C.4.3 Analysis from the perspective of a comprehensive list of markers reported in the literature

Of the three positive ISCT markers, CD90 andCD10 5might be proposed as a substrate-sensitive marker, while CD73appearedas a substrate-stable marker. However, we believe that the concept of substrate-sensitive/stable markers should be consolidated further, thus incorporation of additional markers is needed to propose a comprehensive set of biomaterials-specific markers for potential use in the field of MSCs-based regenerative medicine. The list of 177 hMSCs markers that were reported in various contexts from the literature is examined (Supplementary Table S5C.1). Overall, the expression profiles between them vary to a significant extent. Preferential expressions of certain markers were observed, where, some markers exhibited stable expression and some showed sensitiveness to a change in culture surface conditions. Expression levels of these 177 biomarkers were subjected to principal component analysis and dendrogram analysis. As shown in Figure 5C.3, the effect of chemistry treatments on the gene expression profile was relatively smaller than that of surface topography induced changes, and the samples cultured on flat surfaces exhibited significantly smaller changes to the control cluster than those in the fibrous samples. This feature conformed to the gene expression patterns reported for all genes [36], strongly suggesting that the marker set genuinely represented the overall gene expression. To our knowledge, this study is the first of its kind reporting the effect of substrate topography and chemistry on the expression of 177 biomarkers reported in the literature.

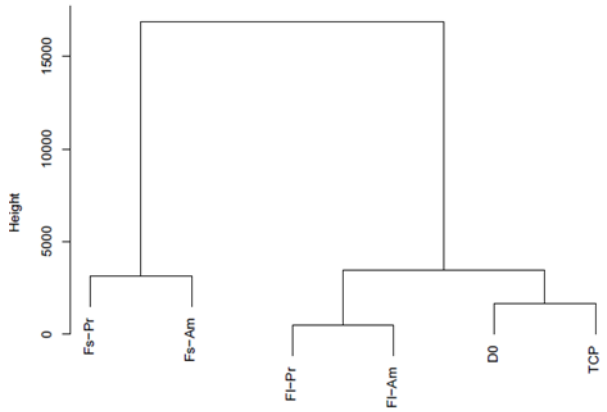

Figure 5C.3: Substrate induced changes in expression of 177 hMSCs biomarkers compiled from the literature: Dendrogram shows that the expression levels of the biomarkers were significantly altered with respect to changes in topography in comparison with chemistry induced changes.

Proceeding further, we have performed a correlation analysis within these 177 biomarker gene expression levels to seek more insights (Figure 5C.4). Out of 177 marker genes, 22 genes were found without any significantly correlated pairs and therefore were excluded from the figure. Amongst the rest, both positive (represented by the green line) and negative (represented by the red line) correlations were discovered. The statistical relationships were not straight forward and intertwined for most of the genes. However, certain genes were found to correlate to only one or a few other genes. For easy reference, the results are interpreted with reference to the ISCT markers. As shown in Figure 5C.4A), the three ISCT markers have been rearranged to the right-hand-side of the figure to highlight their high degrees of connectivity within the network. Overall, the percentiles of the average expression levels across samples are represented by the size of the nodes. The three ISCT markers exhibited considerably significant levels of correlation. A positive correlation was identified between *CD90 (THY1)* and *CD105 (ENG)*, whereas there was no correlation between*CD73 (NT5E)* and either of the other two. Further, the networks

including these three markers and their first-degree-neighbours are isolated and presented in Figure 5C.4B). There are quite a few first-degree-neighbours of *CD90* or *CD105* which showed correlation within this network (Supplementary Table S5C.2). However, none of the first-degree-neighbours of *CD73* exhibited a correlation with those of *CD90* or *CD105*. This may perhaps be due to the functional context of these genes as discussed earlier.

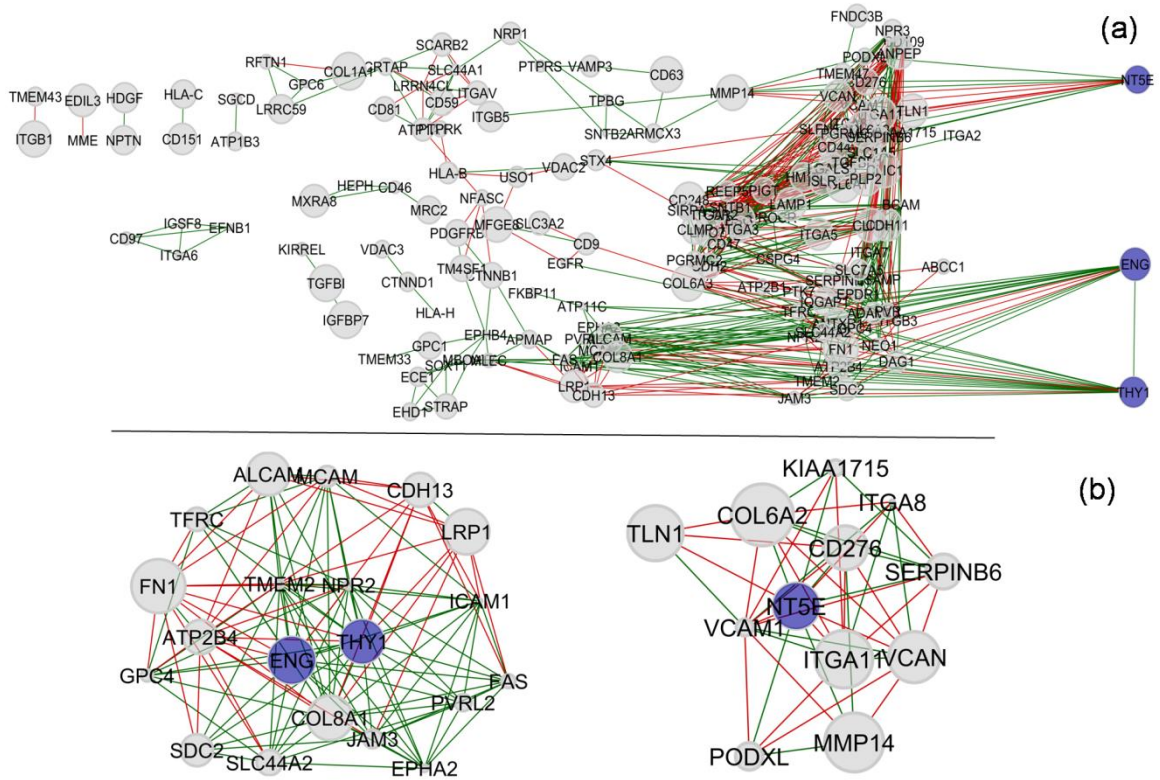

Figure 5C.4: Correlation analysis of gene expression levels of 177 hMSCs biomarkers compiled from the literature: (A) overall observation with reference to three ISCT markers highlighted and (B) first-degree-connections of ISCT markers suggested correlation between *CD90* and *CD105* including its neighbors but no correlation with that of *CD73* and its neighbors. A negative correlation between two genes is shown by a red line and a positive correlation is shown by a green line. The size of the node represents the mean FPKM percentile for that particular gene.

5C.4.4 Findings on biomaterial- stable and sensitive markers

Besides the conventional ISCT markers, we examined the stability of the expressions for the 177 biomarkers as a result of being cultured on different biomaterials. The stability of the gene was quantified by the coefficient of variance (CoV) across samples.

A smaller CoV entails a higher independence of this biomarker gene to the culture substrate. The top 10 genes with the lowest coefficient of variance are shown in Table 5C.1. None of these top 10 genes was found to correlate to the three positive ISCT markers.

Table 5C.1: List of biomaterials-stable hMSCs markers identified from the 177 biomarkers reported in the literature.

Gene ID	Gene Name	D0	Fl-Pr	Fl-Am	Fs-Pr	Fs-Am	TCP	CoV
1495	CTNNA1	117.4	120.1	124.3	117.8	127.6	119.3	0.03
10085	EDIL3	176.2	160.4	159.7	173.2	166.4	172.0	0.04
3916	LAMP1	195.8	187.7	193.8	203.4	194.5	177.4	0.05
6717	SRI	26.0	28.9	25.2	25.8	28.0	26.8	0.05
3490	IGFBP7	1375.9	1304.5	1208.1	1211.9	1166.4	1273.2	0.06
781	CACNA2D1	13.1	12.3	11.8	13.2	11.6	13.6	0.06
6443	SGCB	30.1	31.0	32.3	28.1	27.6	27.8	0.06
8910	SGCE	10.9	10.9	10.9	9.3	11.2	10.5	0.07
3688	ITGB1	810.3	787.9	801.8	942.6	834.5	819.7	0.07
9217	VAPB	8.9	9.0	9.8	7.9	8.7	9.0	0.07

Furthermore, we examined the connectedness of the 177 expressed biomarkers. The positive correlation results from the previous analysis were subjected to cluster analysis to identify the community groupings that maintain the highest level of network integrity. The grouping that yielded the highest network modularity (Q=0.82) was taken as the set of the most representative clusters (Figure 5C.5A)). A total of 48 communities were identified in this network arrangement, among which four communities consisted of more than five genes. The frequency plot describing the

number of genes in each cluster size is shown in Figure 5C.5B). The correlation between genes and clusters are shown in Figure 5C.5C). The list of genes in each of these four communities are closely correlated with each other, in other words, the expression of one marker gene is expected to represent that of the others; the top three most stably (in blue) or variably expressed (in red) genes from each of the communities are shown in Figure 5C.5D) as potential marker genes. Representative genes (stably expressed genes in Figure 5C.5D)) from each community can be selected to capture the expression pattern for that population of markers. Consistent with earlier findings, *CD90* and *CD105* belong to the same community, while *CD73* belongs to another community, and there is no correlation detected between the *CD73* community and the *CD90/ CD105* community.

To further investigate the surface sensible markers, we looked at the biomarkers that displayed greater dependency to a change in culture surfaces, in particular, a change in surface topography (between flat and fibrous surfaces). The 17 biomarkers that were found to be differentially expressed between the samples cultured on different topographies are shown in Table 5C.2, including one of the ISCT markers, *CD90 (THY1)*. Among these biomarkers, 13 displayed significant down-regulation when cultured on fibrous surfaces, whereas the other four experienced significant up-regulation.

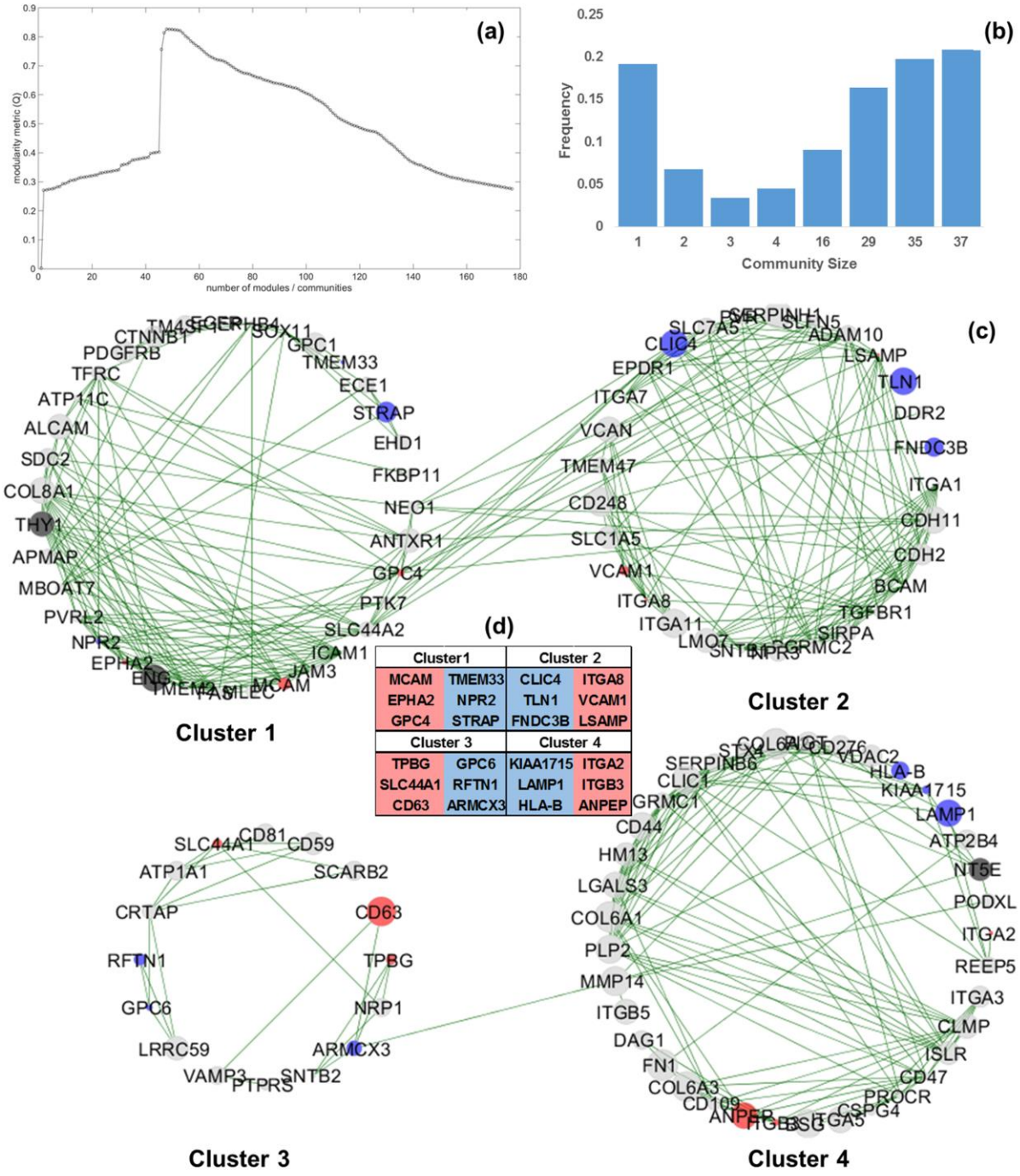

Figure 5C.5: Cluster analysis of the 177 compiled hMSCs markers: (A) network modularity determination figure showing the configuration of 48 communities resulted in the highest modularity. (B) Gene frequency graph, the frequency (number) of genes that was allocated into the different size of communities, as a result of the optimal cluster configuration. (C) The clustered network consists of the circular subplots, each of the parameter circles represents a community/cluster. Each green line represents the positive correlation of the gene expressions. The interactions within each community are noticeably more than the interactions with other communities. The size of the node represents the average expression level of that gene. The three positive ISCT markers are highlighted in grey. The top three stable or variably expressed genes in each community are highlighted in (C) and the gene names in panel (D), in blue and red, respectively.

Table 5C.2: List of biomaterials-sensitive hMSCs markers identified from the 177 biomarkers reported in the literature.

Gene ID	Gene Name	D0	Fl-Pr	Fl-Am	Fs-Pr	Fs-Am	TCP	CoV
4162	MCAM	6.5	34.3	36.1	9.8	9.4	26.9	0.66
3690	ITGB3	10.7	5.6	5.4	17.8	13.9	3.3	0.60
1969	EPHA2	6.2	8.9	6.5	1.8	1.9	6.3	0.53
928	CD9	61.6	26.7	29.9	59.7	83.1	25.3	0.50
3672	ITGA1	4.6	2.6	3.2	1.2	1.7	4.3	0.48
3673	ITGA2	5.8	2.9	3.3	6.9	4.0	1.7	0.46
4059	BCAM	2.2	4.5	4.2	1.8	2.5	5.5	0.43
2239	GPC4	8.0	13.1	13.1	5.3	5.7	13.5	0.40
2335	FN1	7292.7	7148.9	7036.7	15578.7	14296.8	8124.2	0.40
84168	ANTXR1	73.6	121.5	135.6	54.5	60.2	129.1	0.39
4883	NPR3	42.6	51.5	54.2	25.5	24.3	67.7	0.38
1295	COL8A1	113.8	205.7	196.0	85.1	89.0	171.8	0.38
4008	LMO7	92.4	114.1	129.1	54.0	71.3	160.7	0.38
23670	TMEM2	5.5	9.1	8.8	3.3	4.1	7.5	0.38
7070	THY1	156.2	184.9	175.1	73.2	77.0	150.3	0.36
5819	PVRL2	17.7	22.6	17.7	9.4	9.1	16.9	0.34
57153	SLC44A2	29.9	39.2	35.2	19.3	20.4	36.5	0.28

The impact of different chemistry substrates did not significantly alter the expression levels of any of the studied biomarkers. To further illustrate the interactions of surface topography and chemistry, a Venn diagram was prepared to show its differential regulation on both pristine (Pr) and aminated (Am) substrates, as presented in Figure 5C.6. The number of up- and down- regulated genes along with gene names are shown for each chemistry substrate. A total of 17 and 11 biomarkers were found to be differentially regulated by topography, on pristine-based and aminated substrate

surfaces, respectively. Among which, nine biomarkers were consistently down-regulated on fibrous surfaces for both substrates, including *CD90*. The three biomarkers that were significantly up-regulated on fibrous surfaces for both substrates were *FN1*, *CD9* and *ITGB3*. These 11 (eight down-regulated and three up-regulated) genes provide strong evidence demonstrating the sensitivity of these biomarkers to a change in surface topography.

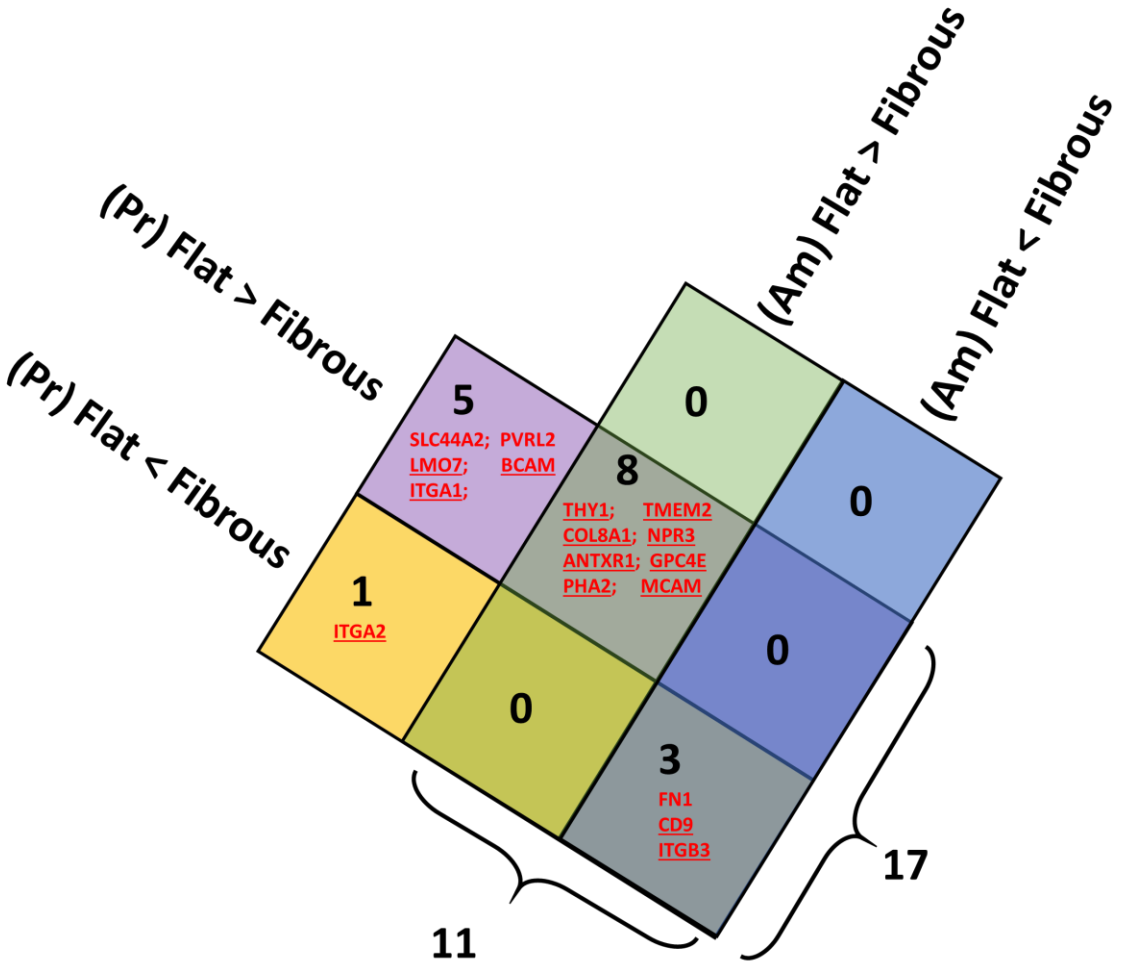

Figure 5C.6: Identification of hMSCs biomarkers that respond to changes in substrate topography: The number of differentially regulated genes (> for up-regulation and < for down-regulation) are shown in each block, along with the gene names listed. The two chemistry substrates are represented by Pr and Am. The underlined genes were also differentially expressed compared to those from TCP.

5C.5 Conclusions

To conclude, we hypothesized that the transcriptome analysis of human bone marrow derived MSCs cultured on standard tissue culture-treated polystyrene and poly(L-lactide)-based artificial substrates with varying topography (Fl: flat and Fs: fibrous) and chemistry (Pr: pristine and Am: aminated) could offer novel insights into substrate-specific markers. Apart from ISCT proposed markers, we have identified and compiled 177 markers that are reported in the literature in various contexts. Comparative gene expression level analysis suggested that *CD90* and *CD105* showed comparable substrate-sensitive response whereas *CD73* showed substrate-stable response. A correlative analysis found 871 genes, out of 17748, to be correlated with ISCT markers, of which, *CD90* and *CD105* showed comparable results that are distinct from *CD73*. Subsequently, a dendrogram of 177 markers suggested that chemistry induced changes on gene expression profile was relatively smaller than that of surface topography induced changes, and the samples cultured on flat surfaces exhibited significantly smaller differences than those in the fibrous samples. From the correlation analysis, the first-degree-connections of ISCT markers and the 177 markers found in the literatureshowed a correlation between *CD90* and *CD105* including its neighbors but no correlation with that of *CD73* and its neighbors. Positive correlation results yielded a top-10 list of substrate-stable and sensitive markers for hMSCs studies in the context of biomaterials research. Furthermore, among the 48 communities identified from the cluster analysis, the 3 most representative and variable genes were reported for each cluster with greater than 5 genes. The study indicates that an omics approach can help analyse the variations in a comprehensive manner and perhaps give clarity on the MSCs identity in the context of biomaterial research. However, in

order to confirm that the changes observed at the gene level are reflected at the protein level, a proteomic analysis may be required.

5C.6 Acknowledgements

We are grateful to China Regenerative Medicine International Limited, Hong Kong for funding this work. We extend our thanks to our colleague Dr. Michelle Kümin for critical reading.

5C.7 Availability of data

All the processed data are presented in the manuscript or in the supplementary information. Information on raw data and materials are available from the NCBI BioProject number PRJNA395968 and from the corresponding authors upon request.

Statement of Authorship for joint/multi-authored papers for PGR thesis

To appear at the end of each thesis chapter submitted as an article/paper

The statement shall describe the candidate's and co-authors' independent research contributions in the thesis publications. For each publication there should exist a complete statement that is to be filled out and signed by the candidate and supervisor **(only required where there isn't already a statement of contribution within the paper itself).**

Title of Paper	Effect of Substrate Topography and Chemistry on Human Mesenchymal Stem Cell Markers: A Transcriptome Study
Publication Status	☐Published
Publication Details	Author list: Zhang, B.*, Kasoju, N.*, Li, Q.*, Ma, J., Yang, A., Cui, Z., ... & Ye, H. (2019). Effect of Substrate Topography and Chemistry on Human Mesenchymal Stem Cell Markers: A Transcriptome Study. International journal of stem cells. * These authors contributed equally to the paper.

Student Confirmation

Student Name:	Bo Zhang		
Contribution to the Paper	• Performed bioinformatics and data analysis • Wrote the majority of the manuscript with Dr. Naresh Kasoju "NK, HY and HW conceived and designed the study. NK, BZ and JM performed the experiments. NK, BZ, QL, JM and HW performed data analysis. NK, BZ and HW wrote the manuscript. ZC, HW, HY and AY reviewed the manuscripts."		
Signature		Date	May 5, 2019

Supervisor Confirmation

By signing the Statement of Authorship, you are certifying that the candidate made a substantial contribution to the publication, and that the description described above is accurate.

Supervisor name and title: Prof. Cathy (Hua) Ye		
Supervisor comments: The supervisor agrees with the student's statement.		
Signature 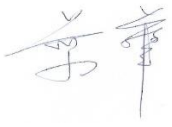	Date	May 10, 2019

This completed form should be included in the thesis, at the end of the relevant chapter.

Chapter 6: Discussion and Conclusions

6.1 Summary of key findings

The findings from this thesis advance the understanding of how oxygen level and culture surface regulate the growth rate of hMSCs. The learnings and the constructed models can be used to optimize the design and control of bioreactors to reach greater *in vitro* production efficiency of hMSCs. The gained insight on key intracellular regulatory pathways also hold significance for the study of similar cell types (e.g. other stem cells, cancer cells). The discoveries in this work will help facilitate the development of cell therapy and regenerative medicine. Results from the constructed mathematical models, experiments, and bioinformatics analysis are summarized in the 5 attached Journal papers.

The exposure of *in vitro* hypoxia significantly affects the growth rate of hMSCs in an oxygen-dependent fashion. Experimental results demonstrated, in two sources of BM-hMSCs, suppressed rates of proliferation under severe hypoxia and enhanced growth rates under mild hypoxia. A constructed single-cell model showed the similar trend of environmental oxygen on the commitment to proliferation, a marker which can represent cellular growth rate. This work demonstrates that, in certain types of hMSCs, hypoxic oxygen levels impose opposing effects (i.e. enhanced or suppressed) on cell growth rate.

The two hypoxic hallmark proteins, HIF1α and HIF2α, are considered to hold heavy significance in regulating hMSCs growth rate under *in vitro* hypoxia. The oxygen-dependent expressions of HIF1α and HIF2α modulate the activity of their downstream

targets, some of which directly and indirectly participate in the rate of cell cycle progression and biomass synthesis.

Maximum hMSCs growth rate was experimentally determined under 1% oxygen with the lowest lactate concentration measured in the culture media. This was hypothesized, with findings from mathematical modelling, to be the result of hypoxic regulation on metabolism, leading to an incomplete progression of the TCA cycle. Glycolysis was found to be playing a major role and correlated with the growth rate of hMSCs cultured under hypoxia. Significant alterations on the metabolic network were mediated by HIF1α activation and meeting the biomass demand associated with enhanced growth rate.

Under normoxia, the full progression of the TCA cycle was found to be dependent on hMSCs specific growth rate. The growth regime of normoxically cultured hMSCs affected their relative utilization of glycolysis and exhibited the opposing trend of specific lactate production. Simulation results suggest that the metabolic network underwent inherent adjustment to satisfy the growing demand at higher growth rates under normoxia.

Surface topography exhibited a significant impact on regulating the transcriptome and growth rate of hMSCs. Despite the small effects imposed by surface substrates independently, it was found that they can synergistically regulate hMSCs transcriptome with a change in topography, i.e. the culture of hMSCs on aminated-PLLA substrate showed a smaller difference between flat and fibrous surfaces than those on pristine-PLLA substrate. The expression of many hMSCs biomarkers was

found to be differentially expressed on different culture surfaces. Lists of commonly used biomarkers sensitive and stable to a change in culture surfaces are reported.

Additionally, this study discovered that culture surfaces can significantly alter hypoxia-regulated genes, including a hypoxic hallmark gene, *HIF2A*. The surface-dependent activation of various surface proteins was found to participate in signaling pathways which subsequently altered the expression of hundreds of hypoxia-regulated genes. This finding suggests a potential in achieving specific activation or suppression of hypoxia-mediated pathways (e.g., HIF2α-mediated) with novel biomaterials.

The findings from this study can facilitate the design and operation of three-dimensional bioreactors for hMSCs production. A reduced oxygen level can increase the rate of proliferation, reduce residence time and enhance operational efficiency. Additional benefits from maintaining a hypoxic environment can also be realized in preserving stemness and reducing senescence. An optimal oxygen level can be determined for the target hMSCs and implemented to improve the overall production output. This study found that the optimal oxygen level of 1% increased hMSCs cell number by 50% - 70% after 3 days; proportional gain in process efficiency may be achieved following the quality assessment on the hMSCs cell pool.

In addition, novel biomaterials can be designed to further enhance the production rate of hMSCs. Surface material, topographical and chemical features can be modified to regulate hMSCs identity, growth, metabolism, and other key functions in maximizing the rate of proliferation while retaining stemness. Static hMSCs culture with three-dimensional scaffolds may result in zones with insufficient nutrients (e.g. oxygen,

glucose, growth factors) or in the case of perfusion bioreactors, creates “dead zones” with negligible flow exchange, both of which may lead to undesired hMSCs status. Findings from this study suggest that biomaterials can be designed to regulate hMSCs metabolic network which may enhance the robustness for cells in these conditions. The induction of hypoxic functions without subjecting hMSCs to a low oxygen environment can eliminate the high operational cost associated with supplying nitrogen gas, which contributed to more than 20% of the operating cost for the hypoxic chamber used in this study. In addition, it may better mimic hMSCs niche environment and reduce shock post-transplantation. By better understanding how hypoxia and culture surfaces regulate hMSCs growth, the design and operation of future bioreactors can utilize these insights in improving their production efficiency.

6.2 Limitations and future work

The work described in this thesis includes experimental measurements and model simulations. A key difference in these two approaches lies in the scale of the boundary condition. Single-cell models were utilized in this study (Chapter 3 and Chapter 4) to better capture the inherent intracellular changes, whereas experimental data reflects the average behavior of the cell pool. Simulation results should be interpreted as plausible hypotheses for the experimental observations. Future work can look into integrating population models (e.g. stochastic models) with the constructed single-cell models to bridge the gap between simulation and experimental findings. Future work shall look into improving the comparability between the experimental setup and simulation parameters, as well as improved means in using simulations to interpret experimental observations.

A number of simplifying assumptions were made in the mathematical model to focus on key mechanisms to be elucidated. For example, the modelling work reported in Chapter 3, the concentration of HIF1α and HIF2α were assumed to be unchanged with hypoxia exposure time, which was not an ideal representation of the protein profile. These factors need to be considered when comparing experimental findings from simulation results.

The hypothesized regulation of HIF1α and HIF2α on cell cycle progression can be tested experimentally with gene modification. Specific knock-out or silencing of HIF1α, HIF2α and their regulatory genes can provide further evidence to confirm whether the observed hypoxia-mediated growth was the direct effect of HIFα on the cell cycle machinery.

The conducted hypoxic culture experiments were limited to a 3-day period. As primary hMSCs have slower growth rates, longer culture periods can determine whether the observed hypoxia-mediated growth suppression was the result of a longer lag period under hypoxia.

Different serum-free media composition shall be tested under 1% oxygen to see if growth rate can be further elevated. A change in hMSCs metabolism under hypoxia may have preferential uptake of certain amino acids or carbon source.

With the time and resources available, this study was not able to carry out a qualitative assessment to determine if the trilineage capacity is preserved after culturing under

different oxygen levels. Future work shall investigate on if the differentiation capacity is affected after hMSCs cultured under different levels of hypoxia.

The available technique for measuring glucose and glutamine concentrations (i.e. through colorimetric assay) yielded large standard deviations. This may due to the inherent instability of the reagent and/or the experimental setup. The large standard deviations in glucose and glutamine measurements also made them infeasible for calibrating the FBA model. Other techniques (e.g. high-performance liquid chromatography, liquid chromatography-mass spectroscopy, Raman spectroscopy, Fourier-transform infrared spectroscopy) may be tested in the future for reducing experimental error. A more accurate dataset will allow a better understanding of how different oxygen levels affect glucose and glutamine uptake and improve accuracy of the FBA model.

The presented FBA model was only calibrated with the experimentally determined lactate production and hMSCs growth data. The availability of additional metabolic uptake data can improve model accuracy and robustness; besides glucose and glutamine, the techniques mentioned in the above paragraph can be used to detect concentrations of different amino acids, carbon and nitrogen sources.

The number of samples processed for RNA sequencing was limited, due to low RNA extraction yield. As a result, the sequencing data presented in Chapter 5A, 5B, and 5C lacks biological repeats. Despite this challenge, certain conclusions/hypotheses could still be made as surface chemistry induced minimal changes on the two tested samples, which could be considered for qualitative comparisons. Consistent findings

on samples with different hydrophobicity were presented. No protein samples were collected in this experiment, therefore, only changes on gene expressions could be identified. Future study shall repeat this experiment to validate the presented findings and carry out protein analysis to determine if the observed changes are reflected on the protein level.

Surfaces with different topographical characteristics shall be tested to further study the linkage between surface proteins and *HIF2A* as well as the stability of different biomarkers. Experiments can be designed to silence genes encoding different surface proteins to determine the key modulator of *HIF2A* expression. HIF2α-target functions shall be tested in long term cultures to determine whether the surface-induced modulation on *HIF2A* expression can be realized biologically.

Appendices

Chapter 3 − Supplementary Information

Experimental data on hMSCs growth under different oxygen levels

This study cultured bone marrow-derived hMSCs from three different sources under various hypoxic levels (0.1%, 1%, 2%, 5% and 8%) in serum-free media. The immortalized hMSCs and a source of primary hMSCs showed enhanced, maximum growth rate under 1% oxygen.

Methodology

The primary bone marrow-derived hMSCs were acquired from PromoCell (C-12974) (P-hMSCs). The immortalized bone marrow-derived hMSCs were acquired from a collaborating laboratory, origin and preparation of these cells is described in [402]. Cells were cultured in incubators at 5% CO_2 in air with 100% relative humidity. Hypoxystation-H35 (Don Whitley Scientific) was used for cell culture under hypoxia, with 5% CO_2, and 85% humidity. Cells were cultured in a serum-free, xeno-free media, MSCs NutriStem (Biological Industries, USA). Cells were cultured in 6-well cell culture plates (Costar, Thermo Fisher, UK) with a seeding density of 5,000 cells/cm^2, counted and harvested after 3 days. The passage number of 4 – 6 were used for the P-hMSCs, and passage number of 6 -10 were used for the immortalized hMSCs for studying cell growth. The cells from a parental cell pool were seeded and cultured parallelly under hypoxia and normoxia and the ratio of the harvested cell number under hypoxia to

those under normoxia after 3 days was used to represent the effect of hypoxia on hMSCs growth.

Results

The hMSCs cultured under different oxygen levels were determined for the impact of hypoxia-mediated growth. The cells from the same parental cell pool was parallelly cultured under *in vitro* hypoxia and normoxia, the ratio between the counted cell numbers at Day 3 was used to determine the relative growth rate. For each set of experiments, with the seeding and counting techniques described in earlier sections, the only variable parameter affecting cell growth was the oxygen level.

Supplementary Figure S3.1A) shows the relative growth rate for the immortalized hMSCs cultured under 0.1%, 1%, 2%, 5% and 8% oxygen, with the number of biological repeats (n) displayed for each oxygen level. Under 0.1% oxygen, a significant growth suppression was observed, on average, the cell number after 3 days was 66% less than those cultured in normoxia. 1% oxygen resulted in the highest growth rate of 1.84 after 3 days, with the cell number 84% higher than its normoxic set. Further alleviation of hypoxic stress reduced growth rate, with the growth rate of 1.18 under 2% oxygen, and 1.02 under 5% oxygen. An increase in oxygen level to 8% elevated its growth rate (by 26%) to be significantly higher than that under normoxia. Results from of the statistical analysis is shown in Supplementary Figure S3.1B).

The population doubling time (PD) varies with each set of experiments due to the heterogeneity of the cell pool, parental cell status, etc. The typical PD for the normoxically cultured hMSCs were measured to be 19 - 30 hours, the PD for the

hypoxically cultured cells vary dependent on the oxygen level. The relative growth rate (Supplementary Figure S3.1A)) is considered to be a better marker in comparing the results from different biological repeats, as it reduces the impact imposed by the change in proliferative status from different parental cells. The PD can be calculated from the measured cell number after 72 hours (Day3) and seeding cell number (Day0) using Equation S3.1.

$$PD = 72 / Log_2 (Day3 / Day0)$$ ***Equation S3.1***

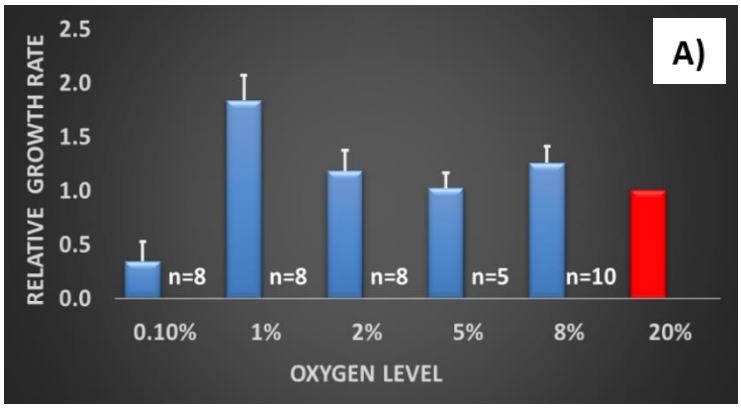

B)

	1%	2%	5%	8%	20%
0.1%	**	**	**	**	**
1%		**	**	**	**
2%			N.S	N.S	N.S.
5%				N.S	N.S
8%					*

Supplementary Figure S3.1: The impact of hypoxia-mediated growth rate for immortalized hMSCs. A) The relative growth rate is shown for the different in vitro hypoxic oxygen levels. The ratio represents the number of cells measured after 3 days of culture between the hypoxically and normoxically cultured cells. The number of biological repeats (n) are shown beside each set of result, with the standard deviation shown as error bars. B) A chart showing the statistical significance between each set of different results. Statistically different sets with $p<0.01$ (**) or $p<0.05$ (*) are shown. Insignificant difference is marked with N.S.

Besides culturing the immortalized hMSCs, primary hMSCs (P-hMSCs) were also studied. Due to experimental limitations and cost, not all presented oxygen levels have 3 or more biological repeats, the preliminary results from these oxygen levels do not affect data interpretation. Their relative growth rate under different oxygen levels is shown in Supplementary Figure S3.2.

The P-hMSCs showed a trend comparable to that of the immortalized hMSCs, with 1% - 8% oxygen facilitated growth rate and the most prominent response observed under 1% oxygen (Supplementary Figure S3.2). A slight growth suppression was observed under 0.1% oxygen level but not statistically significant. Experiments under 0.1%, 1%, 5%, and 8% oxygen were successfully carried out with 3 biological repeats.

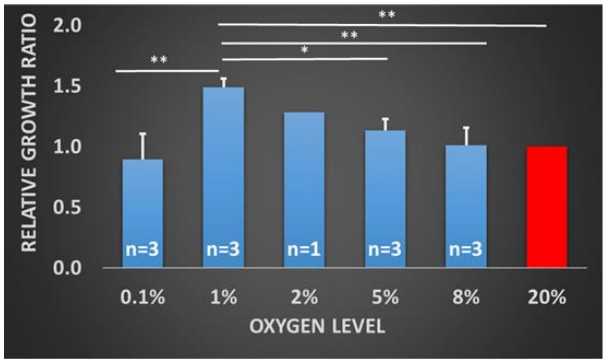

Supplementary Figure S3.2: The impact of hypoxia-mediated growth rate for the primary P-hMSCs. The relative growth rate represents the number of cells measured after 3 days of culture between the hypoxically and normoxically cultured cells. The number of biological repeats (n) are shown for each set of results, standard deviations are shown as error bars. A horizontal bar was used to show significantly different results, with $p<0.01$ (**) or $p<0.05$ (*). The relative growth rate for the P-hMSCs cultured under different oxygen levels.

The PD time for the two primary hMSCs were longer than that of the immortalized hMSCs, ranging from 37 – 70 hours for the P-hMSCs. The immortalized hMSCs have gone through additional cell generations in the same 3-day culture period. The observed hypoxia-mediate growth effects in the primary hMSCs will be further amplified in longer culture periods, e.g. 7 days. Culture periods designed to achieve the same number of cell divisions could provide further insights in comparing the absolute growth rate and PD time among the 3 types of hMSCs used. With the current experimental setup, only qualitative comparisons can be made between the immortalized and the primary hMSCs.

With the immortalized hMSCs and P-hMSCs, hypoxia imposed an oxygen-dependent response on its growth rate. The oxygen level similar to the hMSCs niche condition (1% - 8% [72, 256]) resulted in a facilitated growth, whereas severe hypoxia imposed growth suppression due to limited oxygen availability and the initiated pro-survival responses. In the literature, experimental results showed contrasting results of whether hypoxia facilitates hMSCs growth. The findings from this study showed that the origin of the hMSCs is important in regulating its hypoxia-mediated growth. The different factors among the 3 types of hMSCs used includes the variability in donor cells, heterogeneity of the cell pool, isolation and freezing procedures used by each supplier. In addition, the cultured primary hMSCs had passage numbers below 6. Higher passage numbers of the immortalized hMSCs were used, although their growth behaviour was not expected to be affected due to its immortalized nature.

Chapter 3 − Supplementary Information

Parameter values and initial conditions

Supplementary Table S3.1: Tabulated nominal model parameter values and descriptions.

Parameter	Description	Reference/Note	Model Values
M1	Hif1α multiplication constant	[190]	0.000414
b1	Hif1α exponential constant		9.395
T1	Hif1α normalizing oxygen level	[206]	10%
M2	Hif2α multiplication constant	[185, 189]	0.20497
b2	Hif2α exponential constant		0.44863
kr3A	Hif1α-Myc dissociation	Estimated based on cyclin D – p21/p27 data [201]	0.15 /hr
kf3A	Hif1α and Myc binding		15 /uM/hr
kr3B	Hif2α- Myc dissociation		0.15 /hr
kf3B	Hif2α and Myc binding		15 /uM/hr
T2	Hif2 normalizing oxygen level	[185]	20%
m13	E2F auto-regulation with Myc	[403]	0.4 μM/h
k13	E2F auto-regulation with Myc		0.15 μM
k'13	E2F auto-regulation with Myc		0.15 μM
m_E2F	Myc induced E2F production		0.003 μM/h
k_E2F	Myc induced E2F production		0.15 μM
d_E2F	basal E2F degradation		0.25 /hr
kf12	cycE and p21/p27 association	[192, 201]	18 /uM/h
kr6B	cycD-p/p dissociation	[201]same as in Rb-E2F binding	0.18 /h
kr12	cycE-p/p dissociation		0.18 /h
g_cycD	basal cycD production	[201] 10% w serum	0.045 μM/hr
k_3A	Hif1α direct inhibition	[201] assumed half of MYC-dependent cycD	0.07 μM

		transcription strength	
g_Rb	basal Rb synthesis	[201]	0.06 μM/h
g_p/p	basal p21/p27 synthesis	[201] same as g_RB	0.06 μM/h
d_p/p	basal p21/p27 degradation		0.06 /h
d_cycd_pp	basal degradation of cycD-p/p	[201] same as d_cycE	1.5 /hr
d_cyce_pp	basal degradation of cycE-p/p		1.5 /hr
d_RbP	basal degradation of RbP	[201] same as d_RB	0.06 /hr
d_e2f_rb	basal degradation of E2F-Rb	[201] same as d_E2F	0.25 /hr
m_E2F-RbP	cycD phosphorylation of E2F-Rb		18 /h
k_E2F-RbP	cycD phosphorylation of E2F-Rb		0.92 μM
k8	Rb and E2F association		18 /uM/h
kf6B	cycD and p21/p27 association		18 /uM/h
d_cycE	basal cycE degradation		1.5 /h
k9	E2F dependent production		0.15 μM
m9	E2F dependent production		0.35 μM/h
k5_cycD	Myc-dependent cyclin D transcription		0.15 μM
m5_cycD	Myc-dependent cyclin D transcription		0.03 μM/h
d_cycD	basal cycD degradation		1.5 /h
d_Rb	basal Rb degradation		0.06 /h
k_cycD_RB	cycD phosphorylation of Rb		0.92 μM
m_cycD_Rb	cycD phosphorylation of Rb		18 /h
k_RbP	RbP dephosphorylation		0.01 μM
m_RbP	RbP dephosphorylation		5 μM/h
k_cycE_RbP	cyclin E-mediated hyper-phosphorylation of Rb	[201]	0.92 μM

m_cycE_RbP	cyclin E-mediated hyper-phosphorylation of Rb		18 /h
k_RbnP	RbnP de-phosphorylation to Rb		0.01 μM
m_RbnP	RbnP de-phosphorylation to Rb		5 μM/h
g_myc	basal Myc synthesis		1 μM/h
d_myc	basal Myc degradation		0.7 /h
k4	Myc inhibition of p/p transcription		1 /uM
ε	relative activity strength of Hif2α-Myc over Myc		1.1
d_hif1_mm	basal degradation of Hif1α-Myc		0.1 /hr
d_hif2_mm	basal degradation of Hif2α-Myc		0.1 /hr
n_deg	ROS-facilitated degradation constant	Estimated	1

Supplementary Table S3.2: Tabulated Model Initial Conditions [201].

Species	Initial Concentration (μM)
Hif1α-Myc; Hif2α-Myc; E2F; cycD-p/p; cycE-p/p; cycD; cycE; RbP; Rb-nP; Myc	0
E2F-RB	0.25
RB	0.4
p/p	0.2

Chapter 3 − Supplementary Information

The effect of initial conditions on steady state E2F concentration

The impact of different initial conditions was evaluated by running the simulations with different parameter value sets and initial conditions. The three key parameters (b1, m13, and ε) were selected for the analysis. Parameter values and initial conditions were varied by ±50% sampled by the Sobol sequence. For each parameter and initial condition set, the steady state E2F concentration was evaluated and compared to that predicted with the default initial conditions. The analysis was competed with 100 parameter value sets evaluated against 100 generated initial conditions (i.e. 10,000 scenarios in total). Out of the 10,000 scenarios, 198 scenarios (referred to as "outstanding scenarios") were found to yield a steady state E2F concentration different from that obtained with the default initial conditions, which is less than 2% of the total cases tested. These data points are plotted in Supplementary Figure S3.3 below. These outstanding scenarios plotted on the y-axis resulted in non-zero steady state E2F concentrations, however, the default initial conditions yielded E2F concentration of 0. Contrastingly, the scenarios plotted on the x-axis yielded non-zero steady state E2F concentrations but returned 0 with a new set of initial conditions. From this analysis, these outstanding scenarios only appeared to be caused by a switch between the initially quiescent cells and the commitment to proliferation, and vice versa.

It should be also noted that, out of 100 sets of parameter values tested, only 10 of them showed to lead to multiple steady states, 4 of which accounted for 164 of the 198 such scenarios. In terms of oxygen levels, a large portion of the scenarios with

multiple steady states was observed for the lower oxygen levels (severe hypoxia) and close to normoxia.

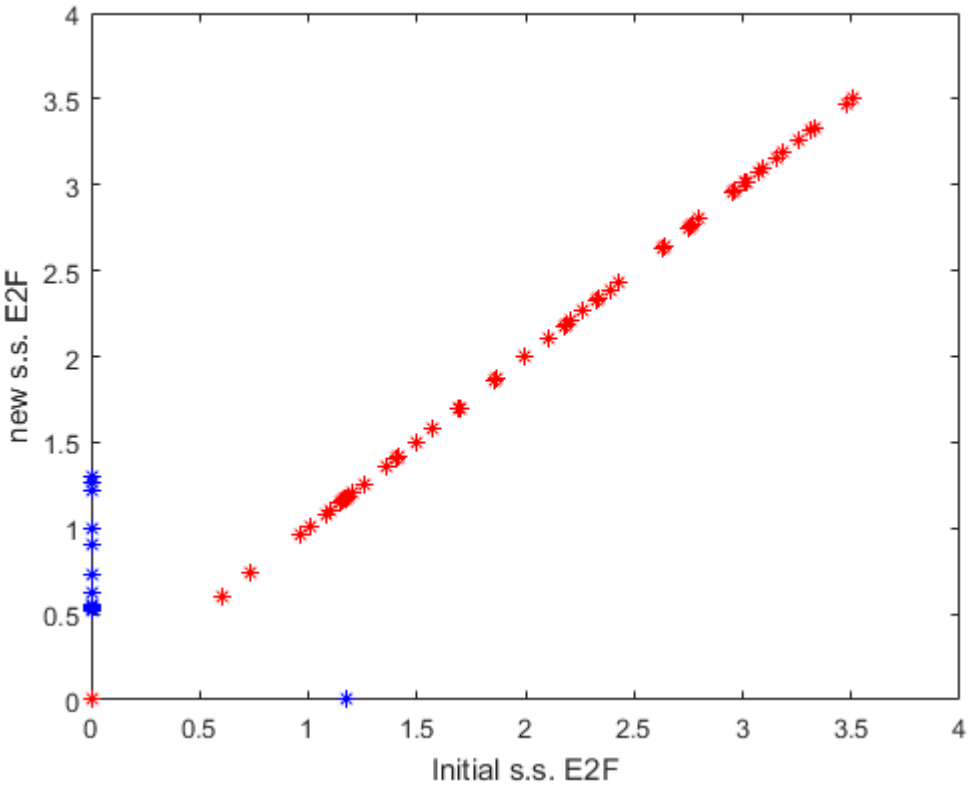

Supplementary Figure S3.3: Simulation results on the steady state E2F concentrations from the simulation results for different parameter value sets and initial conditions. The 9802 simulated results that yielded the same steady state E2F concentrations are shown in red. The 198 cases that showed discrepancies on the steady state E2F levels are plotted in blue.

Chapter 3 − Supplementary Information

Compiled hypoxic MSCs growth data

Supplementary Table S3.3: The compiled hypoxic growth data from the literature for MSCs. The table below corresponds to Figure 3.4.

Hypoxic level	Figure 3.4 reference	Reference
2%	S1	[196]
1%	S2	[81]
2%	S3	[82]
2%	S4	[79]
1%	S5	[83]
0.50%	S6	[90]
2.50%		
0.50%		
2.50%		
1%	S7	[85]
3%		
5%		
10%		
1%	S8	[38]
1%		
2%	S9	[196]
5%	S10	[227]
2%	S11	[224]
5%	S12	[226]
1%	S13	[75]
1%	S14	[223]
5%		
1%		
5%		
2%	S15	[225]

Chapter 4 − Supplementary Information

Additional note on the calibration of experimental measurements for proliferating cells

In this note, additional information is included on how the calibration of the experimental measurements for proliferating cells. Cells were seeded at Day-0, the first 24-hour was assumed as a lag phase that cells were attaching onto the culture surface and adapting to the environment. The increase in cell number between Day-1 and Day-3 was used to calculate the population doubling time. The table below denotes the accounting of the number of proliferating (P_i) and not-actively-proliferating cells (Q_i); the percentages representing these two populations is represented by *P%* and *Q%*, respectively, this percentage is assumed to be preserved after each population doubling. The final cell number at the end of the culture period is represented by *F*.

Supplementary Table S4.1: Accounting of the number of proliferating and resting cells over population doublings

Number of Population doubling (i)	0 @ Day-1	1	2	…	k @ Day-3
Proliferating cells (P_i)	P_0 = m*P%	P_1 = (P_0*2+Q_0)*P%	P_2 = (P_1*2+Q_1)*P%	…	P_k = (P_{k-1}*2+Q_{k-1})*P%
Resting cells (Q_i)	Q_0 = m*Q%	Q_1 = P_1/P%*(1-P%)	Q_2 = P_2/P%*(1-P%)	…	Q_k = P_k/P%*(1-P%)
Sum	m	m*(1+P%)	m*(1+P%)^2		m*(1+P%)^k = F

At the end of culture period, Day-3, the number of proliferating cells (P_k) can also be represented by *F*P%*, the same percentage of proliferating cells in the cell pool. By equating the two expressions of P_k, Equation S4.1 can be obtained.

$$k = \frac{log(\frac{F}{m_0})}{log(1+P\%)} \qquad \textbf{\textit{Equation S4.1}}$$

Chapter 4 − Supplementary Information

Model adjustments made to *iMSC1255*

The following changes were made to iMSC1255 [264].

1. Addition of new reaction

- Addition of the lactate-L exchange reaction via Cobra function addExchangeRxn
- Addition of the reaction LCADi (Lactaldehyde dehydrogenase, h2o[c] + lald---L[c] + nad[c] -> 2 h[c] + lac---L[c] + nadh[c]) via Cobra function addReaction

2. Update of the amino acid exchange flux

The original boundaries of the amino acid exchange fluxes (Table 1 in [1]) were updated, based on the original stoichiometry coefficients, to satisfy the higher growth requirement. The adopted biomass synthesis equation is shown below.

> 0.5056 ala---L[c] + 0.3593 arg---L[c] + 0.2794 asn---L[c] + 0.3526 asp---L[c] + 20.7045 atp[c] + 0.0204 chsterol[c] + 0.039 ctp[c] + 0.0466 cys---L[c] + 0.0132 datp[n] + 0.0094 dctp[n] + 0.0099 dgtp[n] + 0.0131 dttp[n] + 0.2752 g6p[c] + 0.326 gln---L[c] + 0.3859 glu---L[c] + 0.5389 gly[c] + 0.0361 gtp[c] + 20.6508 h2o[c] + 0.1264 his---L[c] + 0.2861 ile---L[c] + 0.5455 leu---L[c] + 0.5921 lys---L[c] + 0.153 met---L[c] + 0.0233 pail-hs[c] + 0.1545 pchol-hs[c] + 0.0554 pe-hs[c] + 0.2595 phe---L[c] + 0.4125 pro---L[c] + 0.0058 ps-hs[c] + 0.3925 ser---L[c] + 0.0175 sphmyln-hs[c] + 0.3127 thr---L[c] + 0.0133 trp---L[c] + 0.1597 tyr---L[c] + 0.0534 utp[c] + 0.3526 val---L[c] + 0.0117 clpn-hs[c] + 0.0029 pglyc-hs[c] -> 20.6508 adp[c] + 20.6508 h[c] + 20.6508 pi[c]

Growth-associated non-essential amino acid uptakes (EX_Lcystin(e), EX_trp_L(e) and EX_ascb(e)) were disabled to avoid uncontrolled disturbance towards simulated growth.

Glutamine uptake was resumed with the upper bound of the exchange flux set to 1 mmol/g-h.

3. Elimination of non-essential reactions

- H2CO3D (carboxylic acid dissociation) and MCD (malonyl-CoA Decarboxylase cytoplasmic) were disabled to eliminate redundant loop in CO2 metabolic pathways;
- HEX7 (hexokinase (D-fructose:ATP)), SBTR (D-sorbitol reductase) and GLCt4 (glucose transport via sodium symport) were disabled to ensure glucose flow was processed via HEX1 (hexokinase (D-glucose:ATP)) and the glycolysis pathway;

- OCOAT1m (3-oxoacid CoA-transferase) was closed to avoid redundant loop at the succinate-CoA node;
- FUMSO3tm, FUMSO4tm and FUMTSULtm were closed to avoid redundant loop at the fumarate node;
- CITtam (citrate transport, mitochondrial) was disabled to avoid redundant loop at the citrate node;
- L_LACt4r (L-lactate reversible transport via sodium symport) and LDH_Lm (L-lactate dehydrogenase in mitochondria) were disabled to avoid redundant loop at the L-lactate node;
- EX_meoh(e), EX_inost(e), EX_sl_L(e) and EX_taur(e) were disabled to prevent the production of irrelevant by-products;

4. Flux direction in pentose phosphate pathway

Flux direction was set to follow the forward direction of the oxidative branch in the pentose phosphate pathway.

5. Insertion of the PRAT constraint

The PRAT constraint shown in the main text was inserted as an extra reaction/constraint to the stoichiometry matrix in *iMSC1255*.

Chapter 4 − Supplementary Information

Experimental results for hMSCs cultured under normoxia and hypoxia

Supplementary Table S4.2: Tabulated experimental results for the hMSCs cultured under 20% oxygen. Growth rate, cell cycle and lactate production data are shown.

		Specific Lactate production (µmol/million cells/hr)	Specific growth rate (hr-1)	PD (hr)	G1 %	S+G2/M)%	Proliferating%
	Set 1	0.77	0.093	17.7	64.3%	35.7%	58.7%
	Set 2	0.77	0.101	16.8	64.3%	35.7%	58.7%
Run 1	Set 3	0.67	0.087	18.3	64.3%	35.7%	58.7%
	Set 4	2.03	0.052	18.2	58.0%	42.0%	66.4%
	Set 5	2.26	0.048	19.0	58.0%	42.0%	66.4%
Run 2	Set 6	1.86	0.036	23.9	58.0%	42.0%	66.4%
	Set 7	2.20	0.072	14.4	58.0%	42.0%	66.4%
	Set 8	1.99	0.062	16.0	58.0%	42.0%	66.4%
Run 3	Set 9	2.19	0.062	16.0	58.0%	42.0%	66.4%
	Set 10	1.98	0.052	28.0	56.1%	43.9%	68.5%
	Set 11	2.06	0.056	27.0	56.1%	43.9%	68.5%
Run 4	Set 12	2.29	0.060	26.1	56.1%	43.9%	68.5%
	Set 13	1.43	0.022	24.9	55.0%	45.0%	69.8%
	Set 14	1.52	0.028	20.6	55.0%	45.0%	69.8%
Run 5	Set 15	1.66	0.027	21.1	55.0%	45.0%	69.8%
	Set 16	1.25	0.087	18.3	59.0%	41.0%	65.2%
	Set 17	1.23	0.084	18.6	59.0%	41.0%	65.2%
	Set 18	1.19	0.092	17.7	59.0%	41.0%	65.2%
	Set 19	1.07	0.091	17.9	59.0%	41.0%	65.2%
Run 6	Set 20	1.09	0.094	17.5	59.0%	41.0%	65.2%
	Set 21	1.13	0.098	14.9	56.0%	44.0%	68.6%
	Set 22	0.95	0.091	14.8	56.0%	44.0%	68.6%
	Set 23	1.16	0.101	14.5	56.0%	44.0%	68.6%
	Set 24	1.08	0.097	14.6	56.0%	44.0%	68.6%
Run 7	Set 25	1.05	0.088	14.0	56.0%	44.0%	68.6%
	Set 26	1.21	0.023	23.4	58.0%	42.0%	66.4%
Run 8	Set 27	0.88	0.028	21.0	58.0%	42.0%	66.4%
	Set 28	1.40	0.083	18.8	59.0%	41.0%	65.2%
	Set 29	1.70	0.087	18.3	59.0%	41.0%	65.2%
Run 9	Set 30	1.62	0.084	18.6	59.0%	41.0%	65.2%
Non-growing cells		0.90	0.000				

Supplementary Table S4.3: Tabulated experimental results for the hMSCs cultured under 1% oxygen. Growth rate, cell cycle and lactate production data are shown.

		Specific Lactate production (µmol/million cells/hr)	Specific growth rate (hr-1)	PD (hr)	G1 %	S+G2/M)%	Proliferating%
	Set 31	1.27	0.0926	17.1	66.5%	33.5%	55.8%
	Set 32	1.42	0.0946	16.9	66.5%	33.5%	55.8%
Run 10	Set 33	1.60	0.0710	20.0	66.5%	33.5%	55.8%
	Set 34	1.92	0.1267	11.0	60.3%	39.7%	63.6%
	Set 35	1.63	0.1299	10.8	60.3%	39.7%	63.6%
Run 11	Set 36	1.82	0.0993	12.8	60.3%	39.7%	63.6%
	Set 37	1.14	0.1117	15.3	67.4%	32.6%	54.6%
	Set 38	1.21	0.1184	14.8	67.4%	32.6%	54.6%
Run 12	Set 39	1.22	0.1205	14.7	67.4%	32.6%	54.6%
	Set 40	4.49	0.1337	16.2	62.0%	38.0%	61.6%
	Set 41	4.20	0.1431	15.8	62.0%	38.0%	61.6%
Run 13	Set 42	4.48	0.1163	17.2	62.0%	38.0%	61.6%
	Set 43	1.07	0.0946	16.9	66.5%	33.5%	55.8%
	Set 44	1.18	0.0710	20.0	66.5%	33.5%	55.8%
	Set 45	0.93	0.0977	16.6	66.5%	33.5%	55.8%
	Set 46	0.84	0.0889	17.5	66.5%	33.5%	55.8%
Run 14	Set 47	1.08	0.0850	17.9	66.5%	33.5%	55.8%
	Set 48	0.21	0.0532	19.9	60.3%	39.7%	63.6%
	Set 49	0.32	0.0475	21.7	60.3%	39.7%	63.6%
Run 15	Set 50	0.29	0.0570	18.9	60.3%	39.7%	63.6%
	Set 51	2.45	0.1247	14.4	67.4%	32.6%	54.6%
	Set 52	2.39	0.1211	14.6	67.4%	32.6%	54.6%
Run 16	Set 53	2.48	0.1125	15.2	67.4%	32.6%	54.6%

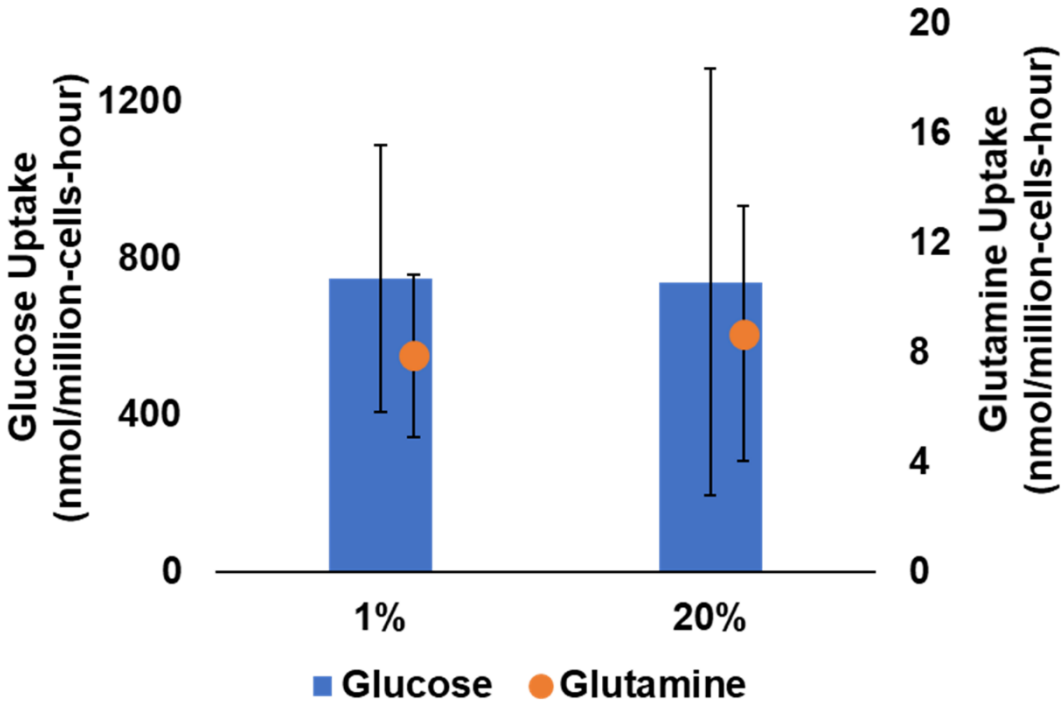

Supplementary Figure S4.1: Experimentally measured average specific glucose and glutamine uptake data under 1% and 20% oxygen culture environment. Glutamine uptake data corresponds to the secondary axis.

Chapter 5A − Supplementary Information

The tabulated FPKM expressions of the detected genes and figures demonstrating sequencing quality

Supplementary Table S5A.1: The FPKM expressions of the detected genes (partial).

Gene ID	Symbol	Day0	Fl-Pr	Fl-Am	Fs-Pr	Fs-Am	TCP
100462981	MTRNR2L2	12303	6151	7034	6139	6496	8449
1277	COL1A1	7846	6206	6507	6104	8943	8809
2335	FN1	7293	7149	7037	15579	14297	8124
100463486	MTRNR2L8	5159	2544	2648	2295	2238	2913
2495	FTH1	4683	7057	7629	8773	8266	6123
9168	TMSB10	3551	4225	4580	4031	4128	4324
7431	VIM	3128	3588	3990	4912	4446	2806
2597	GAPDH	2755	2524	2274	2313	1952	1950
60	ACTB	2451	4527	4473	3382	3441	4177
7178	TPT1	2401	2344	2248	2181	2350	2293
6678	SPARC	2398	1552	1703	1463	1580	1923
1278	COL1A2	2146	1635	1597	1509	1867	2063
7076	TIMP1	2079	1327	1551	1655	1307	876
1915	EEF1A1	2044	1833	1784	1362	1470	1794
302	ANXA2	1970	2227	2364	1829	2076	2233
2512	FTL	1843	1926	1579	1869	1772	1376
5054	SERPINE1	1842	973	839	999	903	1014
6171	RPL41	1699	1486	1667	1369	2047	1525
7045	TGFBI	1636	1003	940	930	858	992
7057	THBS1	1572	1912	1970	235	385	2675
4502	MT2A	1567	1331	1684	2101	1822	733
7114	TMSB4X	1460	1715	1788	1788	2277	1742
3490	IGFBP7	1376	1305	1208	1212	1166	1273
5270	SERPINE2	1340	1216	1119	920	989	1250
6154	RPL26	1249	1406	1799	1277	1478	1516
71	ACTG1	1231	1797	1723	1539	1207	1464
1292	COL6A2	1229	1349	1240	1517	1393	860
6194	RPS6	1207	1235	1469	1075	1250	1413
1291	COL6A1	1192	1215	1172	1483	1430	868
9349	RPL23	1180	1335	1640	1121	1214	1681
100462977	MTRNR2L1	1175	391	403	431	390	424
6229	RPS24	1132	1184	1222	1147	1038	1245
10631	POSTN	1118	1101	1292	719	990	1635
1490	CTGF	1080	838	850	246	324	1168
7169	TPM2	632	1596	1761	913	839	2183

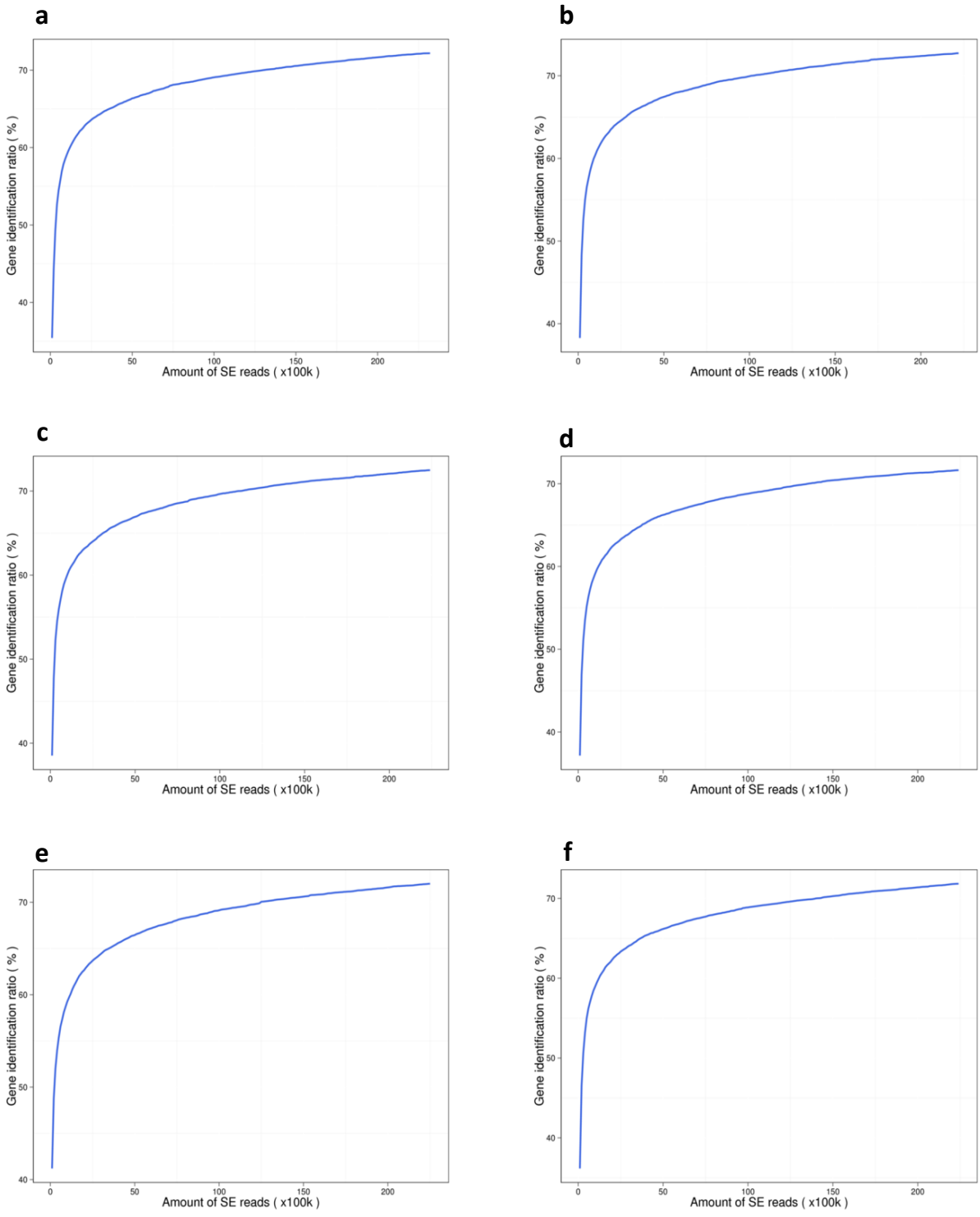

Supplementary Figure S5A.1: Sequencing saturation curves D0 (a), Pr-Fl-PLLA (b), Pr-Fs-PLLA (c), Am-Fl-PLLA (d), Am-Fs-PLLA (e), and TCP (f).

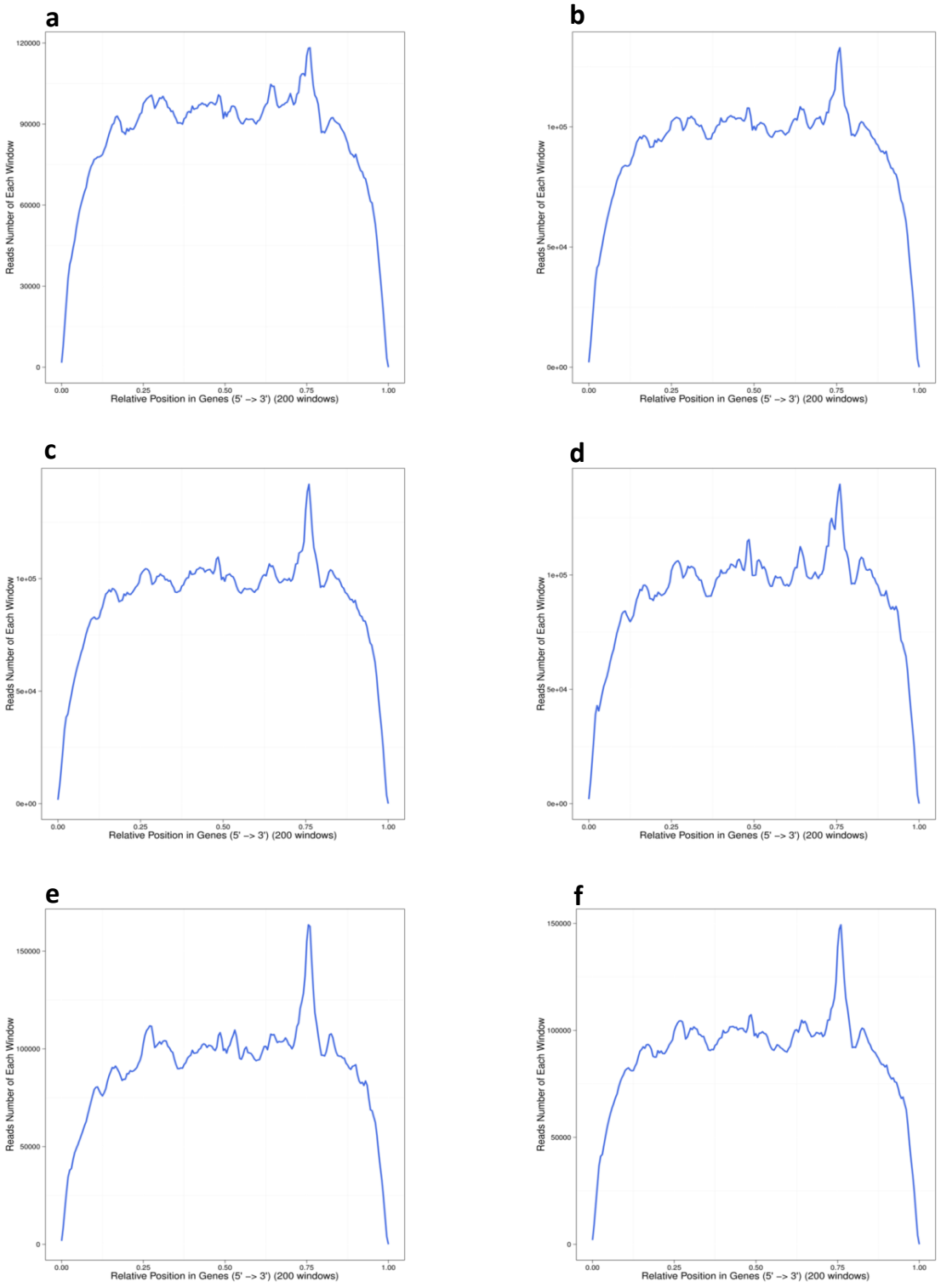

Supplementary Figure S5A.2: Reads distribution on reference genes D0 (a), Pr-Fl-PLLA (b), Pr-Fs-PLLA (c), Am-Fl-PLLA (d), Am-Fs-PLLA (e), and TCP (f).

Chapter 5B − Supplementary Information

Tabulated gene expression values

Supplementary Table S5B.1: The 1,873 detected hypoxia-regulated genes in this study (partial).

Gene ID	Symbol	S1	S2	S3	S4	Control
9249	DHRS3	3.52	3.5	1.09	1.05	9.69
7851	MALL	4.5	2.87	20.36	13.39	1.17
1303	COL12A1	165.72	198	69.96	85.88	415.27
1301	COL11A1	8.7	10.13	3.08	3.22	24.56
9289	GPR56	2.71	2.21	6.21	4.06	0.85
5743	PTGS2	2.88	2.24	6.93	3.68	1.09
5137	PDE1C	23.32	27.68	10.13	12.99	54.15
1294	COL7A1	9.99	7.67	18.11	15.89	3.66
348	APOE	12.53	14.38	2.81	1.83	0.75
22998	LIMCH1	29.8	30.84	8.73	9.14	42.6
22822	PHLDA1	81.41	101	156.92	126.7	28.47
10769	PLK2	29.48	28.61	12.81	13.6	35.24
10763	NES	6.28	6.08	9.03	5.69	2.6
10643	IGF2BP3	0.83	1.06	2.88	1.46	0.26
9708	PCDHGA8	0.8	0.82	1.03	0.78	0.27
9120	SLC16A6	7.29	4.64	8.26	6.07	0.74
9077	DIRAS3	3.44	3.67	2.79	2.63	0.31
9052	GPRC5A	6.46	5.6	1.44	1.22	6.77
8707	B3GALT2	2.84	3.05	0.17	0.05	3.52
8671	SLC4A4	6.65	7	1.85	2.25	6.22
8644	AKR1C3	22.2	21.08	24.21	34.95	5.98
8614	STC2	265.37	269.79	105.28	127.62	315.85
8515	ITGA10	4.81	4.44	4.7	4.85	1.75
8406	SRPX	13.06	11.49	12.09	10.71	5.35
7980	TFPI2	16.54	19.41	16.92	8.67	6.25
7058	THBS2	86.49	79.76	36.69	43.22	164.11
7057	THBS1	1911.5	1969.5	235.37	385.43	2674.92
7052	TGM2	53.87	49.01	25.25	22.14	58.44
7043	TGFB3	4.04	3.87	1.23	1.33	0.96
7042	TGFB2	18.71	21.3	7.12	7.94	24.11
6876	TAGLN	1671.68	1632.9	625.37	676.13	2242.58
6752	SSTR2	2.5	1.53	0.45	0.32	0.11
6696	SPP1	124.8	103.45	108.41	92.3	6.66
6662	SOX9	22.91	21.76	33.57	28.91	8.02

6533	SLC6A6	21.69	19.55	22.12	21.1	7.99
6404	SELPLG	5.02	5.61	2.1	2.3	5.65
6319	SCD	43.87	41.54	43.15	39.4	15.57
6303	SAT1	50.08	49.39	48.51	61.5	19.73
6275	S100A4	4.09	4.29	17.33	11.9	4.93
5997	RGS2	8.13	6.03	7.68	7.11	1.4
5806	PTX3	361.11	357.62	54.66	90.6	497.2
5507	PPP1R3C	44.27	53.58	19.36	24.9	52.9
5332	PLCB4	15.96	17.51	6.37	8.3	20.22
5321	PLA2G4A	7.25	7.62	13.98	13.1	2.95
4982	TNFRSF11B	59.31	57.5	7.41	11.8	81.28
4915	NTRK2	1.3	1.26	0.45	0.5	1.66
4803	NGF	13.13	8.09	4.07	5.4	16.47
4582	MUC1	6.28	6.08	5.44	5.4	15.55
4323	MMP14	578.28	497.12	570.6	523.1	229.72
4082	MARCKS	117.89	112.02	48.84	54.61	119.13
4017	LOXL2	257.91	235.39	113.83	110.2	360.4
4015	LOX	400.48	376.03	140.63	146.0	395.9
3914	LAMB3	6.12	4.87	8.14	7.3	2.27
3855	KRT7	166.05	148.32	25.09	33.1	189.9
3638	INSIG1	35.95	31.16	47.95	45	12.6
3162	HMOX1	179.22	172.32	222.31	194.3	72.6
2354	FOSB	0.76	0.88	2.48	3.6	0.73
2252	FGF7	86.95	106.67	28.13	35.6	166.81
2202	EFEMP1	313.69	301.89	69.36	98.1	526.88
2115	ETV1	3.2	4.02	5.9	4.7	0.55
2034	EPAS1	137.1	135.5	48.2	56.7	214.2
2030	SLC29A1	21.08	17.46	17.8	15.01	4.45
1960	EGR3	4.59	4.11	3.47	3.6	0.58
1958	EGR1	50.45	37.2	61.7	55.2	15.86
1906	EDN1	10.41	9.5	0.56	1.8	9.32
1846	DUSP4	5.02	4.06	7.84	5.91	0.95
1756	DMD	3.76	3.61	1.1	1.64	6.95
1490	CTGF	838.0	849.5	246.45	324.1	1168.5

Supplementary Table S5B.2: The tabulated results of the detected hypoxia-regulated genes involved in the regulation of different cell cycle functions.

Gene ID	Symbol	S1	S2	S3	S4	Control	Involved cell cycle stage/function	
6790	AURKA	15.4	13	5.5	4.7	7.7	M	
4085	MAD2L1	9.4	9	4.8	4.2	3.4	M	
1031	CDKN2C	16.5	12.1	6.5	6.6	7.1		Arrest
990	CDC6	8.1	8.1	5	5.2	3.7	G1	
3838	KPNA2	79.4	65	34.4	40.2	43.4	M	
7040	TGFB1	225.5	211	228	216.9	115.3	M	Arrest
8522	GAS7	1.4	1	1.1	1.3	0.6		Arrest
3624	INHBA	115.2	111.7	80.2	67.9	121.6		Arrest
7057	THBS1	1911.5	1969.5	235.4	385.4	2674.9		Arrest
811	CALR	731.3	820.4	427.7	409.3	651		Arrest
7042	TGFB2	18.7	21.3	7.1	7.9	24.1		Arrest
4088	SMAD3	17.7	17	10.7	12.4	24		Arrest
5311	PKD2	14.9	16.2	10.6	10.9	18.2		Arrest
7046	TGFBR1	13.1	13.4	8.1	9.6	21		Arrest
27352	SGSM3	7.1	5.7	6	5.1	4.7		Arrest
10634	GAS2L1	18.8	16.4	19.3	16	12.9		Arrest
9238	TBRG4	7.7	5.5	5.3	4.6	4.2	G1	Arrest
5536	PPP5C	21.1	20.1	18.9	17.4	13.8	M	
5066	PAM	62	55	68.1	66.7	45.1	M	
1843	DUSP1	27	18.6	13.5	9.9	19.3		Arrest
667	DST	22.2	29.4	49.7	48.8	34.5		Arrest
9221	NOLC1	21	25.3	14.5	13.1	20.6	M	
7157	TP53	15.6	14	8.5	11.5	14.9		Arrest
3592	IL12A	2.2	2.2	1	1.3	1.5		Arrest
1647	GADD45A	52.5	54.9	31.1	58.6	56.1		Arrest
64121	RRAGC	22.9	21.2	22.6	19	20.5		Arrest
58528	RRAGD	1.3	1.3	1.2	1.5	1		Arrest
54962	TIPIN	5.7	6.3	4.7	4.3	4.5	S	
51719	CAB39	14.9	14.5	17.3	15.7	11.9		Arrest
26959	HBP1	23	22.2	21.7	22.9	19.7		Arrest
23645	PPP1R15A	86	84.7	86.2	78.1	86.4		Arrest
23435	TARDBP	24	25.4	20.4	20.4	20.5	M	
25	ABL1	43.5	39.4	32.1	34.8	37.1	S	Arrest

Supplementary Table S5B.3: The 573 detected genes with expressions correlating to that of HIF2A (partial).

Gene ID	Symbol	S1	S2	S3	S4	Control
2495	FTH1	7057.05	7629.03	8772.67	8266.17	6123.25
100463486	MTRNR2L8	2544.2	2648	2295.02	2238.07	2913.06
7431	VIM	3588.39	3990.06	4912.4	4446.4	2806.24
7057	THBS1	1911.5	1969.5	235.37	385.43	2674.92
7168	TPM1	1409.66	1605.05	627.92	716.3	2282.35
6876	TAGLN	1671.68	1632.9	625.37	676.13	2242.58
7169	TPM2	1596.29	1761	913.12	838.65	2182.77
800	CALD1	706.21	807.09	363.53	436.09	1194.83
1490	CTGF	838.02	849.52	246.47	324.15	1168.46
1291	COL6A1	1215.04	1171.82	1482.51	1429.69	868.17
6222	RPS18	716.92	727.4	548.32	544.1	837.48
11167	FSTL1	562.45	588.01	371.41	478.69	748.21
1282	COL4A1	517.6	554.34	264.4	326.01	722.5
26986	PABPC1	636.43	638.72	437.55	430.45	712.6
6144	RPL21	605.79	639.66	490.87	516.74	683.72
618	BCYRN1	255.08	262.61	85.27	93.52	647.56
6136	RPL12	591.05	584.63	482.51	522.49	642.93
6206	RPS12	459.39	510.66	361.41	345.69	578.02
1284	COL4A2	459.28	460.92	270.52	296.6	565.85
2202	EFEMP1	313.69	301.89	69.36	98.13	526.88
8682	PEA15	390.31	406.34	335.23	329.39	499.14
5806	PTX3	361.11	357.62	54.66	90.59	497.16
59	ACTA2	293.08	316.22	83.82	86.74	456.17
87	ACTN1	374.17	367.92	320.55	314.53	434.71
27063	ANKRD1	230.17	266.2	48.54	83.02	400.1
4017	LOXL2	257.91	235.39	113.83	110.23	360.36
301	ANXA1	445.55	472.56	718.23	634.59	342.64
9358	ITGBL1	242.73	266.67	183.67	203.79	321.48
3491	CYR61	290.8	271.96	164.39	176.75	320.68
7077	TIMP2	370.61	378.52	411.04	415.12	316.63
8614	STC2	265.37	269.79	105.28	127.62	315.85
2312	FLG	103.19	126.92	4.91	9.17	292.9
10370	CITED2	204.36	193.91	103.29	116.98	267.04
2034	EPAS1	137.12	135.53	48.25	56.75	214.19
1009	CDH11	173.12	183.6	105.09	116.12	203.56
51474	LIMA1	152.58	168.14	86.92	95.18	199.77
51232	CRIM1	156.69	153.12	46.99	56.44	188.78
1545	CYP1B1	159.03	145.52	106.91	115.99	187.35
595	CCND1	311.97	288.13	468.68	388.61	185.85
6772	STAT1	148.77	147.63	46.39	61.46	184.66
5352	PLOD2	147.79	144.3	89.91	88.11	172.53
10971	YWHAQ	259.32	256.74	348.7	386.69	172.35
2252	FGF7	86.95	106.67	28.13	35.6	166.81

7058	THBS2	86.49	79.76	36.69	43.22	164.11
3159	HMGA1	346.78	319.74	874.38	747.4	160.94
4008	LMO7	114.11	129.12	53.99	71.27	160.69
84624	FNDC1	81.68	104.28	54.65	58.35	155.41
5355	PLP2	219.96	207.13	266.61	240.31	153.59
1266	CNN3	136.52	139.71	107.02	107.93	148.26
23022	PALLD	110.91	111.3	79.45	96.86	142.69
4430	MYO1B	111.22	120.22	72.91	73.69	131.74
960	CD44	185.89	192.57	230.75	226.47	131.69
23576	DDAH1	96.22	92.03	29.95	35.72	127.49
824	CAPN2	157.46	162.93	257.47	254.74	125.93
7296	TXNRD1	96.76	103.36	81.01	76.66	120.28
6510	SLC1A5	91.76	87.62	68.97	72.6	117.78
10979	FERMT2	105.39	110.05	98.52	100.99	115.54
51065	RPS27L	98.72	96.71	80.66	81.53	115.19
7837	PXDN	97.67	91.75	75.3	72.38	115.16
4837	NNMT	90.88	96.03	48.91	54.57	114.83
6897	TARS	87	93.21	67.92	69.21	113.48
55752	40787	96.43	91.26	42.19	46.89	112.06
8878	SQSTM1	177.91	156.62	237.46	217.22	111.96
10577	NPC2	144.88	152.81	171.92	167.28	104.57
54407	SLC38A2	72.3	71.27	52.27	54.01	98.99
968	CD68	172.73	198.85	348.51	307.97	96.21
6741	SSB	77.59	83.14	58.57	62.4	95.52
857	CAV1	136.15	137.79	162.32	174.58	93.84
2273	FHL1	62.19	65.17	21.55	32.53	93.36
441951	ZFAS1	71.23	77.45	52.65	50.93	89.28
2539	G6PD	125.77	106.89	149.03	156.53	84.11
1000	CDH2	69.56	75.05	44.91	52.51	83.7
3958	LGALS3	140.38	130.93	180.35	173.78	82.99
1601	DAB2	66.32	71.38	56.3	58.92	81.8
4982	TNFRSF11B	59.31	57.5	7.41	11.78	81.28
290	ANPEP	126.41	130.11	225.08	216.38	80.18
81502	HM13	99.91	91.94	109.63	111.68	79.81
79827	CLMP	103.54	98.12	137.66	128.28	78.77
1827	RCAN1	47.12	48.01	17.1	19.72	77.11
10983	CCNI	88.38	86.25	107.38	101.1	74.92
54751	FBLIM1	68.68	66.48	54.69	53.29	74.68
9805	SCRN1	27.61	27.95	24.32	25.08	30.46

Supplementary Table S5B.4: The 102 differentially expressed HRGs that involve samples cultured on at least 4 different surfaces.

Gene ID	Symbol	S1	S2	S3	S4	Control
2335	FN1	7148.9	7036.7	15578.7	14297	8124.2
7057	THBS1	1911.5	1969.5	235.4	385.4	2674.9
6876	TAGLN	1671.7	1632.9	625.4	676.1	2242.6
1490	CTGF	838	849.5	246.5	324.2	1168.5
4502	MT2A	1330.9	1684.5	2101.3	1821.8	732.9
2202	EFEMP1	313.7	301.9	69.4	98.1	526.9
5806	PTX3	361.1	357.6	54.7	90.6	497.2
59	ACTA2	293.1	316.2	83.8	86.7	456.2
1303	COL12A1	165.7	198	70	85.9	415.3
4015	LOX	400.5	376	140.6	146	395.9
4017	LOXL2	257.9	235.4	113.8	110.2	360.4
8614	STC2	265.4	269.8	105.3	127.6	315.9
4323	MMP14	578.3	497.1	570.6	523.1	229.7
2034	EPAS1	137.1	135.5	48.3	56.8	214.2
3855	KRT7	166.1	148.3	25.1	33.2	189.9
2252	FGF7	87	106.7	28.1	35.6	166.8
7058	THBS2	86.5	79.8	36.7	43.2	164.1
4082	MARCKS	117.9	112	48.8	54.6	119.1
4982	TNFRSF11B	59.3	57.5	7.4	11.8	81.3
3162	HMOX1	179.2	172.3	222.3	194.3	72.6
7052	TGM2	53.9	49	25.3	22.1	58.4
5137	PDE1C	23.3	27.7	10.1	13	54.2
5507	PPP1R3C	44.3	53.6	19.4	24.9	52.9
4616	GADD45B	44.6	44.2	22.2	25.6	51.6
22998	LIMCH1	29.8	30.8	8.7	9.1	42.6
10769	PLK2	29.5	28.6	12.8	13.6	35.2
6617	SNAPC1	24.8	25.4	10.7	12.9	32.5
5168	ENPP2	28.2	26.6	11.7	15.6	32.1
1382	CRABP2	17.5	21.3	65.1	61.5	31.7
22822	PHLDA1	81.4	101	156.9	126.7	28.5
1052	CEBPD	16.6	14.8	5.6	4.9	27.1
683	BST1	20.6	18.4	5.1	5.5	26.6
1301	COL11A1	8.7	10.1	3.1	3.2	24.6
7412	VCAM1	10.1	13.2	7	10	24.2
7042	TGFB2	18.7	21.3	7.1	7.9	24.1
627	BDNF	21.2	20.2	5.2	6.3	21.5
5332	PLCB4	16	17.5	6.4	8.3	20.2
6303	SAT1	50.1	49.4	48.5	61.5	19.7
182	JAG1	16.1	17.5	8	7.3	16.9
4803	NGF	13.1	8.1	4.1	5.4	16.5
1958	EGR1	50.5	37.2	61.7	55.2	15.9
6319	SCD	43.9	41.5	43.2	39.4	15.6
4582	MUC1	6.3	6.1	5.4	5.4	15.6
11067	C10orf10	12	7.5	6.4	5.4	15.2
104	ADARB1	9.9	9.6	3.5	3.5	12.7
3638	INSIG1	36	31.2	48	45	12.6
991	CDC20	40.8	27.9	7.6	9.5	12.4
5740	PTGIS	5.1	6.1	3.3	3.4	12.1
6347	CCL2	7.9	7.6	3.7	2.8	11.2
133	ADM	11	10.4	2.6	2.5	10.6
9249	DHRS3	3.5	3.5	1.1	1.1	9.7

1906	EDN1	10.4	9.5	0.6	1.8	9.3
6662	SOX9	22.9	21.8	33.6	28.9	8
6533	SLC6A6	21.7	19.6	22.1	21.1	8
6790	AURKA	15.4	13	5.5	4.7	7.7
8519	IFITM1	15.2	14.7	7.3	7.1	7.7
288	ANK3	3.2	3.3	2.4	3.1	7.4
1756	DMD	3.8	3.6	1.1	1.6	7
9052	GPRC5A	6.5	5.6	1.4	1.2	6.8
6696	SPP1	124.8	103.5	108.4	92.3	6.7
7980	TFPI2	16.5	19.4	16.9	8.7	6.3
8671	SLC4A4	6.7	7	1.9	2.3	6.2
8644	AKR1C3	22.2	21.1	24.2	35	6
6404	SELPLG	5	5.6	2.1	2.3	5.7
3161	HMMR	8.7	10	3.7	4.2	5.4
8406	SRPX	13.1	11.5	12.1	10.7	5.4
6275	S100A4	4.1	4.3	17.3	12	4.9
1612	DAPK1	3.2	2.5	1.2	1.7	4.7
10105	PPIF	10.7	9.1	3.5	4.2	4.6
2030	SLC29A1	21.1	17.5	17.8	15.1	4.5
397	ARHGDIB	6.6	6.5	1.4	2.2	4.1
1294	COL7A1	10	7.7	18.1	15.9	3.7
8707	B3GALT2	2.8	3.1	0.2	0.1	3.5
4085	MAD2L1	9.4	9	4.8	4.2	3.4
5228	PGF	5.4	5.9	1.8	1.5	3.2
5321	PLA2G4A	7.3	7.6	14	13.2	3
3983	ABLIM1	1.7	1.7	3.8	3.6	2.9
10763	NES	6.3	6.1	9	5.7	2.6
6546	SLC8A1	3.4	3.4	1.4	1.2	2.5
7804	LRP8	5	4.1	7.5	6	2.4
3914	LAMB3	6.1	4.9	8.1	7.3	2.3
8515	ITGA10	4.8	4.4	4.7	4.9	1.8
1959	EGR2	4	2.3	4.5	3.4	1.7
4915	NTRK2	1.3	1.3	0.5	0.5	1.7
5997	RGS2	8.1	6	7.7	7.1	1.4
7851	MALL	4.5	2.9	20.4	13.4	1.2
5743	PTGS2	2.9	2.2	6.9	3.7	1.1
7043	TGFB3	4	3.9	1.2	1.3	1
1846	DUSP4	5	4.1	7.8	5.9	1
9289	GPR56	2.7	2.2	6.2	4.1	0.9
348	APOE	12.5	14.4	2.8	1.8	0.8
9120	SLC16A6	7.3	4.6	8.3	6.1	0.7
2354	FOSB	0.8	0.9	2.5	3.6	0.7
1960	EGR3	4.6	4.1	3.5	3.7	0.6
8522	GAS7	1.4	1	1.1	1.3	0.6
2115	ETV1	3.2	4	5.9	4.7	0.6
3866	KRT15	1.2	0.9	3.3	2	0.4
9077	DIRAS3	3.4	3.7	2.8	2.6	0.3
9708	PCDHGA8	0.8	0.8	1	0.8	0.3
10643	IGF2BP3	0.8	1.1	2.9	1.5	0.3
4312	MMP1	1.4	0.9	2	1.1	0.1
6752	SSTR2	2.5	1.5	0.5	0.3	0.1

Supplementary Table S5B.5: The 147 HRGs that were correlated with the expression of HIF2A (partial).

Gene ID	Symbol	S1	S2	S3	S4	Control
79572	ATP13A3	34.25	32.88	23.47	22.72	42.69
58494	JAM2	2.85	2.47	0.77	1.44	4.56
26986	PABPC1	636.43	638.72	437.55	430.45	712.6
3241	HPCAL1	25.32	21.35	43.18	37.87	14.35
1266	CNN3	136.52	139.71	107.02	107.93	148.26
404734	ANKHD1-EIF4EBP3	6.19	5.83	7.13	6.86	4.75
8506	CNTNAP1	7.23	7.5	5.22	6.36	9.9
2034	EPAS1	137.12	135.53	48.25	56.75	214.19
6196	RPS6KA2	18.39	18.18	13.01	14.19	24.32
7750	ZMYM2	3.47	3.56	2.73	2.99	3.99
27303	RBMS3	10.27	12.43	4.39	7.06	15.4
3638	INSIG1	35.95	31.16	47.95	45	12.61
2971	GTF3A	55.02	53.3	62.51	60.44	47.46
3914	LAMB3	6.12	4.87	8.14	7.26	2.27
9188	DDX21	35.67	36.61	31.65	28.74	40.9
1294	COL7A1	9.99	7.67	18.11	15.89	3.66
23022	PALLD	110.91	111.3	79.45	96.86	142.69
6347	CCL2	7.92	7.6	3.71	2.78	11.2
23002	DAAM1	2.84	2.76	2.42	2.47	3.34
6038	RNASE4	6.72	7.13	10.42	8.74	4.68
6617	SNAPC1	24.79	25.41	10.69	12.91	32.51
7057	THBS1	1911.5	1969.5	235.37	385.43	2674.92
5836	PYGL	18.18	21.23	11.05	10.98	25.3
1282	COL4A1	517.6	554.34	264.4	326.01	722.5
10370	CITED2	204.36	193.91	103.29	116.98	267.04
56034	PDGFC	37.26	35.82	51.29	48.39	27.84
9877	ZC3H11A	25.43	25	23.83	24.15	27.61
1316	KLF6	42.58	37.5	51.46	54.33	26.47
132	ADK	20.67	20.88	27.75	24.27	16.52
3556	IL1RAP	3.42	3	2.46	2.51	4.39
1545	CYP1B1	159.03	145.52	106.91	115.99	187.35
84706	GPT2	6.12	6.66	4.43	4.6	8.52
22998	LIMCH1	29.8	30.84	8.73	9.14	42.6
1052	CEBPD	16.56	14.8	5.57	4.9	27.1
22822	PHLDA1	81.41	101	156.92	126.7	28.47
8496	PPFIBP1	23.08	22.54	29.67	26.67	14.54
54751	FBLIM1	68.68	66.48	54.69	53.29	74.68
5074	PAWR	22.31	25.8	15.87	13.3	34.1
8614	STC2	265.37	269.79	105.28	127.62	315.85
10687	PNMA2	6.72	6.33	5.78	6.04	7.14
51232	CRIM1	156.69	153.12	46.99	56.44	188.78
3953	LEPR	8.13	7.49	4.85	4.59	10.8
6206	RPS12	459.39	510.66	361.41	345.69	578.02
6662	SOX9	22.91	21.76	33.57	28.91	8.02
523	ATP6V1A	20.07	19.31	22.35	23.18	16.44
595	CCND1	311.97	288.13	468.68	388.61	185.85
6996	TDG	7.39	7.39	6.5	6.32	9.26
862	RUNX1T1	1.48	1.52	1.28	1.24	1.88
55689	YEATS2	9.03	9.25	8.47	8.46	9.58
2296	FOXC1	10.85	9.6	5.47	6.25	12.73
7837	PXDN	97.67	91.75	75.3	72.38	115.16

5587	PRKD1	12.15	12.01	6.45	7.77	14.7
2202	EFEMP1	313.69	301.89	69.36	98.13	526.88
4915	NTRK2	1.3	1.26	0.45	0.51	1.66
1284	COL4A2	459.28	460.92	270.52	296.6	565.85
5137	PDE1C	23.32	27.68	10.13	12.99	54.15
5886	RAD23A	84.5	79.32	109.68	110.17	72.14
25816	TNFAIP8	8.21	7.83	9.97	10.28	6.52
7077	TIMP2	370.61	378.52	411.04	415.12	316.63
10971	YWHAQ	259.32	256.74	348.7	386.69	172.35
2246	FGF1	6.46	6.57	12.74	11.36	4.56
10395	DLC1	27.14	26.38	16.09	19.39	35.55
1490	CTGF	838.02	849.52	246.47	324.15	1168.46
10769	PLK2	29.48	28.61	12.81	13.6	35.24
5321	PLA2G4A	7.25	7.62	13.98	13.15	2.95
6400	SEL1L	26.58	27.72	21.65	21.2	33.51
7058	THBS2	86.49	79.76	36.69	43.22	164.11
54680	ZNHIT6	4.81	4.8	3.86	3.57	5.5
54541	DDIT4	22.1	20.91	15.39	14.78	30.27
90102	PHLDB2	12.17	13.11	8	7.97	17.45
57198	ATP8B2	31.7	30.14	35.01	35.16	25.22
5723	PSPH	5.44	5.56	3.11	3.53	6.44
6272	SORT1	12.73	13.23	8.32	8.34	17.15
3856	KRT8	1.45	1.78	0.88	1.06	2.27
4141	MARS	44.09	44.95	36.96	33.84	52.13
2969	GTF2I	40.63	40.63	37.21	36.38	44.15
57606	SLAIN2	14.39	14.51	15.96	15.8	12.85
10213	PSMD14	25.36	28.12	33.47	30.76	22.4
9747	FAM115A	37.39	43.71	27.39	28.73	53.74
5806	PTX3	361.11	357.62	54.66	90.59	497.16
23034	SAMD4A	10.17	10.52	6.58	7.18	11.74
5352	PLOD2	147.79	144.3	89.91	88.11	172.53
10983	CCNI	88.38	86.25	107.38	101.1	74.92
55107	ANO1	3.52	3.05	5.82	4.75	1.28
11057	ABHD2	19.95	18.19	35.53	29.7	11.05
79134	TMEM185B	6.69	6.5	7.45	7.07	5.45
6446	SGK1	17.54	15.81	12.12	13.09	19.78
3516	RBPJ	25.88	24.37	42.04	36.4	18.54
1612	DAPK1	3.2	2.46	1.22	1.73	4.7
801	CALM1	70.14	67.89	77.33	74.19	64.56
5376	PMP22	67.82	65.75	92.06	87.48	45.46
6713	SQLE	24.04	23.45	33.16	30.37	13.42
2495	FTH1	7057.05	7629.03	8772.67	8266.17	6123.25
2317	FLNB	53.18	54.96	29.94	34.46	74.31
1756	DMD	3.76	3.61	1.1	1.64	6.95
6876	TAGLN	1671.68	1632.9	625.37	676.13	2242.58
9886	RHOBTB1	3.55	3.74	2.71	2.67	5.15
2026	ENO2	13.85	11.16	20.49	19.78	9.2
152503	SH3D19	21.96	22.38	24.12	24.83	20.69
22930	RAB3GAP1	22.7	24.34	19.18	19.3	26.4
59	ACTA2	293.08	316.22	83.82	86.74	456.17
9555	H2AFY	49.03	49.69	58.21	61.29	38.65
2247	FGF2	31.45	33.39	20.84	23.53	45.58
219	ALDH1B1	21.16	20.56	12.11	12.14	33.3

Supplementary Table S5B.6: The 24 genes that were reported on hMSCs surface transcriptome that were correlated with the expression of HIF2A.

Gene ID	Symbol	S1	S2	S3	S4	Control
4059	BCAM	4.48	4.22	1.84	2.46	5.49
6510	SLC1A5	91.76	87.62	68.97	72.6	117.78
79827	CLMP	103.54	98.12	137.66	128.28	78.77
290	ANPEP	126.41	130.11	225.08	216.38	80.18
4883	NPR3	51.47	54.18	25.45	24.31	67.67
6641	SNTB1	6.6	6.39	3.81	4.76	8.76
140885	SIRPA	35.28	39.6	24.91	25.77	46.17
10857	PGRMC1	35.78	34.46	38.94	37.62	29.38
3672	ITGA1	2.62	3.23	1.17	1.71	4.25
3958	LGALS3	140.38	130.93	180.35	173.78	82.99
135228	CD109	20.42	20.54	36.55	33.93	12.85
5355	PLP2	219.96	207.13	266.61	240.31	153.59
4008	LMO7	114.11	129.12	53.99	71.27	160.69
10424	PGRMC2	34.49	32.74	18.36	22.43	40.78
4045	LSAMP	1.57	1.51	0.31	0.22	2.06
1009	CDH11	173.12	183.6	105.09	116.12	203.56
8140	SLC7A5	43.83	38.05	23.05	22.25	50.92
961	CD47	9.08	8.55	12.28	10.7	6.98
81502	HM13	99.91	91.94	109.63	111.68	79.81
1291	COL6A1	1215.04	1171.82	1482.51	1429.69	868.17
7046	TGFBR1	13.12	13.42	8.11	9.57	21.02
960	CD44	185.89	192.57	230.75	226.47	131.69
5817	PVR	28.3	26.21	19.65	17.44	33.21
1000	CDH2	69.56	75.05	44.91	52.51	83.7

Chapter 5C − Supplementary Information

Tabulated gene expression values

Supplementary Table S5C.1: The expression for the compiled 177 hMSCs biomarkers identified in the literature (partial).

Gene ID	Gene Name	D0	Fl-Pr	Fl-Am	Fs-Pr	Fs-Am	TCP	Average	normalized stdev
25923	ATL3	27	23	24	24	22	22	23	0.05
3916	LAMP1	196	188	194	203	194	177	191	0.05
5796	PTPRK	30	26	26	26	23	27	25	0.05
6717	SRI	26	29	25	26	28	27	27	0.06
1500	CTNND1	24	33	33	30	35	31	33	0.06
10082	GPC6	15	9	9	9	8	8	9	0.06
7045	TGFBI	1636	1003	940	930	858	992	945	0.06
23114	NFASC	22	24	25	27	27	28	26	0.06
51566	ARMCX3	24	33	31	32	31	28	31	0.06
4179	CD46	21	17	15	16	16	14	15	0.06
64778	FNDC3B	62	48	51	49	46	55	50	0.07
11171	STRAP	72	70	66	62	58	62	64	0.07
8910	SGCE	11	11	11	9	11	10	11	0.07
781	CACNA2D1	13	12	12	13	12	14	12	0.07
6443	SGCB	30	31	32	28	28	28	29	0.07
3688	ITGB1	810	788	802	943	835	820	837	0.07
3105	HLA-A	261	239	205	220	199	205	213	0.08
9217	VAPB	9	9	10	8	9	9	9	0.08
7416	VDAC1	102	111	119	120	107	99	111	0.08
23180	RFTN1	19	24	24	23	20	21	22	0.08
118429	ANTXR2	16	13	14	15	14	13	14	0.08
55161	TMEM33	5	4	4	4	4	4	4	0.08
27020	NPTN	100	98	109	97	113	92	102	0.09
9218	VAPA	17	16	17	19	15	16	17	0.09
79188	TMEM43	45	34	33	27	31	33	32	0.09
481	ATP1B1	9	10	11	11	12	11	11	0.09
3728	JUP	3	5	5	4	5	5	5	0.09
950	SCARB2	59	54	54	50	49	43	50	0.09
80856	KIAA1715	13	12	11	13	11	10	11	0.09
3068	HDGF	84	112	124	112	130	103	116	0.09
10134	BCAP31	60	70	64	60	69	56	64	0.10
6645	SNTB2	5	5	5	5	5	4	5	0.10
8826	IQGAP1	80	74	81	92	89	76	83	0.10
3106	HLA-B	54	45	42	45	51	39	45	0.10
4267	CD99	403	573	708	644	646	545	623	0.10
10491	CRTAP	31	33	32	30	28	25	30	0.10
10857	PGRMC1	28	36	34	39	38	29	35	0.10
257194	NEGR1	9	11	11	11	8	9	10	0.11
9902	MRC2	100	109	84	94	95	84	93	0.11
4882	NPR2	7	8	8	6	6	8	7	0.11

Supplementary Table S5C.2: The 20 genes with high correlation with CD90 and/or CD105.

								Pearson coefficient	
Gene ID	**Gene Name**	**D0**	**Fl-Pr**	**Fl-Am**	**Fs-Pr**	**Fs-Am**	**TCP**	**with THY1**	**with ENG**
8826	IQGAP1	80.3	73.6	81.0	92.1	89.4	76.5	***-0.92***	***-0.89***
4882	NPR2	7.5	8.1	7.6	6.4	6.3	7.6	***0.98***	***0.93***
214	ALCAM	118.6	131.0	138.7	94.5	96.6	122.5	***0.97***	***0.94***
2022	ENG	169.3	220.3	208.6	148.5	148.2	198.2	***0.92***	***1.00***
83700	JAM3	20.9	21.9	20.3	13.9	15.4	18.3	***0.96***	***0.81***
57136	APMAP	35.2	38.4	35.7	24.7	25.8	28.1	***0.91***	***0.77***
102	ADAM10	42.5	44.2	42.9	28.4	31.5	46.6	***0.93***	***0.85***
4035	LRP1	134.8	122.4	121.1	190.2	186.2	157.7	***-0.97***	***-0.85***
9761	MLEC	19.5	24.8	24.6	16.4	15.6	18.9	***0.90***	***0.91***
286410	ATP11C	9.8	8.4	9.8	5.5	5.4	8.4	***0.91***	***0.70***
5754	PTK7	19.3	20.6	16.5	11.3	11.4	18.5	***0.93***	***0.80***
3383	ICAM1	1.2	1.9	1.6	1.0	1.0	1.4	***0.90***	***0.98***
57153	SLC44A2	29.9	39.2	35.2	19.3	20.4	36.5	***0.96***	***0.97***
493	ATP2B4	68.6	41.6	43.3	82.0	74.2	48.6	***-0.89***	***-0.98***
5819	PVRL2	17.7	22.6	17.7	9.4	9.1	16.9	***0.97***	***0.90***
2335	FN1	7292.7	7148.9	7036.7	15578.7	14296.8	8124.2	***-0.98***	***-0.84***
23670	TMEM2	5.5	9.1	8.8	3.3	4.1	7.5	***0.92***	***0.99***
928	CD9	61.6	26.7	29.9	59.7	83.1	25.3	***-0.79***	***-0.92***
1969	EPHA2	6.2	8.9	6.5	1.8	1.9	6.3	***0.98***	***0.92***
3690	ITGB3	10.7	5.6	5.4	17.8	13.9	3.3	***-0.86***	***-0.91***
7070	THY1	156.2	184.9	175.1	73.2	77.0	150.3		
2022	ENG	169.3	220.3	208.6	148.5	148.2	198.2		

Scholarships and Awards

I have received the following scholarships and awards during my D.Phil.

CRMI D.Phil. scholarship (2016-2019)

Canadian Imperial Bank of Commerce Scholarship (2018)

Salters' Institute Centenary Award (2017)

Thomas Hogg Overseas Scholarship (2017)

Thomas Hogg Overseas Scholarship (2016)

List of Publications

- Brinkhof, B., **Zhang, B.**, Cui, ZF., Ye, H., Wang, H. (Submitted – March 2019). ALCAM (CD166) as a MSC gene expression marker for Improving Mesenchymal Stromal Cell Characterization. *Stem Cells International*.

- **Zhang, B. (*)**, Kasoju, N. (*), Li, Q. (*), Soliman, S., Yang, A., Cui, ZF., Ma, JM., Wang, H., Ye, H. (2019). Using Culture Surfaces to Regulate Hypoxia-Related Genes in Human Mesenchymal Stromal Cells. *Biomedical Materials.*

- **Zhang, B. (*)**, Kasoju, N. (*), Li, Q. (*), Yang, A., Cui, ZF., Ma, JM., Wang, H., Ye, H. (2019). Effect of Substrate Topography and Chemistry on Human Mesenchymal Stem Cell Markers: A Transcriptome Study. *International Journal of Stem Cells.*

- **Zhang, B. (*)**, Ye, H., Yang, A. (2018). Mathematical Modelling of Interacting Mechanisms for Hypoxia Mediated Cell Cycle Commitment for Mesenchymal Stromal Cells. *BMC Systems Biology*.

- Li, Q. (*), **Zhang, B. (*)**, Kasoju, N. (*), Ma, J. (*), Yang, A., Cui, Z., Wang, Hui., Ye, H. (2018). Differential and interactive effects of substrate topography and chemistry on human mesenchymal stem cell gene expression. *International Journal of Molecular Sciences*.

- Firth, A., **Zhang, B**., Yang. A (2018). Quantification of Global Waste Heat and Its Environmental Effects. *Applied Energy.*

- Brinkhof, B., Jia. H., **Zhang. B.**, Cui. ZF., Ye, H., Wang, H. (2018) Improving characterisation of human Multipotent Stromal Cells cultured in 2D and 3D: Design and evaluation of primer sets for accurate gene expression normalisation. *PLOS ONE.*

- Kasoju, N., Wang, H., **Zhang, B.**, George, J., Gao, S., Triffitt, J. T., Cui, ZF., Ye, H. (2017). Transcriptomics of Human Multipotent Mesenchymal Stromal Cells: Retrospective Analysis and Future Prospects. *Biotechnology Advances*.

Papers in preparation:

- Analysis of changes in metabolic profiles of human Mesenchymal stromal cells in different growth regimes

- The effect of hypoxia on the growth of human Mesenchymal stromal cells

- Investigating the differential hypoxic response between human dermal-derived fibroblast and human Mesenchymal stromal cells using RNA sequencing

Conference Posters

Poster 1 - “5th World Congress of Tissue Engineering and Regenerative Medicine International Society”, Kyoto, Japan, Sep 2018.

Differential and Interactive Effects of Substrate Topography and Chemistry on Human Mesenchymal Stem Cell Gene Expression

Bo Zhang[1,3†], Naresh Kasoju[1,†], Qiongfang Li[2,†], Jinmin Ma[2,†], Aidong Yang[3], Zhanfeng Cui[1], Hui Wang[1,2,4,*], and Hua Ye[1,*]

[1]Institute of Biomedical Engineering, Department of Engineering Science, University of Oxford, Oxford, United Kingdom; [2] China National GeneBank-Shenzhen, BGI-Shenzhen, Shenzhen, China; [3] Department of Engineering Science, University of Oxford, Oxford, United Kingdom; [4]Oxford Suzhou Centre for Advanced Research, Suzhou Industrial Park, Jiangsu, China; [†]These authors contributed equally to the paper.

Background

- Human Mesenchymal stem/stromal cells hold therapeutic potential for tissue regeneration, modulating innate and adaptive immune responses, facilitating neovascularization, etc.
- The material used for hMSCs culture was found to affect many cellular processes such as cell adhesion, growth, metabolism, and differentiation.
- The detailed mechanisms of how the topography and chemistry of the culture surface alter the molecular responses of hMSCs remains to be elucidated.
- RNA-sequencing (RNA-seq) is able to explore the whole transcriptome of the studied cells and quantitatively report the gene expression profile.

Experimental Setup

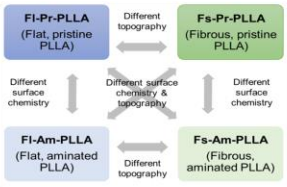

Cell culture: hMSCs obtained from a commercial cell line were cultured for 7 days with media (DMEM) containing 10% serum.

Culture surfaces: Four surfaces were synthesized with poly-L-lactide based substrates into 2 types of topography (electrospun fibrous [Fs] or flat-pressed [Fl]) and 2 types of surface chemistry (with [Am] or without [Pr] aminolysis treatment). 6-well plates were used as the control surface.

RNA- sequencing: The sequencing platform of BGISeq-500 was used to generate a read length of 100-bp. Differentially expressed genes (DEGs) were considered with the pairwise expression ratio >2 and the false discovery rate < 0.001.

Results

1. Material Characterization and Cell Growth

- Cells showed the slowest growth rate in the Fs samples compared to the Fl and control samples.
- Surface chemistry did not significantly impact growth rate.

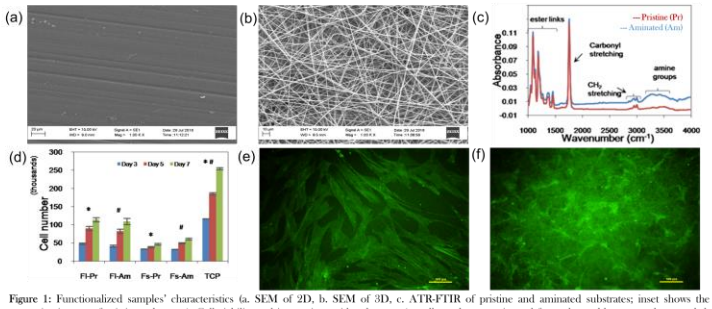

Figure 1: Functionalized samples' characteristics (a. SEM of 2D, b. SEM of 3D, c. ATR-FTIR of pristine and aminated substrates; inset shows the respective images of pristine substrates). Cell viability and interactions with substrates (a. cell number as estimated from alamar blue assay, d., e., and d. CLSM images of phalloidin stained MSCs growing on Fl and Fs substrates respectively). TCP: Tissue culture plate, control sample.

2. Overall Gene Expressions

- The overall gene expression profiles showed the greatest transcriptome variation was induced by surface topography (Fs VS Fl samples).
- Surface chemical treatment induced minimal transcriptomic changes.

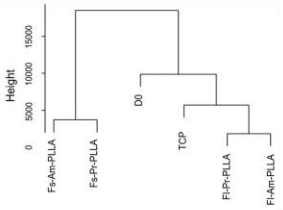

Figure 2: Unsupervised hierarchical clustering dendrogram: Relative sample similarities are represented by the difference in “Height” along the y-axis. Samples or sample groups with greater similarities are arranged under the same hierarchy clades. D0: Day 0 cells prior to seeding.

3. Common Vs Differentially Expressed Genes (DEGs)

- Over 80% of the genes were detected in all samples. The number of commonly expressed and unique genes varies between samples (pairs).
- Among the DEGs induced by surface topography, the change in surface chemistry was able to mitigate or reverse the induced change in expression levels.
- Fibrous surfaces significantly altered several key differentiation markers.

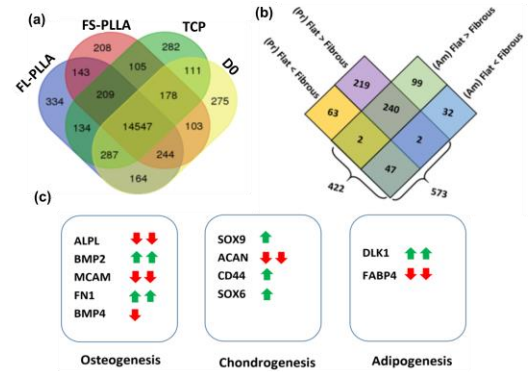

Figure 3: The number of common genes detected in different samples (a). The common genes in the samples with or without chemistry treatment were extracted for the Fl and Fs samples, which were then compared to the D0, and the Control sample. (b) The combined effect of surface topography and surface chemistry. The number of differentially upregulated(>) and downregulated(<) genes in each pairwise comparison is shown. (c) Differences in expression of key differentiation markers observed in the Fs samples compared to the Fl samples. One arrow labels fold changes < 1.75 and two arrows label fold changes > 1.75.

4. Gene Ontology – Cellular Functions

- The majority of the DEGs were associated with cellular biogenesis, metabolism, binding, and organelle functions.

		DEG number			
		Fl-Fs downregulation		Fl-Fs upregulation	
	GO function	Am	Pr	Am	Pr
Biological Functions (Top10)	Cellular process	221	324	48	64
	Metabolic process	148	216	30	38
	Biological regulation	131	193	31	39
	Regulation of biological process	116	169	27	32
	Developmental process	107	151	23	32
	Signaling	97	147	21	34
	Cellular component organization or biogenesis	88	115	16	20
	Response to stimulus	74	108	20	25
	Localization	74	95	15	18
	Signaling process	60	87	11	15
Cellular Component	Cell	261	373	57	82
	Cell part	261	373	57	82
	Organelle	149	225	34	51
	Organelle part	76	123	11	24
	Macromolecular complex	51	59	7	14
	Extracellular region	43	53	12	14
	Extracellular region part	43	53	12	13
	Membrane-enclosed lumen	27	43	4	6
	Synapse	2	3	0	0
Molecular Function	Binding	228	324	51	68
	Catalytic activity	87	131	15	17
	Molecular transducer activity	39	62	5	11
	Enzyme regulator activity	18	24	6	7
	Antioxidant activity	0	2	1	1
	Channel regulator activity	0	2	0	0

Figure 4: Gene ontology analysis for the DEGs. DEGs associated with biological processes (only top 10 are shown), cellular components, and molecular function were grouped and counted.

Conclusions

1. The influence of surface topography was much more influential on regulating cell growth rate, and gene expressions than the chemistry treatments.
2. Surface chemistry and topography were found to have imposed their effects on the gene expression profiles interactively.
3. These findings offer an enriched understanding of the impact of culture surface properties on hMSCs gene expression and facilitate advanced planning when engineering in vitro culture materials for hMSCs.

Results presented in this poster are accepted for publication in International Journal of Molecular Sciences, 2018, Volume 19, special issue: “Cell-Biomaterial Interaction”.

Acknowledgements

The authors are grateful to the financial support from China Regenerative Medicine International (CRMI) Limited. The authors would also like to thank Dr. Julian George and Dr. Michelle Kümin from the University of Oxford for their valuable input.

Poster 2 - “Tissue Engineering and Regenerative Medicine International Society - EU Meeting”, Davos, Switzerland, Jun 2017.

Mathematical Modelling of Interacting Mechanisms for Hypoxia Mediated Cell Cycle Commitment

Bo Zhang [1,2], Aidong Yang [1], Hua Ye [2]
[1] Department of Engineering Science, University of Oxford
[2] Institute of Biomedical Engineering, Department of Engineering Science, University of Oxford
Email: bo.zhang@eng.ox.ac.uk

UNIVERSITY OF OXFORD

ABSTRACT

Currently, there lacks a mechanistic model to determine the optimal oxygen level for maximising *in vitro* cell proliferation. On the other hand, experimental data has shown contrasting observations on how hypoxia affects the proliferation of human mesenchymal stromal cells (hMSCs). In this work, a comprehensive, single-cell mathematical model combining cellular oxygen sensing with hypoxia-mediated cell cycle progression has been constructed to predict cell cycle commitment. With oxygen levels defined for *in vitro* cell culture, the model predicts enhanced proliferation under intermediate (2-8%) and mild (8-15%) hypoxia and cell quiescence under severe (<2%) hypoxia. Global sensitivity analysis and quasi-Monte Carlo simulation revealed that within a certain range (+/-50%), model parameters affect (with varying significance) the minimum commitment time, but not the optimal oxygen tension. It appears that Hif2α counteracts Hif1α and ROS-mediated protein deactivation under intermediate hypoxia and normoxia (20%), respectively, to regulate the response of cell cycle commitment to oxygen tension. Overall, this modelling study offered an integrative framework to capture several interacting mechanisms and allowed *in silico* analysis of their individual and collective roles in shaping hypoxia-mediated commitment to cell cycle. The model qualitatively reconciles existing experimental observations from different studies, and warrants future extension and dedicated experimental validation.

INTRODUCTION

In vitro expansion of adult stem cells has received growing interest crediting it's potential in the fields of regenerative medicine and tissue engineering. Different culture conditions (i.e., hypoxia) have been studied to enhance cell growth. However, in the literature, controversial results have been reported on the effect of hypoxia in regulating stem cell proliferation. Different ranges of *in vitro* oxygen tension have been referred to as hypoxia. Additionally, the distinction between *in vivo* and *in vitro* hypoxia further contribute to the ambiguity and the controversy [1].

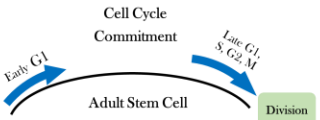

As a part of the integrative effort to enhance bioreactor culture efficiency, this study constructed a mechanistic model in reflecting how a change in *in vitro* oxygen condition affects the rate of cell cycle commitment. Protein interactions between two major hypoxia-induced factors (Hif1α & Hif2α) [2] and higher oxygen-mediated reactive oxygen species (ROS) with cell cycle regulators were made. The time required for cell cycle commitment (in late G1 phase) was simulated, beyond which the completion of cell cycle is imminent.

MODEL OVERVIEW

The model was constructed from 13 ODEs and 3 correlation equations. First order Hill functions and kinetics rate equations were used. Parameter values were acquired or estimated based on literature findings or from comparable cell types.

Selected model equations:

$$[HIF1\alpha] = m_1 * exp\,(b_1 * (1 - abs\,(p_1 - [O_2])\,/\,t_1))$$

$$\frac{d[E2F]}{dt} = m_{E2F} * \frac{[MYC]}{[MYC]+k_{13}} * \frac{[E2F]}{[E2F]+kr13} + m_{E2F} * \frac{[MYC]}{[MYC]+kE_{2F}} + m_{E2F} * \varepsilon * \frac{[HIF2\alpha-Myc]}{[HIF2\alpha-Myc]+k_{13}} * \frac{[E2F]}{[E2F]+kr13} + m_{E2F} * \frac{[HIF2\alpha-Myc]}{[HIF2\alpha-Myc]+kE_{2F}} + m_{E2F\text{-}RbP} * \frac{[E2F-RB]+([cycD]+[cycD-p21/p27])}{[E2F-RB]+kE_{2F\text{-}RbP}} - k_8 * [RB] * [E2F] - d_{E2F} * [E2F] * DEG$$

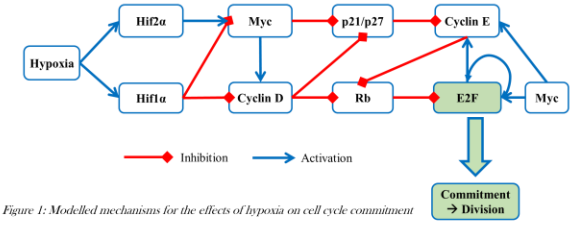

Figure 1: Modelled mechanisms for the effects of hypoxia on cell cycle commitment

RESULTS

Cell Cycle Regulators

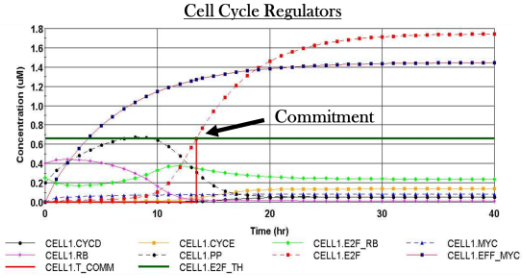

Figure 2: Simulated variation of selected cell cycle regulators under 2% oxygen. E2F threshold level is shown as the horizontal green line. Cell cycle commitment is achieved when E2F threshold is met.

- Cell cycle commitment occurs after 14.3 hours under 2% oxygen.
- Captured time-dependent variations and steady state concentrations of key cell cycle regulators.
- Novel approaches may be designed to facilitate cell growth by alleviating rate limiting factors.

Commitment Time Vs Oxygen Tensions

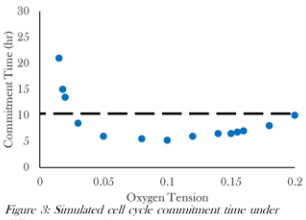

Figure 3: Simulated cell cycle commitment time under different oxygen tensions

- Simulation results show prolonged cell cycle commitment under severe hypoxia.
- Mild hypoxia enables the quickest cell cycle commitment.
- An optimal range of oxygen tension exists for promoting *in vitro* proliferation.

Global Sensitivity Analysis & Quasi Monte Carlo Analysis

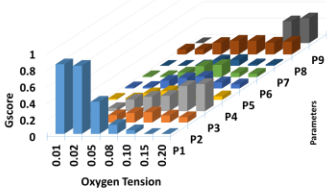

Figure 4: DGSA simulation on the effect of ROS-mediated protein deactivation and HIF2α

Derivative-based global sensitivity analysis (DGSA) [3] highlights the relative significance of individual parameters under different severities of hypoxia.

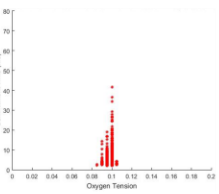

Figure 5: QMC simulation results demonstrate model robustness

Quasi-Monte Carlo (QMC) analysis shows the quickest cell cycle commitment predominantly falls under a narrow range of oxygen tensions over 39,000 simulations.

HIF2α VS (HIF1α and ROS)

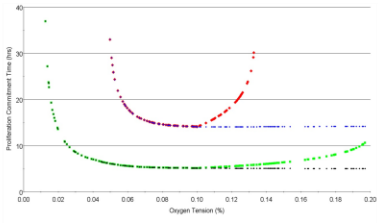

Figure 6: The effects of ROS-mediated protein deactivation and HIF2α on oxygen dependent cell cycle commitment

- HIF2α antagonistically regulates cell cycle commitment with HIF1α and ROS.
- Under severe hypoxia, HIF1α exhibits dominant effect in inducing cell cycle arrest.
- ROS-mediated protein deactivation/degradation prolongs cell cycle commitment under normoxia.

CONCLUSIONS

1. A mathematical model was established to represent the time required for cell cycle commitment under different severities of hypoxia.
2. The simulation results offer reconciliation of the seemingly controversial observations on how hypoxia affects cell proliferation.
3. Fastest cell cycle commitment predominantly occurs under a narrow range of oxygen tensions
4. QMC and DGSA analysis demonstrated model robustness and prioritized parameters for experimental validations.

This work is a part of an integrative effort to improve *in vitro* culture efficiency and establish an optimized bioreactor control strategy for *in vitro* culturing of hMSCs. Future work will incorporate other culture parameters into the existing model and design and utilize a complete set of data for model calibration and validation.

REFERENCES

[1] Ivanovic Z. Hypoxia or in situ normoxia: The stem cell paradigm. Journal of cellular physiology. 2009;219(2):271-5.
[2] Koh MY, Lemos R, Liu X, Powis G. The hypoxia-associated factor switches cells from HIF-1α- to HIF-2α-dependent signaling promoting stem cell characteristics, aggressive tumor growth and invasion. Cancer research. 2011;71(11):4015-27.
[3] Kucherenko S, Rodriguez-Fernandez M, Pantelides C, Shah N. Monte Carlo evaluation of derivative-based global sensitivity measures. Reliability Engineering & System Safety. 2009;94(7):1135-48.

ACKNOWLEDGEMENTS

The authors are grateful to the financial support from China Regenerative Medicine International (CRMI) Limited.

References

1. Caplan, A.I., *Mesenchymal stem cells.* Journal of orthopaedic research, 1991. **9**(5): p. 641-650.
2. U.S. National Institutes of Health, U.S.N.L.o.M. 2019 [cited 2019 May 2].
3. Pittenger, M.F., et al., *Multilineage potential of adult human mesenchymal stem cells.* science, 1999. **284**(5411): p. 143-147.
4. Thirumala, S., W.S. Goebel, and E.J. Woods, *Manufacturing and banking of mesenchymal stem cells.* Expert opinion on biological therapy, 2013. **13**(5): p. 673-691.
5. Abdollahi, H., et al., *The role of hypoxia in stem cell differentiation and therapeutics.* Journal of Surgical Research, 2011. **165**(1): p. 112-117.
6. Brooke, G., et al. *Therapeutic applications of mesenchymal stromal cells*. in *Seminars in cell & developmental biology*. 2007. Elsevier.
7. Carrancio, S., et al., *Optimization of mesenchymal stem cell expansion procedures by cell separation and culture conditions modification.* Experimental hematology, 2008. **36**(8): p. 1014-1021.
8. Sotiropoulou, P.A., et al., *Characterization of the optimal culture conditions for clinical scale production of human mesenchymal stem cells.* Stem cells, 2006. **24**(2): p. 462-471.
9. Venugopal, P., et al., *Isolation, characterization, and gene expression analysis of Wharton's jelly-derived mesenchymal stem cells under xeno-free culture conditions.* Stem cells cloning, 2011. **4**(1): p. 39-50.
10. Caplan, A.I., *Adult mesenchymal stem cells: when, where, and how.* Stem cells international, 2015. **2015**.
11. Caplan, A.I., *Adult mesenchymal stem cells for tissue engineering versus regenerative medicine.* Journal of cellular physiology, 2007. **213**(2): p. 341-347.
12. Trounson, A., et al., *Clinical trials for stem cell therapies.* BMC medicine, 2011. **9**(1): p. 1.
13. Hare, J.M., et al., *A randomized, double-blind, placebo-controlled, dose-escalation study of intravenous adult human mesenchymal stem cells (prochymal) after acute myocardial infarction.* Journal of the American College of Cardiology, 2009. **54**(24): p. 2277-2286.
14. Sharma, S., et al., *Stem cell culture engineering–process scale up and beyond.* Biotechnology journal, 2011. **6**(11): p. 1317-1329.
15. Docherty, K., A.S. Bernardo, and L. Vallier. *Embryonic stem cell therapy for diabetes mellitus*. in *Seminars in cell & developmental biology*. 2007. Elsevier.
16. Wakitani, S., et al., *Repair of articular cartilage defects in the patello‐femoral joint with autologous bone marrow mesenchymal cell transplantation: three case reports involving nine defects in five knees.* Journal of tissue engineering and regenerative medicine, 2007. **1**(1): p. 74-79.
17. Horwitz, E.M., et al., *Isolated allogeneic bone marrow-derived mesenchymal cells engraft and stimulate growth in children with osteogenesis imperfecta: Implications for cell therapy of bone.* Proceedings of the National Academy of Sciences, 2002. **99**(13): p. 8932-8937.
18. Le Blanc, K., et al., *Fetal mesenchymal stem-cell engraftment in bone after in utero transplantation in a patient with severe osteogenesis imperfecta.* Transplantation, 2005. **79**(11): p. 1607-1614.

19. Sun, L., et al., *Umbilical cord mesenchymal stem cell transplantation in severe and refractory systemic lupus erythematosus.* Arthritis & Rheumatism, 2010. **62**(8): p. 2467-2475.
20. Liang, J., et al., *Allogenic mesenchymal stem cells transplantation in refractory systemic lupus erythematosus: a pilot clinical study.* Annals of the rheumatic diseases, 2010. **69**(8): p. 1423-1429.
21. Mohamadnejad, M., et al., *Phase 1 trial of autologous bone marrow mesenchymal stem cell transplantation in patients with decompensated liver cirrhosis.* Arch Iran Med, 2007. **10**(4): p. 459-466.
22. Schächinger, V., et al., *Intracoronary bone marrow–derived progenitor cells in acute myocardial infarction.* New England journal of medicine, 2006. **355**(12): p. 1210-1221.
23. Kim, N. and S.-G. Cho, *Clinical applications of mesenchymal stem cells.* The Korean journal of internal medicine, 2013. **28**(4): p. 387-402.
24. Field, E., *Projected growth of the world-wide stem cell market.* Stem Cells in Regenerative Medicine: Science, Regulation and Business Strategies, 2015: p. 43.
25. Chen, J., et al., *The key regulatory roles of the PI3K/Akt signaling pathway in the functionalities of mesenchymal stem cells and applications in tissue regeneration.* Tissue Engineering Part B: Reviews, 2013. **19**(6): p. 516-528.
26. Baraniak, P.R. and T.C. McDevitt, *Scaffold-free culture of mesenchymal stem cell spheroids in suspension preserves multilineage potential.* Cell and tissue research, 2012. **347**(3): p. 701-711.
27. Chen, A.K.-L., S. Reuveny, and S.K.W. Oh, *Application of human mesenchymal and pluripotent stem cell microcarrier cultures in cellular therapy: Achievements and future direction.* Biotechnology Advances, 2013. **31**(7): p. 1032-1046.
28. Sart, S., S.N. Agathos, and Y. Li, *Process engineering of stem cell metabolism for large scale expansion and differentiation in bioreactors.* Biochemical Engineering Journal, 2014. **84**: p. 74-82.
29. Godara, P., C.D. McFarland, and R.E. Nordon, *Design of bioreactors for mesenchymal stem cell tissue engineering.* Journal of chemical technology and biotechnology, 2008. **83**(4): p. 408-420.
30. Hidalgo-Bastida, L.A., et al., *Modeling and design of optimal flow perfusion bioreactors for tissue engineering applications.* Biotechnology and Bioengineering, 2012. **109**(4): p. 1095-1099.
31. Jossen, V., et al., *Mass production of mesenchymal stem cells: impact of bioreactor design and flow conditions on proliferation and differentiation*. 2014.
32. Ma, T., A.-C. Tsai, and Y. Liu, *Biomanufacturing of human mesenchymal stem cells in cell therapy: Influence of microenvironment on scalable expansion in bioreactors.* Biochemical Engineering Journal, 2016. **108**: p. 44-50.
33. Martin, Y. and P. Vermette, *Bioreactors for tissue mass culture: design, characterization, and recent advances.* Biomaterials, 2005. **26**(35): p. 7481-7503.
34. Rodrigues, C.A., et al., *Stem cell cultivation in bioreactors.* Biotechnology Advances, 2011. **29**(6): p. 815-829.
35. Zhao, F. and T. Ma, *Perfusion bioreactor system for human mesenchymal stem cell tissue engineering: Dynamic cell seeding and construct development.* Biotechnology and Bioengineering, 2005. **91**(4): p. 482-493.

36. Li, Q., et al., *Differential and interactive effects of substrate topography and chemistry on human mesenchymal stem cell gene expression.* International journal of molecular sciences, 2018. **19**(8): p. 2344.
37. HE, S., N. Daisuke, and S.J. Morrison, *Mechanisms of stem cell self-renewal.* Annual Review of Cell and Developmental, 2009. **25**: p. 377-406.
38. Das, R., et al., *The role of hypoxia in bone marrow–derived mesenchymal stem cells: considerations for regenerative medicine approaches.* Tissue Engineering Part B: Reviews, 2009. **16**(2): p. 159-168.
39. Yeatts, A.B. and J.P. Fisher, *Bone tissue engineering bioreactors: dynamic culture and the influence of shear stress.* Bone, 2011. **48**(2): p. 171-181.
40. Yeatts, A.B., D.T. Choquette, and J.P. Fisher, *Bioreactors to influence stem cell fate: augmentation of mesenchymal stem cell signaling pathways via dynamic culture systems.* Biochimica et Biophysica Acta (BBA)-General Subjects, 2013. **1830**(2): p. 2470-2480.
41. Pierantozzi, E., et al., *Pluripotency regulators in human mesenchymal stem cells: expression of NANOG but not of OCT-4 and SOX-2.* Stem cells and development, 2010. **20**(5): p. 915-923.
42. Estrada, J., et al., *Culture of human mesenchymal stem cells at low oxygen tension improves growth and genetic stability by activating glycolysis.* Cell Death & Differentiation, 2012. **19**(5): p. 743-755.
43. Schugar, R.C., et al., *High harvest yield, high expansion, and phenotype stability of CD146 mesenchymal stromal cells from whole primitive human umbilical cord tissue.* BioMed Research International, 2009. **2009**.
44. Muraglia, A., R. Cancedda, and R. Quarto, *Clonal mesenchymal progenitors from human bone marrow differentiate in vitro according to a hierarchical model.* J Cell Sci, 2000. **113**(7): p. 1161-1166.
45. Bork, S., et al., *DNA methylation pattern changes upon long‐term culture and aging of human mesenchymal stromal cells.* Aging cell, 2010. **9**(1): p. 54-63.
46. Wagner, W., et al., *Replicative senescence of mesenchymal stem cells: a continuous and organized process.* PloS one, 2008. **3**(5): p. e2213.
47. Saller, M.M., et al., *Increased stemness and migration of human mesenchymal stem cells in hypoxia is associated with altered integrin expression.* Biochemical and biophysical research communications, 2012. **423**(2): p. 379-385.
48. Lee, J.-S., et al., *Human bone marrow stem cells cultured under hypoxic conditions present altered characteristics and enhanced in vivo tissue regeneration.* Bone, 2015. **78**: p. 34-45.
49. Dominici, M., et al., *Minimal criteria for defining multipotent mesenchymal stromal cells. The International Society for Cellular Therapy position statement.* Cytotherapy, 2006. **8**(4): p. 315-317.
50. Samsonraj, R.M., et al., *Establishing criteria for human mesenchymal stem cell potency.* Stem Cells, 2015. **33**(6): p. 1878-1891.
51. Prockop, D.J., S.E. Prockop, and I. Bertoncello, *Are clinical trials with mesenchymal stem/progenitor cells too far ahead of the science? Lessons from experimental hematology.* Stem Cells, 2014. **32**(12): p. 3055-3061.
52. Caplan, A.I. and D. Correa, *The MSC: an injury drugstore.* Cell stem cell, 2011. **9**(1): p. 11-15.
53. Lv, F.-J., et al., *Concise review: the surface markers and identity of human mesenchymal stem cells.* Stem cells, 2014. **32**(6): p. 1408-1419.

54. Niehage, C., et al., *The cell surface proteome of human mesenchymal stromal cells.* PloS one, 2011. **6**(5): p. e20399.
55. BÜHRING, H.J., et al., *Novel markers for the prospective isolation of human MSC.* Annals of the New York Academy of Sciences, 2007. **1106**(1): p. 262-271.
56. Simmons, P.J. and B. Torok-Storb, *Identification of stromal cell precursors in human bone marrow by a novel monoclonal antibody, STRO-1.* Blood, 1991. **78**(1): p. 55-62.
57. Psaltis, P., et al., *Enrichment for STRO‐1 expression enhances the cardiovascular paracrine activity of human bone marrow‐derived mesenchymal cell populations.* Journal of cellular physiology, 2010. **223**(2): p. 530-540.
58. Park, J.C., et al., *Isolation and characterization of human periodontal ligament (PDL) stem cells (PDLSCs) from the inflamed PDL tissue: in vitro and in vivo evaluations.* Journal of clinical periodontology, 2011. **38**(8): p. 721-731.
59. Quirici, N., et al., *Isolation of bone marrow mesenchymal stem cells by anti-nerve growth factor receptor antibodies.* Experimental hematology, 2002. **30**(7): p. 783-791.
60. Jarocha, D., E. Lukasiewicz, and M. Majka, *Adventage of mesenchymal stem cells (MSC) expansion directly from purified bone marrow CD105+ and CD271+ cells.* Folia histochemica et cytobiologica, 2008. **46**(3): p. 307-314.
61. Gang, E.J., et al., *SSEA-4 identifies mesenchymal stem cells from bone marrow.* Blood, 2007. **109**(4): p. 1743-1751.
62. Schwab, K., P. Hutchinson, and C. Gargett, *Identification of surface markers for prospective isolation of human endometrial stromal colony-forming cells.* Human reproduction, 2008. **23**(4): p. 934-943.
63. Martin‐Rendon, E., et al., *Transcriptional profiling of human cord blood CD133+ and cultured bone marrow mesenchymal stem cells in response to hypoxia.* Stem cells, 2007. **25**(4): p. 1003-1012.
64. Kuroda, Y., et al., *Unique multipotent cells in adult human mesenchymal cell populations.* Proceedings of the National Academy of Sciences, 2010: p. 200911647.
65. Nystedt, J., et al., *Cell surface structures influence lung clearance rate of systemically infused mesenchymal stromal cells.* Stem Cells, 2013. **31**(2): p. 317-326.
66. Lee, R.H., et al., *The CD34-like protein PODXL and α6-integrin (CD49f) identify early progenitor MSCs with increased clonogenicity and migration to infarcted heart in mice.* Blood, 2009. **113**(4): p. 816-826.
67. Martinez, C., et al., *Human bone marrow mesenchymal stromal cells express the neural ganglioside GD2: a novel surface marker for the identification of MSCs*. 2007, Am Soc Hematology.
68. Castrechini, N., et al., *Decidua parietalis-derived mesenchymal stromal cells reside in a vascular niche within the choriodecidua.* Reproductive sciences, 2012. **19**(12): p. 1302-1314.
69. Shi, S. and S. Gronthos, *Perivascular niche of postnatal mesenchymal stem cells in human bone marrow and dental pulp.* Journal of bone and mineral research, 2003. **18**(4): p. 696-704.
70. Larson, B.L., et al., *Sox11 is expressed in early progenitor human multipotent stromal cells and decreases with extensive expansion of the cells.* Tissue engineering Part A, 2010. **16**(11): p. 3385-3394.

71. Bae, S., et al., *Combined Omics Analysis Identifies Transmembrane 4 L6 Family Member 1 as a Surface Protein Marker Specific to Human Mesenchymal Stem Cells.* Stem Cells and Development, 2011. **20**(2): p. 197-203.
72. Mohyeldin, A., T. Garzón-Muvdi, and A. Quiñones-Hinojosa, *Oxygen in Stem Cell Biology: A Critical Component of the Stem Cell Niche.* Cell Stem Cell, 2010. **7**(2): p. 150-161.
73. Ivanovic, Z., *Hypoxia or in situ normoxia: The stem cell paradigm.* Journal of cellular physiology, 2009. **219**(2): p. 271-275.
74. Guzy, R.D. and P.T. Schumacker, *Oxygen sensing by mitochondria at complex III: the paradox of increased reactive oxygen species during hypoxia.* Experimental physiology, 2006. **91**(5): p. 807-819.
75. Tsai, C.-C., et al., *Hypoxia inhibits senescence and maintains mesenchymal stem cell properties through down-regulation of E2A-p21 by HIF-TWIST.* Blood, 2011. **117**(2): p. 459-469.
76. Adesida, A.B., A. Mulet-Sierra, and N.M. Jomha, *Hypoxia mediated isolation and expansion enhances the chondrogenic capacity of bone marrow mesenchymal stromal cells.* Stem cell research & therapy, 2012. **3**(2): p. 9.
77. Basciano, L., et al., *Long term culture of mesenchymal stem cells in hypoxia promotes a genetic program maintaining their undifferentiated and multipotent status.* BMC cell biology, 2011. **12**(1): p. 1.
78. Deschepper, M., et al., *Survival and function of mesenchymal stem cells (MSCs) depend on glucose to overcome exposure to long‐term, severe and continuous hypoxia.* Journal of cellular and molecular medicine, 2011. **15**(7): p. 1505-1514.
79. Dos Santos, F., et al., *Ex vivo expansion of human mesenchymal stem cells: a more effective cell proliferation kinetics and metabolism under hypoxia.* Journal of cellular physiology, 2010. **223**(1): p. 27-35.
80. Drela, K., et al., *Low oxygen atmosphere facilitates proliferation and maintains undifferentiated state of umbilical cord mesenchymal stem cells in an hypoxia inducible factor-dependent manner.* Cytotherapy, 2014. **16**(7): p. 881-892.
81. Fotia, C., et al., *Hypoxia enhances proliferation and stemness of human adipose-derived mesenchymal stem cells.* Cytotechnology, 2015. **67**(6): p. 1073-1084.
82. Grayson, W.L., et al., *Effects of hypoxia on human mesenchymal stem cell expansion and plasticity in 3D constructs.* Journal of cellular physiology, 2006. **207**(2): p. 331-339.
83. Hung, S.P., et al., *Hypoxia promotes proliferation and osteogenic differentiation potentials of human mesenchymal stem cells.* Journal of Orthopaedic Research, 2012. **30**(2): p. 260-266.
84. Ma, T., et al., *Hypoxia and stem cell‐based engineering of mesenchymal tissues.* Biotechnology progress, 2009. **25**(1): p. 32-42.
85. D'Ippolito, G., et al., *Low oxygen tension inhibits osteogenic differentiation and enhances stemness of human MIAMI cells.* Bone, 2006. **39**(3): p. 513-522.
86. Boyette, L.B., et al., *Human Bone Marrow‐Derived Mesenchymal Stem Cells Display Enhanced Clonogenicity but Impaired Differentiation With Hypoxic Preconditioning.* Stem cells translational medicine, 2014. **3**(2): p. 241-254.
87. Lavrentieva, A., et al., *Effects of hypoxic culture conditions on umbilical cord-derived human mesenchymal stem cells.* Cell communication and signaling, 2010. **8**(1): p. 18.

88. Hung, S.-C., et al., *Short-term exposure of multipotent stromal cells to low oxygen increases their expression of CX3CR1 and CXCR4 and their engraftment in vivo.* PloS one, 2007. **2**(5): p. e416.
89. Holzwarth, C., et al., *Low physiologic oxygen tensions reduce proliferation and differentiation of human multipotent mesenchymal stromal cells.* BMC cell biology, 2010. **11**(1): p. 1.
90. Sharma, S. and R. Bhonde, *Mesenchymal stromal cells are genetically stable under a hostile in vivo–like scenario as revealed by in vitro micronucleus test.* Cytotherapy, 2015. **17**(10): p. 1384-1395.
91. Okamoto, T., et al., *Clonal heterogeneity in differentiation potential of immortalized human mesenchymal stem cells.* Biochemical and biophysical research communications, 2002. **295**(2): p. 354-361.
92. Motaln, H., C. Schichor, and T.T. Lah, *Human mesenchymal stem cells and their use in cell‐based therapies.* Cancer: Interdisciplinary International Journal of the American Cancer Society, 2010. **116**(11): p. 2519-2530.
93. Semenza, G.L., *Regulation of Mammalian O2 Homeostasis by Hypoxia-Inducible Factor 1.* Annual Review of Cell and Developmental Biology, 1999. **15**(1): p. 551-578.
94. Wang, G.L., et al., *Hypoxia-inducible factor 1 is a basic-helix-loop-helix-PAS heterodimer regulated by cellular O2 tension.* Proceedings of the national academy of sciences, 1995. **92**(12): p. 5510-5514.
95. Schofield, C.J. and P.J. Ratcliffe, *Oxygen sensing by HIF hydroxylases.* Nature reviews Molecular cell biology, 2004. **5**(5): p. 343-354.
96. Bruick, R.K., *Oxygen sensing in the hypoxic response pathway: regulation of the hypoxia-inducible transcription factor.* Genes & Development, 2003. **17**(21): p. 2614-2623.
97. Kaelin Jr, W.G., *Proline hydroxylation and gene expression.* Annu. Rev. Biochem., 2005. **74**: p. 115-128.
98. Kallio, P.J., et al., *Signal transduction in hypoxic cells: inducible nuclear translocation and recruitment of theCBP/p300 coactivator by the hypoxia‐induciblefactor‐1α.* The EMBO journal, 1998. **17**(22): p. 6573-6586.
99. Poon, E., A.L. Harris, and M. Ashcroft, *Targeting the hypoxia-inducible factor (HIF) pathway in cancer.* Expert reviews in molecular medicine, 2009. **11**: p. e26.
100. Semenza, G.L., *Hypoxia. Cross talk between oxygen sensing and the cell cycle machinery.* American Journal of Physiology-Cell Physiology, 2011. **301**(3): p. C550-C552.
101. Kenneth, N.S. and S. Rocha, *Regulation of gene expression by hypoxia.* Biochemical Journal, 2008. **414**(1): p. 19-29.
102. Semenza, G.L., *HIF-1 mediates metabolic responses to intratumoral hypoxia and oncogenic mutations.* The Journal of clinical investigation, 2013. **123**(9): p. 3664-3671.
103. Jain, S., et al., *Expression of ARNT, ARNT2, HIF1α, HIF2α and Ah receptor mRNAs in the developing mouse.* Mechanisms of Development, 1998. **73**(1): p. 117-123.
104. Ema, M., et al., *A novel bHLH-PAS factor with close sequence similarity to hypoxia-inducible factor 1α regulates the VEGF expression and is potentially involved in lung and vascular development.* Proceedings of the National Academy of Sciences, 1997. **94**(9): p. 4273-4278.

105. Wiesener, M.S., et al., *Widespread hypoxia-inducible expression of HIF-2α in distinct cell populations of different organs.* The FASEB Journal, 2003. **17**(2): p. 271-273.
106. Covello, K.L., et al., *HIF-2α regulates Oct-4: effects of hypoxia on stem cell function, embryonic development, and tumor growth.* Genes & development, 2006. **20**(5): p. 557-570.
107. Gilbertson, R.J. and J.N. Rich, *Making a tumour's bed: glioblastoma stem cells and the vascular niche.* Nature Reviews Cancer, 2007. **7**(10): p. 733-736.
108. Gordan, J.D., et al., *HIF-2α promotes hypoxic cell proliferation by enhancing c-myc transcriptional activity.* Cancer cell, 2007. **11**(4): p. 335-347.
109. Gu, Y.-Z., et al., *Molecular characterization and chromosomal localization of a third α-class hypoxia inducible factor subunit, HIF3α.* Gene expression, 1998. **7**(3): p. 205-213.
110. Weir, L., et al., *Hypoxia-mediated control of HIF/ARNT machinery in epidermal keratinocytes.* Biochimica et Biophysica Acta (BBA)-Molecular Cell Research, 2011. **1813**(1): p. 60-72.
111. Maynard, M.A., et al., *Human HIF-3α4 is a dominant-negative regulator of HIF-1 and is down-regulated in renal cell carcinoma.* The FASEB Journal, 2005. **19**(11): p. 1396-1406.
112. Majmundar, A.J., W.J. Wong, and M.C. Simon, *Hypoxia-inducible factors and the response to hypoxic stress.* Molecular cell, 2010. **40**(2): p. 294-309.
113. Loboda, A., A. Jozkowicz, and J. Dulak, *HIF-1 and HIF-2 transcription factors — Similar but not identical.* Molecules and Cells, 2010. **29**(5): p. 435-442.
114. Lin, Q., X. Cong, and Z. Yun, *Differential hypoxic regulation of hypoxia-inducible factors 1α and 2α.* Molecular Cancer Research, 2011. **9**(6): p. 757-765.
115. Tamama, K., et al., *Differential roles of hypoxia inducible factor subunits in multipotential stromal cells under hypoxic condition.* Journal of cellular biochemistry, 2011. **112**(3): p. 804-817.
116. Hubbi, M.E. and G.L. Semenza, *Regulation of cell proliferation by hypoxia-inducible factors.* American Journal of Physiology-Cell Physiology, 2015. **309**(12): p. C775-C782.
117. Keith, B., R.S. Johnson, and M.C. Simon, *HIF1α and HIF2α: sibling rivalry in hypoxic tumour growth and progression.* Nature Reviews Cancer, 2012. **12**(1): p. 9-22.
118. Gordan, J.D., C.B. Thompson, and M.C. Simon, *HIF and c-Myc: sibling rivals for control of cancer cell metabolism and proliferation.* Cancer cell, 2007. **12**(2): p. 108-113.
119. Semenza, G.L., *Dynamic regulation of stem cell specification and maintenance by hypoxia-inducible factors.* Molecular aspects of medicine, 2016. **47**: p. 15-23.
120. Ejtehadifar, M., et al., *The effect of hypoxia on mesenchymal stem cell biology.* Advanced pharmaceutical bulletin, 2015. **5**(2): p. 141.
121. Ventre, M., et al., *Topographic cell instructive patterns to control cell adhesion, polarization and migration.* Journal of the Royal Society, Interface, 2014. **11**(100): p. 20140687-20140687.
122. Rim, N.G., C.S. Shin, and H. Shin, *Current approaches to electrospun nanofibers for tissue engineering.* Biomedical Materials, 2013. **8**(1): p. 014102.

123. Anderson, H.J., et al., *Mesenchymal stem cell fate: applying biomaterials for control of stem cell behavior.* Frontiers in bioengineering and biotechnology, 2016. **4**: p. 38.
124. Keselowsky, B.G., D.M. Collard, and A.J. García, *Surface chemistry modulates fibronectin conformation and directs integrin binding and specificity to control cell adhesion.* Journal of Biomedical Materials Research Part A, 2003. **66A**(2): p. 247-259.
125. Curran, J.M., R. Chen, and J.A. Hunt, *Controlling the phenotype and function of mesenchymal stem cells in vitro by adhesion to silane-modified clean glass surfaces.* Biomaterials, 2005. **26**(34): p. 7057-7067.
126. DuFort, C.C., M.J. Paszek, and V.M. Weaver, *Balancing forces: architectural control of mechanotransduction.* Nature Reviews Molecular Cell Biology, 2011. **12**: p. 308.
127. Discher, D.E., D.J. Mooney, and P.W. Zandstra, *Growth Factors, Matrices, and Forces Combine and Control Stem Cells.* Science, 2009. **324**(5935): p. 1673-1677.
128. Su, N., et al., *Fibrous scaffolds potentiate the paracrine function of mesenchymal stem cells: A new dimension in cell-material interaction.* Biomaterials, 2017. **141**: p. 74-85.
129. Cukierman, E., et al., *Taking cell-matrix adhesions to the third dimension.* Science, 2001. **294**(5547): p. 1708-1712.
130. Zamani, Y., et al., *Response of Human Mesenchymal Stem Cells to Patterned and Randomly Oriented Poly(Vinyl Alcohol) Nano-fibrous Scaffolds Surface-Modified with Arg-Gly-Asp (RGD) Ligand.* Applied Biochemistry and Biotechnology, 2013. **171**(6): p. 1513-1524.
131. Nedjari, S., F. Awaja, and G. Altankov, *Three Dimensional Honeycomb Patterned Fibrinogen Based Nanofibers Induce Substantial Osteogenic Response of Mesenchymal Stem Cells.* Scientific reports, 2017. **7**(1): p. 15947.
132. Heo, S.J., et al., *Fiber Stretch and Reorientation Modulates Mesenchymal Stem Cell Morphology and Fibrous Gene Expression on Oriented Nanofibrous Microenvironments.* Annals of Biomedical Engineering, 2011. **39**(11): p. 2780-2790.
133. Wang, X., et al., *Regulating the stemness of mesenchymal stem cells by tuning micropattern features.* Journal of Materials Chemistry B, 2016. **4**(1): p. 37-45.
134. Li, R., et al., *Self-assembled N-cadherin mimetic peptide hydrogels promote the chondrogenesis of mesenchymal stem cells through inhibition of canonical Wnt/β-catenin signaling.* Biomaterials, 2017. **145**: p. 33-43.
135. Lanniel, M., et al., *Substrate induced differentiation of human mesenchymal stem cells on hydrogels with modified surface chemistry and controlled modulus.* Soft Matter, 2011. **7**(14): p. 6501-6514.
136. Benoit, D.S., et al., *Small functional groups for controlled differentiation of hydrogel-encapsulated human mesenchymal stem cells.* Nature materials, 2008. **7**(10): p. 816.
137. Chang, J.-C., et al., *Cell orientation and regulation of cell–cell communication in human mesenchymal stem cells on different patterns of electrospun fibers.* Biomedical Materials, 2013. **8**(5): p. 055002.
138. Amjadian, S., et al., *The synergistic effect of nano-hydroxyapatite and dexamethasone in the fibrous delivery system of gelatin and poly(L-lactide) on*

the osteogenesis of mesenchymal stem cells. International Journal of Pharmaceutics, 2016. **507**(1-2): p. 1-11.
139. Woo, K.M., et al., *Nano-fibrous scaffolding promotes osteoblast differentiation and biomineralization.* Biomaterials, 2007. **28**(2): p. 335-343.
140. Kim, J. and T. Ma, *Perfusion regulation of hMSC microenvironment and osteogenic differentiation in 3D scaffold.* Biotechnology and bioengineering, 2012. **109**(1): p. 252-261.
141. Lee, J., A.A. Abdeen, and K.A. Kilian, *Rewiring mesenchymal stem cell lineage specification by switching the biophysical microenvironment.* Scientific Reports, 2014. **4**: p. 5188.
142. Guvendiren, M. and J.A. Burdick, *Stem cell response to spatially and temporally displayed and reversible surface topography.* Advanced healthcare materials, 2013. **2**(1): p. 155-164.
143. Murphy, W.L., T.C. McDevitt, and A.J. Engler, *Materials as stem cell regulators.* Nature materials, 2014. **13**(6): p. 547.
144. Giam, L.R., et al., *Scanning probe-enabled nanocombinatorics define the relationship between fibronectin feature size and stem cell fate.* Proceedings of the National Academy of Sciences of the United States of America, 2012. **109**(12): p. 4377-4382.
145. Choi, S., et al., *Inorganic coatings for optimized non-viral transfection of stem cells.* Scientific reports, 2013. **3**: p. 1567-1567.
146. Phillips, J.E., et al., *Human mesenchymal stem cell differentiation on self-assembled monolayers presenting different surface chemistries.* Acta Biomaterialia, 2010. **6**(1): p. 12-20.
147. Zhang, W., et al., *The synergistic effect of hierarchical micro/nano-topography and bioactive ions for enhanced osseointegration.* Biomaterials, 2013. **34**(13): p. 3184-3195.
148. Sun, M., et al., *Effects of Matrix Stiffness on the Morphology, Adhesion, Proliferation and Osteogenic Differentiation of Mesenchymal Stem Cells.* International journal of medical sciences, 2018. **15**(3): p. 257-268.
149. Engler, A.J., et al., *Matrix Elasticity Directs Stem Cell Lineage Specification.* Cell, 2006. **126**(4): p. 677-689.
150. Wang, N., J.P. Butler, and D.E. Ingber, *Mechanotransduction across the cell surface and through the cytoskeleton.* Science, 1993. **260**(5111): p. 1124-1127.
151. Yim, E.K.F., et al., *Proliferation and differentiation of human mesenchymal stem cell encapsulated in polyelectrolyte complexation fibrous scaffold.* Biomaterials, 2006. **27**(36): p. 6111-6122.
152. Nalluri, S.M., M.J. Hill, and D. Sarkar, *Control of Mesenchymal Stem Cells with Biomaterials*, in *Essentials of Mesenchymal Stem Cell Biology and Its Clinical Translation*. 2013, Springer. p. 139-159.
153. Wang, N., J.P. Butler, and D.E. Ingber, *Mechanotransduction across the cell surface and through the cytoskeleton.* Science, 1993. **260**(5111): p. 1124-7.
154. Murphy, W.L., T.C. McDevitt, and A.J. Engler, *Materials as stem cell regulators.* Nat Mater, 2014. **13**(6): p. 547-557.
155. Meinel, L., et al., *Bone tissue engineering using human mesenchymal stem cells: effects of scaffold material and medium flow.* Annals of biomedical engineering, 2004. **32**(1): p. 112-122.

156. Silva, M.M., et al., *Robust expansion of human pluripotent stem cells: integration of bioprocess design with transcriptomic and metabolomic characterization.* Stem cells translational medicine, 2015. **4**(7): p. 731-742.
157. Liu, Y. and T. Ma, *Metabolic regulation of mesenchymal stem cell in expansion and therapeutic application.* Biotechnology progress, 2015. **31**(2): p. 468-481.
158. Gharibi, B. and F.J. Hughes, *Effects of medium supplements on proliferation, differentiation potential, and in vitro expansion of mesenchymal stem cells.* Stem cells translational medicine, 2012. **1**(11): p. 771-782.
159. Mannello, F. and G.A. Tonti, *Concise Review: No Breakthroughs for Human Mesenchymal and Embryonic Stem Cell Culture: Conditioned Medium, Feeder Layer, or Feeder-Free; Medium with Fetal Calf Serum, Human Serum, or Enriched Plasma; Serum-Free, Serum Replacement Nonconditioned Medium, or Ad Hoc Formula? All That Glitters Is Not Gold!* STEM CELLS, 2007. **25**(7): p. 1603-1609.
160. Gronthos, S. and P. Simmons, *The growth factor requirements of STRO-1-positive human bone marrow stromal precursors under serum-deprived conditions in vitro.* Blood, 1995. **85**(4): p. 929-940.
161. Kuznetsov, S.A., A.J. Friedenstein, and P. Gehron Robey, *Factors required for bone marrow stromal fibroblast colony formation in vitro.* British Journal of Haematology, 1997. **97**(3): p. 561-570.
162. Rodrigues, M., L.G. Griffith, and A. Wells, *Growth factor regulation of proliferation and survival of multipotential stromal cells.* Stem cell research & therapy, 2010. **1**(4): p. 32-32.
163. Fischer, H.P., *Mathematical modeling of complex biological systems: from parts lists to understanding systems behavior.* Alcohol Research & Health, 2008. **31**(1): p. 49.
164. Motta, S. and F. Pappalardo, *Mathematical modeling of biological systems.* Briefings in Bioinformatics, 2012. **14**(4): p. 411-422.
165. Mogilner, A., R. Wollman, and W.F. Marshall, *Quantitative modeling in cell biology: what is it good for?* Developmental cell, 2006. **11**(3): p. 279-287.
166. Brodland, G.W. *How computational models can help unlock biological systems*. in *Seminars in cell & developmental biology*. 2015. Elsevier.
167. Qutub, A.A. and A.S. Popel, *A computational model of intracellular oxygen sensing by hypoxia-inducible factor HIF1α.* Journal of cell science, 2006. **119**(16): p. 3467-3480.
168. Qutub, A.A. and A.S. Popel, *Three autocrine feedback loops determine HIF1α expression in chronic hypoxia.* Biochimica et Biophysica Acta (BBA)-Molecular Cell Research, 2007. **1773**(10): p. 1511-1525.
169. Nguyen, L.K., et al., *A dynamic model of the hypoxia-inducible factor 1α (HIF-1α) network.* J Cell Sci, 2013. **126**(6): p. 1454-1463.
170. Alarcon, T., H. Byrne, and P. Maini, *A mathematical model of the effects of hypoxia on the cell-cycle of normal and cancer cells.* Journal of theoretical biology, 2004. **229**(3): p. 395-411.
171. Pisu, M., A. Concas, and G. Cao, *A novel simulation model for stem cells differentiation.* Journal of biotechnology, 2007. **130**(2): p. 171-182.
172. Glauche, I., M. Herberg, and I. Roeder, *Nanog Variability and Pluripotency Regulation of Embryonic Stem Cells - Insights from a Mathematical Model Analysis.* PLoS ONE, 2010. **5**(6): p. e11238.

173. Orth, J.D., I. Thiele, and B.Ø. Palsson, *What is flux balance analysis?* Nature biotechnology, 2010. **28**(3): p. 245.
174. Wang, Y., et al., *A mathematical model predicting the coculture dynamics of endothelial and mesenchymal stem cells for tissue regeneration.* Tissue engineering. Part A, 2013. **19**(9-10): p. 1155-1164.
175. Arnol, D., et al., *Modelling cell-cell interactions from spatial molecular data with spatial variance component analysis.* bioRxiv, 2018: p. 265256.
176. Peng, T., et al., *Modeling Cell–Cell Interactions in Regulating Multiple Myeloma Initiating Cell Fate.* IEEE Journal of Biomedical and Health Informatics, 2014. **18**(2): p. 484-491.
177. Bartolini, E., et al., *Population balance modelling of stem cell culture in 3D suspension bioreactors.* Chemical Engineering Research and Design, 2015. **101**: p. 125-134.
178. Mokhtari-Jafari, F., et al., *Mathematical modeling of cell growth in a 3D scaffold and validation of static and dynamic cultures.* Engineering in Life Sciences, 2016. **16**(3): p. 290-298.
179. Almeida, H.A. and P.J. da Silva Bártolo, *Mathematical Modeling of 3D Tissue Engineering Constructs.* 3D Printing and Biofabrication, 2017: p. 1-30.
180. Zhao, F., et al., *Effects of oxygen transport on 3 ‐d human mesenchymal stem cell metabolic activity in perfusion and static cultures: Experiments and mathematical model.* Biotechnology progress, 2005. **21**(4): p. 1269-1280.
181. Zhao, F., R. Chella, and T. Ma, *Effects of shear stress on 3-D human mesenchymal stem cell construct development in a perfusion bioreactor system: Experiments and hydrodynamic modeling.* Biotechnology and Bioengineering, 2007. **96**(3): p. 584-595.
182. Lemon, G., et al., *Mathematical modelling of human mesenchymal stem cell proliferation and differentiation inside artificial porous scaffolds.* Journal of theoretical biology, 2007. **249**(3): p. 543-553.
183. Weijers, E.M., et al., *The influence of hypoxia and fibrinogen variants on the expansion and differentiation of adipose tissue-derived mesenchymal stem cells.* Tissue Engineering Part A, 2011. **17**(21-22): p. 2675-2685.
184. Zachar, V., et al., *Hypoxia and adipose-derived stem cell-based tissue regeneration and engineering.* Expert opinion on biological therapy, 2011. **11**(6): p. 775-786.
185. Forristal, C.E., et al., *Hypoxia inducible factors regulate pluripotency and proliferation in human embryonic stem cells cultured at reduced oxygen tensions.* Reproduction, 2010. **139**(1): p. 85-97.
186. Eliasson, P. and J.I. Jönsson, *The hematopoietic stem cell niche: low in oxygen but a nice place to be.* Journal of cellular physiology, 2010. **222**(1): p. 17-22.
187. Ebbesen, P., et al., *Linking measured intercellular oxygen concentration to human cell functions.* Acta Oncologica, 2004. **43**(6): p. 598-600.
188. Ivanovic, Z. and V.-L. M., *Anaerobiosis and StemnessL An Evolutionary Paradigm for Therpeutic Applications.* 2015: Cambridge Academic Press.
189. Närvä, E., et al., *Continuous hypoxic culturing of human embryonic stem cells enhances SSEA-3 and MYC levels.* PloS one, 2013. **8**(11): p. e78847.
190. Jiang, B.-H., et al., *Hypoxia-inducible factor 1 levels vary exponentially over a physiologically relevant range of O2 tension.* American Journal of Physiology-Cell Physiology, 1996. **271**(4): p. C1172-C1180.

191. Wen, W., et al., *Suppression of cyclin D1 by hypoxia-inducible factor-1 via direct mechanism inhibits the proliferation and 5-fluorouracil–induced apoptosis of A549 cells.* Cancer research, 2010. **70**(5).
192. Novak, B. and J.J. Tyson, *A model for restriction point control of the mammalian cell cycle.* Journal of theoretical biology, 2004. **230**(4): p. 563-579.
193. Schofield, C.J. and P.J. Ratcliffe, *Signalling hypoxia by HIF hydroxylases.* Biochemical and biophysical research communications, 2005. **338**(1): p. 617-626.
194. Park, I.-H., et al., *Constitutive stabilization of hypoxia-inducible factor alpha selectively promotes the self-renewal of mesenchymal progenitors and maintains mesenchymal stromal cells in an undifferentiated state.* Experimental & molecular medicine, 2013. **45**(9): p. e44.
195. Zhang, S., et al., *HIF-2α and Oct4 have synergistic effects on survival and myocardial repair of very small embryonic-like mesenchymal stem cells in infarcted hearts.* Cell Death & Disease, 2017. **8**(1): p. e2548.
196. Grayson, W.L., et al., *Hypoxia enhances proliferation and tissue formation of human mesenchymal stem cells.* Biochemical and biophysical research communications, 2007. **358**(3): p. 948-953.
197. Hilton, M.J., et al., *Notch signaling maintains bone marrow mesenchymal progenitors by suppressing osteoblast differentiation.* Nature medicine, 2008. **14**(3): p. 306-314.
198. Dayan, F., et al., *Gene regulation in response to graded hypoxia: the non-redundant roles of the oxygen sensors PHD and FIH in the HIF pathway.* Journal of Theoretical Biology, 2009. **259**(2): p. 304-316.
199. Bedessem, B. and A. Stéphanou, *Role of Compartmentalization on HiF-1α Degradation Dynamics during Changing Oxygen Conditions: A Computational Approach.* PloS one, 2014. **9**(10): p. e110495.
200. Bedessem, B. and A. Stéphanou, *A mathematical model of HiF-1α-mediated response to hypoxia on the G1/S transition.* Mathematical biosciences, 2014. **248**: p. 31-39.
201. Dong, P., et al., *Division of labour between Myc and G1 cyclins in cell cycle commitment and pace control.* Nature communications, 2014. **5**.
202. Lee, T.J., et al., *Stochastic E2F activation and reconciliation of phenomenological cell-cycle models.* PLoS Biol, 2010. **8**(9): p. e1000488.
203. Yao, G., et al., *A bistable Rb–E2F switch underlies the restriction point.* Nature cell biology, 2008. **10**(4): p. 476-482.
204. Higuera, G., et al., *Quantifying in vitro growth and metabolism kinetics of human mesenchymal stem cells using a mathematical model.* Tissue Engineering Part A, 2009. **15**(9): p. 2653-2663.
205. Zhu, C., et al., *Hypoxia-inducible factor-2 alpha promotes the proliferation of human placenta-derived mesenchymal stem cells through the MAPK/ERK signaling pathway.* Scientific reports, 2016. **6**(35489).
206. Bracken, C.P., et al., *Cell-specific regulation of hypoxia-inducible factor (HIF)-1α and HIF-2α stabilization and transactivation in a graded oxygen environment.* Journal of Biological Chemistry, 2006. **281**(32): p. 22575-22585.
207. abcam. *Product Datasheet - Human HIF-1-alpha ELISA Kit ab171577*. [Product Datasheet] [cited 2016 June 15]; Available from: http://www.abcam.com/Human-HIF-1-alpha-ELISA-Kit-ab171577.html.

208. Chen, K., et al., *Human bone marrow-derived stem cell proliferation is inhibited by hepatocyte growth factor via increasing the cell cycle inhibitors p53, p21 and p27.* Bone, 2011. **49**(6): p. 1194-1204.
209. Burdon, T., A. Smith, and P. Savatier, *Signalling, cell cycle and pluripotency in embryonic stem cells.* Trends in cell biology, 2002. **12**(9): p. 432-438.
210. Sherr, C.J. and J.M. Roberts, *CDK inhibitors: positive and negative regulators of G1-phase progression.* Genes & development, 1999. **13**(12): p. 1501-1512.
211. Andreyev, A.Y., Y.E. Kushnareva, and A. Starkov, *Mitochondrial metabolism of reactive oxygen species.* Biochemistry (Moscow), 2005. **70**(2): p. 200-214.
212. Murphy, M.P., *How mitochondria produce reactive oxygen species.* Biochemical Journal, 2009. **417**(1): p. 1-13.
213. Finkel, T., *Oxidant signals and oxidative stress.* Current opinion in cell biology, 2003. **15**(2): p. 247-254.
214. Chance, B., H. Sies, and A. Boveris, *Hydroperoxide metabolism in mammalian organs.* Physiological reviews, 1979. **59**(3): p. 527-605.
215. Moussavi-Harami, F., et al., *Oxygen effects on senescence in chondrocytes and mesenchymal stem cells: consequences for tissue engineering.* Iowa Orthopaedic Journal, 2004. **24**: p. 15-20.
216. Davies, K., S. Lin, and R. Pacifici, *Protein damage and degradation by oxygen radicals. IV. Degradation of denatured protein.* Journal of Biological Chemistry, 1987. **262**(20): p. 9914-9920.
217. Kim, J.H., et al., *The pivotal role of reactive oxygen species generation in the hypoxia-induced stimulation of adipose-derived stem cells.* Stem cells and development, 2011. **20**(10): p. 1753-1761.
218. Guzy, R.D., et al., *Mitochondrial complex III is required for hypoxia-induced ROS production and cellular oxygen sensing.* Cell metabolism, 2005. **1**(6): p. 401-408.
219. Hamanaka, R.B. and N.S. Chandel, *Mitochondrial reactive oxygen species regulate cellular signaling and dictate biological outcomes.* Trends in biochemical sciences, 2010. **35**(9): p. 505-513.
220. Chandel, N.S., et al., *Reactive Oxygen Species Generated at Mitochondrial Complex III Stabilize Hypoxia-inducible Factor-1α during Hypoxia A MECHANISM OF O2 SENSING.* Journal of Biological Chemistry, 2000. **275**(33): p. 25130-25138.
221. Kiparissides, A., et al., *Global sensitivity analysis challenges in biological systems modeling.* Industrial & Engineering Chemistry Research, 2009. **48**(15): p. 7168-7180.
222. Kucherenko, S., et al., *Monte Carlo evaluation of derivative-based global sensitivity measures.* Reliability Engineering & System Safety, 2009. **94**(7): p. 1135-1148.
223. Chung, D.-J., et al., *Osteogenic proliferation and differentiation of canine bone marrow and adipose tissue derived mesenchymal stromal cells and the influence of hypoxia.* Research in veterinary science, 2012. **92**(1): p. 66-75.
224. Sheng, L., et al., *Effect of the PI3K/AKT signaling pathway on hypoxia‐induced proliferation and differentiation of bone marrow‐derived mesenchymal stem cells.* Experimental and Therapeutic Medicine, 2017. **13**(1): p. 55-62.
225. Valorani, M., et al., *Pre‐culturing human adipose tissue mesenchymal stem cells under hypoxia increases their adipogenic and osteogenic differentiation potentials.* Cell Proliferation, 2012. **45**(3): p. 225-238.

226. Peng, L., et al., *Effects of hypoxia on proliferation of human cord blood-derived mesenchymal stem cells.* Cytotechnology, 2016. **68**(4): p. 1615-1622.
227. Kurosawa, H., et al., *Effect of oxygen on in vitro differentiation of mouse embryonic stem cells.* Journal of Bioscience and Bioengineering, 2006. **101**(1): p. 26-30.
228. Hubbi, M.E., et al., *A nontranscriptional role for HIF-1α as a direct inhibitor of DNA replication.* Science signaling, 2013. **6**(262): p. ra10.
229. Semenza, G.L., *Regulation of oxygen homeostasis by hypoxia-inducible factor 1.* Physiology, 2009. **24**(2): p. 97-106.
230. Tsai, C.-C., et al., *Benefits of hypoxic culture on bone marrow multipotent stromal cells.* Am J Blood Res, 2012. **2**(3): p. 148-159.
231. Moriyama, H., et al., *Role of notch signaling in the maintenance of human mesenchymal stem cells under hypoxic conditions.* Stem cells and development, 2014. **23**(18): p. 2211-2224.
232. Borodkina, A., et al., *Interaction between ROS dependent DNA damage, mitochondria and p38 MAPK underlies senescence of human adult stem cells.* Aging (Albany NY), 2014. **6**(6): p. 481-495.
233. Guachalla, L.M. and K.L. Rudolph, *ROS induced DNA damage and checkpoint responses: influences on aging?* Cell cycle, 2010. **9**(20): p. 4058-4060.
234. Bertolo, A., et al., *Oxidative status predicts quality in human mesenchymal stem cells.* Stem Cell Research & Therapy, 2017. **8**(1): p. 3.
235. Pfau, J.C., et al., *Environmental oxygen tension affects phenotype in cultured bone marrow-derived macrophages.* American Journal of Physiology-Lung Cellular and Molecular Physiology, 2004. **286**(2): p. L354-L362.
236. Nicolaije, C., M. Koedam, and J.P. van Leeuwen, *Decreased oxygen tension lowers reactive oxygen species and apoptosis and inhibits osteoblast matrix mineralization through changes in early osteoblast differentiation.* Journal of cellular physiology, 2012. **227**(4): p. 1309-1318.
237. Fandrey, J., S. Frede, and W. Jelkmann, *Role of hydrogen peroxide in hypoxia-induced erythropoietin production.* Biochemical Journal, 1994. **303**(2): p. 507-510.
238. Peterson, K.M., et al., *Improved survival of mesenchymal stromal cell after hypoxia preconditioning: role of oxidative stress.* Life sciences, 2011. **88**(1): p. 65-73.
239. Brunelle, J.K., et al., *Oxygen sensing requires mitochondrial ROS but not oxidative phosphorylation.* Cell metabolism, 2005. **1**(6): p. 409-414.
240. Koh, M.Y., et al., *The hypoxia-associated factor switches cells from HIF-1α-to HIF-2α-dependent signaling promoting stem cell characteristics, aggressive tumor growth and invasion.* Cancer research, 2011. **71**(11): p. 4015-4027.
241. Raval, R.R., et al., *Contrasting properties of hypoxia-inducible factor 1 (HIF-1) and HIF-2 in von Hippel-Lindau-associated renal cell carcinoma.* Molecular and cellular biology, 2005. **25**(13): p. 5675-5686.
242. Covello, K.L., M.C. Simon, and B. Keith, *Targeted replacement of hypoxia-inducible factor-1α by a hypoxia-inducible factor-2α knock-in allele promotes tumor growth.* Cancer research, 2005. **65**(6): p. 2277-2286.
243. Hu, X., et al., *Severe hypoxia exerts parallel and cell-specific regulation of gene expression and alternative splicing in human mesenchymal stem cells.* BMC genomics, 2014. **15**(1): p. 303.

244. Anokhina, E., L. Buravkova, and S. Galchuk, *Resistance of rat bone marrow mesenchymal stromal precursor cells to anoxia in vitro.* Bulletin of experimental biology and medicine, 2009. **148**(1): p. 148-151.
245. Rylova, J. and L. Buravkova, *Anoxia resistance of cultured multipotent mesenchymal stromal cells from adipose tissue.* Cell and Tissue Biology, 2015. **9**(2): p. 79-86.
246. Kasoju, N., et al., *Transcriptomics of human multipotent mesenchymal stromal cells: Retrospective analysis and future prospects.* Biotechnology Advances, 2017.
247. Maurer, M.H., *Proteomic definitions of mesenchymal stem cells.* Stem cells international, 2011. **2011**.
248. Cramer, C., et al., *Persistent high glucose concentrations alter the regenerative potential of mesenchymal stem cells.* Stem cells and development, 2010. **19**(12): p. 1875-1884.
249. Cheng, N.-C., et al., *High glucose-induced reactive oxygen species generation promotes stemness in human adipose-derived stem cells.* Cytotherapy, 2016. **18**(3): p. 371-383.
250. Dulbecco, R. and G. Freeman, *Plaque production by the polyoma virus.* Virology, 1959. **8**(3): p. 396.
251. Vander Heiden, M.G., L.C. Cantley, and C.B. Thompson, *Understanding the Warburg effect: the metabolic requirements of cell proliferation.* science, 2009. **324**(5930): p. 1029-1033.
252. Lunt, S.Y. and M.G. Vander Heiden, *Aerobic glycolysis: meeting the metabolic requirements of cell proliferation.* Annual review of cell and developmental biology, 2011. **27**: p. 441-464.
253. Schuster, S., et al., *Mathematical models for explaining the Warburg effect: a review focussed on ATP and biomass production.* Biochemical Society Transactions, 2015. **43**(6): p. 1187-1194.
254. Hsu, P.P. and D.M. Sabatini, *Cancer cell metabolism: Warburg and beyond.* Cell, 2008. **134**(5): p. 703-707.
255. Wheaton, W.W. and N.S. Chandel, *Hypoxia. 2. Hypoxia regulates cellular metabolism.* American Journal of Physiology-Cell Physiology, 2011. **300**(3): p. C385.
256. Bahsoun, S., et al., *The Role of Dissolved Oxygen Levels on Human Mesenchymal Stem Cell Culture Success, Regulatory Compliance, and Therapeutic Potential.* Stem cells and development, 2018. **27**(19): p. 1303-1321.
257. Pattappa, G., et al., *The metabolism of human mesenchymal stem cells during proliferation and differentiation.* Journal of cellular physiology, 2011. **226**(10): p. 2562-2570.
258. Tsai, A.C., Y.J. Liu, and T. Ma, *Expansion of human mesenchymal stem cells in fibrous bed bioreactor.* Biochemical Engineering Journal, 2016. **108**: p. 51-57.
259. Schop, D., et al., *Growth, metabolism, and growth inhibitors of mesenchymal stem cells.* Tissue Engineering Part A, 2009. **15**(8): p. 1877-1886.
260. Chen, T., Y. Zhou, and W.-S. Tan, *Influence of lactic acid on the proliferation, metabolism, and differentiation of rabbit mesenchymal stem cells.* Cell biology and toxicology, 2009. **25**(6): p. 573.

261. Phinney, D.G., *Functional heterogeneity of mesenchymal stem cells: implications for cell therapy.* Journal of cellular biochemistry, 2012. **113**(9): p. 2806-2812.
262. Phinney, D.G., *Biochemical heterogeneity of mesenchymal stem cell populations: clues to their therapeutic efficacy.* Cell cycle, 2007. **6**(23): p. 2884-2889.
263. Zhang, B., H. Ye, and A. Yang, *Mathematical modelling of interacting mechanisms for hypoxia mediated cell cycle commitment for mesenchymal stromal cells.* BMC systems biology, 2018. **12**(1): p. 35.
264. Fouladiha, H., S.A. Marashi, and M. Shokrgozar, *Reconstruction and validation of a constraint‐based metabolic network model for bone marrow‐derived mesenchymal stem cells.* Cell proliferation, 2015. **48**(4): p. 475-485.
265. Damiani, C., et al., *A metabolic core model elucidates how enhanced utilization of glucose and glutamine, with enhanced glutamine-dependent lactate production, promotes cancer cell growth: The WarburQ effect.* PLoS computational biology, 2017. **13**(9): p. e1005758.
266. Shlomi, T., et al., *Genome-scale metabolic modeling elucidates the role of proliferative adaptation in causing the Warburg effect.* PLoS computational biology, 2011. **7**(3): p. e1002018.
267. Duarte, N.C., et al., *Global reconstruction of the human metabolic network based on genomic and bibliomic data.* Proceedings of the National Academy of Sciences, 2007. **104**(6): p. 1777-1782.
268. Rolfsson, O., B.Ø. Palsson, and I. Thiele, *The human metabolic reconstruction Recon 1 directs hypotheses of novel human metabolic functions.* BMC systems biology, 2011. **5**(1): p. 155.
269. Bordbar, A. and B.O. Palsson, *Using the reconstructed genome‐scale human metabolic network to study physiology and pathology.* Journal of internal medicine, 2012. **271**(2): p. 131-141.
270. Fouladiha, H. and S.-A. Marashi, *Biomedical applications of cell-and tissue-specific metabolic network models.* Journal of biomedical informatics, 2017. **68**: p. 35-49.
271. Basan, M., et al., *Overflow metabolism in Escherichia coli results from efficient proteome allocation.* Nature, 2015. **528**(7580): p. 99.
272. Ruppin, E., et al., *Metabolic reconstruction, constraint-based analysis and game theory to probe genome-scale metabolic networks.* Current opinion in biotechnology, 2010. **21**(4): p. 502-510.
273. Quek, L.-E., et al., *Metabolic flux analysis in mammalian cell culture.* Metabolic engineering, 2010. **12**(2): p. 161-171.
274. Molenaar, D., et al., *Shifts in growth strategies reflect tradeoffs in cellular economics.* Molecular systems biology, 2009. **5**(1): p. 323.
275. Schuster, S., et al., *Combining metabolic pathway analysis with evolutionary game theory. Explaining the occurrence of low-yield pathways by an analytic optimization approach.* Biosystems, 2011. **105**(2): p. 147-153.
276. Heirendt, L., et al., *Creation and analysis of biochemical constraint-based models: the COBRA Toolbox v3. 0.* arXiv preprint arXiv:1710.04038, 2017.
277. "Gurobi Optimization, L. *Gurobi Optimizer Reference Manual*. 2018; Available from: http://www.gurobi.com.
278. DeBerardinis, R.J., et al., *The biology of cancer: metabolic reprogramming fuels cell growth and proliferation.* Cell metabolism, 2008. **7**(1): p. 11-20.

279. Valcourt, J.R., et al., *Staying alive: metabolic adaptations to quiescence.* Cell cycle, 2012. **11**(9): p. 1680-1696.
280. Pavlides, S., et al., *Warburg meets autophagy: cancer-associated fibroblasts accelerate tumor growth and metastasis via oxidative stress, mitophagy, and aerobic glycolysis.* Antioxidants & redox signaling, 2012. **16**(11): p. 1264-1284.
281. Chen, X., Y. Qian, and S. Wu, *The Warburg effect: evolving interpretations of an established concept.* Free Radical Biology and Medicine, 2015. **79**: p. 253-263.
282. Feizi, A. and S. Bordel, *Metabolic and protein interaction sub-networks controlling the proliferation rate of cancer cells and their impact on patient survival.* Scientific reports, 2013. **3**: p. 3041.
283. Balliet, R.M., et al., *Mitochondrial oxidative stress in cancer-associated fibroblasts drives lactate production, promoting breast cancer tumor growth: understanding the aging and cancer connection.* Cell cycle, 2011. **10**(23): p. 4065-4073.
284. del Valle, L.G., *Oxidative stress in aging: Theoretical outcomes and clinical evidences in humans.* Biomedicine & Aging Pathology, 2011. **1**(1): p. 1-7.
285. Woo, D.K. and G.S. Shadel, *Mitochondrial stress signals revise an old aging theory.* Cell, 2011. **144**(1): p. 11-12.
286. Loike, J., et al., *Hypoxia induces glucose transporter expression in endothelial cells.* American Journal of Physiology-Cell Physiology, 1992. **263**(2): p. C326-C333.
287. Marin‐Valencia, I., et al., *Glucose metabolism via the pentose phosphate pathway, glycolysis and Krebs cycle in an orthotopic mouse model of human brain tumors.* NMR in biomedicine, 2012. **25**(10): p. 1177-1186.
288. Gaitonde, M., E. Evison, and G. Evans, *The rate of utilization of glucose via hexosemonophosphate shunt in brain.* Journal of neurochemistry, 1983. **41**(5): p. 1253-1260.
289. Ben-Yoseph, O., P.A. Boxer, and B.D. Ross, *Noninvasive assessment of the relative roles of cerebral antioxidant enzymes by quantitation of pentose phosphate pathway activity.* Neurochemical research, 1996. **21**(9): p. 1005-1012.
290. Baquer, N., J. Hothersall, and P. McLean, *Function and regulation of the pentose phosphate pathway in brain*, in *Current topics in cellular regulation*. 1988, Elsevier. p. 265-289.
291. Kathagen-Buhmann, A., et al., *Glycolysis and the pentose phosphate pathway are differentially associated with the dichotomous regulation of glioblastoma cell migration versus proliferation.* Neuro-oncology, 2016. **18**(9): p. 1219-1229.
292. Young, J.D., *Metabolic flux rewiring in mammalian cell cultures.* Current opinion in biotechnology, 2013. **24**(6): p. 1108-1115.
293. Hakim, A., G. Moss, and S. Gollomp, *The effect of hypoxia on the pentose phosphate pathway in brain.* Journal of neurochemistry, 1976. **26**(4): p. 683-688.
294. Gao, Q. and M.S. Wolin, *Effects of hypoxia on relationships between cytosolic and mitochondrial NAD (P) H redox and superoxide generation in coronary arterial smooth muscle.* American Journal of Physiology-Heart and Circulatory Physiology, 2008. **295**(3): p. H978-H989.

295. Fogal, V., et al., *Mitochondrial p32 protein is a critical regulator of tumor metabolism via maintenance of oxidative phosphorylation.* Molecular and cellular biology, 2010. **30**(6): p. 1303-1318.
296. Sun, R.C. and N.C. Denko, *Hypoxic regulation of glutamine metabolism through HIF1 and SIAH2 supports lipid synthesis that is necessary for tumor growth.* Cell metabolism, 2014. **19**(2): p. 285-292.
297. Vatrinet, R., et al., *The α-ketoglutarate dehydrogenase complex in cancer metabolic plasticity.* Cancer & metabolism, 2017. **5**(1): p. 3.
298. Metallo, C.M., et al., *Reductive glutamine metabolism by IDH1 mediates lipogenesis under hypoxia.* Nature, 2012. **481**(7381): p. 380.
299. Mullen, A.R., et al., *Reductive carboxylation supports growth in tumour cells with defective mitochondria.* Nature, 2012. **481**(7381): p. 385.
300. Wise, D.R., et al., *Hypoxia promotes isocitrate dehydrogenase-dependent carboxylation of α-ketoglutarate to citrate to support cell growth and viability.* Proceedings of the National Academy of Sciences, 2011. **108**(49): p. 19611-19616.
301. DeBerardinis, R.J., et al., *Beyond aerobic glycolysis: Transformed cells can engage in glutamine metabolism that exceeds the requirement for protein and nucleotide synthesis.* Proceedings of the National Academy of Sciences, 2007. **104**(49): p. 19345-19350.
302. de Groof, A.J., et al., *Increased OXPHOS activity precedes rise in glycolytic rate in H-RasV12/E1A transformed fibroblasts that develop a Warburg phenotype.* Molecular cancer, 2009. **8**(1): p. 1.
303. Ramanathan, A., C. Wang, and S.L. Schreiber, *Perturbational profiling of a cell-line model of tumorigenesis by using metabolic measurements.* Proceedings of the National Academy of Sciences, 2005. **102**(17): p. 5992-5997.
304. Li, H.Q., et al., *Micropatterning Extracellular Matrix Proteins on Electrospun Fibrous Substrate Promote Human Mesenchymal Stem Cell Differentiation Toward Neurogenic Lineage.* Acs Applied Materials & Interfaces, 2016. **8**(1): p. 563-573.
305. Bagher, Z., et al., *Cellular activity of Wharton's Jelly‐derived mesenchymal stem cells on electrospun fibrous and solvent‐cast film scaffolds.* Journal of Biomedical Materials Research Part A, 2016. **104**(1): p. 218-226.
306. Sreerekha, P.R., et al., *Fabrication of electrospun poly (lactide-co-glycolide)–fibrin multiscale scaffold for myocardial regeneration in vitro.* Tissue Engineering Part A, 2012. **19**(7-8): p. 849-859.
307. Haque, N., et al., *Hypoxic culture conditions as a solution for mesenchymal stem cell based regenerative therapy.* The Scientific World Journal, 2013. **2013**.
308. Marycz, K., et al., *Application of bone marrow and adipose-derived mesenchymal stem cells for testing the biocompatibility of metal-based biomaterials functionalized with ascorbic acid.* Biomedical Materials, 2013. **8**(6): p. 065004.
309. Ren, H., et al., *Proliferation and differentiation of bone marrow stromal cells under hypoxic conditions.* Biochemical and biophysical research communications, 2006. **347**(1): p. 12-21.
310. Tsai, C.-C., et al., *Oct4 and Nanog directly regulate Dnmt1 to maintain self-renewal and undifferentiated state in mesenchymal stem cells.* Molecular cell, 2012. **47**(2): p. 169-182.

311. Yang, D.-C., et al., *Hypoxia inhibits osteogenesis in human mesenchymal stem cells through direct regulation of RUNX2 by TWIST.* PloS one, 2011. **6**(9): p. e23965.
312. Kaelin Jr, W.G., *ROS: Really involved in Oxygen Sensing.* Cell Metabolism, 2005. **1**(6): p. 357-358.
313. Williams, A.R. and J.M. Hare, *Mesenchymal stem cells.* Circulation research, 2011. **109**(8): p. 923-940.
314. Al-Nbaheen, M., et al., *Human stromal (mesenchymal) stem cells from bone marrow, adipose tissue and skin exhibit differences in molecular phenotype and differentiation potential.* Stem Cell Reviews and Reports, 2013. **9**(1): p. 32-43.
315. Strioga, M., et al., *Same or not the same? Comparison of adipose tissue-derived versus bone marrow-derived mesenchymal stem and stromal cells.* Stem cells and development, 2012. **21**(14): p. 2724-2752.
316. Curtis, A. and M. Riehle, *Tissue engineering: the biophysical background.* Physics in Medicine & Biology, 2001. **46**(4): p. R47.
317. Jiao, Y.-P. and F.-Z. Cui, *Surface modification of polyester biomaterials for tissue engineering.* Biomedical Materials, 2007. **2**(4): p. R24.
318. Palin, E., H. Liu, and T.J. Webster, *Mimicking the nanofeatures of bone increases bone-forming cell adhesion and proliferation.* Nanotechnology, 2005. **16**(9): p. 1828.
319. Cochis, A., et al., *Bioreactor mechanically guided 3D mesenchymal stem cell chondrogenesis using a biocompatible novel thermo-reversible methylcellulose-based hydrogel.* Scientific Reports, 2017. **7**: p. 45018.
320. Hettiaratchi, M.H., R.E. Guldberg, and T.C. McDevitt, *Biomaterial strategies for controlling stem cell fate via morphogen sequestration.* Journal of Materials Chemistry B, 2016. **4**(20): p. 3464-3481.
321. Walters, N.J. and E. Gentleman, *Evolving insights in cell–matrix interactions: Elucidating how non-soluble properties of the extracellular niche direct stem cell fate.* Acta Biomaterialia, 2015. **11**: p. 3-16.
322. Zhang B, K.N., Li Q, Ma J, Yang A, Cui Z, Wang H, Ye H., *Effect of Substrate Topography and Chemistry on Human Mesenchymal Stem Cell Markers: A Transcriptome Study.* International Journal of Stem Cells, 2019 (In Press).
323. Cukierman, E., et al., *Taking Cell-Matrix Adhesions to the Third Dimension.* Science, 2001. **294**(5547): p. 1708.
324. Kim, J.-w., et al., *HIF-1-mediated expression of pyruvate dehydrogenase kinase: A metabolic switch required for cellular adaptation to hypoxia.* Cell Metabolism, 2006. **3**(3): p. 177-185.
325. Guo, S., et al., *Glucose up‐regulates HIF‐1α expression in primary cortical neurons in response to hypoxia through maintaining cellular redox status.* Journal of neurochemistry, 2008. **105**(5): p. 1849-1860.
326. Ishizuka, T., T. Hinata, and Y. Watanabe, *Superoxide induced by a high-glucose concentration attenuates production of angiogenic growth factors in hypoxic mouse mesenchymal stem cells.* Journal of Endocrinology, 2011. **208**(2): p. 147-159.
327. McMurray, R.J., *Nanoscale surfaces for the long-term maintenance of mesenchymal stem cell phenotype and multipotency*. 2011, University of Glasgow.

328. Song, H., et al., *Reactive oxygen species inhibit adhesion of mesenchymal stem cells implanted into ischemic myocardium via interference of focal adhesion complex.* Stem Cells, 2010. **28**(3): p. 555-563.
329. Raheja, L.F., et al., *Hypoxic regulation of mesenchymal stem cell migration: the role of RhoA and HIF‐1α.* Cell biology international, 2011. **35**(10): p. 981-989.
330. Azevedo, M.M., et al., *Hypoxia inducible factor-stabilizing bioactive glasses for directing mesenchymal stem cell behavior.* Tissue Engineering Part A, 2014. **21**(1-2): p. 382-389.
331. Mardis, E.R., *The impact of next-generation sequencing technology on genetics.* Trends in genetics, 2008. **24**(3): p. 133-141.
332. Schuster, S.C., *Next-generation sequencing transforms today's biology.* Nature methods, 2008. **5**(1): p. 16.
333. Vallabhaneni, K.C., et al., *Extracellular vesicles from bone marrow mesenchymal stem/stromal cells transport tumor regulatory microRNA, proteins, and metabolites.* Oncotarget, 2015. **6**(7): p. 4953.
334. Kaur, H., et al., *Next-generation sequencing: a powerful tool for the discovery of molecular markers in breast ductal carcinoma in situ.* Expert review of molecular diagnostics, 2013. **13**(2): p. 151-165.
335. Zhu, Y., et al., *In-depth study on aminolysis of poly(ε-caprolactone): Back to the fundamentals.* Science China Chemistry, 2012. **55**(11): p. 2419-2427.
336. Khurana, P., et al., *HypoxiaDB: a database of hypoxia-regulated proteins.* Database, 2013. **2013**.
337. Cho, K.-A., et al., *RNA sequencing reveals a transcriptomic portrait of human mesenchymal stem cells from bone marrow, adipose tissue, and palatine tonsils.* Scientific reports, 2017. **7**(1): p. 17114.
338. Kanehisa, M., *The KEGG database.* silico simulation of biological processes, 2002. **247**: p. 91-103.
339. Dennis, G., et al., *DAVID: database for annotation, visualization, and integrated discovery.* Genome biology, 2003. **4**(9): p. R60.
340. Mathew, S.A., B. Chandravanshi, and R. Bhonde, *Hypoxia primed placental mesenchymal stem cells for wound healing.* Life Sciences, 2017.
341. Zhang, J., et al., *Identification of the haematopoietic stem cell niche and control of the niche size.* Nature, 2003. **425**(6960): p. 836-841.
342. Gao, L., R. McBeath, and C.S. Chen, *Stem cell shape regulates a chondrogenic versus myogenic fate through Rac1 and N‐Cadherin.* Stem cells, 2010. **28**(3): p. 564-572.
343. Zhuang, Y., et al., *Chemokine stromal cell-derived factor 1/CXCL12 increases homing of mesenchymal stem cells to injured myocardium and neovascularization following myocardial infarction.* Chinese medical journal, 2009. **122**(2): p. 183-187.
344. Peled, A., et al., *Dependence of human stem cell engraftment and repopulation of NOD/SCID mice on CXCR4.* Science, 1999. **283**(5403): p. 845-848.
345. Yamashita, T., et al., *The microenvironment for erythropoiesis is regulated by HIF-2α through VCAM-1 in endothelial cells.* Blood, 2008. **112**(4): p. 1482-1492.
346. Dahl, K.D.C., et al., *Hypoxia-inducible Factor Regulates αvβ3 Integrin Cell Surface Expression.* Molecular Biology of the Cell, 2005. **16**(4): p. 1901-1912.

347. Aomatsu, E., et al., *Cell-cell adhesion through N-cadherin enhances VCAM-1 expression via PDGFRβ in a ligand-independent manner in mesenchymal stem cells.* International journal of molecular medicine, 2014. **33**(3): p. 565-572.
348. Leonel, J.C.M.V., *Engineering biomaterial surfaces with N-cadherin*. 2014: University of Illinois at Urbana-Champaign.
349. Haÿ, E., et al., *N‐Cadherin/Wnt Interaction Controls Bone Marrow Mesenchymal Cell Fate and Bone Mass During Aging.* Journal of cellular physiology, 2014. **229**(11): p. 1765-1775.
350. Vega, S.L., et al., *Single Cell Imaging to Probe Mesenchymal Stem Cell N-Cadherin Mediated Signaling within Hydrogels.* Annals of biomedical engineering, 2016. **44**(6): p. 1921-1930.
351. Xu, L., et al., *N-cadherin regulates osteogenesis and migration of bone marrow-derived mesenchymal stem cells.* Molecular biology reports, 2013. **40**(3): p. 2533-2539.
352. Liu, F., et al., *Changes in the expression of CD106, osteogenic genes, and transcription factors involved in the osteogenic differentiation of human bone marrow mesenchymal stem cells.* Journal of bone and mineral metabolism, 2008. **26**(4): p. 312-320.
353. Petruzzelli, R., et al., *HIF-2α regulates NANOG expression in human embryonic stem cells following hypoxia and reoxygenation through the interaction with an Oct-Sox cis regulatory element.* PloS one, 2014. **9**(10): p. e108309.
354. Du, W., et al., *VCAM-1+ placenta chorionic villi-derived mesenchymal stem cells display potent pro-angiogenic activity.* Stem cell research & therapy, 2016. **7**(1): p. 49.
355. Feng, W., et al., *The angiogenic response is dictated by β3 integrin on bone marrow–derived cells.* J Cell Biol, 2008. **183**(6): p. 1145-1157.
356. Carmeliet, P., *Integrin indecision.* Nature medicine, 2002. **8**(1): p. 14-16.
357. Kumar, C.C., et al., *Targeting Integrins α v β 3 and α v β 5 for Bloking Tumor-Induced Angiogenesis*, in *Angiogenesis*. 2000, Springer. p. 169-180.
358. Gutheil, J.C., et al., *Targeted antiangiogenic therapy for cancer using Vitaxin: a humanized monoclonal antibody to the integrin αvβ3.* Clinical Cancer Research, 2000. **6**(8): p. 3056-3061.
359. Di, Q., et al., *Impaired cross-activation of β 3 integrin and VEGFR-2 on endothelial progenitor cells with aging decreases angiogenesis in response to hypoxia.* International journal of cardiology, 2013. **168**(3): p. 2167-2176.
360. Kračun, D., et al., *The β3-Integrin Binding Protein β3-Endonexin Is a Novel Negative Regulator of Hypoxia-Inducible Factor-1.* Antioxidants & redox signaling, 2014. **20**(13): p. 1964-1976.
361. Hayashi, H., et al., *The Foxc2 transcription factor regulates angiogenesis via induction of integrin β3 expression.* Journal of Biological Chemistry, 2008. **283**(35): p. 23791-23800.
362. Robinson, S.D. and K.M. Hodivala-Dilke, *The role of β3-integrins in tumor angiogenesis: context is everything.* Current opinion in cell biology, 2011. **23**(5): p. 630-637.
363. Martin, S.K., et al., *Hypoxia-inducible factor-2 is a novel regulator of aberrant CXCL12 expression in multiple myeloma plasma cells.* Haematologica, 2010. **95**(5): p. 776-784.

364. Skuli, N., et al., *Endothelial deletion of hypoxia-inducible factor–2α (HIF-2α) alters vascular function and tumor angiogenesis.* Blood, 2009. **114**(2): p. 469-477.
365. Wouters, J., et al., *A novel hypoxia-associated subset of FN1highMITFlow melanoma cells: identification, characterization, and prognostic value.* Modern Pathology, 2014. **27**(8): p. 1088-1100.
366. Hughes, M.D., et al., *HIF-2α downregulation in the absence of functional VHL is not sufficient for renal cell differentiation.* Cancer cell international, 2007. **7**(1): p. 13.
367. Busletta, C., et al., *Dissection of the Biphasic Nature of Hypoxia‐Induced Motogenic Action in Bone Marrow‐Derived Human Mesenchymal Stem Cells.* Stem cells, 2011. **29**(6): p. 952-963.
368. Kondo, K., et al., *Inhibition of HIF2α is sufficient to suppress pVHL-defective tumor growth.* PLoS Biol, 2003. **1**(3): p. e83.
369. Shang, J., et al., *Roles of Hypoxia During the Chondrogenic Differentiation of Mesenchymal Stem Cells.* Current Stem Cell Research & Therapy, 2014. **9**(2): p. 141-147.
370. Corbion. *PURASORB® PL 24 Product data sheet*. 2015 March 2015 [cited 2016 Feb]; Available from: https://www.corbion.com/static/downloads/datasheets/46d/PURASORB%20PL%2024.pdf.
371. Abagnale, G., et al., *Surface topography guides morphology and spatial patterning of induced pluripotent stem cell colonies.* Stem cell reports, 2017. **9**(2): p. 654-666.
372. Abagnale, G., et al., *Surface topography enhances differentiation of mesenchymal stem cells towards osteogenic and adipogenic lineages.* Biomaterials, 2015. **61**: p. 316-326.
373. Jin, C., et al., *Nanoscale surface topography enhances cell adhesion and gene expression of madine darby canine kidney cells.* Journal of Materials Science: Materials in Medicine, 2008. **19**(5): p. 2215-2222.
374. Fiedler, J., et al., *The effect of substrate surface nanotopography on the behavior of multipotnent mesenchymal stromal cells and osteoblasts.* Biomaterials, 2013. **34**(35): p. 8851-8859.
375. Song, S., et al., *The synergistic effect of micro-topography and biochemical culture environment to promote angiogenesis and osteogenic differentiation of human mesenchymal stem cells.* Acta biomaterialia, 2015. **18**: p. 100-111.
376. Ullah, I., Raghavendra B. Subbarao, and Gyu J. Rho, *Human mesenchymal stem cells - current trends and future prospective.* Bioscience Reports, 2015. **35**(2): p. e00191.
377. Song, L. and R.S. Tuan, *Transdifferentiation potential of human mesenchymal stem cells derived from bone marrow.* Faseb j, 2004. **18**(9): p. 980-2.
378. Gao, F., et al., *Mesenchymal stem cells and immunomodulation: current status and future prospects.* Cell Death & Disease, 2016. **7**(1): p. e2062.
379. Dominici, M., et al., *Minimal criteria for defining multipotent mesenchymal stromal cells. The International Society for Cellular Therapy position statement.* Cytotherapy, 2006. **8**.
380. Suila, H., et al., *Are globoseries glycosphingolipids SSEA-3 and -4 markers for stem cells derived from human umbilical cord blood?* Journal of Molecular Cell Biology, 2011. **3**(2): p. 99-107.

381. Pham, H., et al., *CD73, CD90, CD105 and Cadherin-11 RT-PCR Screening for Mesenchymal Stem Cells from Cryopreserved Human Cord Tissue.* International journal of stem cells, 2018. **11**(1): p. 26.
382. Lv, F.-J., et al., *Concise Review: The Surface Markers and Identity of Human Mesenchymal Stem Cells.* STEM CELLS, 2014. **32**(6): p. 1408-1419.
383. Zhang, Z., M.J. Gupte, and P.X. Ma, *Biomaterials and stem cells for tissue engineering.* Expert Opinion on Biological Therapy, 2013. **13**(4): p. 527-540.
384. Mahara, A. and T. Yamaoka, *Continuous separation of cells of high osteoblastic differentiation potential from mesenchymal stem cells on an antibody-immobilized column.* Biomaterials, 2010. **31**(14): p. 4231-4237.
385. Sambu, S., et al., *RGDS-fuctionalized alginates improve the survival rate of encapsulated embryonic stem cells during cryopreservation.* Cryo Letters, 2011. **32**(5): p. 389-401.
386. Choi, Y.S., S.-N. Park, and H. Suh, *Adipose tissue engineering using mesenchymal stem cells attached to injectable PLGA spheres.* Biomaterials, 2005. **26**(29): p. 5855-5863.
387. Dalby, M.J., N. Gadegaard, and R.O.C. Oreffo, *Harnessing nanotopography and integrin-matrix interactions to influence stem cell fate.* Nat Mater, 2014. **13**(6): p. 558-569.
388. Jang, H.-K. and B.-S. Kim, *Modulation of stem cell differentiation with biomaterials.* International journal of stem cells, 2010. **3**(2): p. 80.
389. McMurray, R.J., et al., *Nanoscale surfaces for the long-term maintenance of mesenchymal stem cell phenotype and multipotency.* Nat Mater, 2011. **10**(8): p. 637-644.
390. Dalby, M.J., et al., *The control of human mesenchymal cell differentiation using nanoscale symmetry and disorder.* Nat Mater, 2007. **6**(12): p. 997-1003.
391. Benoit, D.S.W., et al., *Small functional groups for controlled differentiation of hydrogel-encapsulated human mesenchymal stem cells.* Nat Mater, 2008. **7**(10): p. 816-823.
392. Mendicino, M., et al., *MSC-Based Product Characterization for Clinical Trials: An FDA Perspective.* Cell Stem Cell, 2014. **14**(2): p. 141-145.
393. Duffy, C.R., et al., *Long term mesenchymal stem cell culture on a defined synthetic substrate with enzyme free passaging.* Biomaterials, 2014. **35**(23): p. 5998-6005.
394. Kasoju, N., et al., *Transcriptomics of human multipotent mesenchymal stromal cells: Retrospective analysis and future prospects.* Biotechnology Advances, 2017. **35**(4): p. 407-418.
395. Sargent, A., et al., *Transcriptional Profiling of Mesenchymal Stem Cells Identifies Distinct Neuroimmune Pathways Altered by CNS Disease.* International journal of stem cells, 2018. **11**(1): p. 48.
396. Shannon, P., et al., *Cytoscape: a software environment for integrated models of biomolecular interaction networks.* Genome research, 2003. **13**(11): p. 2498-2504.
397. Girvan, M. and M.E. Newman, *Community structure in social and biological networks.* Proceedings of the national academy of sciences, 2002. **99**(12): p. 7821-7826.
398. Bounova, G., *Octave Networks Toolbox.* Zenodo, 2015, August 2.
399. Skardal, A., et al., *Substrate elasticity controls cell proliferation, surface marker expression and motile phenotype in amniotic fluid-derived stem cells.*

Journal of the Mechanical Behavior of Biomedical Materials, 2013. **17**: p. 307-316.
400. Zamparelli, A., et al., *Growth on poly(l-lactic acid) porous scaffold preserves CD73 and CD90 immunophenotype markers of rat bone marrow mesenchymal stromal cells.* Journal of Materials Science: Materials in Medicine, 2014. **25**(10): p. 2421-2436.
401. Colgan, S.P., et al., *Physiological roles for ecto-5'-nucleotidase (CD73).* Purinergic Signalling, 2006. **2**(2): p. 351-360.
402. Mihara, K., et al., *Development and functional characterization of human bone marrow mesenchymal cells immortalized by enforced expression of telomerase.* British journal of haematology, 2003. **120**(5): p. 846-849.
403. Yao, G., et al., *Origin of bistability underlying mammalian cell cycle entry.* Molecular systems biology, 2011. **7**(1): p. 485.